Modeling Effects of External Convective Heat Transfer on Rotating Blades in Anti-Icing Operations

by

Abdallah SAMAD

THESIS PRESENTED TO ÉCOLE DE TECHNOLOGIE SUPÉRIEURE
IN PARTIAL FULFILLMENT FOR THE DEGREE OF
DOCTOR OF PHILOSOPHY
Ph.D.

MONTRÉAL, 23 FEBRUARY 2021

ÉCOLE DE TECHNOLOGIE SUPÉRIEURE
UNIVERSITÉ DU QUÉBEC

BOARD OF EXAMINERS

THIS THESIS HAS BEEN EVALUATED

BY THE FOLLOWING BOARD OF EXAMINERS

Mr. François Morency, Thesis Supervisor
Mechanical Engineering Department at École de Technologie Supérieure

Mr. Christophe Volat, Thesis Co-Supervisor
Department of Applied Sciences at Université du Québec à Chicoutimi

Mr. James Lapalme, President of the Jury
Department of Systems Engineering at École de Technologie Supérieure

Mr. François Garnier, Member of the Jury
Mechanical Engineering Department at École de Technologie Supérieure

Mr. Mathieu Olivier, External Examiner
Mechanical Engineering Department at Université Laval

THIS THESIS WAS PRESENTED AND DEFENDED

IN THE PRESENCE OF A BOARD OF EXAMINERS AND THE PUBLIC

ON FEBRUARY 4TH 2021

AT ÉCOLE DE TECHNOLOGIE SUPÉRIEURE

ACKNOWLEDGMENTS

Thank you Prof. *François Morency* for being my research director. For the last four years, I have been highly inspired by your professionalism, punctuality, and guidance. I am glad and grateful for working with you. I wish you all the best in your future endeavors.

From the ÉTS team, *Gitsuzo Tagawa* was a great source of help with the CFD simulations of this work so for this, I would like to express for him my sincere gratitude. Many thanks to the UQAC team for helping with the experimental work of this thesis. Special thanks to Prof. *Christophe Volat*, *Éric Villeneuve* and *Carol Mercier*.

To my father *Majed* and mother *Sahar*, the greatest people I have known. This thesis is a token of appreciation for the years of your lives that you spent raising me and my siblings. Many thanks to you for the never-ending support. Over the years, I know how much you sacrificed for the sole purpose of seeing me succeed. I am sure I will never be able to fully repay you, but I do hope this makes you proud.

To my lovely wife *Aya*, who is the most amazing, loving, and kindest person I have known. Thank you for choosing to share your life with me, supporting me, pushing me to succeed and for sharing my dreams. You shared with me some of the most difficult times of my life, but you also brought the most joyous and happiest. I hope I spend my life next to you, loving you and living the best life we could.

To my first boy *Majed*, this work is dedicated to you. I hope it inspires you throughout your life to become the best at whatever you choose to do. Until then, I hope that me, your mom, and you spend our years in uttermost joy and love.

Finally, thank you for my siblings and my friends for believing in me and helping me. Without your good company and support, I would not have done it.

Modeling Effects of External Convective Heat Transfer on Rotating Blades in Anti-Icing Operations

Abdallah SAMAD

RÉSUMÉ

Le calcul du transfert de chaleur convectif en régime non permanent sur les pales d'hélicoptère est une première étape dans la prévision de l'accrétion de glace et la conception de systèmes de protection contre la glace. Les simulations CFD sont considérées comme un modèle haute fidélité de l'aérodynamique complexe des rotors ainsi que du transfert de chaleur sur les surfaces des pales. La littérature indique que des méthodes de couplage ont émergé pour modéliser des problèmes aérodynamiques d'une manière rapide et efficace, utile pour une conception conceptuelle. Les méthodes de couplage sont définies comme le couplage de méthodes aérodynamiques classiques avec des bases de données CFD visqueuses, dans le but d'augmenter la fidélité du modèle classique tout en maintenant sa solution relativement peu coûteuse en calcul. L'objectif principal de cette thèse est de développer des outils numériques basés sur une nouvelle méthodologie de couplage pour calculer le transfert de chaleur convectif externe sur des pales rotatives lors d'un chauffage lors de l'antigivrage. Quatre objectifs spécifiques sont fixés: 1- Construire une base de données visqueuses et de transfert de chaleur pour un profil aérodynamique; 2- Développer un outil aérodynamique rotor basse fidélité couplé à la base de données CFD; 3- Développer un outil aérodynamique rotor de moyenne fidélité couplé à la base de données CFD; et 4 - Comparer les résultats des outils basse et moyenne fidélité à ceux des travaux expérimentaux menés sur une voilure fixe chauffée et un rotor à 2 pales. La nouveauté de cette recherche provient de l'introduction d'une couche supplémentaire de la technique de couplage pour prédire le transfert de chaleur des pales de rotor à l'aide de la Blade Element Momentum Theory (BEMT) et de la Unsteady Vortex Lattice Method (UVLM). La nouvelle approche met en œuvre le couplage visqueux des deux méthodes d'une part et introduit un lien vers une corrélation de transfert de chaleur déterminée par CFD. De cette façon, le transfert de chaleur convectif sur les pales du rotor est estimé tout en bénéficiant de l'extension visqueuse du BEMT et UVLM. Une base de données de transfert de chaleur pour un profil aérodynamique est construite à l'aide de simulations CFD RANS pour une large gamme de Re et α ainsi que pour deux conditions aux limites thermiques différentes TBC. Une méthode d'ajustement de courbe est appliquée sur les nombres de Frossling moyens Fr_{Avg} et maximum Fr_{Max} obtenus. Quatre corrélations sont alors proposées pour le Fr_{Avg} et le Fr_{Max}, deux pour chaque (TBC). La prédiction du transfert de chaleur CFD est vérifiée à l'aide des corrélations existantes pour une plaque plane et validée en comparant le transfert de chaleur prévu sur le profil aérodynamique aux données expérimentales de la littérature. Les prévisions de poussée de l'UVLM et du BEMT mis en œuvre concordent à 92% et 80% par rapport aux données expérimentales pour les rotors en vol stationnaire, axial et horizontal. Les tourbillons de bout d'aile par l'UVLM sont prédits à moins de 90%. Les résultats finaux se présentent comme une estimation du transfert de chaleur pour un rotor de queue d'hélicoptère léger typique pour quatre modes de vol. Concernant les expériences à voilure fixe, les comparaisons de simulations CFD indiquent un écart entre 5% et 32%, suspecté d'être dû à des effets de transition d'écoulement. Pour les essais de rotor, la plupart des points des expériences

concordaient avec les prédictions BEMT-RHT et UVLM-RHT entre 5% et 12%, bien qu'un écart maximal de 80% ait été trouvé. Les essais du rotor ont montré que pour un rotor soumis à un écoulement d'air, la turbulence sera présente dans toutes les sections de pale. Cela entraînera des augmentations du transfert de chaleur à travers les sections de profil aérodynamique qui sont plus élevées que ce que l'on trouve sur un écoulement autour d'un profil aérodynamique à faible turbulence. L'utilisation de la base de données CFD entièrement turbulente avec le BEMT-RHT et l'UVLM-RHT a donc été utile pour calculer le transfert de chaleur sur les pales du rotor. Cependant, sa principale limite résidait dans l'estimation correcte de l'effet de transition sur le transfert de chaleur.

Mots-Clés: Méthode Instationnaire Vortex Lattice; Théorie de l'Élément du Moment de Pale; Transfert de Chaleur par Convection; Givrage / Dégivrage; Rotorcraft

Modeling Effects of External Convective Heat Transfer on Rotating Blades in Anti-Icing Operations

Abdallah SAMAD

ABSTRACT

Calculating the unsteady convective heat transfer on helicopter blades is a first step in the prediction of ice accretion and the design of ice-protection systems. CFD simulations are considered a high-fidelity model of the complex aerodynamics of rotors as well as the heat transfer on blade surfaces. The literature indicates that coupling methods have emerged to model aerodynamic problems in a fast and efficient way, convenient for a conceptual design. Coupling methods are defined as the coupling of classical aerodynamic methods with viscous CFD databases, with the purpose of increasing the classical model fidelity yet maintaining its relatively computationally inexpensive solution. The main objective of this thesis is to develop numerical tools based on a new methodology of coupling to calculate the external convective heat transfer onto rotating blades while heated during anti-icing. Four specific objectives are set : 1- Build a viscous and heat transfer database for an airfoil; 2- Develop a low-fidelity rotor aerodynamic tool coupled with the CFD database; 3- Develop a medium-fidelity rotor aerodynamic tool coupled with the CFD database; and 4 – Compare results from the low and medium fidelity tools to those of experimental work conducted on a heated fixed wing and 2-blade rotor. The novelty of this research originates from the introduction of an added layer of the coupling technique to predict rotor blade heat transfer using the Blade Element Momentum Theory (BEMT) and the Unsteady Vortex Lattice Method (UVLM). The new approach implements the viscous coupling of the two methods from one hand and introduces a link to a new airfoil CFD-determined heat transfer correlation. This way, the convective heat transfer on rotor blades is estimated while benefiting from the viscous extension of the BEMT & UVLM. An airfoil viscous and heat transfer database is built using CFD RANS simulations for a wide range of Re and α as well as two different thermal boundary conditions TBC. A curve fitting method is applied on the obtained average and maximum Frossling Number Fr_{Avg} and Fr_{Max}. Four correlations are then proposed for the Fr_{Avg} and Fr_{Max}, two for each TBC. The CFD heat transfer prediction is verified using existing correlations for a flat plate and validated by comparing the predicted airfoil heat transfer to experimental data from the literature. Thrust predictions by the implemented UVLM and BEMT agree within 92% and 80% compared to experimental data for rotors in hover, axial and forward flight. Tip vortex locations by the UVLM are predicted within 90%. The end results present as an estimate of the heat transfer for a typical lightweight helicopter tail rotor for four flight modes. Regarding the fixed wing experiments, comparisons CFD simulations indicate a discrepancy between 5% and 32%, suspected to be due to flow transition effects. For the rotor tests, most points of the experiments agreed with BEMT-RHT and UVLM-RHT predictions between 5% and 12%, although a maximum discrepancy of 80% was found. The rotor tests showed that for a rotor subjected to a freestream of air, turbulence will be present throughout the blade sections. This will cause increases of the heat transfer throughout the airfoil sections that are higher than what's found on a no-to-low turbulence airfoil flow. The use of the fully turbulent CFD database with the BEMT-RHT and UVLM-RHT was therefore useful in calculating the heat transfer on the rotor

X

blades. Its main limitation however was in the lack of a proper estimation of the transition effect on heat transfer.

TABLE OF CONTENTS

XIV

LIST OF TABLES

LIST OF FIGURES

LIST OF ABBREVIATIONS & ACRONYMS

BET	Blade Element Theory
BEMT	Blade Element Momentum Theory
UVLM	Unsteady Vortex Lattice Method
RHT	Rotor Heat Transfer
TBC	Thermal Boundary Condition
RTD	Resistance Temperature Detector
P-SRB	Powered Spinning Rotor Blades
RHS	Right Hand Side
SU2	Stanford University Unstructured (Software)
CFD	Computational Fluid Dynamics
RANS	Reynolds Averaged Navier-Stokes
S-A	Spalart–Allmaras (Turbulence Model)
NACA	National Advisory Committee for Aeronautics
L.E.	Leading Edge
T.E.	Trailing Edge
OGE	Out-of-Ground-Effect
IGE	In-Ground-Effect

LIST OF SYMBOLS & UNITS OF MEASUREMENTS

Symbols

A	Rotor Disk Area (m^2)	Q	Rotor Torque (N)
(A, B, C, m)	Correlation Coefficients	Q_S	Surface Heat Flux (W/ m^2)
		Q_c	Blade Lattice Collocation Point
AR	Advance Ratio	Q_F	Blade Lattice Corner Point
CH	Ground Clearance (m)	Q_W	Wake Lattice Corner Point
CR	Climb Ratio	Q_{Elec}	Electric Heat Input (W/m^2)
C_{L-visc}	Viscous Lift Coefficient	Q_{Rad}	Radiative Heat Transfer (W/m^2)
C_{L-inv}	Inviscid Lift Coefficient	Q_{Cond}	Conductive Heat Transfer (W/m^2)
C_{L0}	Lift Coefficient at 0 AOA	r	Rotor Radial Increment
C_{Ly}	Sectional Lift Coefficient	r_c	Vortex Core Size (m)
C_D	Drag Coefficient	r_0	Vortex Initial Core Size (m)
C_T	Thrust Coefficient	$R - R_{Tip}$	Blade Tip Radius (m)
C_{Ty}	Sectional Thrust Coefficient	R_{Root}	Rotor Root Radius (m)
C_P	Power Coefficient	R''	Thermal Resistance (m^2.K/W)
C_{Pi}	Induced Power Coefficient	Re_L	Reynold's Number (Length of Flat Plate)
C_{Po}	Profile Power Coefficient	Re_d	Reynold's Number (Cylinder Diameter)
C_p	Specific Heat Capacity (kJ/kg.K)	Re_c	Reynold's Number (Airfoil Chord)
C_f	Friction Coefficient	R_G	Specific Gas Constant (N.m/kg.K)
$C_{L\alpha}$	Slope of Viscous Lift Curve	S	Surface Wrap Distance (m)
D	Drag Force (N)	S/c	Dimensionless Surface Wrap Distance
f	Prandtl's Tip Loss Parameter	T	Rotor Thrust (N)
F	Prandtl's Tip Loss Factor	T_∞	Freestream Temperature (K)
Fr_x	Local Frossling Number	T_S	Blade Surface Temperature (K)
Fr_{Avg}	Average Frossling Number	T_f	Film, or median, Temperature (K)
FM	Figure of Merit	T_{rec}	Recovery Temperature (K)
h	Convective Heat Transfer Coefficient (W/m^2.K)	T_T	Total Air Temperature (K)
h/R	Ground Clearance Ratio	TI	Turbulence Intensity (%)
I_A	Current (Amps)	U_V	Voltage (Volts)
I	Number of Lattices in the Chord Direction	U_T	Tangential Velocity Component (m/s)

J	Number of Lattices in the Span Direction	U_P	In-Plane Velocity Component (m/s)
		U	Resultant Velocity (m/s)
k	Thermal Conductivity (W/m.K)	U_R	Radial Velocity Component (m/s)
L	Lift Force (N)	(u, v, w)	Blade Induced Velocities (m/s)
Ma	Mach Number	(u_w, v_w, w_w)	Wake Induced Velocities (m/s)
N_A	Number of Revolutions Traveled	v_i	Rotor Induced Velocity (m/s)
N_b	Number of Blades	V_∞	Freestream Velocity (m/s)
N_{SS}	Slow-Start Number of Revolutions	V_c	Climb Velocity (m/s)
N_{Total}	Total Number of Revolutions	x/c	Dimensionless Chord Distance
Nu_x	Local Nusselt Number	(x, y, z)	Coordinates in Body-fixed Frame of Reference (m)
Nu_{Avg}	Average Nusselt Number	(X, Y, Z)	Coordinates in Inertial Frame of Reference (m)
P	Rotor Power		
P_{dyn}	Dynamic Pressure (N/m^2)		
Pr	Prandtl Number		

Greek Letters

ϕ	Roll Angle (°)	Ω	Rotor Angular Velocity (rad/s)
Ψ	Azimuth Angle (°)	θ	Blade Pitch Angle (°)
β	*Glauert* Compressibility Correction Factor	φ	Inflow Angle (°)
n	Normal Vector	α	Angle of Attack (°)
γ	Specific Heat Ratio	α_{Eff}	Effective Angle of Attack (°)
σ	Blade Rigidity	α_i	Induced Angle of Attack (°)
σ_{SB}	Stefan-Boltzmann Constant	α_0	Zero Lift Line Angle of Attack (°)
υ	Emissivity	μ	Dynamic Viscosity (N.s/m^2)
δ	Thickness (m)	ω	Induced Velocity (m/s)
λ	Inflow Ratio	Γ	Vortex Strength (m^2/s)
λ_i	Induced Inflow Ratio	Δt	Timestep (s)
λ_c	Climb Inflow Ratio	Δp	Pressure Difference (N/m^2)
ε_1	Convergence Criterion for λ	ν	Kinematic Viscosity (m^2/s)
ε_2	Vortex Core Size Limit (m)	Λ_x	Turbulence Length Scale
ε_3	Convergence Criterion for Viscous Coupling Algorithm		

INTRODUCTION

Icing is a serious problem that faces aircraft operations. Relatively low ice thicknesses disrupt the air flow around lifting elements and control surfaces of aircrafts. During flight, liquid water impinging on an aircraft will freeze to its surfaces even when the Outside Air Temperature (OAT) is above 0°C (*Guidelines for Aircraft Ground Icing Operations 4th Edition*, 2019). Rotorcrafts are vulnerable to in-flight and pre-flight icing which considerably limits their operation. Indeed, icing causes flight delays during ground de-icing interventions, flight cancellations because of forecast or actual in-cloud icing. According to (*Helicopter Flying Handbook*, 2012), pilot reduced visibility is a direct result of in-flight ice accumulation on windscreen and instrument ports. In addition, added weight on the airframe reduces the load capacity and increases fuel consumption. In the case of a helicopter, the most adverse effect of blade contamination comes from the aerodynamics of the iced main rotor blade which will result in reduced lift and an increase in drag. A subsequent loss of thrust and possible flow separation generated by the main and tail rotors may lead to total loss of control. Severe vibrations may also be induced by the symmetric shedding of ice that can force emergency landings. All in all, icing poses major security concerns for helicopters. Although the primary concern is with the main rotor, protection of the tail rotor requires similar considerations.

A Brief History

With the turn of the 20th century, aviation emerged as a fast and convenient way to transport people, luggage and cargo and has made remarkable advances ever since (Shaw, 2014). Pilots and operators were rarely concerned with the problem of icing in the first two decades of powered flight, and their best way to avoid ice was to avoid clouds, or to not fly altogether. The situation changed when the U.S. Air Mail Service attempted to maintain scheduled day-and-night operations between New York and Chicago in the mid 1920's. In 1926, the first non-fatal icing related accident was documented, the first fatal occurrence however was only a year later and were both for Air Mail Service aircrafts (Leary, 2002).

To respond to a growing number of reported icing-related incidents and accidents, NACA's Langley Memorial Aeronautical Laboratory (now part of NASA) officially began flight icing related research in 1928 (Potapczuk, 2013). The early in-flight investigations in the same year made the first distinction between the types of ice: rime ice and glaze ice. Also in 1928, laboratory research began at Langley's refrigerated wind tunnel. According to (Leary, 2002), the first tests were done on a Clark Y mahogany airfoil where different coatings were studied as possible ice-prevention substances. Researchers unsuccessfully tested substances ranging from lubricating oil to Vaseline to goose grease. The first substance that was seen to provide some degree of ice protection was White Karo corn syrup. They also made a remarkable conclusion where they noted that the ice formed only on the leading edge of the airfoil in all their tests and that it required special attention.

Ice protection research boomed around the year 1950, helicopter manufacturers and government agencies raced to conduct research and development on various methods of icing protection for helicopter rotors. In those years, NACA transferred its ice-prevention program to the Lewis Icing Research Tunnel (IRT) and emphasized heavily on the study of the physics of icing clouds (Leary, 2002). In 1945, Sikorsky Aircraft Corporation began researching inflight icing, developing and producing ice protection system (Flemming, 2003). It would later experiment on a hot air running-wet rotor anti-icing system between 1949 and 1953, rotor ice phobic tapes in the mid 1950's and electrothermal rotor ice protection technology in 1957. Worthy to mention that the latter was tested on Sikorsky H-34 helicopter in the National Research Council of Canada (NRC) icing spray rig in Ottawa. Bell Flight (previously Bell Helicopter) followed and its earliest rotorcraft icing tests was in 1958 (Aubert, 2003). It would later develop and test a main and tail rotor fluid anti-icing system in 1960, an electro vibratory de-icing system in 1978 and a pneumatic rotor de-icing system in 1984.

Ice protection research have come a long way since then and the importance of ice protection systems grew proportionally to the ever-increasing need for air travel and transport. With the advent of computers in the early 1980's, ice prediction codes emerged and allowed the resolution of the Navier-Stokes equations. Among the first codes was LEWICE (Wright,

2008), created in 1983. It was based on the solution of a potential flow in 2D and the solution of boundary layer equations. With the turn of the new millennium, several icing/de-icing tools have been developed internationally such as LEWICE (Wright, 2008), ONERA (Guffond & Brunet, 1988; Montreuil et al., 2009), FENSAP-ICE (Beaugendre, Morency, & Habashi, 2003) and CANICE (Gouttebroze, Saeed, & Paraschivoiu, 2000; Morency, Tezok, & Paraschivoiu, 1999). Between each other, these codes can conduct icing/de-icing simulations for problems ranging from isolated wings to rotors and complete aircraft configurations (Aliaga, Aubé, Baruzzi, & Habashi, 2011; Beaugendre, Morency, & Habashi, 2006; Habashi, 2009; Habashi et al., 2004; Pendenza, Habashi, & Fossati, 2015; Pourbagian & Habashi, 2012).

Solutions for Rotorcraft Icing

According to (*Guidelines for Aircraft Ground Icing Operations 4th Edition*, 2019), it is forbidden to fly an aircraft that has frost, ice or snow adhering to any of its critical surfaces in Canada. Ground de-icing techniques for fixed wings involve using heated glycol deicing solutions that may be damaging to rotorcraft composite material components. Transport Canada recommends hangar storage for helicopters as the best way to ensure no ice and snow build up in freezing weather conditions. Although mechanical removal of ice by means of chipping or thermal tools such as hot air and infrared heating may be useful, a great deal of caution should be exercised to ensure no damage of blades or critical surfaces is done.

There are two types for in-flight ice protection, anti-icing and de-icing (*Helicopter Flying Handbook*, 2012). The source defined anti-icing as the process of preventing ice formation on aircraft surfaces. One form of anti-icing is the application of certain chemicals on critical surfaces that continuously delay the reformation, or adhesion, of ice for a certain period of time. De-icing is also defined as continuous process of ice formation and elimination. This process typically allows a thin layer of ice to form on the surface before being removed, the process of ice formation/elimination is then repeated throughout flight. Over the years and on different rotorcraft models, different anti-icing/de-icing techniques have been developed.

Pneumatic de-icing boots are made of layers (or chambers) of rubber or other elastomers, typically placed on the leading edge of wings or propellers. The chambers are rapidly inflated and deflated causing a rapid change of shape, breaking the adhesive force between the ice and the rubber and carrying the shed ice with the wind flowing past the aircraft. The pneumatic de-icing boot is most appropriate for low and medium speed aircraft, the device is not suitable for use on turbojet aircraft nor does it offer efficient de-icing for rotorcrafts, although it has been used on UH-1 rotor blades in the past (Coffman, 1987).

A bleed hot-air system is an efficient anti-icing/de-icing system that is commonly used by larger jet aircraft to either keep flight surfaces above the freezing temperature required for ice to accumulate or to cyclically de-ice the surface in flight. The hot air is "bled" off the engine exhaust into piccolo tubes routed through wings, tail surfaces, and engine inlets. Holes in the lower surface of the wing then shoot the hot air towards the ice layer, causing it to melt. A similar concept anti-icing system for rotorcrafts is the hot gas anti-icing system described in (Richardson, Wahl, & Clifford, 1958). The latter involves the addition of a burner element near the rotor hub throughout a fuel-air mixture is burned and its hot exhaust transported through the blades. The hot gas anti-icing system for rotorcraft is now considered obsolete.

Electro-vibratory systems (recently identified as Piezo-Electric systems) work by "shaking" the blade at a frequency matching the blade's natural frequency, delivering enough force to break-off the ice (Coffman, 1983). Although they have been developed a few decades ago, recent research shows their re-emergence as potential rotorcraft de-icing systems (Villeneuve, Volat, & Ghinet, 2020).

The most common ice protection system used on rotorcrafts however is the electrothermal de-icing system (Potapczuk, 2013). It consists of heating elements in the form of wires, foils or spray-mats that are buried in the blade composite material layers. Heating elements can be distributed on separate zones across the blade chord and span to offer periodic and cyclic de-icing. They can operate in anti-icing mode; an impractical power consumption is however needed to prevent ice formation altogether. Electrothermal de-icing systems are reliable and

have been in development since the 1950s (Richardson et al., 1958). They continue to be studied to this day particularly in optimization studies based on cyclic patterns and solutions for runback and refreeze.

Other ice protection systems for rotorcrafts include fluid anti-icing systems that have been on a UH-1H and were safe and reliable. A lack of funding caused no further development for fluid anti-icing systems on rotorcrafts, it was however later developed and implemented on passenger jets by the TKS company in the UK (Coffman, 1983). Electro-impulse rotor de-icing systems offer another form of ice protection by means of a small amplitude; high acceleration "hit" delivered by a capacitor discharge in copper coils installed inside the blades. The coils and wirings of electro-impulse systems are difficult to install on rotor blades compared to larger fixed wings, especially near the leading edge (Coffman, 1987). Lastly, the newest research is investigating lightweight ice-phobic (anti-icing) materials or coatings as new ice protection methods. These materials are placed in strategic areas could significantly reduce ice formation and improve performance (*Helicopter Flying Handbook*, 2012).

Problematic

Even with the capability of rotorcrafts to operate in icy conditions considered a necessity, the area of de-icing and anti-icing remains a largely unfulfilled aspiration (Aubert, 2015; Ryerson, Peck, & Martel, 2003). The only ice protection systems in use today are electro-thermal systems consisting of periodically heating iced leading edge of rotor blades; although they have been in research and development for several decades as was noted earlier (Gent, Moser, Cansdale, & Dart, 2003). According to (SAE, 2013), a rather small number of helicopter types have achieved full icing qualification to either civil or military certification specifications. The same source indicates that the main reason for this is the high energy load required for heating as well as the high electrical current flowing in the slip rings and the long cabling required. Therefore, only the main rotors of large rotorcrafts can be currently equipped with certified electro-thermal de-icing systems. This leaves smaller helicopters prohibited from flying in icy

conditions since they cannot be equipped with an electro-thermal de-icing system because of the low power available.

Despite the years-long studies related to icing and ice prevention and elimination, there is a lack of basic understanding of in-flight ice adhesion and shedding processes, especially those prevailing on a rotating blade where centrifugal forces exert, according to (Aubert, 2015). Moreover, a complete design process for aircrafts, systems and components takes years, passes through many stages of design, with each requiring different fidelity-methods and precisions, and costs an enormous amount of funding (Piperni, DeBlois, & Henderson, 2013). According to (Rizzi, 2011), a significant portion of that cost is spent in the initial design stages, where preliminary design errors can accumulate and echo more costs in later design steps. In the conceptual design stage, which is one of the earliest in the design chain during which feasibility studies take place, methods that are reliable, quick, and computationally inexpensive are favored (Piperni et al., 2013).

Recent computing advances led to the development of high-fidelity software on thermal exchanges occurring on fixed wings or rotors heated for de-icing. High-fidelity software and existing icing/de-icing codes however require large computing resources that makes them impractical for a conceptual design. A medium fidelity tool that predicts heat transfer on rotor blades with less computing power and with a quicker solution offers a competitive approach for conceptual designs. To the best of our knowledge, such a software does not exist nor has been tried out in the past and remains to be developed.

Project ENV 702

This thesis corresponds to the research related to goal #4 of the project ENV 702. Titled "Low Power De-icing Systems for Lightweight Helicopters", the project is a joint National Research Council of Canada (NRC) and Consortium for Research and Innovation in Aerospace of Québec (CRIAQ) granted project involving as partners a team of three Canadian industries: Bell Flight (Previously Bell Helicopter Textron Canada BHTC), MagChem Canada (MCC),

and Iders Canada IC; three universities and a government laboratory: the Université du Québec à Chicoutimi (UQAC) with its Anti-Icing Materials Laboratory (AMIL), the École Polytechnique de Montréal (Poly), the École de Technologie Supérieure (ÉTS) of Montréal and the National Research Council Institute for Aerospace Research (NRC-IAR).

That proposal aims to investigate the three low-energy approaches demonstrated in two previous NSERC-subsidized projects. These are ice-phobic coatings, piezo-electric actuators, and MMG technology. The project also aims to develop a better understanding of the ice adhesion and heat exchange processes involved in rotating blade de-icing. The main goals of the project are fivefold, with the current thesis corresponding to the work conducted for goal #4.

1. Develop new erosion resistant ice-phobic coatings (UQAC – AMIL);
2. Develop durable piezoelectric de-icing actuator system (UQAC – AMIL);
3. Develop a wireless system to control the heating of rotorcraft blades through an MMG (Poly);
4. Modelling effects of external convective heat transfer during rotating blade de-icing (ÉTS);
5. Modelling of ice adhesion (UQAC – AMIL).

Thesis Objectives

The main objective of this thesis is to develop numerical tools that calculate the external convective heat transfer onto rotating blades while heated during anti-icing. This is achieved by implementing a new methodology of coupling between CFD determined viscous plus heat transfer databases and classical rotor aerodynamic methods as a computationally inexpensive approach. Specifically, the classical aerodynamics methods would be the low-fidelity Blade Element Momentum Theory (BEMT) and the medium-fidelity Unsteady Vortex Lattice Method (UVLM). The thesis will be responsible of defining the physical and thermodynamic aspects pertaining to the theoretical work. Low and medium-fidelity models will help quantify

the influence of the design's convective heat transfer and its distribution over the span of the rotating blade in a computationally inexpensive way. The main objective is split into four specific objectives as follows:

- Build a database of airfoil viscous and heat transfer data using 2D CFD simulations and correlate the average heat transfer data using a curve fitting method
- Develop & validate a low-fidelity (steady-state) numerical tool that uses a viscous implementation of the BEMT as a rotor aerodynamic modeling tool, and apply a coupling method to the heat transfer correlations to allow blade heat transfer calculation
- Develop & validate a medium-fidelity (unsteady) numerical tool that uses a viscous implementation of the UVLM as a rotor aerodynamic modeling tool, and apply a coupling method to the heat transfer correlations to allow blade heat transfer calculation
- Compare the convective heat transfer predictions of the low and medium fidelity tools to measurements obtained through experimental work designed and conducted in the Icing Wind Tunnel (IWT) of the UQAC on the surface of a heated fixed wing and a heated 2-blade rotor

Thesis Plan

The first chapter of the thesis will be addressed towards a review of the state-of-the-art literature. This is done to justify our choice of a coupling between CFD databases from one hand and the BEMT and UVLM from another to develop rotor heat transfer prediction tools. First, coupling methods are reviewed to determine how researchers are benefiting from a coupling between CFD databases from one hand and classical aerodynamic methods from another. A closer look is then taken on how the convective heat transfer is calculated on basic geometric surfaces, such as the flat plate and cylinder. Specifically, correlations for those geometries are investigated, together with the thermodynamic parameters and boundary conditions they are valid at. Next, experimental works that measured the heat transfer on fixed wing airfoils and rotors are reviewed. The search is focused here on a possible correlation effort for airfoil heat transfer. Finally, the literature is reviewed for the BEMT and UVLM, and

how they are currently used in state-of-the-art rotor modeling publications. This includes compressibility and viscous corrections as well as schemes used to avoid potential singularities.

Chapter 2 will outline the implemented methods to solve the mathematical models of the low and medium fidelity rotor heat transfer prediction tools. It is broken down into three main parts. The first is related to the conducted CFD simulations and begins with a verification on the use of CFD for heat transfer estimation. The details of the airfoil CFD simulations are then described along with the procedure in post-processing to estimate the convective heat transfer. The form of the new heat transfer correlation is lastly presented. The second and third parts of Chapter 2 follow the same trend but with the former being for the BEMT and the latter for the UVLM. Both those parts list the mathematical models behind the corresponding numerical method, and the manipulations done to make it comparable to similar uses in state-of-the-art works. Finally, the link to the new CFD-determined correlation to allow rotor blade heat transfer estimation is presented.

The experimental component of the thesis is described in Chapter 3. Experimental work had been carried out to measure the heat transfer on a fixed wing as well as a rotor in the IWT. The chapter lists the details of geometry, construction, testing plan of both the fixed wing and rotor. The technique followed to transform the measured data into comparable values to the developed numerical tools is also described in that chapter.

Chapter 4 is dedicated for the presentation of the results related to the numerical developments of Chapter 2. Similar to the latter, the former also comprises three main parts. The first begins with a verification of the airfoil CFD heat transfer data by comparing the predicted heat transfer to experimental and analytical data from the literature. The same data are then analyzed to study the effect of Re, α and boundary conditions on airfoil heat transfer. As will be seen, the averaging of the heat transfer poses the possibility of a correlation whose constants are determined based on a curve fitting scheme. A set of correlations is then proposed to calculate the airfoil average heat transfer without the need to redo any CFD work. The second part of

the chapter is dedicated to the validation of the implemented BEMT and UVLM. The validation is done against experimental and numerical data from the literature for 2 and 4 blade rotors in hover, axial and forward flight as well as rotors in ground effect. The last part of Chapter 4 presented the originality of this thesis with a study on the heat transfer distribution on a modified form of the Bell 429 tail rotor in 4 different flight configurations.

The last chapter of the thesis concerns the experimental results of the fixed wing and rotor tests. Quantifying the experimental error is done first, followed by a verification of the obtained results by comparing them to previous experimental efforts. For the fixed wing, the results are analyzed based on the different Re, α, and chordwise locations. As for the rotor, the heat transfer effects are studied based on variations of the rotor speed, pitch, radial and chordwise locations. Finally, the results of the BEMT-RHT and the UVLM-RHT are compared to the results of the rotor experiments.

CHAPTER 1

LITERATURE REVIEW

The introduction served to describe a brief history of rotorcraft icing, the development of ice protection systems and advancements in numerical simulations. The problematic of this research was also put forward, being the need for a computationally inexpensive tool to estimate rotor heat transfer in the conceptual design stage, where a high-fidelity computationally expensive approach is not favored. The objective of this thesis was also defined as to develop low and a medium-fidelity numerical tools to quantify the rotor heat transfer. It was also decided that the sought-after tools would be based on a coupling between CFD databases from one hand and the BEMT and UVLM from another.

In order to justify the choice of the CFD simulations for airfoil heat transfer calculation, BEMT and UVLM for rotor modeling and the coupling technique for a heat transfer estimation on rotors, a review of the state-of-the-art research is done in this chapter. The first section will explore how current icing/de-icing codes operate. Specifically, the review will focus on how the convective heat transfer is calculated in these numerical applications. Next, the review will move to explore correlations that exist for the basic geometries of a flat plate and a cylinder. Later, several experimental efforts to measure the heat transfer over airfoils are explored. More specifically, the review will focus on whether a correlation for the airfoil heat transfer has been reported in the literature.

The review then moves on to explore the concept of coupling algorithms and how they are applied in aerodynamic modeling numerical tools. The purpose of which is to determine how researchers are coupling aerodynamic modeling tools to CFD viscous databases. In the present research, the reasoning is to add an extra layer of this coupling to now only account for viscous effects, but to also calculate heat transfer. Finally, state-of-the-art rotor modeling works are reviewed for the BEMT and UVLM.

1.1 State-of-the-Art Icing/De-icing Simulations

Most icing codes usually operate on a 2D scale while a few operate in 3D conditions such as FENSAP-ICE, LEWICE and ONERA. Icing codes may use a 2D or 3D potential flow solver to obtain the flow field or use a high-fidelity code such as a Navier-Stokes code to capture viscous and unsteady effects. Water droplet collection on the surface of the blades is solved using either the Eulerian (FENSAP-ICE (Beaugendre et al., 2003) – ONERA (Guffond & Brunet, 1988; Montreuil et al., 2009)) or Lagrangian (LEWICE (Wright, 2008) – ONERA (Guffond & Brunet, 1988; Montreuil et al., 2009) – CANICE (Gouttebroze et al., 2000; Morency et al., 1999)) approaches. The general algorithm of icing codes may be described in the sequence shown in Figure 1.1 and broken down as follows:

1. The external aerodynamics of the clean, un-iced configuration are modeled and the convective heat transfer near the surface is calculated (Airflow Solver)
2. The collection efficiency is determined. It is a measure of water that impinges the aerodynamic surface and that has a possibility of later freezing on it (Droplet Solver)
3. The water mass and energy balance equations are applied within the viscous layer at the solid surface (Ice Accretion Solver)
4. If electro-thermal heating needs to be modeled, the effect of the internal heat generation is transferred to the mass and energy balance equations by a conductive heat transfer term (Conjugate Heat Transfer)
5. The predicted ice shape on the aerodynamic surface is updated, establishing an iced configuration
6. Steps 1 to 6 are repeated for the desired time interval with the corresponding time increment
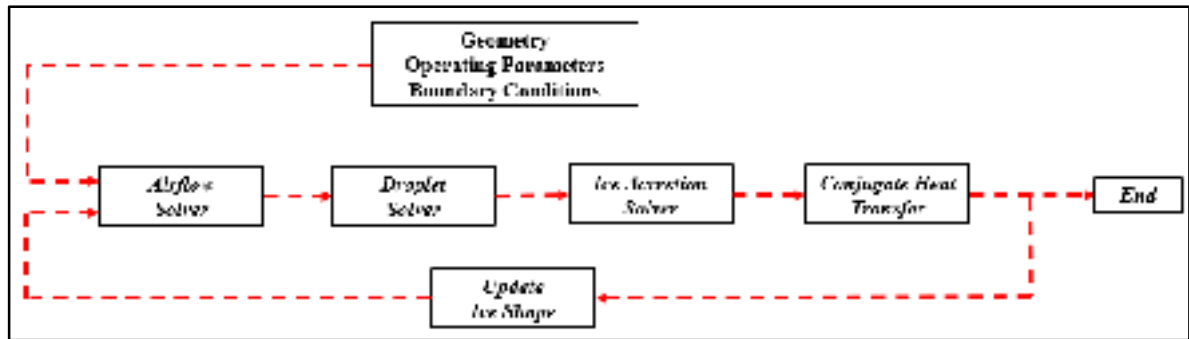
Figure 1.1 General Solution Sequence of Icing Codes

The presented structure of icing/de-icing codes shows that the airfoil solver is the first step towards icing/de-icing numerical modeling. Therefore, a good calculation of the convective heat transfer on the rotor blades is essential for the following sequence of an icing simulation. The rest of this section is now aimed at examining state-of-the-art research that uses high-fidelity icing codes to perform de-icing/anti-icing simulations on aircrafts and rotorcrafts. The purpose of which is determine how the convective heat transfer terms is calculated in these works. Usually, it is calculated using one of two methods.

The first method to calculate the forced convection is considered of high fidelity and relies on the direct solution of the RANS equations. This was used by (Reid, Baruzzi, & Habashi, 2012) when they applied a Conjugate Heat Transfer technique implemented in FENSAP-ICE to model unsteady in-flight electro-thermal anti-icing/de-icing of a NACA 0012 airfoil. FENSAP-ICE generally consists of four solvers: airflow, droplet, ice accretion and conjugate heat transfer solvers. (Pourbagian & Habashi, 2015) optimized the work of (Reid et al., 2012) to take into account a cyclic heating behavior in order to determine the optimum zone-specific, heating time and power. The calculation of the airflow convective heat transfer is based on the solution of the RANS equations using the *S-A* turbulence model.

In a similar approach as FENSAP-ICE, (Mu, Lin, Shen, Bu, & Zhou, 2018) also calculated the convective heat transfer based on the solution of the RANS equations using the *S-A* turbulence model. They presented a 3-D unsteady model based on CFD RANS simulations of in-flight electro-thermal anti-icing to simulate phenomena of convection, water runback, phase change,

and solid heat conduction. (Peng, Yuanli, Yupeng, & Xunan, 2018) also used the *S-A* turbulence model to calculate the convective heat transfer but used FLUENT to discretize the control volume. They studied the transient behavior of electric heating and de-icing of a wing based on a thermal convection coupling method with CFD simulations. One more example for the use RANS equations in convection estimation is the work of (Lavoie, Pena, Hoarau, & Laurendeau, 2018). They studied and assessed four different thermodynamic models that are popular among icing codes. The convection terms were obtained using a Navier-Stokes solver in a method based on FENSAP-ICE (Beaugendre et al., 2003).

The second method used to calculate convective heat transfer in state-of-the-art works is by the integral method which is considered of lower fidelity than CFD. The boundary layer growth is modeled and the C_f is calculated, which in turn is converted into surface heat transfer. (Özgen & Canıbek, 2009) who studied in-flight ice accumulation on multi-element airfoils. They used the Extended Messinger Model to compute ice accretion rates. Their numerically predicted ice shapes were comparable to experimental data both for rime and glaze ice. They also conducted a study on the computed ice shapes and masses for realistic flight scenarios. They found that the smaller elements in multielement configurations accumulate similar and often greater amount of ice compared to larger elements.

Another use of the integral method for convective heat transfer calculation was seen in the work of (Han & Palacios, 2017) who proposed an improved ice-accretion model by introducing a novel scaling coefficient relating the Stanton and Reynolds numbers for heat transfer. They performed their comparisons and modeling in the turbulent regime together with LEWICE. They also ran a series of 10 experimental icing tests and validated their numerical tool within 3% of experimental ice shape results. The convective heat transfer was calculated using an improved model based on solution of integral boundary layer equations of LEWICE-2D.

1.2   Coupling Methods

For aerodynamic conceptual designs, viscous coupling methods have recently grown popular. According to the thesis of (Gallay, 2016), they are defined by the coupling of classical aerodynamic methods with viscous CFD databases to increase the classical model fidelity yet maintain its relatively computationally inexpensive solution. They are used to improve inviscid linear computation methods by coupling them with nonlinear viscous data, usually obtained using CFD simulations or experimental data. Although full-fledged CFD simulations provide an unmatched higher fidelity analysis, the computationally inexpensive approach combined with the time-efficient solution makes coupling methods interesting for a conceptual design. The coupling allows the viscous flow to be characterized on aerodynamic surfaces and can be used to predict stall, shock waves or in the case of this research, heat transfer.

(Gallay, 2016) discussed the coupling of 3D potential flow methods and 2D viscous sectional data. One of the types of non-linear coupling methods he identified was termed "Potential-RANS" and fit the purpose of the present research. According to the author, there are two Potential-RANS coupling techniques that can be used with the UVLM. The first is known as the Γ- method in which a viscous correction implemented on the circulation Γ calculated by a typical VLM method. In this method, the effective angle of attack α_{Eff} is calculated first based on the induced angle of attack α_i. The α_{Eff} is in turn used to interpolate the viscous database to obtain the viscous lift coefficient C_{L-visc} at each section. Next, The C_{L-visc} is used to calculate the viscous circulation Γ_{visc} using the Kutta-Joukowski theorem. Finally, an iterative solution is followed between the inviscid circulation Γ predicted by the typical UVLM calculation and with Γ_{visc} until a convergence criterion ε is met. It was reported that the Γ- method requires hundreds of iterations with an under-relaxation factor of 0.05 to converge. It is also limited to the pre-stall regions, as no convergence can be achieved post-stall.

The other coupling method is called the α- method (Van Dam, 2002), it involves an iterative procedure where a viscous correction is applied between the C_{L-visc} from the viscous database and inviscid C_{L-inv} obtained by a typical UVLM. The α_{Eff} is first calculated based on the

geometric angle of attack α_{Geo} and the viscous lift curve slope $C_{L\alpha}$. The α_{Eff} is then used to interpolate the viscous database and obtain $C_{L\text{-}visc}$ at each section. Next, a correction parameter based on the $C_{L\text{-}inv}$ and $C_{L\text{-}visc}$ is calculated and used to re-calculate α_{Eff} until a convergence criterion ε is met. (Gallay, 2016) reported that the α-method converges faster without needing a relaxation factor compared to the Γ-method that requires an important under-relaxation factor to converge. The α-method was also reported as successful in the post-stall region so it could be used to capture stall angles. It has a limitation though near the point of maximum lift where the $C_{L\alpha}$ becomes zero.

(Gallay & Laurendeau, 2015) used a modified Weissinger method as the inviscid code coupled with the α-method and modeled an elliptical wing in pre/post-stall flow conditions. They were able to prove that this coupling presented excellent predictions (with respect to a conceptual design) of the pre/post-stall lift coefficients with fast convergence, even at high angles of attack. In a later work, they promoted the modified α-method to allow the prediction of aerodynamic coefficients and lifting surface pressure distribution on high-lift systems (Gallay & Laurendeau, 2016). They found that the coupling of the inviscid Weissinger code to a 2.5D RANS determined sectional airfoil data provided better estimation than traditional 2D simulations. A better agreement with wind-tunnel and/or high-fidelity numerical data was also found for the prediction of the maximum lift coefficient C_{Lmax} and the post-stall behavior.

An attempt by (Parenteau, Plante, Laurendeau, & Costes, 2017) used the modified α-method to couple the Unsteady Vortex Lattice Method (UVLM) with two sets of RANS viscous sectional data. The first set was based on 2D RANS data and the other was based on more complex 2D URANS data. According to the author, the first coupling was simple to implement as an aerodynamic conceptual design tool and provided comparable viscous results to full URANS simulations. It was however limited to low angles of attack and failed in capturing dynamic stall. The second coupling could capture dynamic stall but was more time consuming and had limited applicability where only periodic simulation forced by the motion can be performed.

Another attempt by (Parenteau, Sermeus, & Laurendeau, 2018) applied the modified α-method as a coupling method between the Vortex Lattice Method (VLM) as an inviscid code and 2.5D RANS viscous sectional data. The authors found that the prediction of C_{Lmax}, stagnation points and span loads over the a swept-wing flap was obtained within 7% discrepancy, even when compared to 3D RANS simulations.

Recent work by (Bourgault-Cote, Parenteau, & Laurendeau, 2019) applied the modified α-method as a coupling method between the VLM and 2.5D RANS icing solver to generate viscous databases and predict ice accretion over a 3D swept wing. The viscous aerodynamic calculations as well as the ice accretion were performed using NSCODE-ICE, a software developed at Polytechnique Montréal. The result was a Quasi-3D multi-layer ice accretion model based on a coupling between the VLM and a 2.5 RANS ice-accretion CFD database. After the typical VLM was solved, the α_{Eff} at each wing section was calculated using the α-method and the information was fed into the database to predict the ice layer formed on different sections of a swept wing. Comparisons of results with experimental data of the GLC305 swept wing in glaze ice conditions showed that similar ice shapes could be reproduced using the coupled analysis.

1.3 Heat Transfer & Icing Literature

The previous section showed that most modern icing codes rely on CFD simulations to directly calculate the convective heat transfer on fixed wings or rotors. However, the objective of this research is to develop numerical tools for rotors whose convection rates can be readily obtained by a correlation or from a database, without the need to go through complete calculations every step of the way. From the other hand, the previous section showed a coupling method could be a convenient and rapid way to increase the fidelity of classical inviscid aerodynamic tools. Therefore, if a coupling method were to be implemented on the BEMT or the UVLM to allow them to compute rotor heat transfer, then a database representing the convective heat transfer on airfoils is needed.

Assuming an airfoil heat transfer database is found based on *Re* and α, then its data could be extracted via a double interpolation on the *Re* and α. Another way to represent a database is in the form of a correlation. As the following literature review will show, correlations offer a solution to access the database. Assuming *Re* and α are known, then the convective heat transfer could be obtained by using the appropriate values.

In that scope, the literature review of this section will explore research regarding correlations for forced convective heat transfer. It should be noted that for the present research, the heat transfer on smooth surfaces only is inspected. The effects are roughness are out of the scope of this research. The test cases of the flat plate and cylinder are examined first. The existing correlations available to quantify heat transfer on the cylinder and the flat plate are explored, in terms of the Nusselt Number *Nu* and Frossling Number *Fr*. Next, experimental efforts that measured the convective heat transfer on 2D airfoils are explored. In particular, the research is focused on attempts made to correlate the heat transfer on airfoils.

1.3.1   Heat Transfer on Flat Plates

Figure 1.2 shows a typical flow over a flat plate with the boundary layer growing as the airflow moves across the plate. The flow starts off with a laminar flow that transitions into turbulence at a critical $Re_{x,c}$ = 500,000, after the transition phase and for higher *Re*, the flow becomes dominantly turbulent. For forced convection analysis over a smooth flat plate, the heat exchange occurring between the plate and the air is mostly governed by two non-dimensional parameters and TBC imposed on the surface of the plate. The parameters are the Reynolds Number *Re* and the Prandtl Number *Pr* whereas TBCs could take many forms. In this work, only the constant surface temperature T_S and the constant surface heat flux Q_S were investigated.
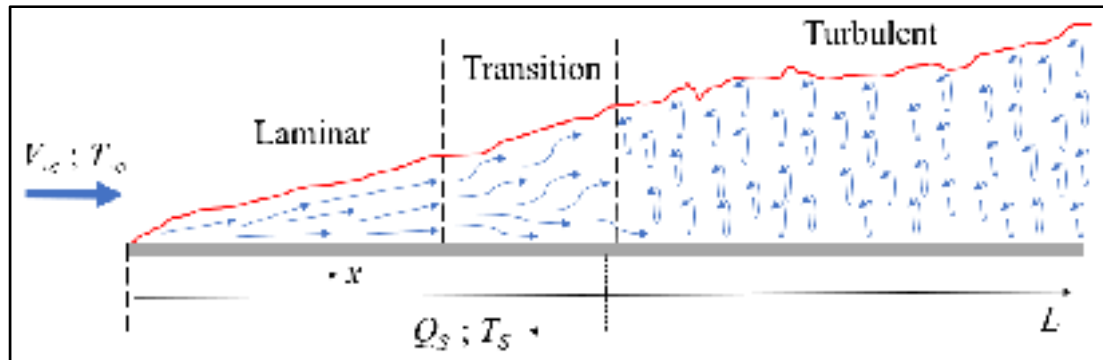
Figure 1.2 Flow Development over a Flat Plate

Correlations describing the *Nu* variation are well documented for a wide range of *Re* and TBCs. (Incropera, Lavine, Bergman, & DeWitt, 2007) and (Kays & Crawford, 1993) reported a set of correlations for the local *Nu* on a smooth flat plate with a constant freestream velocity V_∞. These correlations provide *Nu* values within 15% of experiments and depend solely on the *Re*, *Pr* as well as experimentally determined constants. The constants depend of the nature of flow (whether it is laminar or turbulent) and on the thermal TBC imposed on the plate wall (constant *Ts* or *Qs*).

A new study by (Lienhard, 2020) examined the previously mentioned correlations for the convection on a smooth flat plate. The paper particularly examined the transition occurring between the laminar and turbulent flows. According to the author, few previous attempts were made to properly correlate the heat transfer at transition or to incorporate it in the existing laminar and turbulent correlations. In that scope, the author examined datasets from previous research and was able to come up with a new and more representative correlations for the *Nu* for laminar, transitional and fully turbulent flows.

On the other hand, if the *Fr* (which is defined as the *Nu* divided by $Re^{0.5}$) is used to represent the non-dimensional heat transfer on the flat plate, the laminar flow correlations show an independence from the *Re* and only the turbulent flow shows a dependence of the *Fr* on the *Re*.

1.3.2   Heat Transfer on Cylinders

Figure 1.3 shows the boundary layer growth pertaining to a cylinder in crossflow. The flow exhibits a laminar to turbulent transition similar to the case of the flat plate. The heat transfer depends on the diameter-based Reynolds Number Re_D, Pr, the TBC on the cylinder wall but also depends on the cylinder azimuth angle θ_{cyl}. (Achenbach, 1975) experimented on smooth cylinders in laminar, transitional and turbulent regimes. He measured heat transfer rates via static pressure and skin friction for half of the cylinder surface and coined the term *Frossling Number* $Fr = \dfrac{Nu}{\sqrt{Re_D}}$, with respect to the work of (Froessling, 1958). The *Fr* allowed the heat transfer rates to be scaled in the laminar regime, in other words, it was proven that the *Re* had no effect on the *Fr* as long as the flow is laminar and that the *Fr* only varied with the *Re* when the flow transitions into turbulence.
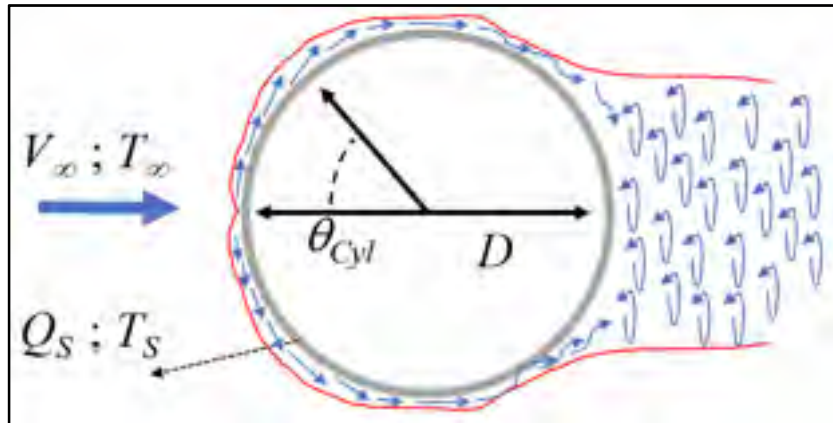
Figure 1.3 Flow Development over Cylinder

In terms of correlations, numerous described the heat transfer on the surface of a smooth cylinder. (Incropera et al., 2007) reported a correlation for the local *Nu* on the stagnation point of the cylinder based on a boundary layer analysis. An empirical correlation by (Hilpert, 1933) was proposed for the average *Nu* of the cylinder based solely on the Re_D, *Pr* and two empirically determined constants. Another correlation for the average *Nu* of a cylinder was also proposed by (Churchill & Bernstein, 1977).

1.3.3 Heat Transfer on Airfoils

The typical flow over an airfoil with a chord c is depicted in Figure 1.4 where the boundary layer grows from laminar to turbulence. An added parameter to the case of heat transfer on an airfoil compared to the flat plate and cylinder is the angle of attack α. This angle will cause stagnation point to move on the skin of the airfoil and the convection to vary between the upper and bottom surfaces. Airfoils are also constructed in a variety of profiles, each with a different thickness and camber. Flow separation is also a factor that affects the convection, similar to the phenomenon of aerodynamic degradation. Ice protection research can be traced back to the 1940's (Rodert, Clousing, & McAvoy, 1942), few studies however exist that provide a complete analysis of heat transfer on airfoils.
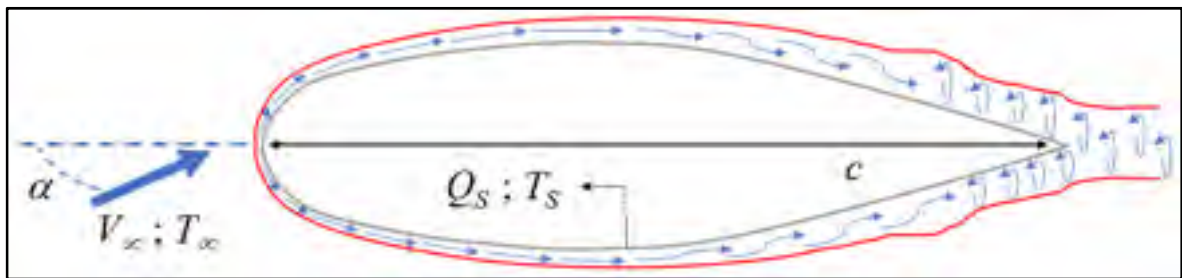
Figure 1.4 Flow Development over 2D Airfoil

The works of (Newton, Vanfossen, Poinsatte, & Dewitt, 1988) and (Poinsatte, 1990) provided a comprehensive analysis of airfoil heat transfer when they quantified the heat transfer on the leading edge of a smooth and roughened NACA 0012. Their data were gathered from in-flight measurements of the NASA Lewis Twin Otter icing research aircraft (Newton et al., 1988) as well as experiments in the IRT. The experimented airfoil's leading edge up was maintained on a constant surface temperature using embedded heating gauges located between -3.6% and 9.5% of the dimensionless wrap distance S/c. A total of 46 tests were done for $-6° \leq \alpha \leq 8°$ and $1.2 \times 10^6 \leq Re \leq 2.4 \times 10^6$. The measured heat transfer on the airfoil was compared to the results of flat plate under laminar and turbulent flow conditions as well as the cylinder correlations. For the smooth tests, their work affirmed the use of the Fr and showed that the

behavior of heat transfer in the laminar flow portion was similar to the behavior seen on the cylinder and the flat plate for the same flow conditions. The Fr curves collapsed into one regardless of the Re. When surface roughness was applied and its density increased, they proved that a dramatic disturbance of the boundary layer occurred. This led to an early flow transition and a respective increase of heat transfer downstream of the stagnation point.

Between 2006 and 2008, the average Nu on the surface of a hollowed NACA 63-421 was measured. The experimented airfoil was equipped with heating strips installed on the inner edges of the airfoil. The heaters were set to provide a constant heat flow of 500W that was transferred to the airflow by conduction through the airfoil material. A total of 25 thermocouples were distributed across the chord on the exterior and interior surfaces of the airfoil to measure the temperature differences. Correlations for the Nu_{Avg} similar to the cylinder correlation of *Hilpert* (Hilpert, 1933) based on the Re and Pr were formed for dry air for $\alpha = 0°$ (Wang, Naterer, & Bibeau, 2007b), dry air for $0° \leq \alpha \leq 25°$ (Wang, Naterer, & Bibeau, 2008a), for a Liquid Water Content $0 \leq LWC \leq 4.98$ g/m^3 for $\alpha = 0°$ (Wang, Naterer, & Bibeau, 2007a) and for $0 \leq LWC \leq 4.98$ g/m^3 for $0° \leq \alpha \leq 25°$ (Wang, Naterer, & Bibeau, 2008b).

(Li, Gutmark, Ruggeri, & Mabe, 2009) measured the static pressure and heat transfer rates on the surface of a thick BO28 airfoil at locations covering 90% of both the top and bottom surfaces for $-8.5° \leq \alpha \leq 19.5°$ and $Re = 2.5 \times 10^5$, 5.82×10^5 and 1.085×10^6. The airfoil had 23 embedded heating tiles that were heated to a specified constant temperature. They paid close attention to the effect of flow transition on the increased heat transfer between the laminar and turbulent flow regions by calculating the Fr on various chord locations. Their tests again showed an independence of the Fr on the Re in the laminar flow region on the airfoil, confirming the results of (Poinsatte, 1990). When the Re was fixed and the α was increased, flow transition on the suction side of the airfoil moved closer to the leading edge and an abrupt increase of heat transfer was seen. On the pressure side, the transition point was pushed towards the trailing edge and a similar abrupt increase of heat transfer was also seen. When the α was fixed and the Re was increased, the increase of heat transfer due to flow transition was pushed closer to leading edge on both surfaces of the airfoil. For all tests, high Fr values were seen on

the stagnation point however, the highest *Fr* values were actually seen on locations where the flow transitioned from laminar to turbulent. The abrupt increase of *Fr* at the transition point was followed by a less severe yet rapid decrease of *Fr* values downstream towards the trailing edge.

1.4 Rotor Aerodynamic Models

The methods of choice for the rotor aerodynamic modeling of this thesis are the BEMT and the UVLM. The literature indicates that rotor modeling is possible using CFD simulations providing high fidelity performance calculation and wake predictions (Butsuntorn & Jameson, 2008; Gao & Agarwal, 2019; Sugiura, Tanabe, Sugawara, Matayoshi, & Ishii, 2017). The literature also shows that rotor modeling by a coupled analysis can be successfully done using the Potential Method (Tan & Wang, 2013a, 2013b; Wie, Lee, & Lee, 2009), Viscous Vortex Particle Method (He & Zhao, 2009) or Free Wake – CFD coupled methods (Farrokhfal, Pishevar, & Management, 2014; Filippone et al., 2011). This section focuses on exploring the state-of-the-art research on rotor aerodynamic modeling using the BEMT and UVLM. The review will particularly explore published research on linear/non-linear coupling methods based on the last two mentioned methods.

1.4.1 Blade Element Momentum Theory

The BEMT is a combination of the Blade Element Theory and the Momentum Theory for rotor modeling (Leishman, 2000). It is considered as an extension of Prandtl's lifting line theory for rotary wings. In its basic form, the BEMT needs two assumptions to operate adequately. First, each 2D airfoil section on the blade is independent from the others and second, the 2D sectional lift C_L and drag C_D coefficients as well as the lift curve slope $C_{L\alpha}$ at each blade element is known. The advantage of the BEMT is that it can calculate the α_{Eff} through its original formulation without the need for a coupling algorithm, making the process of linking it to a CFD database straightforward. As will be discussed in the coming paragraphs, state-of-the-art

applications of the BEMT involve a coupled BEMT-CFD modeling of wind turbines rotors. A method that could also be applied for helicopter rotors.

(Edmunds, Malki, Williams, Masters, & Croft, 2014) termed their procedure as RANS-BEM where RANS CFD simulations were coupled with the BEMT to study the radial variation of force over wind turbine blades. The k-ω turbulence model was used for the RANS simulations. They laid out a methodology for modeling turbines in different geometric configurations such as axially aligned, transverse contrarotating and single row fence turbines. They calculated the power performance estimates to account for the improved total power production. (Masters et al., 2015) later compared the RANS-BEM method to experimental measurements of three different rotors of a turbine and showed good agreement in the far wake region.

(Sun, Chen, Shen, & Zhu, 2016) Proposed an improved model of the BEMT where the calculation of the axial and radial induction factors of the typical BEMT are modified and obtained using an empirical correlation determined by (Spera, 1994) that links the axial induction factor to the thrust coefficient. Another modification they proposed was the replacement of the typical Glauert's tip loss factor with a new Shen's tip correction factor (Shen, Mikkelsen, Sørensen, & Bak, 2005). Through these manipulations and without the need to go through computationally expensive solutions, they showed the calculated rotor forces agreed better with the results of experiments than the typical BEMT.

(Olczak, Stallard, Feng, & Stansby, 2016) presented a coupled RANS - BEM method that models tidal turbine arrays that they described of medium computational cost. The method is capable of modeling wake rotation in the far-wake region. The RANS-BEM was implemented in the CFD code StarCCM+ and uses the k-ω SST turbulence model to provide predictions of actuator disc wakes. The method takes the form of an iterative solution where the source terms of the BEMT are updated at each iteration from the RANS solution. They found that for an array of up to 12 consecutive turbines, the average thrust predicted through the RANS – BEM is typically within 10% of experiments.

1.4.2   Unsteady Vortex Lattice Method

The UVLM is an extension of Prandtl's lifting line theory that can either be solved in steady state or time-dependent (unsteady) mode (Katz & Plotkin, 2001). It is a classical and popular lifting surface modeling method based on the assumption of an inviscid, incompressible and irrotational flow. The lifting surface is represented by a finite number of vortex rings placed along the camberline. The wake trailing due to the motion of the lifting surface is also modeled using vortex rings that are shed at each timestep. The goal of the UVLM is to determine the circulation Γ of each vortex ring leading to an estimation of the lift distribution. In terms of applying the UVLM for rotor modeling, state-of-the-art applications typically include a viscous correction scheme in the calculation of the induced velocities, and the introduction of a slow start method to maintain a stable wake formation.

(Colmenares, López, & Preidikman, 2015) applied their General Unsteady Aerodynamics Vortex-Lattice Method (GUAVLAM) code that uses the UVLM to a two-rotor aircraft in different geometric configurations in hover. The methodology adopts the usual UVLM formulation with a few modifications. To better represent the wake during the first few rotations, the rotor speed was assumed to increase linearly until the desired velocity is reached at the 2nd or 3rd revolution (Chung, Kim, Ryu, Lee, & Lee, 2006). To account for singularities that may arise during the calculation of induced velocity vectors, such as when the rotor blades interact with the wake, the Vatistas vortex core model (Vatistas, Kozel, & Mih, 1991) was used instead of the usual Biot Savart Law. Finally, the elimination of the circulation of the root vortices was studied and it was reported that no effect on the thrust calculation or wake shape prediction was noted.

(Ferlisi, 2018) used the UVLM to model the wake development and to calculate the performance of multi-blade rotors in hover and axial flight. An extensive review of the implementation of the Vatistas vortex core model (Vatistas et al., 1991) as well as Lamb-Oseen vortex core model with the vortex diffusion and stretching implementation of (Bhagwat & Leishman, 2002) was conducted. He validated his tool in terms of predicted performance

parameters and wake shape with experimental data for a 2-blade rotor in hover, 2-blade rotor in axial flight and a 4-blade rotor in ground effect.

(Pérez, Lopez, & Poroseva, 2019) simulated the rotor of small Unmanned Aerial Vehicles (UAVs) in hover using CFD simulations as well as an implementation of the UVLM. They used a viscous core model based on the Vatistas vortex model combined with the vortex stretching and diffusion model of (Bhagwat & Leishman, 2002). When compared to experimental data for the thrust, the authors reported CFD values within 3.34% compared to 11.89% for the UVLM. The torque predicted agreed with experiments within 15.79% and 4.75%, respectively. They also highlighted the computationally inexpensive solution of the UVLM compared to CFD.

More works that used the UVLM in the recent literature were discussed in section 1.2 and implemented the VLM/UVLM as part of a coupling analysis. To avoid repetition, the reader is suggested to check the review of the works of (Parenteau et al., 2017), (Parenteau & Laurendeau, 2018), (Parenteau et al., 2018) and (Bourgault-Cote et al., 2019) in section 1.2.

1.5   Originality

The presented literature review went through the state-of-the-art research done to model convective heat transfer on rotor blades. It was determined that implementations of icing codes and CFD simulations offer the possibility of a high-fidelity calculation of the convective heat transfer and icing simulation on rotor blades. However, is was also shown that for a conceptual aerodynamic design, coupling methods offer a faster calculation approach with a medium-fidelity approach.

According to section 1.2, there is a growing interest in the application of lower fidelity coupled tools to solve viscous aerodynamic problems. At least one recent work that used the coupled algorithm for ice accretion prediction on wings was also found. The validations and verifications presented in the reviewed works show that although full-fledged CFD simulations

provide an unmatched higher fidelity analysis, the computationally inexpensive approach combined with the time-efficient solution makes coupling methods interesting for a conceptual design. To align this conclusion with the aim of the present thesis, where a coupled technique was adopted for rotor heat transfer calculation, it was decided that an inviscid rotor aerodynamic modeling tool plus an airfoil heat transfer CFD database were needed.

The examination of the test cases of a flat plate and cylinder show that correlations to calculate the heat transfer on those geometries are well documented in the literature. A correlation is seen as one way to manipulate the database without the need to redo any CFD work nor any interpolations. For the flat plate and cylinder, the correlations for the *Nu* depend solely on the *Re*, *Pr*, the nature of the flow (laminar or turbulent) and on the TBC. As for airfoil heat transfer, few works were found to measure the heat transfer. However, the work of (Poinsatte, 1990) was especially helpful in documenting the *Fr* values near the stagnation point of a NACA 0012 and the effect of a laminar boundary layer. Similarly, (Li et al., 2009) provided an understanding of the *Fr* variation in laminar, transitional and turbulent flow conditions on the BO 28 airfoil by varying the *Re* and α. Most interestingly however, (Wang et al., 2008a) offered correlations of the *Nu*_{Avg} for a NACA 63-421. The correlations were based on the *Re*, *Pr* and α, without a clear identification on the effect of turbulence or the TBC.

Moreover, the literature also showed that rotor aerodynamic modeling has been implemented with a variety of tools. Those tools ranged from complete CFD simulations all the way to classical lifting line methods. However, a notable finding was that the BEMT & UVLM are becoming more attractive in recent research. The increased interest in reviving the two classical methods is due to coupling algorithms that could link the BEMT & UVLM to viscous databases and allow them to account for viscous effect, stall, and ice accretion prediction. Therefore, the two tools could be used as a way to model rotor aerodynamics and benefit from their coupling to calculate rotor heat transfer. To the best of the author's knowledge, the proposed coupling is new to the scientific community and has not been tried in the past.

28

1.6   Structure of the Coupled Technique for Heat Transfer

With that kind of analysis in mind, the main objective of this thesis was defined by developing two numerical tools that estimate convection rates on rotor blades. The tools of choice had limitations as they had to be classical aerodynamic methods and they had to calculate rotor heat transfer in a less computationally expensive manner than direct CFD simulations. The first numerical tool is of low fidelity and implements the use of the BEMT coupled with a viscous and heat transfer CFD database called "BEMT-RHT" and the other is the "UVLM-RHT", a tool of medium fidelity that uses the unsteady UVLM coupled with the viscous and heat transfer database.

The general structure of the BEMT-RHT and UVLM-RHT may be described by Figure 1.5. This figure represents the workflow of the two numerical methods based on the input consisting of the rotor geometry, operating parameters (rotation velocity, pitch angle etc...) and TBCs. If a steady-state solution is desired, the BEMT-RHT is used whereas the UVLM-RHT is used for an unsteady and finer solution. For both methods, the CFD viscous and heat transfer database will be used to provide a radial distribution of heat transfer. The following sections will provide a summary of the steps taken to achieve the specific objectives of this thesis.

1.6.1   Building the CFD Database

In accordance with the first objective of this thesis from section 0, the heat transfer on a smooth 2D airfoil needs to be calculated and correlated. To do that, CFD RANS simulations using the *S-A* turbulence model will be run using *Stanford University Unstructured* (*SU2*) on an airfoil at various *Re* and α as well as two different TBCs. The CFD simulations will also serve to generate the viscous data (C_L, $C_{L\alpha}$ & C_D) needed to increase the fidelity of the BEMT and UVLM.
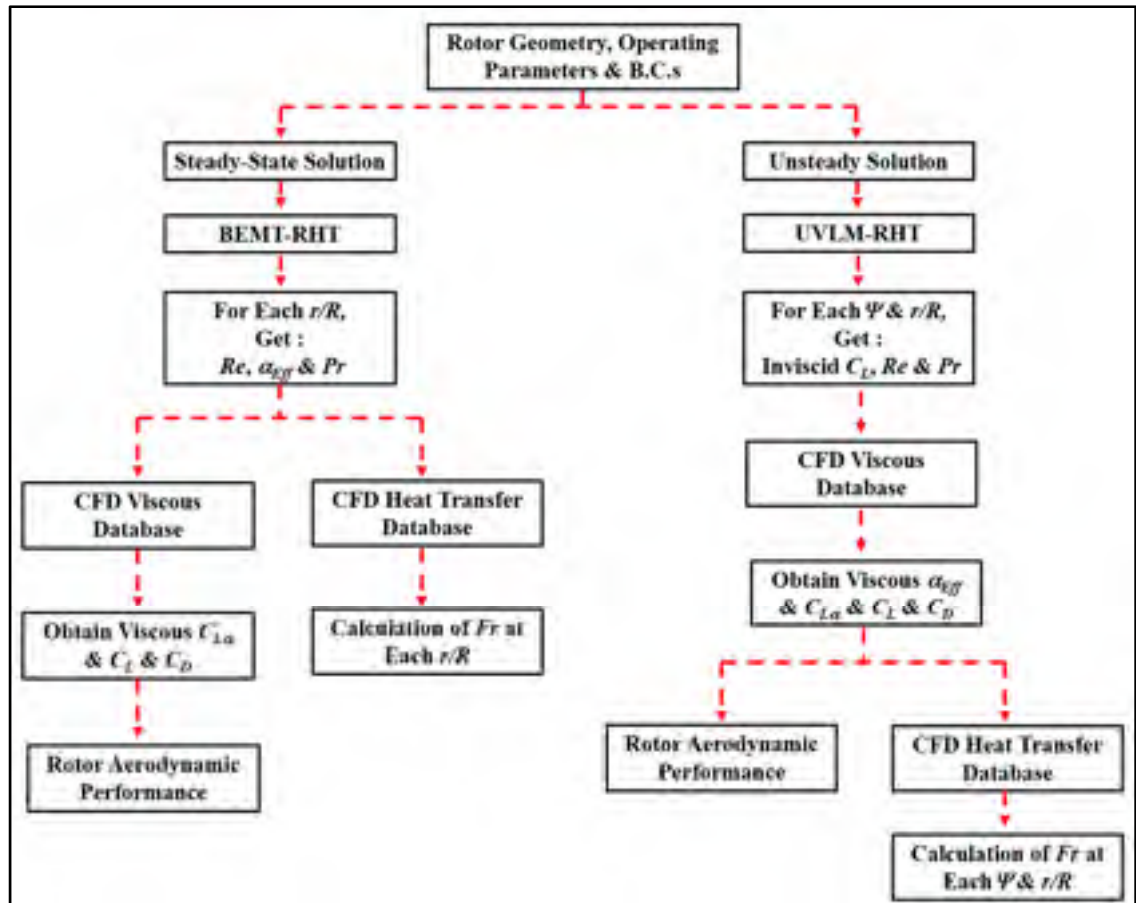
Figure 1.5 Workflow of the BEMT-RHT & UVLM-RHT

It was shown by (Poinsatte, 1990; Poinsatte, Newton, De Witt, & Van Fossen, 1991) and later reaffirmed by (Li et al., 2009) that for a laminar flow, the Re had no effect on the Fr and effects only existed after the flow transitions into turbulence. This was consistent with the results obtained under similar flow conditions for flat plates and cylinders. These studies showed that sufficient data exist in the literature to quantify the heat transfer on airfoils under laminar flow conditions, so it was decided that all CFD simulations in this research will assume a fully turbulent flow.

The non-dimensional heat transfer will be described by the Fr and calculated for each individually simulated test case for a unique Re and α. In terms of the Fr_{Avg}, the cases of the flat plate and cylinder indicate that the Fr_{Avg} was simplified into correlations. At least one

previous study showed this was also possible for an airfoil. Therefore, a new correlation for the airfoil Fr_{Avg} is proposed that depends on the Re, α, Pr and constants determined by curve fitting. The Fr_{Avg} correlation could be directly linked to the BEMT or UVLM without the need for a database interpolation. For a more detailed heat transfer variation in the chordwise direction, the Fr_x was used and could be obtained by the BEMT and UVLM based on a database interpolation of the Re and α.

1.6.2   BEMT-RHT

As per the second objective, a low fidelity numerical tool that uses the BEMT for helicopter rotor aerodynamic modeling coupled with heat transfer estimation is developed. The BEMT was considered a low fidelity tool due to its steady state nature, no wake representation and due to its inviscid nature. Its advantages however include its very quick solution process (no more than one minute on a single core computer), relatively good predicted results (15% thrust discrepancy) and its direct computation of the α_{Eff} on the blade, an essential parameter needed to link with the heat transfer database as will be seen later on. The developed numerical tool will be capable of modeling multi-blade rotors in hover or axial flight and will be validated against experimental results from the literature accordingly.

Previous research indicates that the BEMT can be successfully coupled with higher order methods to increase the fidelity of modeling wind turbine applications. In that scope, the viscous data obtained from the CFD simulations will be used as an input (by interpolation) to the method as required, in a similar way as the literature. Similarly, the developed numerical tool will be coupled to the CFD heat transfer correlation/database to provide radial and chord wise distributions of heat transfer rates. To successfully interpolate data from the database, the Re and α_{Eff} must be provided. The formulation of the steady-state BEMT allows these parameters to be calculated without the need of a viscous coupling algorithm, hence a simple link could be established between the BEMT and the heat transfer database. This numerical tool was baptized and named "BEMT-RHT", where RHT stands for "*Rotor Heat Transfer*".

1.6.3   UVLM-RHT

The development of a medium fidelity numerical tool that uses the UVLM for helicopter rotor aerodynamic modeling is the third objective of this work. The UVLM assumes an inviscid, irrotational and incompressible flow. It has no exact representation of the two surfaces of the blades but rather only acts on the camberline and requires a viscous coupling algorithm to link it to the heat transfer database. It also takes longer time to solve the UVLM than the BEMT, a typical application on a single core computer of the UVLM in this thesis took around 20 hours whereas the BEMT is solved in less than a minute. Moreover, to make use of viscous and heat transfer data, the α_{Eff} is not directly obtained from the UVLM but rather through a viscous coupling algorithm similar to the one proposed by (Van Dam, 2002).

On the other hand, and as added features compared to the BEMT, the UVLM provides a time-dependent solution and could therefore provide an instantaneous prediction of the heat transfer, not only limited to the blade radius. It also provides a wake structure whose influence on the blade could be accounted for and its solution fineness could be controlled by changing its mesh size and timestep. The range of applicability of this tool is also wider than the BEMT-RHT. Other than hover and axial flight, the UVLM-RHT could also account for multi-blade rotors in forward flight and for the ground effect. The UVLM was considered a higher fidelity method than the BEMT but would still be regarded as medium fidelity tool in practice.

The proposed tool of this thesis was named "UVLM-RHT" and will use the heat transfer database to calculate the radial and chord wise distributions of heat transfer rates. The heat transfer rates will also be obtained as a function of time based on the azimuth angle Ψ. This will help relate the heat transfer rates to the location of the blade in its plane of rotation due to the unsteady nature of the tool.

1.6.4   Experimental Work

The final objective of this thesis is to conduct experimental work in the IWT on a fixed wing and a 2-blade rotor. The aim of these experiments was to quantify the heat transfer at different locations on the surface of the wing and rotor and compare it to results predicted by the CFD simulations, the BEMT-RHT and the UVLM-RHT.

The fixed wing tests were conducted as a preliminary step to the rotor tests, mainly to obtain average Fr values and compare measurements to the CFD simulations. The literature discussed in section 1.3.3 shows that heat transfer was previously measured on airfoils and for laminar, turbulent and transitional regimes. The present experiments however provide measurements for a wide range of Re, α and S/c, making it possible to obtain averaged Fr values for the NACA 0012. The profile wall will be almost 90% covered with heating elements to ensure a heat-maintained surface. Different angles of attack will be tested, as well as a range of Re. Resistance Temperature Detectors (RTDs) will be distributed on the surface to provide measurements at different locations across the chord.

For the rotor experiments, and to the best of our knowledge, there are no works in the literature that provide comparable data that we can validate with. That is, there are no published works showing convective heat transfer measurements across the chord and radius of ice-clean rotor blades. Let alone Fr_x values with varying θ and Ω. Extensive experimental efforts have been made on iced rotors in the past, they were limited however to custom applications and revolved mostly around the icing effect with no heat transfer quantification. In this work, a 2-blade rotor is used with the blades covered with heating elements. Two pitch angles will be tested to study the effect of the varying angle. The rotor speeds will also be varied between to accommodate a range of Re between the different r/R and Ω. The RTDs will be distributed across the radius and the chord to provide measurements at different locations in the two directions. The purpose of the rotor experiments is to provide an original contribution to the scientific community, and to compare the heat transfer measurements to the predictions of the BEMT-RHT and the UVLM-RHT.

CHAPTER 2

NUMERICAL METHODOLOGY

In this chapter, the numerical methods and mathematical models implemented in the thesis to develop the low and medium fidelity rotor heat transfer prediction tools are presented. Specifically, this chapter has three objectives. The first is to develop a CFD-determined viscous and heat transfer database for airfoils. The second objective is to increase the fidelity of the classical BEMT (low fidelity) by incorporating 2D viscous data from one hand and by linking it to the 2D heat transfer database from another. Similarly, the last objective is to promote the classical UVLM (medium fidelity) into a viscous rotor aerodynamic tool as well as allowing it to predict heat transfer on rotors.

In this chapter, the airfoil CFD simulations are presented first and are done using the software *SU2*. The main advantage of these simulations is that they provide both viscous and thermal data. Each airfoil simulation is done at a different Re and α, whereas post-processing provides both a local and average variation of the Fr. In a similar attempt to what researchers proposed in the literature, a new correlation representing the average Fr on the simulated airfoil is proposed. The correlation provides a simpler approach than interpolating a database, since the calculation of the heat transfer depends solely on the Re, α_{Eff} and the Pr.

The BEMT used in this work is based on the work of (Leishman, 2000) with a few modifications to increase its fidelity. Instead of using the aerodynamic data at each blade element from the theory of steady linearized aerodynamics, the viscous data from the CFD simulations are interpolated based on the Re and α_{Eff}. This is relatively simple to apply since the BEMT provides an estimate of the α_{Eff} through its original solution procedure. In a similar fashion, the Re and α_{Eff} at each blade element are used together with the Fr correlation to predict the blade heat transfer.

In this thesis, numerous modifications and additions are introduced to the classical UVLM (Katz & Plotkin, 2001) to increase its fidelity and to allow it to predict heat transfer. The equations of the UVLM are first rewritten and adjusted to accommodate rotor modeling instead of a fixed wing. This allowed the UVLM to model rotors in hover, axial or forward flight and to also model the ground effect. In its typical form, the UVLM calculates the induced velocities due to the blade and wake lattices based on the Biot-Savart Law which may cause singularities to arise. To eliminate those singularities, the Lamb-Oseen viscous core model is added (Leishman, Bhagwat, & Bagai, 2002). Similarly, the Prandtl-Glauert compressibility correction is added to include the effect of the *Ma* (Glauert, 1928). A fundamental addition to the UVLM is the introduction of the viscous coupling algorithm based on the α- method (Van Dam, 2002). The algorithm is essential to calculate the α_{Eff} that will be used together with the *Re* at each blade section to incorporate the 2D viscous data and to satisfy the *Fr* correlation.

2.1 Airfoil CFD Viscous & Heat Transfer Simulations

The compressible Reynolds-Averaged Navier–Stokes (RANS) flow equations are solved to compute the heat transfer and the temperature at the wall of the simulated body. The turbulence model used is the *Spalart-Allmaras* model. The fluid model is set to standard air, with the specific gas constant R_G = 287.058 *N.m/kg.K* and the specific heat ratio γ= 1.4.

2.1.1 Proposed Form of the Average *Fr* Correlation for Airfoils

Correlations that describe the local and average *Fr* based on the *Re* exist in the literature for flat plates and cylinders. A common correlation that is used for a cylinder in crossflow is the one proposed by (Hilpert, 1933) presented in equation (2.1) where *A* and *m* are experimentally determined constants that depend on the diameter-based Re_D. A similar correlation can also be found in (Incropera et al., 2007) for a fully turbulent flat plate with a constant T_S TBC in equation (2.2). For a constant Q_S TBC, the flat plate correlation has the same form as equation (2.2) but 4% greater, Re_L is the *Re* based on the length of the plate. In the recent literature, experimental work by (Wang et al., 2008a) showed that a correlation similar to the one of

Hilpert of can be formed for a NACA 63-421 airfoil based on α, *Pr* and the chord-based Re_c in the form of equation (2.3).

$$Fr_{Cyl} = A \times \mathrm{Re}_D^m \times \mathrm{Pr}^{1/3} \tag{2.1}$$

$$Fr_{FP} = 0.037 \times \mathrm{Re}_L^{0.3} \times \mathrm{Pr}^{1/3} \tag{2.2}$$

$$Fr_{NACA63-421} = \begin{cases} 0.094 \times (0.75 + 0.017 \times \alpha) \, \mathrm{Re}_c^{0.136} \times \mathrm{Pr}^{1/3} & \mathrm{Re} > 5 \times 10^5 \\ 2.482 \times (0.75 + 0.013 \times \alpha) \, \mathrm{Re}_c^{-0.189} \times \mathrm{Pr}^{1/3} & \mathrm{Re} \leq 5 \times 10^5 \end{cases} \tag{2.3}$$

To estimate the *Fr* on an airfoil, equation (2.1) could be used if an approximation to a cylinder is assumed. The same applies for equation (2.2) if the airfoil is approximated to a flat plate. The problem is that the *Fr* values would not also correspond to the correct geometry and that with either approximation, the effect of α cannot be modeled. On the other hand, and based on the results of this work, it is found that the Fr_{Avg} variation on an airfoil would not be accurately represented with a linear variation of α such as the one in equation (2.3). Therefore, a new correlation valid for all simulated *Re* is sought. The new correlation implies that the Fr_{Avg} would be better represented on an airfoil with a quadratic or a cubic variation of α, in the form of equation (2.4).

$$Fr_{Avg} = A \left(1 + B \times \alpha_{Eff} + C \times \alpha_{Eff}^2 + D \times \alpha_{Eff}^3 \right) \mathrm{Re}^m \, \mathrm{Pr}^{1/3} \tag{2.4}$$

In that scope, the present work uses the results of CFD simulations on a 2D airfoil to build a correlation for the Fr_{Avg}. Each simulation produced a specific Fr_{Avg} for each unique combination of the *Re* and α. These data are in turn used to build a correlation in the proposed form of equation (2.4) where *A*, *B*, *C*, *D* and *m* are parameters determined based on a curve

fitting method. The proposed correlation implies that to complete the coupling between either the BEMT or UVLM to the heat transfer database, only the *Re* and α_{Eff} are required.

2.1.2 Geometry Discretization

The discretized airfoil undergoing forced convection is shown in Figure 2.1. When a freestream of air passes with a velocity V_∞ and temperature T_∞ over it, a transfer of heat will exist between the airfoil surface and the air. For the considered cases of CFD simulations previously described, the airfoil wall is discretized into a specified number of points, as seen in the figure, with the locations of each point in the domain in the *x* and *y* directions known.
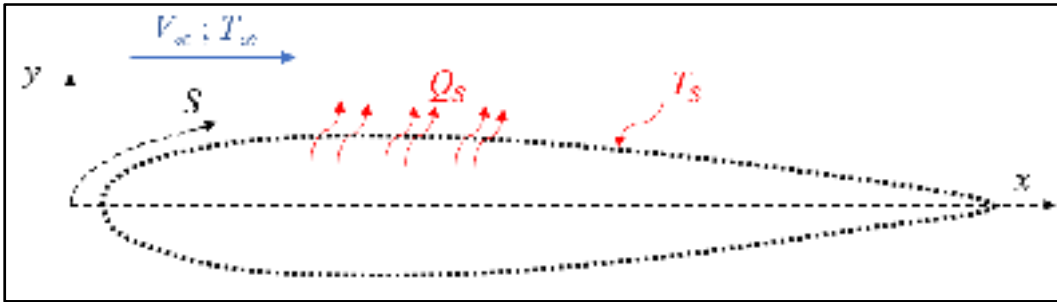
Figure 2.1 Representation of Discretized Points on Airfoil Wall with Convection

The location on the airfoil wall is defined by the non-dimensional curvilinear distance *S/c*. It represents the true length on the airfoil wall. Considering the L.E. at $i = 1$ and the T.E. is at $i = N$, then *S/c* is calculated using equation (2.5). A positive sign is adopted for the *S* on the upper surface and a negative indicated that the *S* is considered on the bottom surface.

$$S_i = \begin{cases} \sum_{2}^{N} \sqrt{(x_i - x_{i-1})^2 + (y_i - y_{i-1})^2} & i > 1 \\ 0 & i = 1 \end{cases} \tag{2.5}$$

2.1.3   Convective Heat Transfer

To estimate the convection rate, Newton's Law of Cooling is applied to the results of the 2D CFD simulations. At each discretized point, equation (2.6) is applied to calculate the local heat transfer coefficient h_x. The recovery temperature T_{rec} is used in that equation instead of the freestream temperature T_∞ to account for the effect of air velocity on heat transfer. The relation between T_{rec} and T_∞ is described in equation (2.7) where the specific heat capacity of air is c_P = 1006 $kJ/kg.K$.

$$h_x = \frac{Q_S}{(T_S - T_{rec})} \tag{2.6}$$

$$T_{rec} = T_\infty \left(1 + r_{coeff} \frac{V_\infty^2}{2c_P}\right) \tag{2.7}$$

For the presented CFD simulations, the flow is considered fully turbulent, so the recovery coefficient is set at $r_{coeff} = Pr^{1/3}$, according to (Kays & Crawford, 1993). With the calculated h_x, the local Nu_x is calculated based on the chord using equation (2.8) where k is the thermal conductivity of air. The thermal properties are evaluated at a film temperature T_f using equation (2.9).

$$Nu_x = \frac{h_x c}{k} \tag{2.8}$$

$$T_f = \frac{T_{rec} + T_S}{2} \tag{2.9}$$

In order to move from a local, point-by-point, representation into a global and general view, the average values for the heat transfer are computed. First, the average heat transfer coefficient h_{Avg} is obtained by calculating the sum-product of each h_x with its corresponding incremental

curvilinear distance ΔS_i and then averaging the total by diving by the airfoil chord as shown in equation (2.10). The Nu_{Avg} is then calculated over the whole airfoil wall as shown in equation (2.11).

$$h_{Avg} = \frac{1}{c} \sum_{i=1}^{N} h_{x,i} \times \Delta S_i \qquad (2.10)$$

$$Nu_{Avg} = \frac{h_{Avg} c}{k} \qquad (2.11)$$

Finally, to partially remove the dependency of the calculated Nu on the Re, the Fr is used by dividing the Nu from equations (2.8) or (2.11) with the square root of the chord based Re_c as shown in equation (2.12) for the Fr_x and equation (2.13) for the Fr_{Avg}. The Re_c used is based on the chord and is defined by equation (2.14).

$$Fr_x = \frac{Nu_x}{\sqrt{Re_c}} \qquad (2.12)$$

$$Fr_{Avg} = \frac{Nu_{Avg}}{\sqrt{Re_c}} \qquad (2.13)$$

$$Re_c = \frac{\rho V_\infty c}{\mu} \qquad (2.14)$$

2.1.4   Zone with Maximum *Fr*

Calculating the Fr_{Avg} over the airfoil is useful to obtain an estimate of the overall convection. However, the flow over the airfoil wall as well as the movement of the stagnation point due to an increase in α will cause some zones over the wall to experience higher heat transfer than

others. It is therefore important to determine the location of maximum heat transfer, or the zone that experiences the highest cooling rates and could be the most vulnerable for icing.

As will be presented later on in the results of sections 4.1.2.4 and 4.1.2.7, it is found that when the Re and α are increased up to α_{Stall} (the angle at which stall first occurs) the zone on the suction side of the airfoil near the L.E. experiences a continuous rise in Fr_x values that is higher than all other locations on the airfoil wall. This zone shows the maximum Fr_x values, up to twice as high as the average, and extends up to 20% of the c after the L.E. To calculate the average Fr at this zone, the airfoil is divided into 10 zones as shown in Figure 2.2. Each zone measures 20% of the chord in length. The zones are numbered from 1 to 10 as depicted. Zones 1 to 5 are on the suction side and 6 to 10 are on the pressure side of the airfoil.
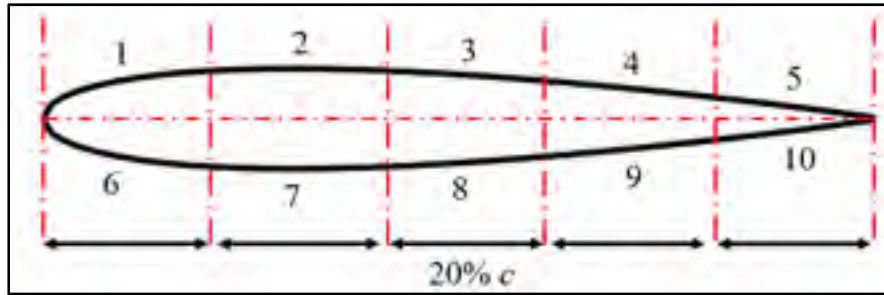
Figure 2.2 Depiction of Zone Divisions on NACA 0012 Wall

On each zone, the Fr_{Avg} is calculated for each simulated Re and α in a similar way to equation (2.10) but based on the respective start and end points of each zone. The average Fr value specific for zone 1 is termed Fr_{Max} and will also be correlated in the form of equation (2.15). Unlike the Fr_{Avg} correlation, the correlation for the Fr_{Max} is satisfied with a quadratic variation of α. The range of applicability of the Fr_{Max} is limited to pre-stall conditions. In this thesis, stall is identified based on flow observations as well as a comparison of the C_L variation with α. A specific α_{Stall} will be identified as the stall angle below which the Fr_{Max} correlation is valid.

$$Fr_{Max} = A\left(1 + B \times \alpha_{Eff} + C \times \alpha_{Eff}^2\right) Re^m \, Pr^{1/3} \tag{2.15}$$

2.1.5   Viscous Data

Aside from the heat transfer data, the CFD simulation by SU2 will produce viscous data for each simulated case of the airfoil at a specific Re and α. The terms of interest for this research are the Lift Coefficient C_L, Viscous Lift Curve Slope $C_{L\alpha}$ and the Drag Coefficient C_D. The need for these terms is primarily for their incorporation in the solution procedure of the BEMT and UVLM. It is discussed earlier in section 1.4.1 that to solve the BEMT, the 2D sectional $C_{L\alpha}$, C_L and C_D at each blade element must be provided. While they are usually obtained using an inviscid correlation, in this research they are imported from the viscous results of the CFD simulations. A similar use of the viscous data applies to the UVLM, but a viscous coupling algorithm based on the α-method presented in section 1.2 is needed for implementation. Based on the CFD simulations, the viscous data depend only on the Re and α. Therefore, for each radial position on the blade, the BEMT or the UVLM will be required to calculate the Re and α. The last two parameters will in turn be used as an input to the viscous database and an interpolation will be done to estimate the $C_{L\alpha}$, C_L and C_D at the specific radial location having a specific Re and α.

The procedure by which the aerodynamic tools use the viscous database can be outlined by Figure 2.3. This figure shows a sample of the C_L and C_D variation versus the simulated α. For clarification purposes, only the curves at $Re = 5 \times 10^5$ and $Re = 1 \times 10^6$ are shown. The CFD-determined values are represented by the $\times$ symbol and are joined by the solid black lines determined through a Modified Akima Cubic Hermite interpolation defined in MATLAB toolbox (MATLAB, 2019a). According to MATLAB, it produces fewer undulations than a spline interpolation, but does not flatten as aggressively.
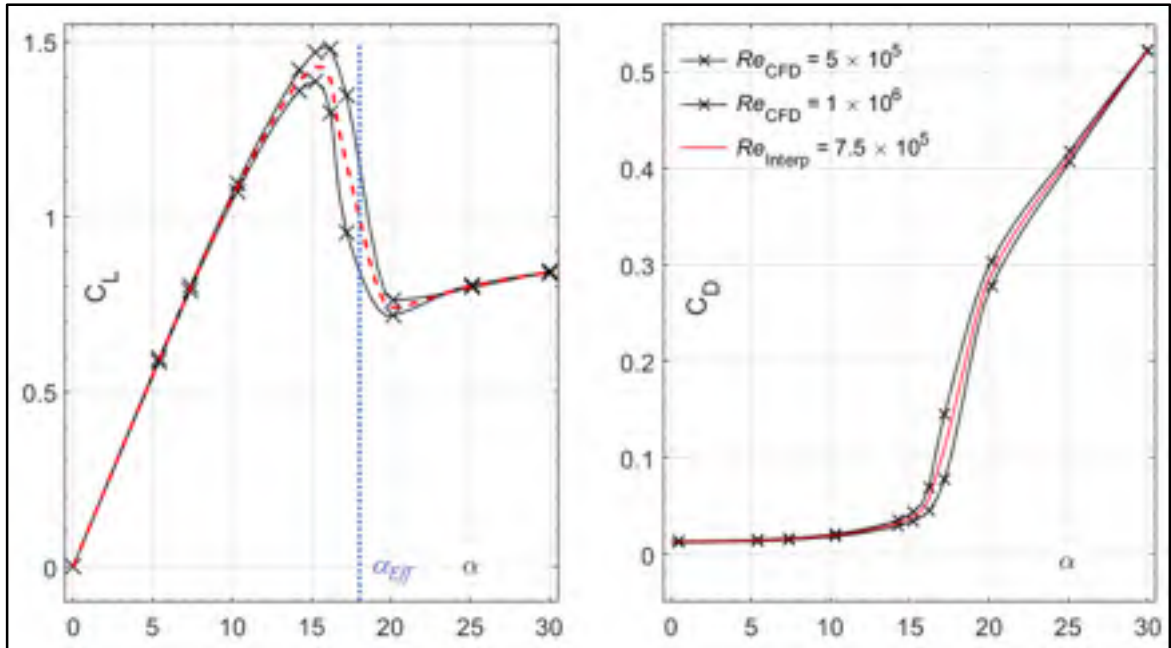
Figure 2.3 Example of the Interpolation Scheme Done on the CFD-Determined C_L and C_D

Assuming that at a certain radial position, the Re and α are $Re = 7.5 \times 10^5$ and $\alpha_{Eff} = 18°$, then the C_L and C_D are obtained using a double interpolation on the Re and the α. The first interpolation is done between the two closest CFD-determined Re, in this case these are $Re = 5 \times 10^5$ and $Re = 1 \times 10^6$. The results are shown in the figure by the dashed red line and represents the variation of the corresponding viscous term versus α. The second interpolation is then done between the two closest CFD-determined Re, in this case these are $\alpha = 17°$ and $\alpha = 20°$. Finally, for the $C_{L\alpha}$, a single interpolation to obtain the C_L vs. α variation at $Re = 7.5 \times 10^5$ is done. The $C_{L\alpha}$ is then calculated using the closest CFD-determined α in equation (2.16). In the equation, i is the index of the α on which the interpolation is occurring.

$$C_{L_\alpha}(i) = \frac{C_L(i+1) - C_L(i-1)}{\alpha(i+1) - \alpha(i-1)} \qquad (2.16)$$

2.2   Blade Element Momentum Theory

The BEMT is a low-fidelity steady state approach to obtain rotor performance that can account for camber, twist and different rotor configurations. However, it follows a simplified procedure to calculate the induced velocities and the inviscid assumption eliminates viscous effects. This thesis followed the implementation of the BEMT by (Leishman, 2000) with modifications on the incorporation of viscous lift & drag data and on the calculation of heat transfer through a link to the CFD database.

2.2.1   Blade Element Theory

Figure 2.4 shows the side view of a rotor blade with the respective loads and velocities. The aerodynamic forces are assumed to arise only from the velocities and angle of attack normal to the leading edge of the blade. As the rotor spins with an angular velocity Ω at a pitch θ, the normal and axial forces are created giving way to the lift L and drag D to be calculated.
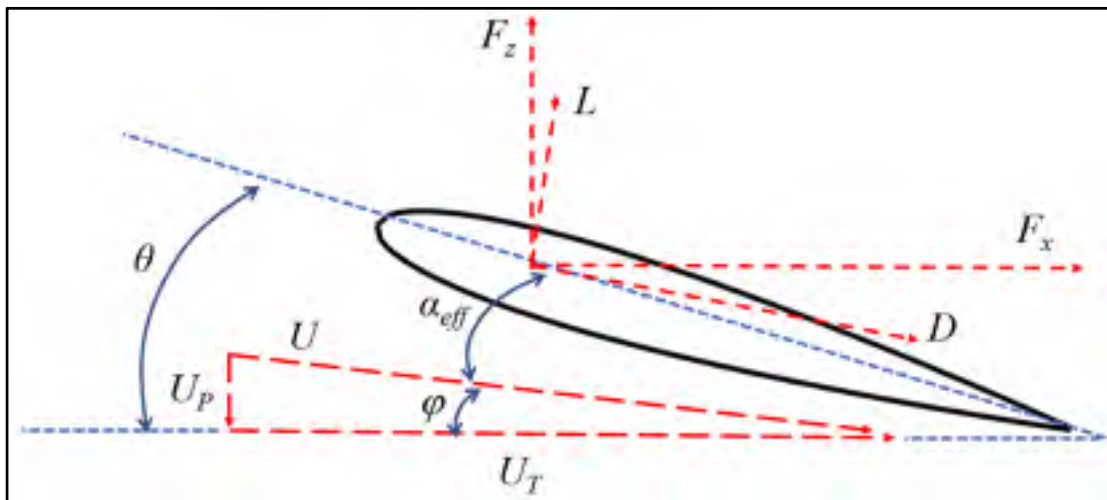
Figure 2.4 Aerodynamic Forces & Velocities Present on a Blade Element

For the BET, the blade is divided into n elements between the tip radius R and root radius R_0, each of equal length dy as shown in Figure 2.5. For a rotor in hover or axial flight only, it is assumed that the resultant local flow velocity U (equation (2.17)) at any blade element at a

radial distance r from the rotational axis has an out-of-plane component U_p (equation (2.18)) as a result of climb and induced velocities as well as an in-plane component U_T because of the rotation of the blade (equation (2.19)). For hover and axial flight, the radial velocity component U_R is assumed to be zero. The inflow ratio λ is defined by equation (2.20) as the ratio of tip values of the U_p to U_T.

$$U = \sqrt{U_P^2 + U_T^2} \tag{2.17}$$

$$U_P = V_c + v_i \tag{2.18}$$

$$U_T = \Omega \times y \tag{2.19}$$

$$\lambda = \frac{V_c + v_i}{\Omega R} \tag{2.20}$$
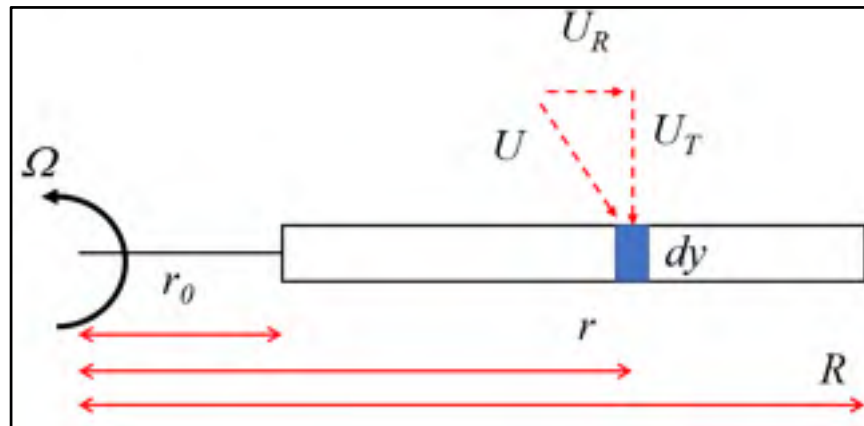
Figure 2.5 Velocities Acting on Blade Element

An induced angle of attack φ is assumed to arise due to induced velocities of the rotor and its wake. This angle modifies the direction of U, the value of the 2-D angle of attack as well as the lift vector creating a source of induced drag. For helicopters, the φ is assumed to be small

and may be calculated using equation (2.21). The effective angle of attack α_{Eff} is then the difference between the pitch θ and φ (equation (2.22)).

$$\varphi = \tan^{-1}\frac{U_P}{U_T} \tag{2.21}$$

$$\alpha_{Eff} = \theta - \varphi \tag{2.22}$$

The incremental lift & drag forces can expressed by equation (2.23) per unit span of the blade element where C_L and C_D are the lift and drag coefficients. These forces can be resolved into the force terms perpendicular and parallel to the rotor plane as per equation (2.24).

$$dL = 0.5 \times \rho c U^2 C_L dy$$
$$dD = 0.5 \times \rho c U^2 C_D dy \tag{2.23}$$

$$dF_z = dL\cos\varphi - dD\sin\varphi$$
$$dF_x = dL\sin\varphi + dD\cos\varphi \tag{2.24}$$

For a rotor with an N_b number of blades, the thrust T, torque Q and power P terms of the rotor can be expressed by equation (2.25). To get this equation, a few assumptions are made. First, the φ is small enough to set $\cos\varphi = 1$ and $\sin\varphi = 0$. Second, the drag term is at least ten orders of magnitude smaller than the lift, so $dD\varphi = 0$. Finally, the U_P is much larger than U_T leading to $U \approx U_T$. The last assumption follows that λ may be expressed by equation (2.26).

$$dT = N_b dL$$
$$dQ = N_b (\varphi dL + dD) y$$
$$dP = N_b (\varphi dL + dD) \Omega y \tag{2.25}$$

$$\lambda = \varphi\, r \tag{2.26}$$

Using the previous equation with the expressions of the non-dimensional coefficients, the coefficients for the thrust C_T, torque C_Q and power C_P can be expressed by equation (2.27). The solidity σ is determined based on equation (2.28) where N_b is the number of rotor blades.

$$dC_T = 0.5 \times \sigma C_L r^2 dr$$
$$dC_Q = dC_P = 0.5 \times \sigma \left(\varphi C_L + C_D \right) r^3 dr \tag{2.27}$$

$$\sigma = \frac{N_b c}{\pi R} \tag{2.28}$$

There exists another representation for the incremental thrust coefficient dC_T if the C_L in equation (2.27) is replaced with the lift curve slope $C_{L\alpha}$ from steady linearized aerodynamics as shown in equation (2.29), α_0 in that equation corresponds to the zero lift angle. If φ is introduced from equation (2.26) along with the lift replacement, the other representation for dC_T may be expressed by equation (2.30).

$$C_L = \left(\alpha - \alpha_0 \right) C_{L\alpha} = \left(\theta - \alpha_0 - \varphi \right) C_{L\alpha} \tag{2.29}$$

$$dC_T = 0.5 \times \sigma C_{L\alpha} \left[\left(\theta - \alpha_0 \right) r^2 - \lambda r \right] dr \tag{2.30}$$

2.2.2   Upgrade of the BET to BEMT

Figure 2.6 shows the assumptions of the conservation laws of the momentum theory applied to a rotor disk. The left side of the figure shows an annulus section on the rotor disk at a distance y from the axis of rotation, of width dy and of area $dA = 2\pi y\, dy$. The right side shows a cross

sectional view of the rotor disk with the velocity component due to climb V_c as well as the variation of the induced velocities v_i above and below the rotor disk. It is determined from the application of the 1-D momentum theory that the v_i below the rotor disk are twice the v_i above the disk for both hover and axial flight (Leishman, 2000).
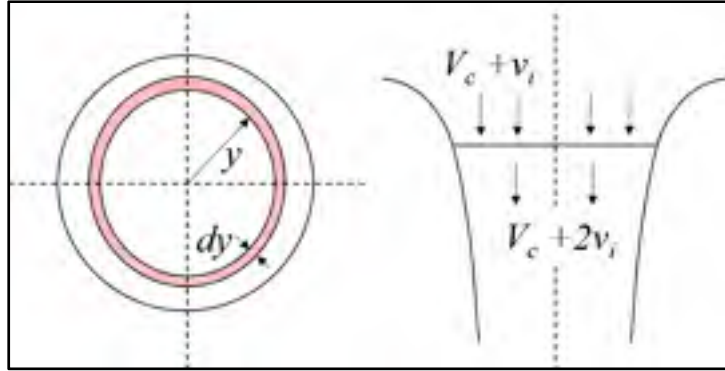
Figure 2.6 Top & Side View of Momentum Analysis on
an Annulus of Rotor Disk

If the conservation laws are applied to an annulus on the rotor disk, the incremental thrust dT may be calculated on the basis of the momentum theory. This is done by first calculating the mass flow rate of air $d\dot{m}$ through the annulus, as presented in equation (2.31), and then calculating dT by multiplying $d\dot{m}$ by twice the induced velocity at that annulus section (equation (2.32)).

$$d\dot{m} = 2\pi\rho\left(V_c + v_i\right)y\,dy \tag{2.31}$$

$$dT = 2v_i d\dot{m} = 4\pi\rho\left(V_c + v_i\right)v_i y\,dy \tag{2.32}$$

The nondimensional form of thrust can now take the form presented in equation (2.33). For a simplified representation, the inflow ratio λ may be used alongside an induced inflow ratio $\lambda_i = \dfrac{v_i}{\Omega R}$ or a climb inflow ratio $\lambda_c = \lambda - \lambda_i$ and the result is expressed by equation (2.34). By

an expanded analysis, dC_P is calculated by summing the induced and profile power coefficients dC_{Pi} and dC_{Po} as represented by equation (2.35).

$$dC_T = \frac{dT}{\rho\left(\pi R^2\right)\left(\Omega R\right)^2} = 4\frac{\left(V_c + v_i\right)}{\Omega R}\frac{v_i}{\Omega R}\frac{y}{R}d\left(\frac{y}{R}\right) \tag{2.33}$$

$$dC_T = 4\lambda\lambda_i r dr = 4\lambda\left(\lambda - \lambda_c\right)r dr \tag{2.34}$$

$$\left.\begin{aligned} dC_{P_i} &= 4\lambda^2\left(\lambda - \lambda_c\right)r dr = \lambda\frac{dC_T}{dr}dr \\ dC_{P_o} &= \frac{1}{2}\sigma C_D r^3 dr \end{aligned}\right\} dC_P = dC_{P_i} + dC_{P_o} \tag{2.35}$$

2.2.3   Prandtl's Tip Loss Factor

The work of *Prandtl* is used to model the loss of lift near the tips of blades resulting from induced effects associated with a finite number of blades. The importance of this factor can be exemplified in Figure 2.7 that shows two sample calculations of the BEMT with and without the tip loss factor. The primary effect of the tip loss-effect is to reduce the thrust production near the blade tip. According to (Leishman, 2000), a tip loss correction factor F is expressed by equation (2.36), where the f is calculated based on equation (2.37). F is introduced to the incremental thrust expression from equation (2.34) and the result is shown in equation (2.38).

$$F = \frac{2}{\pi}\cos^{-1}\left(e^{-f}\right) \tag{2.36}$$

$$f = \frac{N_b}{2}\left(\frac{1-r}{\varphi r}\right) \tag{2.37}$$

$$dC_T = 4F\lambda(\lambda - \lambda_c)r\,dr \tag{2.38}$$
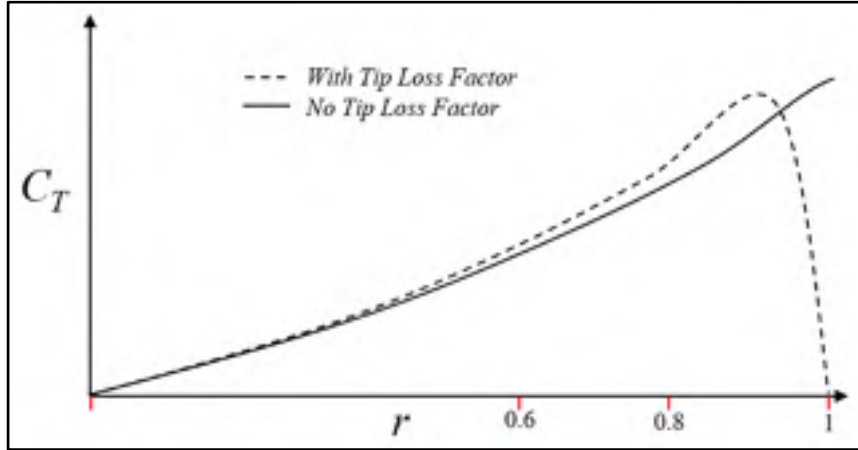
Figure 2.7 Sample C_T Obtained with and without Tip Loss Effect

2.2.4   Numerical Solution of the BEMT with Prandtl's Tip Loss

The solution of the BEMT equations with *Prandtl*'s tip loss correction are obtained by solving for the inflow ratio λ at each blade element. A final arrangement of equations is done by equating the dC_T with the tip loss (equation (2.38)) to the dC_T obtained from equation (2.30) and re-arranging the two sides of the equations into an expression for λ, the result is expressed in equation (2.39) where the parameter ζ is expressed by equation (2.40). In the case of a hovering rotor, the $\lambda_c = 0$ and the equation reduces to equation (2.41).

$$\lambda(r) = \frac{1}{\zeta}\left[\sqrt{1 - \zeta[2(\theta - \alpha_0)r + \lambda_c(4\zeta - 1)]} + \frac{\zeta\lambda_c}{2} - 1\right] \tag{2.39}$$

$$\zeta = \frac{16F}{\sigma C_{L_\alpha}} \tag{2.40}$$

$$\lambda(r) = \frac{1}{\chi}\left[\sqrt{1 - 2\zeta(\theta - \alpha_0)r} - 1\right] \tag{2.41}$$

The solution is not straightforward since F is a function of λ, so an iterative solution procedure is followed as presented in Table 2.1. The convergence criterion is set on the value of λ after each iteration, where the solution is considered converged when $|\lambda_{New} - \lambda_{Old}| \leq \varepsilon_l$. ε_l is usually equal to 10^{-5}. This solution procedure assumes that the blade radius R, chord c, pitch θ, rotor speed Ω, zero lift angle α_0, number of blades N_b and climb velocity V_c are all provided to begin with. The $C_{L\alpha}$, C_L and C_D should also be provided and may be calculated using a simplified correlation or, as implemented in this thesis and will be seen later, are interpolated from a viscous database based on the calculated α_{Eff}.

Table 2.1 Classical BEMT Iterative Solution

	Task
1	Guess a value for λ
2	Calculate α_{eff} & ϕ
3	Input C_L & C_D & $C_{L\alpha}$
4	Calculate tip loss factor F
5	Redo 1 to 4 until convergence $|\lambda_{New} - \lambda_{Old}| \leq \varepsilon_l$
6	Calculate incremental dC_T, dC_{Pi} & dC_{Po}
7	Sum Incremental values to get C_T, C_P & C_Q

2.2.5   Forces Calculation

To obtain the total aerodynamic coefficients from the BEMT, the C_T, C_P & C_Q are obtained by simply summing all the corresponding incremental values of each coefficient for all r as shown in equation (2.42) (Leishman, 2000). The sum of all elements of equation (2.38) produced the C_T where the C_P and C_Q are obtained by summing the elements of equation (2.35).

$$C_T = \sum_{r=1}^{n} dC_T(r) \quad C_P = C_Q = \sum_{r=1}^{n}\left[dC_{P_i}(r) + dC_{P_o}(r)\right] \tag{2.42}$$

The thrust, torque and power forces are all then determined using equations (2.43), (2.44) and (2.45) respectively.

$$T = \frac{1}{2}\rho\pi R^2 \times C_T \times (\Omega R)^2 \tag{2.43}$$

$$Q = \frac{1}{2}\rho\pi R^2 \times C_Q \times (\Omega R)^2 \times R \tag{2.44}$$

$$P = \frac{1}{2}\rho\pi R^2 \times C_P \times (\Omega R)^3 \tag{2.45}$$

For the figure of merit *FM*, describing the ratio of the ideal to actual power produced by the rotor, equation (2.46) is used.

$$FM = \frac{\sqrt[3/2]{C_T}}{C_Q\sqrt{2}} \tag{2.46}$$

2.2.6   BEMT-RHT

The final workflow breakdown of the medium fidelity rotor heat transfer prediction tool BEMT-RHT is outlined in Figure 2.8. The user begins with inputting the rotor radius R, chord c, pitch angle θ, twist angle θ_T, climb velocity V_c, rotation speed Ω, the number of blades N_b and the desired number of blade elements n. Through the work of this thesis, it is found that the change in predicted C_T and C_Q changes by less than 0.1% for values of $n > 200$. The thermal TBC on the blade surfaces should also be provided with the input.

The code initiates calculations by first dividing the rotor blade into n elements. At each one of these elements, the U, U_P and U_T as well as the φ and α_{Eff} are all calculated based on the

classical implementation of the BEMT (Leishman, 2000). The Re at each r is also calculated at this step. The first modification of the code is implemented at this step to increase the fidelity of the method, the Re & α_{Eff} combination at all r is sent to viscous database to interpolate for the viscous $C_{L\alpha}$, C_L and C_D. This is done to avoid using a completely inviscid approach and to incorporate the viscous data based on the interpolation scheme discussed in section 2.1.5.
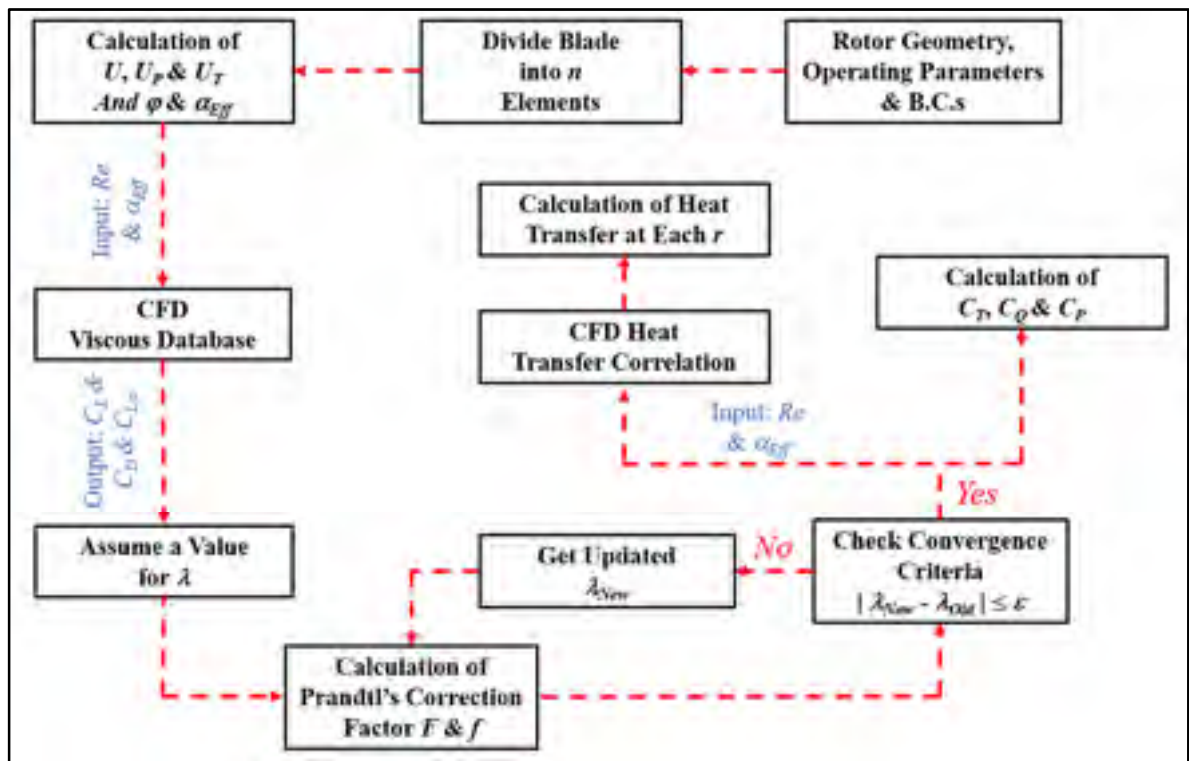
Figure 2.8 Workflow Breakdown of the BEMT-RHT

At this stage, the λ must be determined to obtain the C_T, C_P & C_Q. To do that, *Prandtl*'s tip loss equations are applied by first guessing a value for the $\lambda = \lambda_{Old}$. With this guessed value, the F and f equations are applied and a new $\lambda = \lambda_{New}$ is calculated. The convergence criterion is checked to see if $| \lambda_{New} - \lambda_{Old} | \leq \varepsilon_1$, if the criterion isn't met, the code sends back the λ_{New} to redo the F and f equations and come up with a newer λ. This procedure is repeated until the convergence criterion is valid and the code moves to the next step of calculations. The code applies the equations for the incremental dC_T, dC_{Pi} & dC_{Po} at each blade element r, sums all the incremental values and produces the C_T, C_P & C_Q.

The novelty of this research is to calculate the heat transfer at the blade radial positions. For the BEMT-RHT, this is achieved in the last step of the code execution. The previously calculated Re and α_{Eff} at each r are used for that purpose. The Fr_{Avg} correlation is applied using the two parameters using equation (2.4) and the average heat transfer at each radial location is then obtained.

2.3 Unsteady Vortex Lattice Method

The UVLM implementation of (Katz & Plotkin, 2001) is adjusted in this thesis to enable rotor blade modeling. The method assumes an inviscid, irrotational and incompressible flow around blades, therefore in its usual form compressibility and separation effects can not be modeled.

2.3.1 Discretization & Grid Generation

Figure 2.9 shows a typical vortex lattice distribution on a single blade. The blade is divided into an I number of lattices in the chordwise direction and J spanwise lattices. The lattices are placed on the blades' camberline forming the corner points Q_F, the leading segment of the lattice is placed on the panel's 1/4 chord line and the collocation point Q_C is at the center of the 3/4 chord line where the normal vector n_k is defined.

The blade geometry is described by $Root_X$ and $Root_Y$, the spacing between the blade and the centre of rotation O in the x and y directions, respectively. The span of the blade is denoted by R and the chord is c. For each timestep Δt, the blade rotated by an azimuth angle Ψ around the z axis and shed a new row of wake lattices. The Q_C of the shed wake elements at each timestep is placed at a distance equal to 30% of the length of the shed wake according to (Katz & Plotkin, 2001). Due to higher velocity near the tips, the wake elements closer to the root of the blade are smaller in size compared to those near the tips. The strength of each new shed wake panel is set equal to that of the trailing edge in the previous time step as in equation (2.47) according to the *Helmholtz* theorem.

$$\Gamma_W(t) = \Gamma_{T.E.}(t - \Delta t) \qquad\qquad (2.47)$$
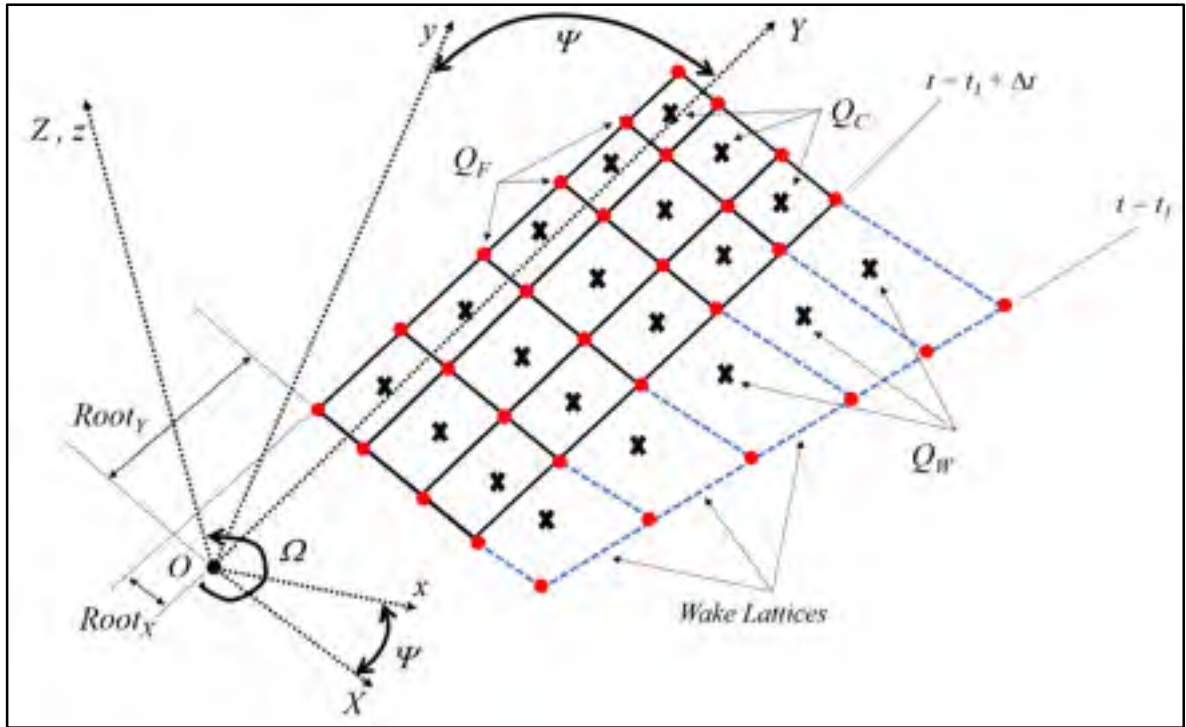
Figure 2.9 Vortex Lattice Distribution on Blade with Shed Wake Lattices

2.3.2 Kinematics

When time-dependent motions of bodies are treated, the selection of the coordinate systems is very important. Figure 2.10 shows the typical depiction of the frames of reference used in the application of the UVLM. The unsteady motion of the surface is described in a body-fixed frame of reference (x, y, z) while the motion of its origin O is then prescribed in an inertial frame of reference (X, Y, Z). The velocities in the respective x, y and z positive directions are defined as U_∞, V_∞, and W_∞ while the rotational changes in the azimuth, angle of attack and roll angles with respect to time are defined as Ψ, θ and ϕ.
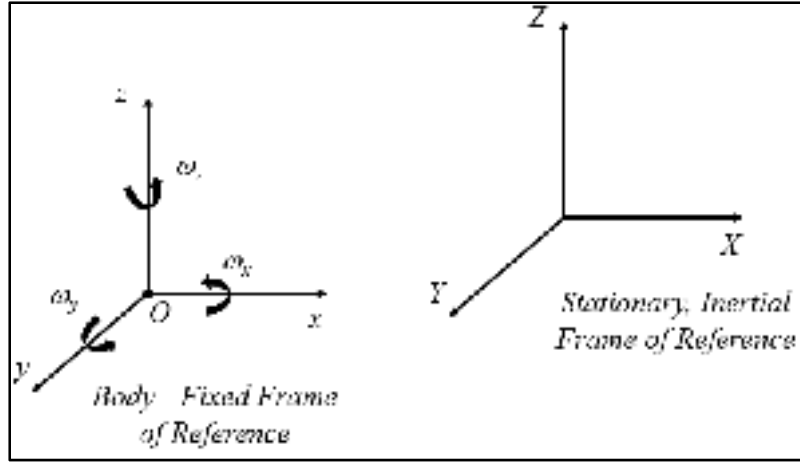
Figure 2.10 Body Fixed & Inertial Frames of Reference used
in UVLM

For the UVLM calculations, a transformation is established between the two coordinate systems that will be used for the velocities transformation. Such a three-dimensional transformation is uniquely defined by an order of rotation first by $\Psi(t)$ about the z axis (2.48), then $\theta(t)$ about the y axis (2.49), and finally $\phi(t)$ about the x axis (2.50).

$$
\begin{pmatrix} U_1 \\ V_1 \\ W_1 \end{pmatrix} = \begin{pmatrix} \cos\Psi & \sin\Psi & 0 \\ -\sin\Psi & \cos\Psi & 0 \\ 0 & 0 & 1 \end{pmatrix} \times \begin{pmatrix} -U_\infty \\ -V_\infty \\ -W_\infty \end{pmatrix}
\tag{2.48}
$$

$$
\begin{pmatrix} U_2 \\ V_2 \\ W_2 \end{pmatrix} = \begin{pmatrix} \cos\theta & 0 & -\sin\theta \\ 0 & 1 & 0 \\ \sin\theta & 0 & \cos\theta \end{pmatrix} \times \begin{pmatrix} U_1 \\ V_1 \\ W_1 \end{pmatrix}
\tag{2.49}
$$

$$
\begin{pmatrix} U_3 \\ V_3 \\ W_3 \end{pmatrix} = \begin{pmatrix} 1 & 0 & 0 \\ 0 & \cos\phi & \sin\phi \\ 0 & -\sin\phi & \cos\phi \end{pmatrix} \times \begin{pmatrix} U_2 \\ V_2 \\ W_2 \end{pmatrix}
\tag{2.50}
$$

The solution for the three step sequence of rotation transformation is summarized in equation (2.51) after the matrix multiplications are done. The total and general representation of the velocities due to translation and rotation of the body-fixed frame of reference as seen in the stationary inertial frame of reference is finally given by equation (2.52). The Δx, Δy and Δz terms in that equation are the distances travelled by the origin O between two timesteps in the respective x, y and z positive directions.

$$\begin{pmatrix} U_3 \\ W_3 \\ V_3 \end{pmatrix} = \begin{pmatrix} -\left(U_\infty \cos \Psi + V_\infty \sin \Psi\right) \cos \theta + W_\infty \sin \theta \\ -\left(U_\infty \sin \Psi + V_\infty \cos \Psi\right) \cos \phi - \left[\left(U_\infty \cos \Psi + V_\infty \sin \Psi\right) \cos \theta + W_\infty \sin \theta\right] \sin \phi \\ \left(U_\infty \sin \Psi + V_\infty \cos \Psi\right) \sin \phi - \left[\left(U_\infty \cos \Psi + V_\infty \sin \Psi\right) \sin \theta + W_\infty \cos \theta\right] \cos \phi \end{pmatrix} \quad (2.51)$$

$$\begin{pmatrix} U(t) \\ V(t) \\ W(t) \end{pmatrix} = \begin{pmatrix} U_3 \\ V_3 \\ W_3 \end{pmatrix} + \begin{pmatrix} -\omega_y \times \Delta z + \omega_z \times \Delta y \\ -\omega_z \times \Delta x + \omega_x \times \Delta z \\ -\omega_x \times \Delta y + \omega_y \times \Delta x \end{pmatrix} \quad (2.52)$$

In this thesis, a rotor is modeled for the cases of hover, axial and forward flight. It is assumed that the blades do not roll ($\phi = 0$), have a constant pitch angle ($\theta = \theta_c$) and that the rotation speed of the rotor is constant around the z axis at $\omega_z = \Omega$. For the case of a hovering rotor, there are no translational velocity components, so $U_\infty = V_\infty = W_\infty = 0$ and the rotation is purely around the z axis so $\omega_x = \omega_y = 0$. Equation (2.52) is then reduced to equation (2.53).

$$\begin{pmatrix} U(t) \\ V(t) \\ W(t) \end{pmatrix} = \begin{pmatrix} 0 \\ 0 \\ 0 \end{pmatrix} + \begin{pmatrix} \Omega \times y \\ -\Omega \times x \\ 0 \end{pmatrix} \quad (2.53)$$

For the case of a rotor in axial flight, $U_\infty = V_\infty = 0$ and $W_\infty \neq 0$ with $\omega_x = \omega_y = 0$ and equation (2.54) described the velocities measured in the inertial frame of reference.

$$\begin{pmatrix} U(t) \\ V(t) \\ W(t) \end{pmatrix} = \begin{pmatrix} W_\infty \sin\theta_c \\ 0 \\ -W_\infty \cos\theta_c \end{pmatrix} + \begin{pmatrix} \Omega \times y \\ -\Omega \times x \\ 0 \end{pmatrix} \tag{2.54}$$

For the case of a rotor in forward flight, $V_\infty = W_\infty = 0$ and $U_\infty \neq 0$ with $\omega_x = \omega_y = 0$. Similar to the previous analysis, equation (2.52) is reduced to equation (2.55).

$$\begin{pmatrix} U(t) \\ V(t) \\ W(t) \end{pmatrix} = \begin{pmatrix} -U_\infty \cos\Psi \cos\theta_c \\ -U_\infty \sin\Psi \\ -U_\infty \cos\Psi \sin\theta_c \end{pmatrix} + \begin{pmatrix} \Omega \times y \\ -\Omega \times x \\ 0 \end{pmatrix} \tag{2.55}$$

It is desirable to express the velocity vector that is perpendicular to the blade's leading edge by $V_{local} = U(t)$. According to the previous analysis, V_{local} varied from one radial position to the other due to the rotation speed of the blades and had different terms originating from the axial or forward velocity depending on the rotor flight condition. V_{local} is especially helpful in calculating the Re at each blade radius as expressed in equation (2.56) as well as estimating the local dynamic pressure P_{dyn} needed for the non-dimensional coefficient calculations, equation (2.57).

$$Re = \frac{\rho \times V_{local} \times c}{\mu} \tag{2.56}$$

$$P_{dyn} = \frac{1}{2} \rho V_{local}^2 \tag{2.57}$$

2.3.3   Induced Velocities Calculation

Typically, the velocity induced by each vortex segment on an arbitrary point is calculated using the Biot-Savart Law given in equation (2.58). This is also the proposed form by (Katz &

Plotkin, 2001). The three-dimensional solution of such a problem is possible by using constant-strength vortex-line segments, which can be used to model the wing or the wake. If the vortex segment points extend from point 1 to point 2, as shown in Figure 2.11, then the velocity at an arbitrary point P can be obtained by equation (2.58).

$$\vec{u}_{1,2} = \frac{\Gamma}{4\pi} \frac{\vec{r}_1 \times \vec{r}_2}{\left|\vec{r}_1 \times \vec{r}_2\right|^2} \vec{r}_0 \cdot \left(\frac{\vec{r}_1}{r_1} - \frac{\vec{r}_2}{r_2}\right)$$

(2.58)
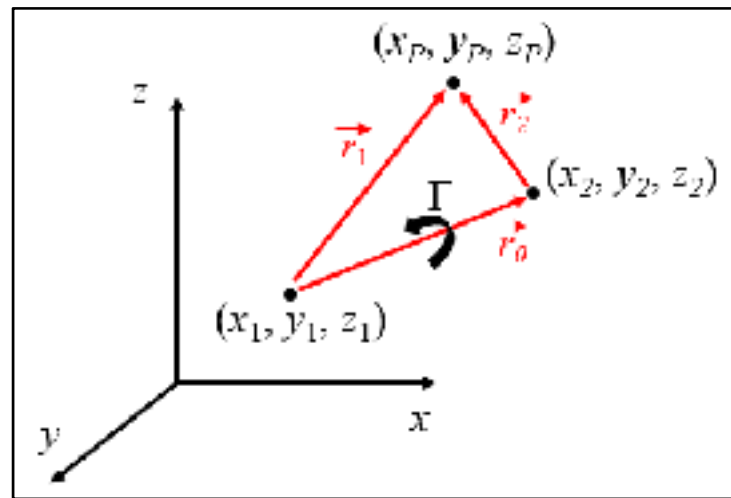
Figure 2.11 Induced Velocity of Segment 1-2 on Point P

For numerical computation in a Cartesian system where the (x, y, z) values of the points 1, 2, and P are given, the velocity can be calculated by first calculating the vector product of the position vectors, its absolute value and the distances between the two points 1 and 2 as shown in equations (2.59), (2.60) and (2.61) respectively.

$$
\begin{aligned}
\left(\vec{r}_1 \times \vec{r}_2\right)_x &= \left(y_p - y_1\right) \cdot \left(z_p - z_2\right) - \left(z_p - z_1\right) \cdot \left(y_p - y_2\right) \\
\left(\vec{r}_1 \times \vec{r}_2\right)_y &= -\left(x_p - x_1\right) \cdot \left(z_p - z_2\right) + \left(z_p - z_1\right) \cdot \left(x_p - x_2\right) \\
\left(\vec{r}_1 \times \vec{r}_2\right)_z &= \left(x_p - x_1\right) \cdot \left(y_p - y_2\right) - \left(y_p - y_1\right) \cdot \left(x_p - x_2\right)
\end{aligned}
$$

(2.59)

$$\left|\vec{r}_1 \times \vec{r}_2\right|^2 = \left(\vec{r}_1 \times \vec{r}_2\right)_x^2 + \left(\vec{r}_1 \times \vec{r}_2\right)_y^2 + \left(\vec{r}_1 \times \vec{r}_2\right)_z^2 \tag{2.60}$$

$$r_1 = \sqrt{\left(x_p - x_1\right)^2 + \left(y_p - y_1\right)^2 + \left(z_p - z_1\right)^2}$$
$$r_2 = \sqrt{\left(x_p - x_2\right)^2 + \left(y_p - y_2\right)^2 + \left(z_p - z_2\right)^2} \tag{2.61}$$

A check for singularity is usually conducted here, in the case when the point P lies on the vortex. A special treatment is needed in the vicinity of the vortex segment which is assumed to have a very small radius $\varepsilon_2 \approx 10^{-4}$ known as the vortex core size limit. If any of the conditions in equation (2.62) is true, then $u = v = w = 0$.

$$r_1 < \varepsilon \quad r_2 < \varepsilon \quad \left|\vec{r}_1 \times \vec{r}_2\right|^2 < \varepsilon_2 \tag{2.62}$$

The dot product of the vectors is calculated and the resulting induced velocity components u, v and w can then be found as shown in equations (2.63) and (2.64) respectively when the parameter χ relates to the circulation Γ of the vortex and is given by equation (2.65).

$$\vec{r}_0 \cdot \vec{r}_1 = \left(x_2 - x_1\right)\left(x_p - x_1\right) + \left(y_2 - y_1\right)\left(y_p - y_1\right) + \left(z_2 - z_1\right)\left(z_p - z_1\right)$$
$$\vec{r}_0 \cdot \vec{r}_2 = \left(x_2 - x_1\right)\left(x_p - x_2\right) + \left(y_2 - y_1\right)\left(y_p - y_2\right) + \left(z_2 - z_1\right)\left(z_p - z_2\right) \tag{2.63}$$

$$u = \chi \cdot \left(\vec{r}_1 \times \vec{r}_2\right)_x$$
$$v = \chi \cdot \left(\vec{r}_1 \times \vec{r}_2\right)_y \tag{2.64}$$
$$w = \chi \cdot \left(\vec{r}_1 \times \vec{r}_2\right)_z$$

$$\chi = \frac{\Gamma}{4\pi \left|\vec{r}_1 \times \vec{r}_2\right|^2} \left(\frac{\vec{r}_0 \cdot \vec{r}_1}{r_1} - \frac{\vec{r}_0 \cdot \vec{r}_2}{r_2}\right) \tag{2.65}$$

The disadvantage of this approach is the presence of a singularity point such as when the blade interacts with the wake as is demonstrated in equation (2.62). To solve this problem, the *Lamb-Oseen* viscous core model is used.

2.3.4   Lamb-Oseen Viscous Core Model

The *Lamb-Oseen* viscous core model is obtained by solving the Navier-Stokes equations in one dimension (Leishman et al., 2002). The *Lamb-Oseen* corrected *Biot-Savart* Law is given by equation (2.66) where r_c is the core size and the *Oseen* parameter is $\xi = 1.25643$.

$$\vec{u} = \frac{\Gamma}{4\pi} \frac{\vec{r}_1 \times \vec{r}_2}{|\vec{r}_1 \times \vec{r}_2|} \vec{r}_0 \left(\frac{\vec{r}_1}{|\vec{r}_1|} - \frac{\vec{r}_2}{|\vec{r}_2|} \right) \left(1 - e^{-\xi \left(\frac{|\vec{r}_1 \times \vec{r}_2|}{|\vec{r}_0| r_c} \right)^2} \right) \tag{2.66}$$

The equation for the vortex core size obtained from the original *Lamb-Oseen* formulation showed that the core grows with respect to time. However, the strength of a vortex in a fluid weakens with time due to viscous diffusion. Therefore, a turbulent eddy viscosity parameter to correct the ξ is added based on the model by (Bhagwat & Leishman, 2002). This way, the value of the turbulent eddy viscosity is determined, leading to a corrected core size r_c given in equation (2.67) where v is the static viscosity, Δt is the time and a is determined empirically and is around $a \approx 10^{-4}$. In this work, the typical Biot-Savart (equation (2.58)) is replaced with equation (2.66) where the r_c is calculated using equation (2.67).

$$r_c = \sqrt{r_0^2 + 4\xi \left(1 + a\frac{\Gamma}{v} \right) v \times \Delta t} \tag{2.67}$$

2.3.5   Influence Coefficients

Figure 2.12 shows a sample distribution of the blade vortex lattice distribution inspired by the work of (Katz & Plotkin, 2001). Each lattice is formed out of 4 different segments whose corresponding circulation is shown by the circulating arrows in the figure. These segments may be common with another adjoining lattice. The induced velocities of each lattice is the summation of the induced velocities of its respective four segments (subscripts 1 to 4) as shown in equation (2.68). Similarly, the induced velocity due to the trailing segments only, or the segments parallel to the flow, is given by equation (2.69).

$$\left(u,v,w\right)_{K,L} = \left(u,v,w\right)_1 + \left(u,v,w\right)_2 + \left(u,v,w\right)_3 + \left(u,v,w\right)_4 \tag{2.68}$$

$$\left(u,v,w\right)_{K,L}^* = \left(u,v,w\right)_2 + \left(u,v,w\right)_4 \tag{2.69}$$

The four corners of each lattice are the corner point Q_F and the center of each is defined as the collocation (or center) point Q_C. At each Q_C, the normal vector is defined and is calculated by the cross product of the diagonal vectors AA_k and BB_k (equation (2.70)).

$$n_K = AA_K \times BB_K \tag{2.70}$$
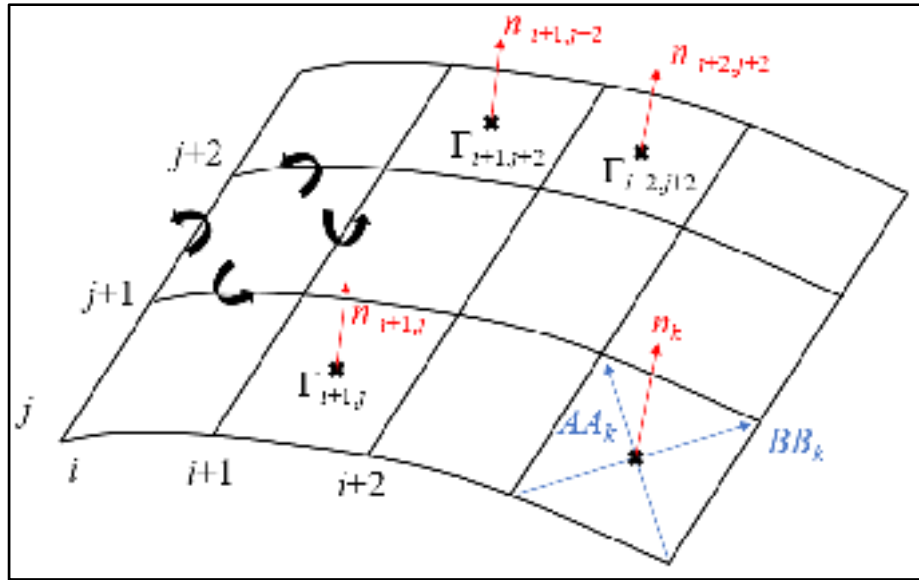
Figure 2.12 Typical Lattice Distribution with Normal Vectors on Collocation Points

The influence coefficients of the blade vortex rings are stored in the $a_{K,L}$ matrix where the counters K and L are defined by $K = 1 \rightarrow I \times J$ and $L = 1 \rightarrow I \times J$. The influence coefficients are calculated for each Q_C and represented the velocities induced due to the influence of all other blade bound vortex lattices. To obtain all the elements of the $a_{K,L}$ matrix, the calculations are repeated until all Q_C's are accounted for (equation (2.71)). In parallel, the $b_{K,L}$ matrix is calculated (equation (2.72)) in a similar way but with accounting only for trailing segments as explained previously. The $b_{K,L}$ served for later induced drag calculations.

$$a_{K,L} = (u,v,w)_{K,L} \cdot \vec{n}_K \qquad (2.71)$$

$$b_{K,L} = (u,v,w)^*_{K,L} \cdot n_K \qquad (2.72)$$

It should be noted that the influence coefficient $a_{K,L}$ comprised not only the influence of the blade's lattices on itself but rather the influence of other blades (if a multi-blade rotor is modeled) as well as the influence of the mirror images to account for the ground effect. For example, if a 2-blade rotor is modeled in ground effect, equation (2.71) would be expanded

into equation (2.73). The first term on the right hand of the equation is the induced velocities of the first blade and the second term corresponded to the second blade. It is assumed in this equation that the 2 blades are symmetric in the circular plane of their motion, so the only difference corresponded to the negative sign in front of the induced velocity component in the *y* axis. The third and fourth terms are for the induced velocity components of the mirror images of blades 1 and 2. A symmetry here is assumed with respect to the ground plane so the negative sign is imposed in front induced velocity component in the *z* axis.

$$a_{K,L} = (u,v,w)_{K,L} \cdot \vec{n}_K + (u,-v,w)_{K,L} \cdot \vec{n}_K + (u,v,-w)_{K,L} \cdot \vec{n}_K + (u,-v,-w)_{K,L} \cdot \vec{n}_K \qquad (2.73)$$

$$\underbrace{\qquad}_{Blade\ 1} \quad \underbrace{\qquad}_{Blade\ 2} \quad \underbrace{\qquad}_{Mirror\ Blade\ 1} \quad \underbrace{\qquad}_{Mirror\ Blade\ 2}$$

2.3.6   Calculations & Solution of RHS Matrix

The RHS matrix is formed by enforcing the zero normal velocity boundary condition on the surface of the blade and the resulting form is shown in equation (2.74). The *U(t)*, *V(t)*, and *W(t)* terms are the time-dependent kinematic velocity components determined previously from equation (2.55) whereas the u_w, v_w and w_w terms are the induced velocity components due to the wake lattices.

$$RHS_K = -\left[U(t) + u_W, V(t) + v_W, W(t) + w_W \right]_K \cdot n_K \qquad (2.74)$$

Finally, the solution for the circulation components Γ_k is introduced. After calculating the influence coefficients $a_{K,L}$ and enforcing the zero normal flow boundary condition on all of the blade's collocation points, the set of algebraic equations are written in their matrix form (equation (2.75)). The matrix is solved in its indicial form (equation (2.76)) where $a_{K,L}^{-1}$ are the coefficients of the inverted matrix.

$$\begin{pmatrix} a_{1,1} & a_{1,2} & \cdots & a_{1,m} \\ a_{2,1} & \vdots & \cdots & a_{2,m} \\ \vdots & \vdots & \ddots & \vdots \\ a_{m,1} & a_{m,2} & \cdots & a_{m,m} \end{pmatrix} \times \begin{pmatrix} \Gamma_1 \\ \Gamma_2 \\ \vdots \\ \Gamma_m \end{pmatrix} = \begin{pmatrix} RHS_1 \\ RHS_2 \\ \vdots \\ RHS_m \end{pmatrix} \tag{2.75}$$

$$\Gamma_K = \sum_{L=1}^{m} a_{K,L}^{-1} \times RHS_K \tag{2.76}$$

2.3.7   Prandtl-Glauert Compressibility Correction

To account for compressibility effects, (Glauert, 1928) proposed a compressibility correction β to high subsonic Mach numbers to include the compressibility effects in the calculations of VLM methods (Parenteau et al., 2017). It is known as the Prandtl–Glauert compressibility correction factor (equation (2.77)). In particular, β is introduced to the calculation of the vortex's circulation and equation (2.76) is modified into the form of equation (2.78).

$$\beta_K = \sqrt{1 - Ma_K^2} \tag{2.77}$$

$$\Gamma_K = \sum_{L=1}^{m} \frac{1}{\beta_K} a_{K,L}^{-1} \times RHS_K \tag{2.78}$$

2.3.8   Forces Calculation

The pressure distribution calculations needed the local circulation so that the fluid dynamic loads can be computed using the *Bernoulli* equation. At the leading edge, the local circulation is equal to $\Gamma_{i,j}$ but for all elements behind the leading edge, it is equal to $\Gamma_{i,j} - \Gamma_{i-1,j}$. The pressure difference is then given by equation (2.79) where Δb and Δc are the spanwise and chordwise lengths of the lattices. τ_i and τ_j are each panel's tangential vectors in the i and j directions.

$$\Delta p_{i,j} = \rho \left\{ \left[U(t) + u_W, V(t) + v_W, W(t) + w_W \right]_{i,j} \cdot \left[\tau_i \frac{\Gamma_{i,j} - \Gamma_{i-1,j}}{\Delta c_{i,j}} + \tau_j \frac{\Gamma_{i,j} - \Gamma_{i,j-1}}{\Delta b_{i,j}} \right] + \frac{\partial}{\partial t} \Gamma \right\} \quad (2.79)$$

The force contribution of each lattice in the body's three axes is then described by equation (2.80) where ΔS is the area of each lattice and $n_{i,j}$ is the normal vector of each lattice in the desired force direction. For the thrust calculations, $n_{i,j}$ is the vector in the Z axis direction and for the torque, $n_{i,j}$ is the vector in the X axis direction. The thrust and torque forces are then obtained by summing all the incremental forces from all lattices as shown in equations (2.81) and (2.82). The C_T is then obtained using equation (2.83) and a similar analysis is followed to obtain the torque coefficient C_Q (equation (2.84)). The FM is finally expressed by equation (2.85).

$$\Delta F = -\left(\Delta p \Delta S \right)_{i,j} \cdot n_{i,j} \quad (2.80)$$

$$T = \sum_{j=1}^{J} \sum_{i=1}^{I} \left(\Delta p \Delta S \right)_{i,j} \cdot n_{i,j}^{Z} \quad (2.81)$$

$$Q = \sum_{j=1}^{J} \sum_{i=1}^{I} \left(\Delta p \Delta S \right)_{i,j} \cdot n_{i,j}^{X} \quad (2.82)$$

$$C_T = \frac{T}{\pi R^2 \times P_{dyn}} \quad (2.83)$$

$$C_Q = \frac{Q}{\pi R^2 \times P_{dyn} \times R} \quad (2.84)$$

$$FM = \frac{\sqrt[3/2]{C_T}}{C_Q \sqrt{2}}$$ (2.85)

To calculate the inviscid sectional lift coefficient C_{L_y} at each blade radial position, the sectional lift force is first calculated using equation (2.86) by summing all the product of all the lattices in the chord direction of the blade. In other words, at each spanwise location j, the lift of all the lattices between $1 \leq i \leq I$ is added. The C_{L_y} is then represented by equation (2.87) where A_y is the area at each position j of all lattices between $1 \leq i \leq I$.

$$L_y = \sum_{i=1}^{I} \left(\Delta p \Delta S \right)_{i,j}$$ (2.86)

$$C_{L_y} = \frac{L_y}{A_y \times P_{dyn}}$$ (2.87)

2.3.9   Slow-Start Method

For free-wake calculations on rotor blades starting from rest, nonphysical instabilities of the initial wake are present. The root velocity influence is larger than the downward velocity and this will cause the strong root-vortex circulation to move upwards. This problem is encountered when the UVLM implementation of (Katz & Plotkin, 2001) is adjusted for rotor modeling.

To solve this problem, this work uses a slow-starting method to overcome and avoid large fluctuations of simulation results proposed by (Chung et al., 2006) and used by (Colmenares et al., 2015) in their UVLM rotor implementation. The angular velocity of the rotor is increased linearly during a specified initial number of rotations as described in equation (2.88) where N_{SS} is the slow-starting number of revolutions and N_A is number of revolutions actually traveled. In this work, it is found that two or three revolutions are enough to develop a stable wake.

$$\Omega_{SS} = \Omega \times \frac{N_A}{N_{SS}}$$
(2.88)

2.3.10 Viscous Coupling Algorithm

To successfully link the UVLM to the CFD viscous and heat transfer database/correlation, the α_{Eff} is needed at each radial section. The method chosen is the one proposed by (Van Dam, 2002) and referred to as the α-method when used by (Gallay & Laurendeau, 2015) and (Gallay & Laurendeau, 2016). The α-method is favored since it provided results even in post-stall angles according to these works. The function of this method is depicted in Figure 2.13 where for each section on the rotor blade, the angle of attack is corrected for each inviscid lift coefficient obtained by the UVLM, at each iteration. The term $\Delta\alpha_{visc}$ is the calculated based on the difference between the viscous and inviscid C_L, calculated at each blade section. The viscous lift coefficient $C_{L\text{-}visc}$ is obtained by an interpolation from the CFD viscous database for each Re & α_{Eff}.
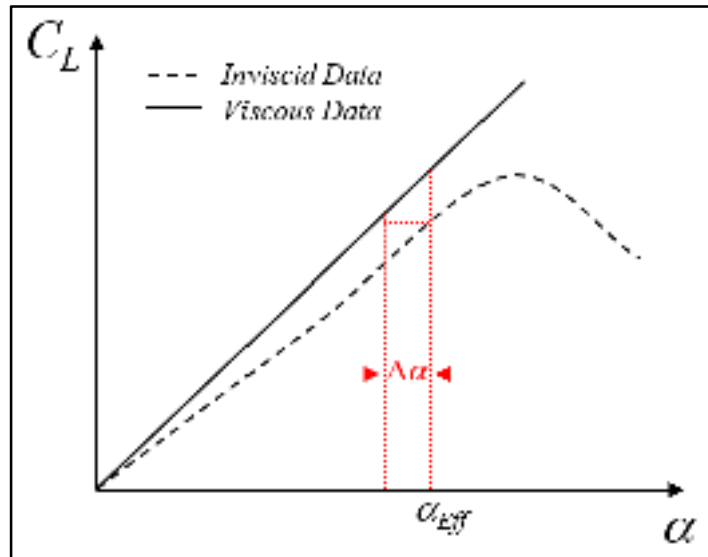
Figure 2.13 Representation of the α_{Eff} Correction Scheme

The approach followed an iterative procedure between the inviscid lift coefficient $C_{L\text{-}inv}$ (obtained using UVLM as C_{Ly}, equation (2.87)), the viscous lift coefficient $C_{L\text{-}visc}$ (obtained using CFD simulations) and the viscous lift-curve slope $C_{L\alpha}$ at each blade section. The breakdown of the approach is described in the following steps:

1- Calculate α_{Eff} based on equation (2.89)

$$\alpha_{Eff} = \frac{C_{L-inv}}{C_{L\alpha}} - \Delta\alpha_{visc} + \alpha_{Geo} \qquad (2.89)$$

2- Use the calculated α_{Eff} to interpolate the viscous database, equation (2.90), and obtain C_{Lvisc}

$$\alpha_{Eff} \Rightarrow C_{L-visc}\left(\alpha_{Eff}\right) \qquad (2.90)$$

3- Calculate, using equation (2.91), the correction for the angle of attack $\Delta\alpha_{visc}$

$$\Delta\alpha_{visc} = \frac{C_{L-visc} - C_{L-inv}}{C_{L\alpha}} \qquad (2.91)$$

4- Use the new $\Delta\alpha_{visc}$ in equation (2.89) and redo the process from 1 to 3
5- Repeat steps 1 to 4 until the convergence criterion in equation (2.92) is met

$$\left|C_{L-inv} - C_{L-visc}\right| \leq \varepsilon_3 \qquad (2.92)$$

α_{Geo} is the geometric angle of attack and the convergence criterion is $\varepsilon_3 = 10^{-3}$ (Van Dam, 2002). It should be mentioned that at the first step of the iterative approach, the $C_{L\alpha}$ is calculated based on the α_{Geo} since α_{Eff} is not known. For the subsequent iterations, the $C_{L\alpha}$ is calculated based

on the α_{Eff} from the previous iteration. Using this method, the α_{Eff} is determined at each radial position of the blade.

The parameters of equation (2.4) would now be satisfied, where the α_{Eff} & Re are now both known at each blade radial location. The originality of this research shows up with the following modifications. The two parameters are applied to the new heat transfer correlation to obtain the Fr at each blade section. With the $C_{L\text{-}visc}$ at each blade section also known, the UVLM-calculated inviscid C_{Ly} can now be replaced with the viscous term. An interpolation scheme based on the method of section 2.1.5 can also be used to interpolate the viscous $C_{D\text{-}visc}$ term at each blade section. The new $C_{L\text{-}visc}$ is used to reverse-engineer equations (2.87) and (2.86) to get an updated pressure distribution. This in turn is used in equations (2.81) and (2.82) to get an updated thrust and torque coefficient based on the $C_{L\text{-}visc}$ instead to the UVLM-calculated inviscid one.

2.3.11 Wake Roll-Up

The UVLM assumes that the wake produced by the blades is force free and is therefore free to move with local stream velocity. This local velocity is a result of the induced velocity components by the blades as well as the wake itself and is calculated at each corner point of each wake vortex lattice. The displacement of the corner points in the respective X, Y and Z directions are denoted by Δx_w, Δy_w and Δz_w and calculated by equation (2.93).

$$\left(\Delta x_w, \Delta y_w, \Delta z_w\right) = \left(u, v, w\right)_{Roll-Up} \times \Delta t \qquad (2.93)$$

The $\left(u, v, w\right)_{Roll-Up}$ terms in the previous equation are obtained using equation (2.94). They are formed based on the induced velocities due to the blades $\left(u, v, w\right)_b$ and the induced velocities due to the wake $\left(u, v, w\right)_w$. Each of those terms is calculated depending on the x, y and z coordinates of each corner point using the method described in sections 2.3.3 and 2.3.4.

$$(u,v,w)_{Roll-Up} = (u,v,w)_b + (u,v,w)_w \qquad (2.94)$$

2.3.12 UVLM-RHT

The final workflow breakdown of the medium fidelity rotor heat transfer prediction tool UVLM-RHT is outlined in Figure 2.14. For the input, the user specifies the rotor span R, chord c, blade airfoil profile, pitch angle θ, twist angle θ_T, spacing of the blades from the center of rotation $Root_X$ and $Root_Y$, rotation speed Ω, axial or forward speed (V_Z or V_X) and ground clearance CH. The user also needs to provide the number of discretizing lattices in the chord and span directions (I & J) as well as the incremental azimuthal angle $\Delta\Psi$ by which the rotor will turn from one timestep to the other and the total number of desired simulated revolutions N_{Total}. The code then initiates the timer and the calculations begin; calculations terminate when N_{Total} is reached.

Based on the method of (Katz & Plotkin, 2001) and just before the code initiates the first timestep, the geometric input is analyzed and the corner point Q_F, collocation points Q_C and normal vectors n are identified for each lattice. When a new timestep is considered, the row of newly shed wake lattices is created and its coordinates are calculated based on the kinematic information from the input that are different if the rotor is in hover, axial or forward flight. Next, the influence coefficients are calculated, and these include the effect of the blade and wake lattices on each blade lattice as well as on each wake lattice. As opposed to the original UVLM and based on a similar application by (Colmenares et al., 2015) and (Ferlisi, 2018), the influence coefficients are calculated based on the *Lamb-Oseen* model of (Leishman et al., 2002) and the core size of (Bhagwat & Leishman, 2002).
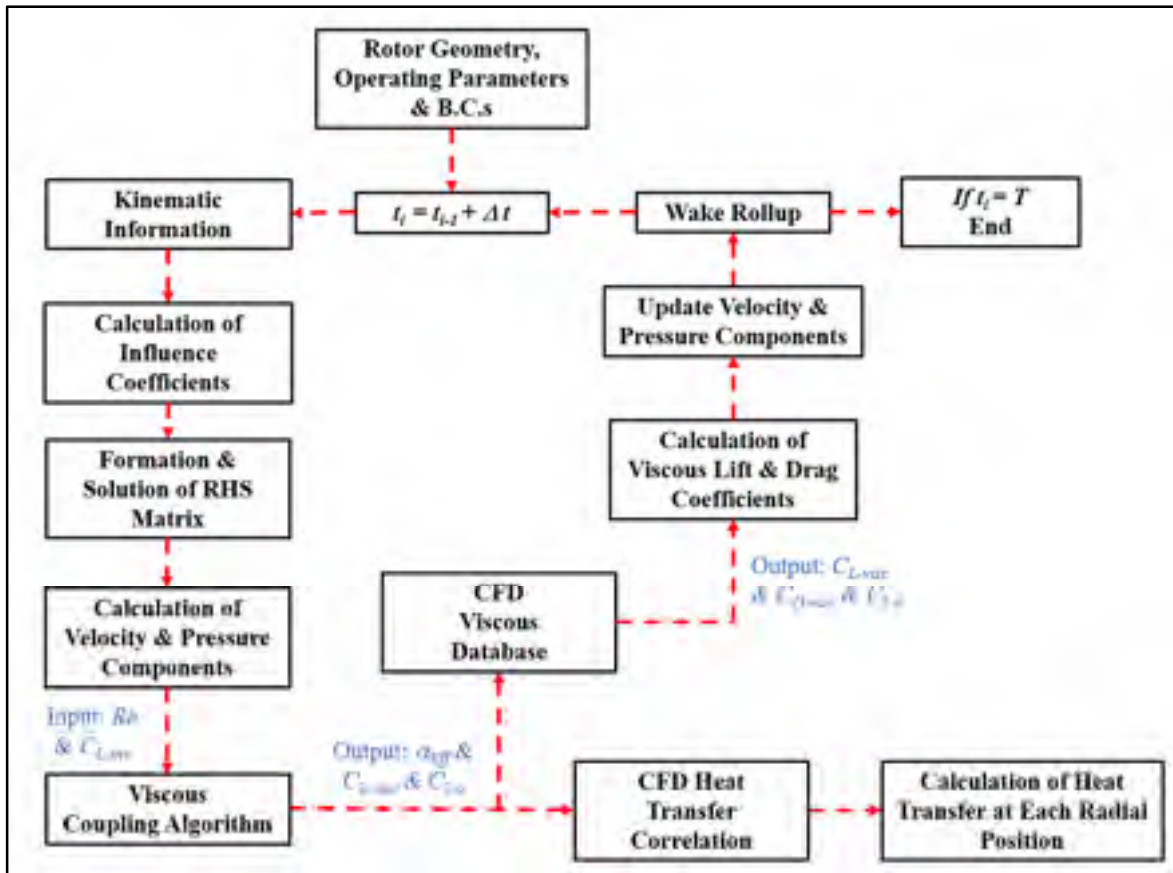
Figure 2.14 Workflow Breakdown of the UVLM-RHT

Next, the *RHS* matrix is formed and the circulation on each blade lattice is solved for as outlined, taking into account the added *Prandtl–Glauert* compressibility correction as used by (Parenteau et al., 2017). With the circulation terms known, the equations of section 2.3.8 can be applied to calculate the pressure difference through the camberline, followed by the required coefficients of lift, thrust, torque and induced drag. Based on the method proposed by (Van Dam, 2002), the viscous coupling algorithm is applied on the inviscid C_{Ly} and *Re* that are fed into the CFD viscous database to obtain the C_{Lvisc} and α_{Eff}, as seen in (Gallay & Laurendeau, 2015). The viscous terms are then used to update the force and velocity components. The wake roll-up is then accounted for and the wake lattices are moved according to the respective geometric deformation.

Up until this point, the code is running with in a comparable fashion to other implementations of the literature for the UVLM for rotors. At the following step, the originality of the research of calculating the blade heat transfer is achieved. The Re and α_{Eff} will then be fed into the CFD heat transfer correlation (equation (2.4)) to calculate the non-dimensional heat transfer on each blade section in the form of Fr_{Avg}. Finally, the code initiates the next timestep and the rotor is rotated by $\Delta\Psi$, a new row of shed wake lattices is added. The whole procedure is then repeated until the total number of desired revolutions is attained and the heat transfer is calculated at all r and Ψ.

2.4   Conclusion

This chapter presented the numerical methods and mathematical models implemented for the numerical applications of this thesis. In it, three main objectives were achieved. The first was regarding establishing a CFD-based viscous and heat transfer database for a 2D airfoil. Next, the methodology followed to implement, modify and link a typical mathematical BEMT model to the CFD database is outlined. Similarly, the third objective was to present the mathematical and physical model the UVLM that was modified and linked to the viscous and heat transfer database.

Although coupling methods were seen in the literature, this kind of BEMT/UVLM coupled with a heat transfer database/correlation can not be found in the literature nor has been tried in the past, to the best of the author's knowledge. The results of this coupling will be presented later in Chapter 4 when the BEMT-RHT and UVLM-RHT are used to model a modified Bell 429 tail rotor in various flight conditions. Before preceding to the complete results however, Chapter 4 will analyze the heat transfer variations on the airfoil before presenting the final form of the Fr_{Avg} correlation. An extensive validation procedure on the implemented BEMT and UVLM will be done to make sure they are capable of correctly modeling the aerodynamics of rotors.

With the numerical component of this thesis covered in this chapter, the next chapter will present the methodology followed for the experimental part of this thesis. The experiments were done in the Icing Wind Tunnel to measure the convective heat transfer from a fixed wing airfoil as well as a rotor. The main purpose of these experiments is to validate the developed numerical tools of this chapter.

CHAPTER 3

EXPERIMENTAL METHODOLOGY

The past chapter presented the numerical models that were implemented to couple a CFD-determined fully turbulent heat transfer database to the BEMT & UVLM. The BEMT-RHT & UVLM-RHT were presented as two coupled numerical tools that calculate the heat transfer on rotor blades. To validate the tools, experiments were required but no work in the literature was found to provide comparable data. Specifically, no rotor test case with convective heat transfer measurements on the blade was found. This chapter presents the methodology followed for the experimental work of this thesis. The experiments were carried out at the Icing Wind Tunnel (IWT) located at the Laboratoire International des Matériaux Antigivre (LIMA), a facility of the Université du Québec à Chicoutimi (UQAC).

The experimental work consisted of two phases. The first phase measured the heat transfer coefficients on a fixed wing with a constant airfoil section. The goal was to validate the 2D airfoil CFD simulations by comparing the measured Fr on the experimented airfoil at different Re (airspeeds), angles of attack α and chord locations S/c. The second phase consisted of measuring the heat transfer on blades of a spinning rotor at different rotor speeds Ω, pitch angles θ as well as radial r/R and chord locations S/c. The goal was to validate the implementation of the UVLM-RHT & BEMT-RHT as numerical rotor heat transfer prediction tools.

The first section of this chapter gives a brief introduction and describes the Icing Wind Tunnel in which all the experimental work was conducted. The second section is about the methodology followed for the fixed wing experiments. Here, the geometry of the wing and its construction are first described along with the TBC imposed. The description then moves towards the test environment and test plan with the individual test IDs and corresponding air freestream velocity, temperature, and angle of attack. The third section of the chapter is regarding the rotor experiments. Similar to the previous section, it begins with a description of

the spinning rotor blades geometry and construction, moves to method followed to capture the data and place the RTDs and presents the test plan for the specific tests with the corresponding rotor speed, pitch angle as well as the chordwise and radial location of the RTDs. The final section describes the method followed to calculate the heat transfer coefficients and the corresponding *Fr*. Finally, the data reduction, data averaging and experimental error estimation techniques are presented.

3.1 Wind Tunnel Description

The fixed wing experimental setup was designed for testing in a refrigerated wind tunnel at the LIMA. Figure 3.1 shows a general photo of the IWT in which all the experiments were conducted. The wind tunnel meets the conditions (Villeneuve & Perron, 2012) of the SAE Aerospace Recommended Practice for icing wind tunnel ARP5905 (SAE, 2003) and Aerospace Information Report for droplet sizing AIR4906 (SAE, 1995). The IWT is a closed-loop low speed refrigerated wind tunnel able to operate at sub-zero temperatures at sea level pressure and has two test sections. The smaller test section was used for the fixed wing experiments and is 0.5 m wide by 0.6 m high and tests can be run at air speeds up to 110 m/s at room temperature. The larger test section was used for the rotor experiments, it is 0.91 m wide by 0.76 m high and tests can be run at air speeds up to 50 m/s at room temperature. The IWT test section air speed is controlled by computer via a control program and data acquisition card. The test section air speed is calculated with the Bernoulli equation. The speed in the test section is given by equation (3.1).

$$V_{Test Section} = \sqrt{2\left(1 - \frac{A_{Test Section}^2}{A_{Ramp Section}^2}\right)^{-1} \frac{p_{Ramp Section} - p_{Test Section}}{\rho_{air}}} \qquad (3.1)$$

Figure 3.1 Icing Wind Tunnel

Figure 3.2 shows a general view of the IWT. The tunnel is a closed recirculating type that cools the flow immediately downstream of the test section. The refrigeration system capacity can vary the total air temperature between -48°C and 22°C. This is achieved by passing the air through a heat exchanger of 1.6 m by 1.6 m, powered by a compressor and a glycol pump.

1	Test section	9	Spray nozzles
2	Corner vanes	10	Motor control panel
3	Access doors	11	Control console
4	Access panels	12	Traps
5	Thermal expansion joints	a	Evaporator
6	Drains	b	Expansion valve
7	Fan and Motor	c	Condenser
8	Contraction cone 9.4:1	d	Compressor
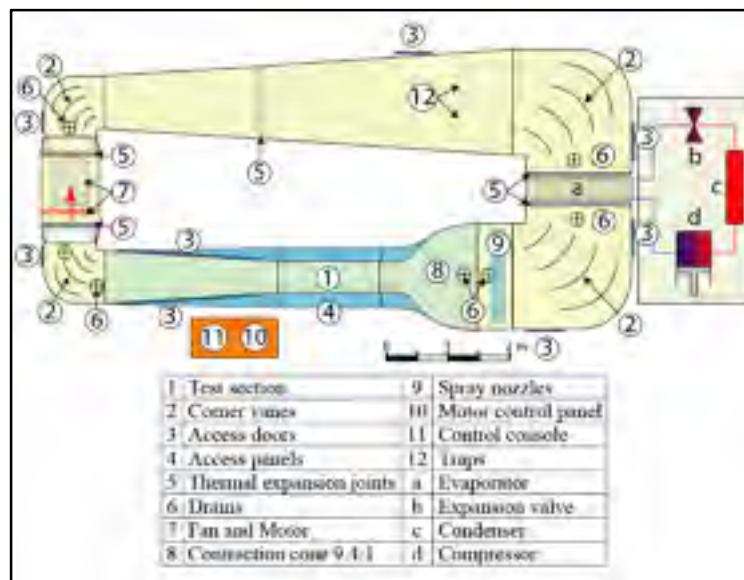
Figure 3.2 Icing Wind Tunnel Schematic (Villeneuve & Perron, 2012)

3.2 Fixed Wing Experiments

The fixed wing experiments were done as a verification of the data acquisition process. The testing for convection and conduction measurements was done separately. The convection tests allowed the quantification of heat transfer on different chord locations of the airfoil at different wind speeds V_∞ and different angles of attack α. While the conduction tests served to get an estimate of the heat lost to conduction in the airfoil walls and entourage.

3.2.1 Experimented NACA 0012 Airfoil (Convection Tests)

The base aluminum airfoil consisted of a NACA 0012 profile, as shown in Figure 3.3, with a 30.5 cm (12") span by 20.3 cm (8") chord. The airfoil was covered with 15 strip heating elements that provided a constant heat flux once activated. The size of each heating element was 2.5 cm x 30.5 cm (1" × 12") with a maximum power of 300 W. Heaters 1 to 8 (leading edge and suction side) were connected to DC power source A whereas heaters 9 to 15 (pressure side) were connected to DC source B. To obtain a uniform heat flux of $Q_{Elec} \approx 1000$ W/m^2, 62 W were needed by source A and 55 W by source B before testing.

Wiring limited the number of possible calibrated RTD thermocouples to 10, they were distributed across the chord of the airfoil to measure the temperatures at these different locations via an RTD recorder at a rate of 1 recording per second. The locations of the RTDs are shown in Figure 3.4 with the gray cylinder symbol. The strip heating elements are represented by the divided zones on the skin of the airfoil in Figure 3.4 and are numbered in roman numerals I to XV. Table 3.1 presents the position of the RTDs in terms of the non-dimensional curve length as a fraction to the chord S/c. The RTDs were installed at the middle of the heating elements in the chordwise direction and at the half-span in the spanwise direction.
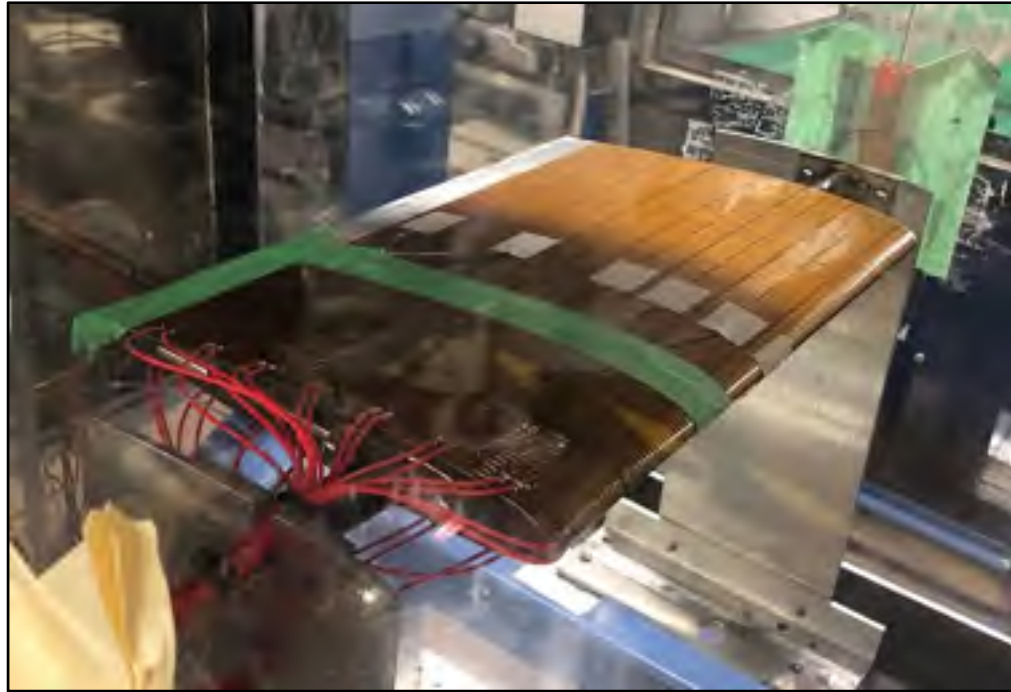
Figure 3.3 NACA 0012 Airfoil in IWT Test Section
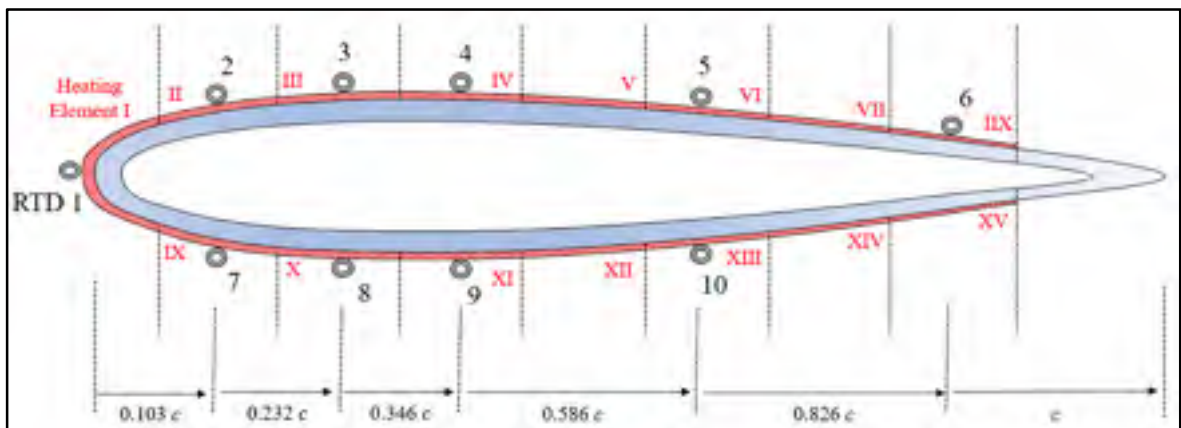
Figure 3.4 NACA0012 Convection Tests with Outer Heating Elements & RTDs Locations

Table 3.1 Chord-Wise Position of Fixed Wing Outer RTDs

RTD#	10	9	8	7	1	2	3	4	5	6
S/c	- 0.625	- 0.374	- 0.248	- 0.124	0	0.124	0.248	0.374	0.625	0.874
x/c	- 0.608	- 0.358	- 0.232	- 0.108	0	0.108	0.232	0.358	0.608	0.856

3.2.2 Fixed Wing Convection Testing Plan

Table 3.2 shows the details for all tests conducted on the profile. Each test had a unique ID# that corresponded to a specific V_∞ and α. The table also shows the approximate Re for each test based on the T_∞ and V_∞ (the actual values will be presented with the results). In total, 55 tests were done at $T_\infty = 0\ °C$ for $\alpha = 0°$, $5°$, $10°$ and $15°$. 13 more tests were done at $T_\infty = 263.15$ K and $\alpha = 0°$ for the purpose of estimating the randomness error.

Table 3.2 Fixed Wing Test Plan with Respective V_∞, α and Re

$\approx Re$	V_∞(m/s)	Tests ID# - T_∞= 273.15 K				V_∞ (m/s)	Tests ID# - T_∞= 263.15 K
		$\alpha = 0°$	$\alpha = 5°$	$\alpha = 10°$	$\alpha = 15°$		$\alpha = 0°$
1×10^5	6.31		14	28	42	6.31	
2×10^5	12.62	1	15	29	43	11.79	56
3×10^5	18.93	2	16	30	44	17.69	57
4×10^5	25.25	3	17	31	45	23.59	58
5×10^5	31.56	4	18	32	46	29.49	59
6×10^5	37.87	5	19	33	47	35.39	60
7×10^5	44.18	6	20	34	48	41.29	61
8×10^5	50.49	7	21	35	49	47.9	62
9×10^5	56.81	8	22	36	50	53.09	63
1×10^6	63.12	9	23	37	51	58.99	64
1.1×10^6	69.43	10	24	38	52	64.88	65
1.2×10^6	75.74	11	25	39	53	70.78	66
1.3×10^6	82.05	12	26	40	54	76.68	67
1.4×10^6	89.4	13	27	41	55	88.01	68

3.2.3 Experimented NACA 0012 Airfoil (Conduction Tests)

To estimate the conduction in the airfoil skin, another set of tests was done where four RTDs were installed inside the airfoil skin at mid span with another four on the outer surface. They were placed in the areas judged most critical of the airfoil as shown in Figure 3.5. RTD 2 was positioned on the inner nose of the leading edge, RTD 3 was at $S/c = 0.124$ of the bottom side of the airfoil and RTDs 1 and 4 were placed at $S/c = 0.312$ on either side of the airfoil, as described in Table 3.3. Each of the inner RTDs was placed perpendicularly adjacent to another RTD from the outer surface of the airfoil. This way, $T_{i,1}$ was directly below $T_{0,1}$, $T_{i,2}$ was directly on the right side of $T_{0,2}$, $T_{i,3}$ was directly above $T_{0,3}$ and $T_{i,4}$ was directly above $T_{0,4}$. The main assumption was that the conductive heat transfer will be most significant in the perpendicular direction compared to the lateral direction due to the great scale between the airfoil chord c and its thickness δ, similar to the assumption used in (Wang et al., 2008a).
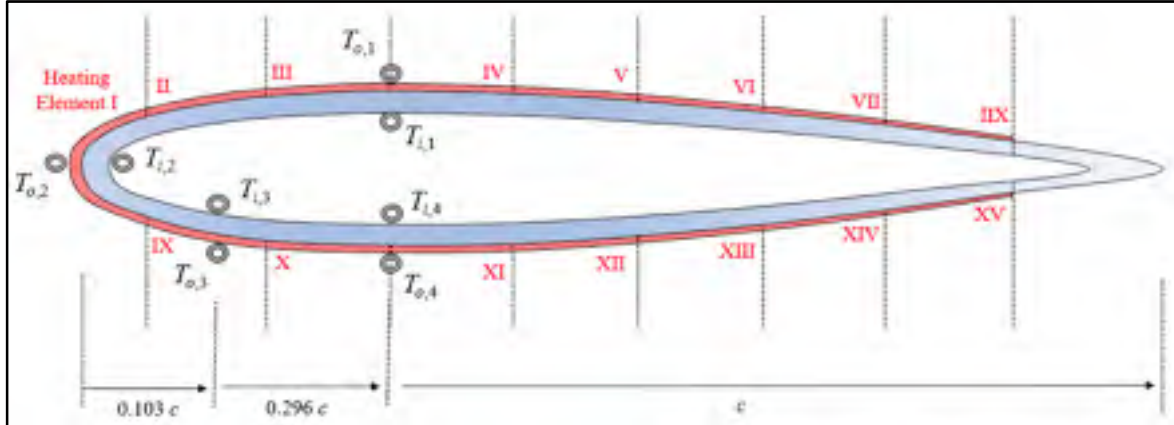
Figure 3.5 NACA0012 Conduction Tests With Inner RTDs Locations

Table 3.3 Chord-Wise Position of Fixed Wing Inner RTDs

RTD	$T_{i,1}$ & $T_{o,1}$	$T_{i,2}$ & $T_{o,2}$	$T_{i,3}$ & $T_{o,3}$	$T_{i,4}$ & $T_{o,4}$
S/c	0.312	0	- 0.124	- 0.312
x/c	0.296	0	- 0.108	- 0.296

3.2.4 Fixed Wing Conduction Testing Plan

Table 3.4 shows the details for all the conduction tests done on the profile. Each test had a unique ID# that corresponded to a specific V_∞ and α. The table also shows the approximate Re for each test based on the T_∞ and V_∞. In total, 12 tests were done at $T_\infty = 273.15$ K for $\alpha = 0°$ and $10°$.

Table 3.4 Fixed Wing Test Plan with Respective V_∞, α and Re

$\approx Re$	V_∞ (m/s)	Tests ID# - T_∞= 273.15 K	
		$\alpha = 0°$	$\alpha = 10°$
1×10^5	6.31	1	7
2×10^5	12.62	2	8
3×10^5	18.93	3	9
4×10^5	25.25	4	10
5×10^5	31.56	5	11
6×10^5	37.87	6	12

3.3 Rotor Experiments

The rotor experiments were done to quantify the heat transfer on different radius and chord locations of the rotor. Different rotor speeds Ω were tested as well as 2 different pitch angles θ. The main objective of these tests was to validate the UVLM-RHT and the BEMT-RHT as rotor heat transfer prediction tools.

3.3.1 Powered Spinning Rotor Blade (P-SRB)

The Powered Spinning Rotor Blade (P-SRB) setup was designed by modifying the Spinning Rotor Blade (SRB) setup developed at AMIL more than 10 years ago. The original setup is composed of two blades in horizontal rotation connected to a hub and driven by a motor and a power shaft transmission. The SRB diameter, which is restricted by the AMIL IWT test

section, is 0.780 m. The original setup is used to measure adhesion of representative atmospheric icing on different substrates, which can then be compared to bare aluminum or fiberglass blades to evaluate their ice Adhesion Reduction Factor (ARF) (Fortin & Perron, 2009).

In the P-SRB, modifications were brought to the setup to bring electrical power to the spinning blades with the help of a IEC-FR-LC-10 Slipring by IEC Corporation (http://ieccorporation.com/flange-mount/). The hub was connected to a 3600 RPM 10 hp motor by a 2.54 cm (1") diameter power steel shaft connected to a 10 hp drive. The maximum spinning speed was limited to 1500 RPM. To safely operate the P-SRB in the IWT, the test section windows are made of polycarbonate thermoplastic resin (Lexan) which has a high impact resistance. The motor generator was computer-controlled and set at a constant rotor speed. The spinning rotor blade angular speed is measured by an optical encoder. The hub was a homemade modification of a G4 raptor hub with a diameter of 200 mm, as shown in Figure 3.6. This hub has no stabilizers. The blade pitch angle can be set at 0 and 6 degrees. Power to supply the heating elements was generated by an Elektro-Automatik EA-PS3150-04B laboratory power supply.

Figure 3.6 Rotor Blades Hub

3.3.2 Blades

The rotor blades were untwisted extruded 6063-T6 aluminum NACA0012 profiles with a mill finish used for tail rotor blades of small helicopters (Figure 3.7). The extruded rotor blade could easily be modified to suit the test requirements and were free of rivets or other imperfections. The blades characteristics are presented in Table 3.5. The span is the rotor blade length from the rotation point to the blade tip. The length is the blade length from the hand attachment to the blade tip.

Figure 3.7 Isolated Rotor Blade

Table 3.5 P-RSB Geometric Characteristics

Blade Root Distance	75.0 mm
Blade Span (Radius)	390.0 mm
Blade Chord	69.8 mm
Blade Twist	0 °
Blade Number	2
Airfoil	NACA0012
Material	6063-T6 Al

3.3.3 Rotor Construction

The airfoil section had a NACA0012 profile made of aluminum. Figure 3.8 shows the complete setup of the experimented rotor. Each blade was covered with a strip heating element that provided a constant heat flux once activated (Figure 3.8). The size of each heating element was

12.7 × 30.48 cm with a maximum power of 300 W. The supplied voltage was $U_V = 100$ Volts and the current was $I_A = 2.31$ Amps. The total electric heating power was then 231 W, which translated into a heating density of around $Q_{Elec} \approx 5976.5$ W/m^2.

Figure 3.9 shows a close up on the blade with 3 placed RTDs. To help minimize losses, an aluminum tape was used to cover the heating element and to try to provide an even distribution of heat. At each test and as shown in the figure, 3 calibrated thermocouples were distributed across the radius of the experimented blade to measure the temperatures at these different locations via a thermocouple recorder at a rate of 5 recordings per second. The blade vibration rates were observed by the SRB software to guarantee stable rotation.

Figure 3.8 Rotor Prototype in Wind Tunnel with Exposed
Heating Elements

Table 3.6 provides the details of the test environment as well as the heating element size and specifications. Two pitch angles were tested, $\theta = 0°$ and $\theta = 6°$. At $\theta = 0°$ three different rotor speeds were used $\Omega = 500$, 1000 and 1500 rpm. At $\theta = 6°$ and due to vibrations in the system, the highest Ω was 1300 rpm so the three different rotor speeds used were $\Omega = 500$, 1000 and 1300 rpm. The temperature in the tunnel was maintained at $T_\infty = 248.15$ K thanks to a freestream circulating air velocity of $V_\infty = 5$ m/s.
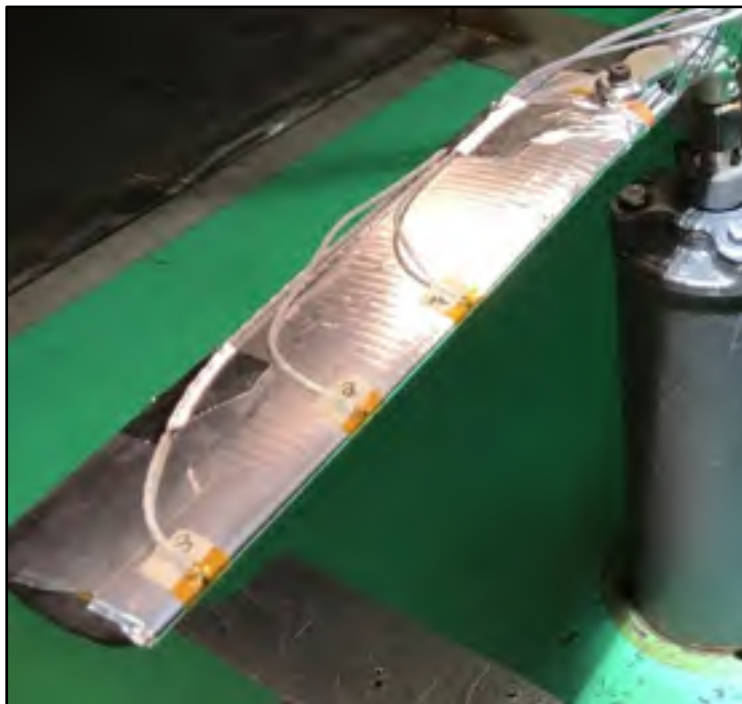
Figure 3.9 Aluminum Tape Covering the Heating
Elements and the Blade with 3 RTDs Shown

Table 3.6 Details of Test Environment & Heaters

Rotor Speed	Air Speed V_∞	Air Temperature T_∞	Blade Pitch θ
$500 < \Omega < 1500$	5 m/s	248.15 K	0° - 6°
Heater Area	Heating Power	Heating Density	Heating Elements
387.1 cm² (60 in²)	231 W	5976.5 W/m²	1 per Blade

3.3.4 RTD Placement

Figure 3.10 shows a sketch of the experimented blade with the radial locations of interest. For each test, a maximum of 3 RTDs could be fitted on the blade so at each test, a specific x/c was set (for example $x/c = 0$ or $x/c = 1/7$ etc...) and the RTDs were placed at $r/R = 0.6$, 0.75 and 0.95. The non-dimensional radial location r/R was described by the ratio of the distance to the placed RTD by the tip radius of the blade.
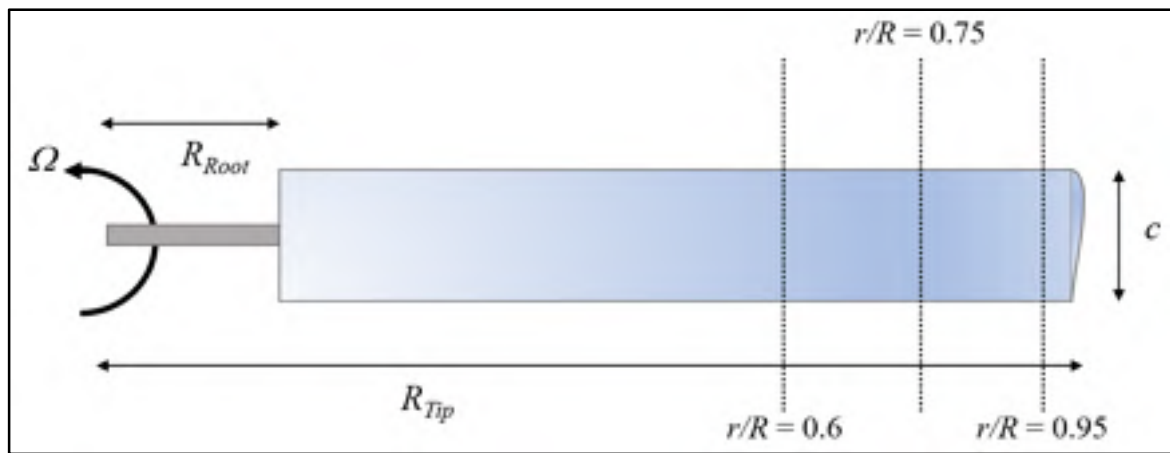
Figure 3.10 Sketch of Experimented Blade with Radial Positions of Interest

This configuration was used to do tests at the three different rotor speeds before the x/c was changed. Figure 3.11 shows a sketch of the airfoil section with the chordwise positions x/c of interest. It should be noted that at any test, only a specific x/c was tested at the same time. This means that the RTDs were first placed at $x/c = 0$ and three tests were carried out for the three Ω. The RTDs are then taken off and placed on the next x/c at the same previously mentioned r/R and the three rotor speeds were again tested sequentially. This was repeated until all the desired number of x/c positions were tested.
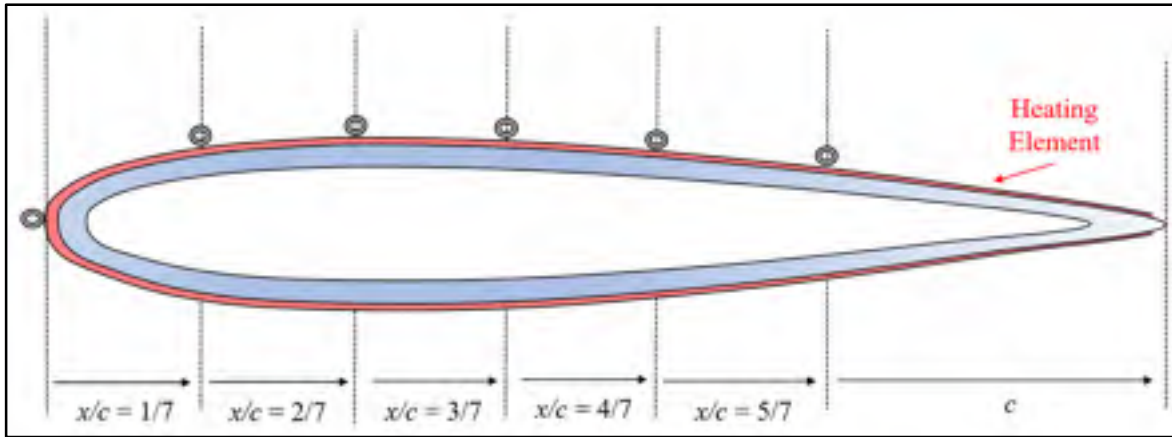
Figure 3.11 Sketch of Experimented Blade Cross Section with Chordwise Positions of Interest

3.3.5   Rotor Testing Plan

Table 3.7 shows the details for all tests conducted on the profile when $\theta = 0°$. Table 3.8 lists the test plan for tests at $\theta = 6°$. All tests were done with $V_\infty = 5$ m/s. Each test had a unique ID# that corresponded to a specific Ω and RTD placements on specified r/R. In total, 30 tests were done at $T_\infty = 248.15$ K for $\theta = 0°$ and $\theta = 6°$. It should also be noted that at $S/c = 0$, another set of r/R was tested. These were presented in the tables under tests ID 4 to 6 and 19 to 21. The purpose for these tests was to measure the heat transfer at other radii from one hand, and to check for tip loss effects very close to the tip ($r/R = 0.97$) from another.

Table 3.7 Rotor Test Plan at $V_\infty = 5$ m/s & $\theta = 0°$

x/c	S/c	500 RPM	1000 RPM	1500 RPM	r/R
0	0	1	2	3	0.95, 0.75 & 0.6
0	0	4	5	6	0.97, 0.87 & 0.51
1/7	0.155	7	8	9	0.95, 0.75 & 0.6
2/7	0.299	10	11	12	0.95, 0.75 & 0.6
3/7	0.443	13	14	15	0.95, 0.75 & 0.6

Table 3.8 Rotor Test Plan at $V_\infty = 5$ m/s & $\theta = 6°$

x/c	S/c	500 RPM	1000 RPM	1300 RPM	r/R
0	0	16	17	18	0.95, 0.75 & 0.6
0	0	19	20	21	0.97, 0.87 & 0.51
1/7	0.155	22	23	24	0.95, 0.75 & 0.6
2/7	0.299	25	26	27	0.95, 0.75 & 0.6
4/7	0.586	28	29	30	0.95, 0.75 & 0.6

3.4 Data Reduction, Calculation & Error Estimation

The previous sections presented the geometries, construction and tests plans of both the fixed wing and rotor experiments. This section is dedicated to describing the mathematical approach followed to transform the experimental data into non-dimensional heat transfer data. First, the convective heat calculation equations are explained. Next, the approximate solution followed to estimate the conduction losses in the aluminum body of the fixed wing is presented. Later, the procedure followed for data reduction and averaging during testing is explained. Finally, the method of (Moffat, 1988) that was used to get an estimate of the experimental error is laid out.

3.4.1 Convective Heat Transfer Calculation

The air properties vary with the temperature of the air. Therefore, a reference temperature T_f was chosen to estimate those properties. The density ρ, viscosity μ and thermal conductivity of the air k were calculated at T_f through equation (3.2). The total air temperature T_T was the one recorded by the IWT probe.

$$T_f = \frac{T_\infty + T_{RTD}}{2}$$

(3.2)

For the fixed wing, the *Re* was calculated based on the wind velocity in the tunnel V_∞ using equation (3.3). As for the rotor, the *Re* was calculated using equation (3.4) where V_r was the local velocity on each radial position of the blade. The two terms of velocity originate from the rotation of the blade from one hand, and the air velocity (normalized by θ) in the wind tunnel from another.

$$\mathrm{Re} = \frac{\rho \times V_\infty \times c}{\mu} \tag{3.3}$$

$$\mathrm{Re} = \frac{\rho \times V_r \times c}{\mu} \quad V_r = \Omega \times r + V_\infty \cos(\theta) \tag{3.4}$$

For each RTD, the heat transfer coefficient h_{RTD} was calculated using equation (3.5). Q_{Elec} is the supplied electrical power and was known ($Q_{Elec} \approx 1000$ W/m^2 for the fixed wing and $Q_{Elec} \approx 5976.5$ W/m^2 for the rotor). Q_{Rad} is the heat lost due to radiation, calculated using equation (3.6). σ_{SB} was the Stefan-Boltzmann constant and v was the emissivity of aluminum. Q_{Cond} is the heat lost due to conduction in the wing aluminum material. Finally, the local Nu_{RTD} and Fr_{RTD} were calculated using equations (3.7) and (3.8) at each test.

$$h_{RTD} = \frac{Q_{Elec} - Q_{Rad} - Q_{Cond}}{\left(T_{RTD} - T_T\right)} \tag{3.5}$$

$$Q_{Rad} = \sigma_{SB} \times v \left(T_T^4 - T_{RTD}^4\right) \tag{3.6}$$

$$Nu_{RTD} = \frac{h_{RTD} \times c}{k} \tag{3.7}$$

$$Fr_{RTD} = \frac{Nu_{RTD}}{\sqrt{Re}} \tag{3.8}$$

For the fixed wing experiments, Q_{Cond} was calculated based on the conduction tests and using equation (3.9). $T_{i,x}$ is the temperature recorded by the RTD on the inner surface of the wing and $T_{o,x}$ is the temperature recorded by the RTD on the outer surface at the same respective S/c of the considered $T_{i,x}$ divided by the thermal resistance R''. The detailed procedure for the calculation of Q_{Cond} through the conduction tests is outlined in the next section.

$$Q_{Cond} = \frac{\left(T_{RTD,i} - T_{RTD,o}\right)}{R''} \tag{3.9}$$

For the rotor experiments, there were no conduction loss measurements, so an approximation was implemented based on the fixed wing conduction tests. The latter indicated that Q_{Cond} had a maximum conduction heat loss of 8% of Q_{Elec} near the leading edge. Moreover, for the range of Re obtained in the rotor tests, the conduction losses in the fixed wing were between 4% and 8% of Q_{Elec}.

There were two differences between the fixed wing and rotor experiments that are believed to have minimized the conduction losses in the rotor tests compared to the fixed wing. First, the fixed wing was hollower compared to the rotor blades in terms of the larger thickness to chord ratio. And second, the rotor blades were completely covered with an insulating tape to trap the heat inside whereas the fixed wing surface was open to the air. These hypotheses are believed to be a reason for lower conduction losses in the rotor tests compared to the fixed wing since at steady-state conditions, the heat inside the blade should be even and be very small.

Although the hypotheses may be true, they were not enough to neglect the Q_{Cond} in the rotor experiments. However, they show that the conduction loss was not greater than what was found through the fixed wing tests. Therefore, the Q_{Cond} in the rotor tests is assumed equal to those

found in the fixed wing tests at the same *Re*. It should be noted that this also increases the uncertainty in the Fr_x calculations, as will discussed later in the results section.

3.4.2   Conductive Heat Transfer Calculation

The exact solution for the conduction across the airfoil skin was complex due to the curvature of the profile and the presence of a multi-layered conduction. An approximate solution seen in the works (Poinsatte, 1990) and (Wang et al., 2007b, 2008a) was implemented where the leading edge of the airfoil was approximated to a cylinder (Figure 3.12a) and the rest of the airfoil is modeled as a flat plate (Figure 3.12b). In the experiments of this thesis, the airfoil was made of aluminum with a thickness $\delta_{Al} = 2$ mm. At the leading edge, the aluminum thickness was almost 3 times greater. The heating elements presented another layer through which conduction occurred; they were made of polyimide with a thickness around $\delta_{Poly} = 0.762$ mm (0.03").
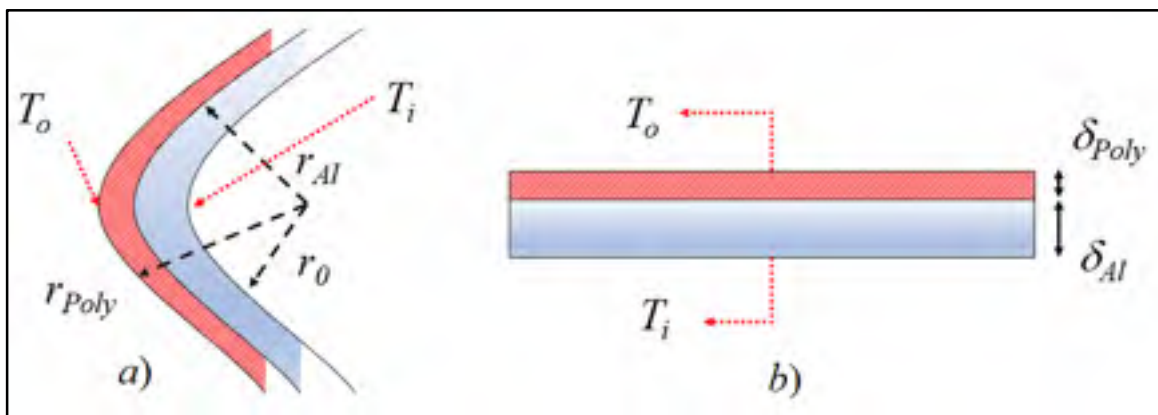
Figure 3.12 Heat Conduction Approximation of Airfoil Surface to a) Cylinder and b) Flat Plate

Figure 3.12b shows the two-layered approximation of the airfoil wall to a flat plate, dimensions are not to scale. For this case, the total thermal resistance R''_{FP} could be written in the form of equation (3.10) where the first thermal resistance term is for aluminum, the second is for polyimide and $R''_{t,c}$ is the contact resistance of adhesion of the heating element to the surface of the aluminum (Incropera et al., 2007).

$$R_{T,FP}^{"} = \frac{\delta_{Al}}{k_{Al}} + \frac{\delta_{Poly}}{k_{Poly}} + R_{t,c}^{"} \qquad (3.10)$$

Figure 3.12a shows the approximation of the leading edge of the NACA 0012 to a cylinder. r_0 in Figure 3.12a was determined through the approximation of the leading edge of the NACA 0012 to a cylinder with a diameter equivalent to 3.16% of its chord c according to (Poinsatte, 1990). The total thermal resistance $R"_{Cyl}$ may be written in the form of equation (3.11) where the first term is the radial thermal resistance of the polyimide layer, the second is the similar term but for aluminum and the last term is the contact resistance.

$$R_{Cyl}^{"} = \frac{\ln\left(r_{Poly}/r_{Al}\right)}{2\pi k_{Poly}} + \frac{\ln\left(r_{Al}/r_0\right)}{2\pi k_{Al}} + R_{t,c}^{"} \qquad (3.11)$$

3.4.3   Data Reduction & Averaging

The procedure followed during tests of both the fixed wing and the rotor experiments was similar and is detailed in APPENDIX I for each set of experiments. The procedure could generally be illustrated by Figure 3.13 that shows an example of the results for a fixed wing test. In the figure, the air and RTDs temperature variation versus the test time in seconds is shown.

For the specific test of the figure, the heaters are activated at $t = 60$ sec and the RTD readings increase before reaching steady state at around $t = 400$ sec. At $t = 600$ sec, the heaters are turned off and the temperature drop to a value close to that of the air around $t = 800$ sec. The data in Figure 3.13 correspond to the test #2 of Table 3.2, the lowest temperature was recorded by the RTD at the L.E. $S/c = 0$ and the highest was the nearest to the L.E. at $S/c = 0.124$.
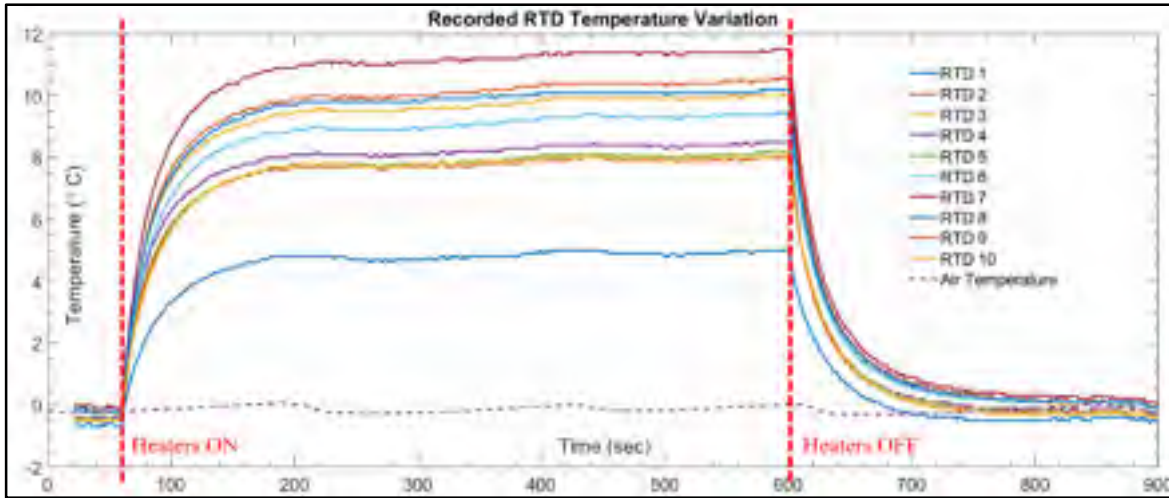
Figure 3.13 Air & RTDs Temperature Variation Vs. Time for $Re = 3 \times 10^5$; $\alpha = 0°$

Similarly, the results of Figure 3.13 are then used to calculate the convective heat transfer and the Fr_x for each RTD at each second. The results will turn out to be in the form shown in Figure 3.14. This represents the instantaneous variation of the Fr_x for each RTD. The highest Fr_x was at $S/c = 0$ and the lowest was the nearest to the L.E. at $S/c = 0.124$.
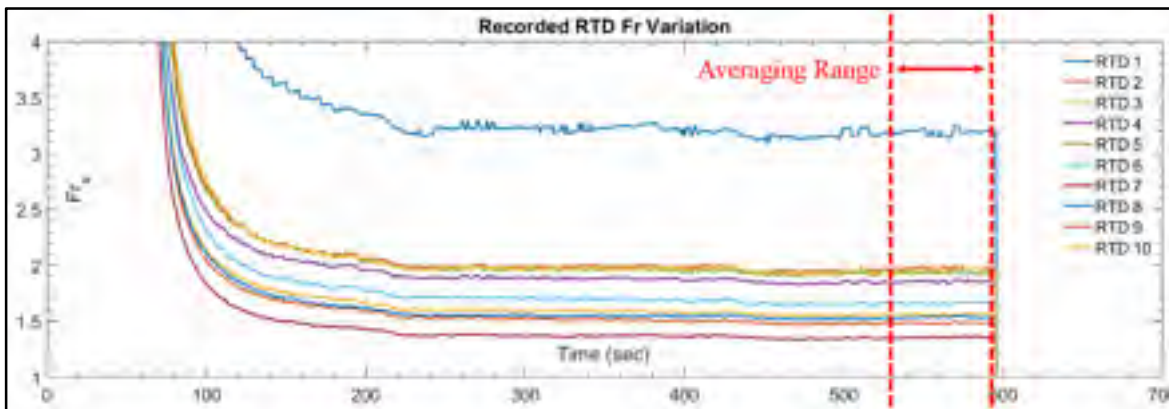
Figure 3.14 Fr Variation for all RTDs Vs. Time for $Re = 3 \times 10^5$; $\alpha = 0°$

Finally, the mean of the data in Figure 3.14 is calculated for the interval spanning the last minute before the heaters are turned off. For the case shown in Figure 3.14, the interval is 540 sec $< t_i < 600$ sec but as the exact time length of each test was different, however the mean was

always calculated in the last minute before the heaters were turned off. This way the mean value of Fr for each RTD and test is obtained.

3.4.4   Turbulence Intensity Calculation

The turbulence intensity TI was also calculated for each of the fixed wing and rotor tests. For the duration of the test, the local velocity V_{local} at the airfoil section is first calculated. For the fixed wing, it is based only on the recorded air speed by the IWT. For the rotor tests, the V_{local} is based on the velocity due to rotation $\Omega \times r$ plus the velocity due to the freestream of air V_∞ as shown in equation (3.12). The turbulence intensity percentage can then be found based on the mean of the V_{local} and its RMS value as shown in equation (3.13).

$$V_{local} = \Omega(t) \times r + V_\infty(t) \times \cos(\Psi) \tag{3.12}$$

$$TI(\%) = 100 \times \frac{\left(\overline{V_{local}} - V_{local}\right)_{RMS}}{\overline{V_{local}}} \tag{3.13}$$

To estimate the effect of the TI on the heat transfer measurements, the works (Van Fossen, Simoneau, & Ching, 1995) and of (Yeh, Hippensteele, & Van Fossen, 1993) are used. These works indicate that the rates of increase in heat transfer due to an increasing TI at low Re are more significant compared to higher Re. A correlation to estimate the Fr at the stagnation point on a cylinder within 4% accuracy, is given by in the form of equation (3.14) by (Van Fossen et al., 1995). It provides the Fr_0 which is based on the equivalent L.E. diameter and also uses the diameter based Re_D to calculate it. d is the equivalent L.E. diameter (3.16% for the NACA 0012 as per (Poinsatte, 1990)), C is the zero-turbulence $Fr = 0.939$ and Λ_x is the length scale of the used turbulence grids. In the case of the present experiments, no turbulence grids are used, so according to (Yeh et al., 1993) the test section width may be used as an approximation. The Re_d and Fr_d are linked to their chord based counterparts by equation (3.15), respectively.

$$Fr_0 = 0.008\sqrt{TI \times Re_d^{0.8} \times \left(\frac{\Lambda_x}{d}\right)^{-0.574}} + C \qquad (3.14)$$

$$Re_d = \frac{d}{c} Re_c \quad Fr_d = \frac{d}{c} \times \frac{\sqrt{Re_c}}{\sqrt{Re_d}} \times Fr_c \qquad (3.15)$$

3.4.5 Experimental Error Estimation

In this section, two types of error are identified, and they are the measurement error and the randomness error. In order to estimate the measurement error in the measured heat transfer values, the method of (Moffat, 1988) is used. It consists of an equation to calculate the error in the measured heat transfer coefficient, in this thesis the equation was applied to equation (3.5) and the result took of the form of equation (3.16). The equation first represents the error in the measurement of the electric heat input that is represented by $Q_{Elec} = U_V \times I_A$ where U_V is the voltage and I_A is the current and second, the temperature measurements of both the RTD and the air.

$$\frac{\partial h}{h} = \sqrt{\left[\frac{\partial(T_{RTD} - T_T)}{(T_{RTD} - T_T)}\right]^2 + \left[\frac{\partial I_A}{I_A}\right]^2 + \left[\frac{\partial U_V}{U_V}\right]^2} \qquad (3.16)$$

In the equation, there are sources of error that have been neglected that are the error in estimating the Q_{Rad} and the Q_{Cond}. Both terms were minor heat transfer losses from the system. On average, the Q_{Rad} and Q_{Cond} represented around 1.5% and 4% of the Q_{Elec}, respectively. Therefore, the error due to those two terms was very small (< 0.5%) to contribute to the convective heat transfer calculation and was neglected. This way, there were three main sources of the measurement error: 1- temperature measurements, 2- voltage fluctuations and 3- current fluctuations.

For the fixed wing experiments, the error from temperature measurements was determined to be around 1%. The voltage fluctuations represented an error of 3.2% and the current fluctuations represented 4.1% of error. For the rotor experiments and by listing the errors in the same order as the fixed wing, the error percentages were 1%, 1.8% and 2.7% respectively. The error from the temperature measurements was based on an accuracy of 0.1 and a 10 K temperature gradient. The fluctuations of both the U_V and I_A were determined based on the average of measured values during tests.

On the other hand, to estimate the randomness error in the values measured experimentally, several tests were repeated under the same test conditions. The discrepancy obtained between the results of the same tests was then defined as the randomness error. For the fixed wing experiments, most tests at $\alpha = 0°$, $\alpha = 5°$ and $\alpha = 10°$ were rerun at least twice for all Re, with some tests repeated three times. Only 3 tests at $\alpha = 15°$ were rerun twice, at $Re = 9 \times 10^5$, 1×10^6 and 1.1×10^6. The Fr values obtained for each RTD were then compared for all test repetitions and the randomness error was calculated with equation (3.17).

$$Error = 100 \times \frac{Fr_{Test_1} - Fr_{Test_2}}{Fr_{Test_1}} \tag{3.17}$$

For the rotor experiments, 3 of the tests were repeated 4 times each. These were for the rotor at : 1- $\Omega = 500$ RPM and $\theta = 0°$, 1- $\Omega = 1000$ RPM and $\theta = 0°$ and 3- $\Omega = 1300$ RPM and $\theta = 6°$. The same procedure of calculating the Fr was followed for each test.

3.5   Conclusion

This chapter presented the details of the methodology followed to complete the fixed wing as well as the rotor experiments. The goal of these experiments was to validate the developed numerical tools, the BEMT-RHT and the UVLM-RHT. The results of the experimental validation are presented in Chapter 5.

The fixed wing tests were done for a range of $0° \leq \alpha \leq 15°$ and $1 \times 10^5 \leq Re \leq 1.4 \times 10^6$ with 10 RTDs distributed across the chord of the tested airfoil. The tested wing had a NACA 0012 airfoil shape. Heating elements covered the skin of the wing and provided a constant heat flux at its wall. This was done to obtain a local variation of the heat transfer across the airfoil as the Re and α.

As for the rotor experiments, they were done on a 2-blade rotor with a NACA 0012 blade profile. The blades were covered with heating elements providing a constant heat flux, two pitch angles were tested $\theta = 0°$ and $\theta = 6°$. At each test, 3 RTDs were on different r/R and S/c to measure the temperature at different blade positions. The areas of interest were between 60% and 95% of the radius whereas across the chord, measurements were made from the L.E. all the way to $S/c \approx 5/7$. With these kinds of measurements, the heat transfer variation in the radial as well as the chordwise directions will be covered.

CHAPTER 4

NUMERICAL RESULTS

This chapter presents the results of the numerical component of this thesis, based on the methodology of Chapter 2. The first objective of the chapter is to validate CFD viscous and heat transfer database as well as to present the novel airfoil Fr_{Avg} correlation. The second objective is to validate the implementation of the BEMT and UVLM as rotor aerodynamic modeling tools with no heat transfer prediction. Finally, the last objective is to apply the coupling between the novel Fr_{Avg} correlation and the BEMT as well as the UVLM, promoting the methods into rotor heat transfer prediction tools.

The first section of the chapter begins with a heat transfer verification procedure on the CFD simulations. This is done on both a flat plate test case as well as the airfoil simulation. For the airfoil, experimental data of a cylinder as well as another airfoil are used for validation of the results at the stagnation point. Turbulent flat plate correlations are used to verify the predicted heat transfer rates in the chordwise direction. Since the goal of these simulation is to produce a correlation for the Fr_{Avg} and Fr_{Max}, a study on the effect of the Re on the Fr is first done. This is followed by another study on how the Fr varies with the α. The results of a constant Q_S TBC are then compared to those of a constant T_S TBC. Finally, the novel correlations for the airfoil Fr_{Avg} and Fr_{Max} are presented.

In the second section, the implemented BEMT and UVLM are validated as rotor aerodynamic modeling tools. Four experimental test cases from the literature are used for the purpose. The cases correspond to rotors in hover, axial and forward flight as well as one for a hovering rotor in ground effect. One of the test cases is also used in a parametric study on the discretization of each the BEMT and the UVLM.

The last section presents the results of the heat transfer prediction, using the BEMT-RHT and the UVLM-RHT, on a modified Bell 429 tail rotor. This section highlights the originality of

this research. The results are shown in terms of the heat transfer contours of the Fr_{Avg} and Fr_{Max} across the radial and azimuthal locations of the blade. Four test cases are presented for rotors in hover, axial and forward flight as well as one for a hovering rotor in ground effect.

4.1   CFD Heat Transfer Simulations

The turbulent flat plate test case is chosen as a validation step for the thermal prediction capabilities of *SU2*. First, a flat plate test case is simulated, and the predicted friction coefficient C_f is compared to correlations from the literature. To compare the predicted Fr_x, correlations as well as other CFD implementations of the *S-A* turbulence model from the literature are used. Both the constant surface heat flux Q_S and the constant surface temperature T_S TBCs are used for the flat plate verification. For the airfoil, the predicted Fr_x values on the stagnation point are compared to experimental data of both a cylinder and an airfoil from the literature. In the chordwise direction of the airfoil, no fully turbulent Fr_x data for an airfoil are found in the literature so the CFD results are compared to fully turbulent correlations of a flat plate. Next, the airfoil Fr_x predictions are presented and a study on the effect of *Re*, α and flow separation is conducted. The section then moves on to quantify the difference of Fr_x and Fr_{Avg} if a constant Q_S TBC is used instead of a constant T_S. Finally, the novel correlations for the airfoil Fr_{Avg} and Fr_{Max} are presented.

4.1.1   Flat Plate

For the verification test case of the flat plate, the grid used is the one from *NASA's* website (Rumsey, 2014a) with a 2 meters length, the *Re* based on a length of 1 meter is 5×10^6 and the Mach number is *Ma* = 0.15. Two TBCs are examined. First, the wall surface temperature is set constant at T_S = 280 K and the far field temperature is T_∞ = 300 K. Second, the constant wall heat flux is set constant to Q_S = 2000 W/m² and the far field temperature is T_∞ = 281.66 K. In both cases, the flat plate wall is discretized with 450 elements.

4.1.1.1 Verification with Friction Coefficient Correlations

Figure 4.1 shows the comparison between the C_f from the CFD simulations versus the calculated values using correlations. The first C_f correlation in the figure correspond to equation (4.1) and the second C_f correlation is for equation (4.2), both from (Kays & Crawford, 1993). The subfigure on the left is for the simulation using the constant T_S BC and the one on the right is for the constant Q_S. The C_f variation is described by the increasing Re_x across the plate length.

$$C_f/2 = 0.0287\,\mathrm{Re}_x^{-0.2} \tag{4.1}$$

$$C_f/2 = 0.185(\log_{10}\mathrm{Re}_x)^{-2.584} \tag{4.2}$$
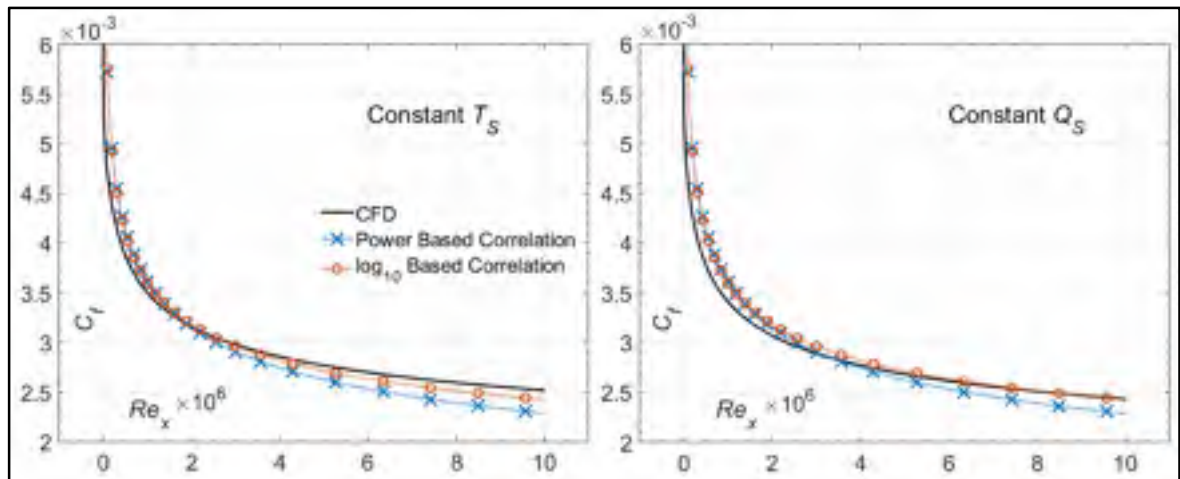
Figure 4.1 Flat Plate Comparison of C_f at constant T_S and constant Q_S

Based on the results from Figure 4.1, the change of TBC caused a difference of C_f values by no more than 5% for any Re. However, when compared to the correlation values, the constant T_S simulation agreed better with the correlation values at $Re < 3 \times 10^6$, with around 6% discrepancy. For higher Re, the constant Q_S simulation performed better than the one with constant T_S, with around 2% discrepancy. For both simulations, the discrepancy is acceptable.

4.1.1.2 Validation of Heat Transfer Calculations

In this section, a comparison is done between the Fr_x obtained using the CFD simulations by two different approaches. The first approach is to compare the CFD results with the constant T_S TBC to flat plate correlations from the literature with the same TBC. The other approach is to compare the CFD results with the constant Q_S TBC to two other implementations of the S-A turbulence model from the literature, also with a similar TBC. For the constant T_S simulation, the flat plate correlations corresponded to equations (4.3) (Incropera et al., 2007) and (4.4) (Kays & Crawford, 1993). Re_x is the local Reynold's Number and Re_L is the Reynold's Number based on the length of the plate. The Fr_x variation is described by the increasing Re_x.

$$Fr_x = 0.0296 \times Re_x^{4/5} \times Pr^{1/3} / \sqrt{Re_L} \tag{4.3}$$

$$Fr_x = 0.0287 \times Re_x^{4/5} \times Pr^{0.6} / \sqrt{Re_L} \tag{4.4}$$

For the simulation with constant Q_S, a comparison with literature implementations of the S-A turbulence model for heat transfer prediction, the numerical results of (Aupoix & Spalart, 2003) and (Abdollahzadeh, Esmaeilpour, Vizinho, Younesi, & Pàscoa, 2017) are chosen. Both provided the local Stanton Number St_x for a flat plate with a constant Q_S TBC. The St_x is transformed into the Fr_x by $Fr_x = (St_x \times Re_x \times Pr) / \sqrt{Re_L}$. In this work, each TBC is simulated using CFD and the computational details described in section 4.1.1. The results of the comparisons are shown in the right side of Figure 4.2.
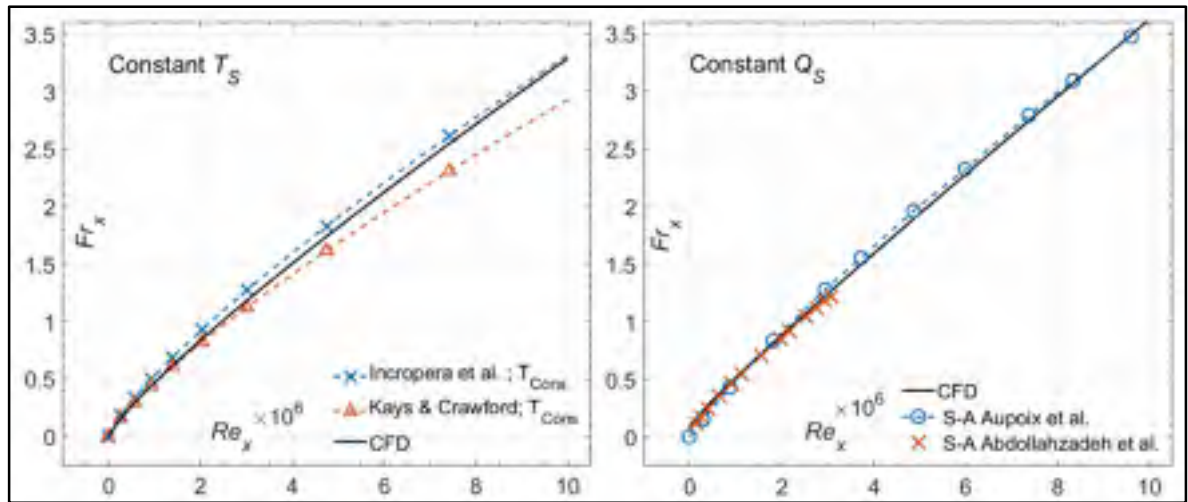
Figure 4.2 Flat Plate Fr_x Comparison at constant T_S and constant Q_S

Figure 4.2 shows the Fr_x variation versus the increasing Re_x across the plate length. The subfigure on the left is for the simulation using the constant T_S TBC and the one on the right is for the constant Q_S. For either B.C. the Fr_x increases across the plate due to a direct increase of the Re_x. For the case of constant T_S, the discrepancy between the results of CFD and the correlation of (Incropera et al., 2007) is around 7% for all Re_x. The discrepancy compared to the (Kays & Crawford, 1993) correlation is around 7% for $Re_x < 5 \times 10^6$ and 12% for $Re_x > 5 \times 10^6$. It should be noted that both correlations claim an accuracy within 15%, so the discrepancy found with CFD results is satisfactory. For the constant Q_S simulation, the S-A implementation of this work as well as those from the literature all provide very similar results with no more than 2% discrepancy, mainly due to the different discretization of each numerical implementation.

4.1.2   NACA 0012 Airfoil

The NACA 0012 simulations used the computational domain defined on *NASA's* website (Rumsey, 2014b). The chord for the NACA0012 is $c = 1$ m. The far field boundary is located 500 chords away from the airfoil. The airfoil wall is discretized with 512 elements and the far field with 1408 elements., the Mach Number is $Ma = 0.15$, the freestream temperature is $T_\infty = 281.66$ K and α is varied between 0° and 30° to account for stall effects. Two TBCs are

examined. For the constant airfoil surface temperature, the Re is varied between 2×10^5 and 3×10^6 and the $T_s = 273.15$ K. For the constant airfoil surface heat flux, the Re is fixed at $Re = 1 \times 10^6$ and $Q_S = 2000$ W/m^2.

4.1.2.1   Comparison with Flat Plate Correlations

Figure 4.3 shows the comparison between the Fr_x obtained using the CFD simulations versus flat plate correlations. In the figure, the turbulent flat plate correlations correspond to equations (4.3) (Incropera et al., 2007) and (4.4) (Kays & Crawford, 1993). All the presented results are for the simulations and correlations corresponding to a constant T_S TBC. Each subfigure of Figure 4.3 corresponded to a specific $Re = 2 \times 10^5$, 5×10^5, 1×10^6 and 3×10^6 as indicated. For the flat plate, the Fr_x is divided by S/c for similarity with airfoil data. For the airfoil, the angle of attack is $\alpha = 0°$.

Based on the comparison presented in Figure 4.3, the CFD simulations generally agrees with the Fr_x of the flat plate correlations. For the cases of $Re = 2 \times 10^5$ and 5×10^5, the discrepancy is between 1% and 4% compared to the flat plate correlations. There is however a higher discrepancy at the extremities of the two geometries. At low S/c (≤ 0.1), a higher discrepancy is found due to the different geometry between the flat plate tip and the thicker airfoil leading edge. At high S/c (≥ 0.9), the Fr_x variation on the trailing edge of the NACA 0012 deviates from the flat plate correlations.

When the higher Re are examined, it is noted that the discrepancies with the flat plate correlations augments. At $Re = 1 \times 10^6$, the discrepancy is 5% at $S/c \leq 0.1$, between 1% and 6% at $0.1 \leq S/c \leq 0.9$ and 4% at $S/c \geq 0.9$. For the highest Re case of 3×10^6, the discrepancy is between 5% and 22% at $S/c \leq 0.1$, 6% and 20% at $0.1 \leq S/c \leq 0.9$ and 6% at $S/c \geq 0.9$.
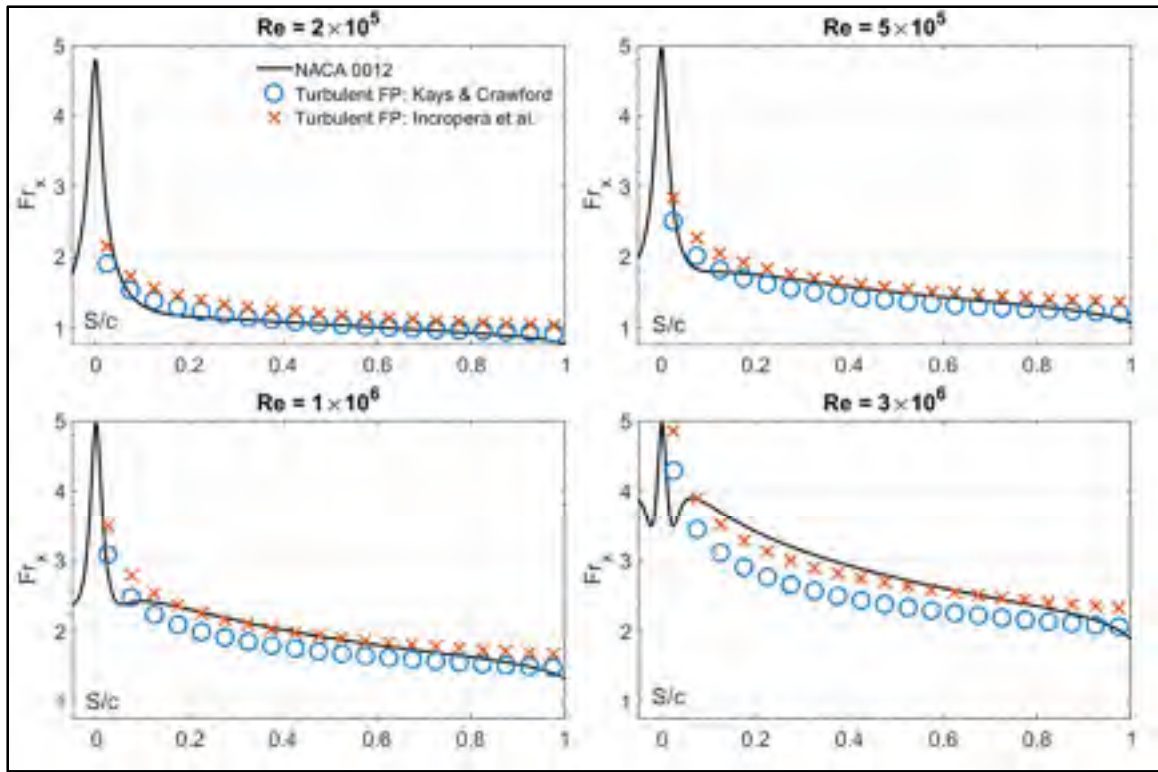
Figure 4.3 NACA 0012 CFD Data Versus Turbulent Flat Plate Correlations

These discrepancies could be explained by the different geometry between the two bodies. The aerodynamic shape of the NACA 0012 will cause the local velocity over the airfoil to increase, leading directly to an increase in Fr_x values. This is especially clear when the stretch $0.1 \leq S/c \leq 0.9$ is examined. Also, the extremities of the NACA 0012 shows higher discrepancies compared to the flat plate correlations, for the same reason of geometry difference. However, the CFD simulations generally predict comparable results to the correlations from the literature, especially for $Re \leq 1 \times 10^6$.

4.1.2.2   Comparison with Leading Edge Measurements

To validate the Fr_x on the leading edge of the airfoil, the CFD data are compared to L.E. experimental measurements of a NACA 0012 as well as near the stagnation point of a cylinder. The Fr_x comparison is shown in Figure 4.4 between - $0.03 \leq S/c \leq 0.08$. The experimental NACA 0012 data are extracted from the work of (Poinsatte, 1990). Three different Re are

presented: $Re = 1.3 \times 10^6$, 1.9×10^6 and 2.5×10^6 and all cases are for $\alpha = 0°$. The cylinder data are taken from (Poinsatte, 1990) but are the result of the work of (Froessling, 1958). The presented CFD data are at Re similar to those of the NACA 0012 experiments, with no more than 1% discrepancy (indicated on the figure). Both the CFD data and the experimental values are for a flow under a constant T_S TBC.

The variation of the Fr_x on the cylinder near the stagnation point is considered in the laminar flow portion. According to the (Poinsatte, 1990), the Fr_x would not change for a laminar flow. This explains why only one set of values are presented without a specified Re. This is also evidenced if the experimental NACA 0012 are checked, the Fr_x are all reduced into almost the same value (within $\pm 5\%$) and vary only by the location S/c. The author is able to show that for the laminar portion of the flow, the Fr_x is independent of the Re which agrees with the data of the laminar flat plate. This is not observed in the CFD results, where the Fr_x at different Re are only equal for $-0.01 \leq S/c \leq 0.01$ and then higher Re cause an increase in Fr_x values. This is expected since the CFD data are for a fully turbulent flow and the experiments are done in the Icing Research Tunnel IRT with laminar to turbulent transition.

The stagnation point can be compared however since there is no effect of the flow condition on it. If the CFD data from Figure 4.4 are compared, it can be seen that at the stagnation point, the CFD data fall in between the experimental NACA 0012 and cylinder measurements. More specifically, the CFD-determined Fr_x at the nose of the airfoil ($S/c = 0$) are 8% lower than that of the cylinder and 8% higher than that of the experimented NACA 0012. Moreover, the CFD results show that the Fr_x at the stagnation does not change between $-0.01 \leq S/c \leq 0.01$, regardless of the inspected Re. Therefore, it is determined that the CFD simulations provide a satisfactory estimation of the Fr_x at the stagnation point of the airfoil, within 8% of experimental measurements.
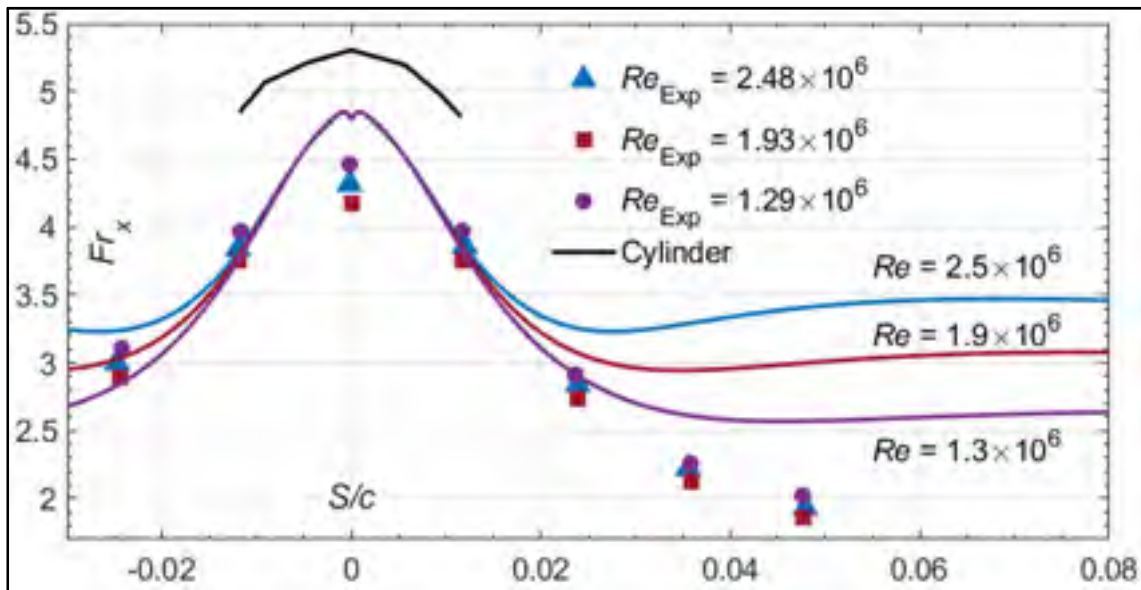
Figure 4.4 Leading Edge NACA 0012 CFD Data Versus Experimental NACA 0012 &
Cylinder Measurements

4.1.2.3   Heat Transfer Effect of Reynold's Number

In this section, the Re effect on the predicted Fr_x variation is investigated. Figure 4.5 shows the variation of the Fr_x versus the S/c on both sides of the NACA 0012. The upper subfigure shows the results for a variety of simulated Re, indicated on the figure, at $\alpha = 0°$. The lower subfigure shows the results at $\alpha = 20°$ for the same simulated Re as the upper subfigure.

For the case of $\alpha = 0°$, it is determined that the increase of Re causes the Fr_x to increase for all point of S/c except at the stagnation point $S/c = 0$. At that α and for any Re, the maximum Fr_x is at the stagnation point of the airfoil and a severe drop is seen moving away till $S/c \approx \pm 0.04$. Afterwards, an increase in Fr_x is noted for $\pm 0.04 \leq S/c < \pm 0.08$ before a drop in values is continuously seen till the T.E. Based on the results of CFD, an increase of Re caused the Fr_x to increase at all point except $S/c = 0$.

The same is also determined by checking the Fr_x variation at $\alpha = 20°$ with the difference in the stagnation point location. The positive α causes the stagnation point to move away from the L.E. on the bottom surface of the airfoil. For that case, the stretch of $-0.08 \leq S/c < -0.01$ shows

unchanging values of Fr_x. Outside that range, the turbulent flow becomes dominant. For $S/c \geq$ - 0.08, the Fr_x increases before stabilizing at around a constant value throughout the bottom surface towards the T.E. For $S/c \geq$ - 0.01, a significant increase in Fr_x is first encountered (due to increase in Re) before a drop in values continues till $S/c \approx 0.2$. For higher S/c, the Fr_x tends to increase all the way to the T.E. as a result of flow separation as will be explained in the upcoming section.
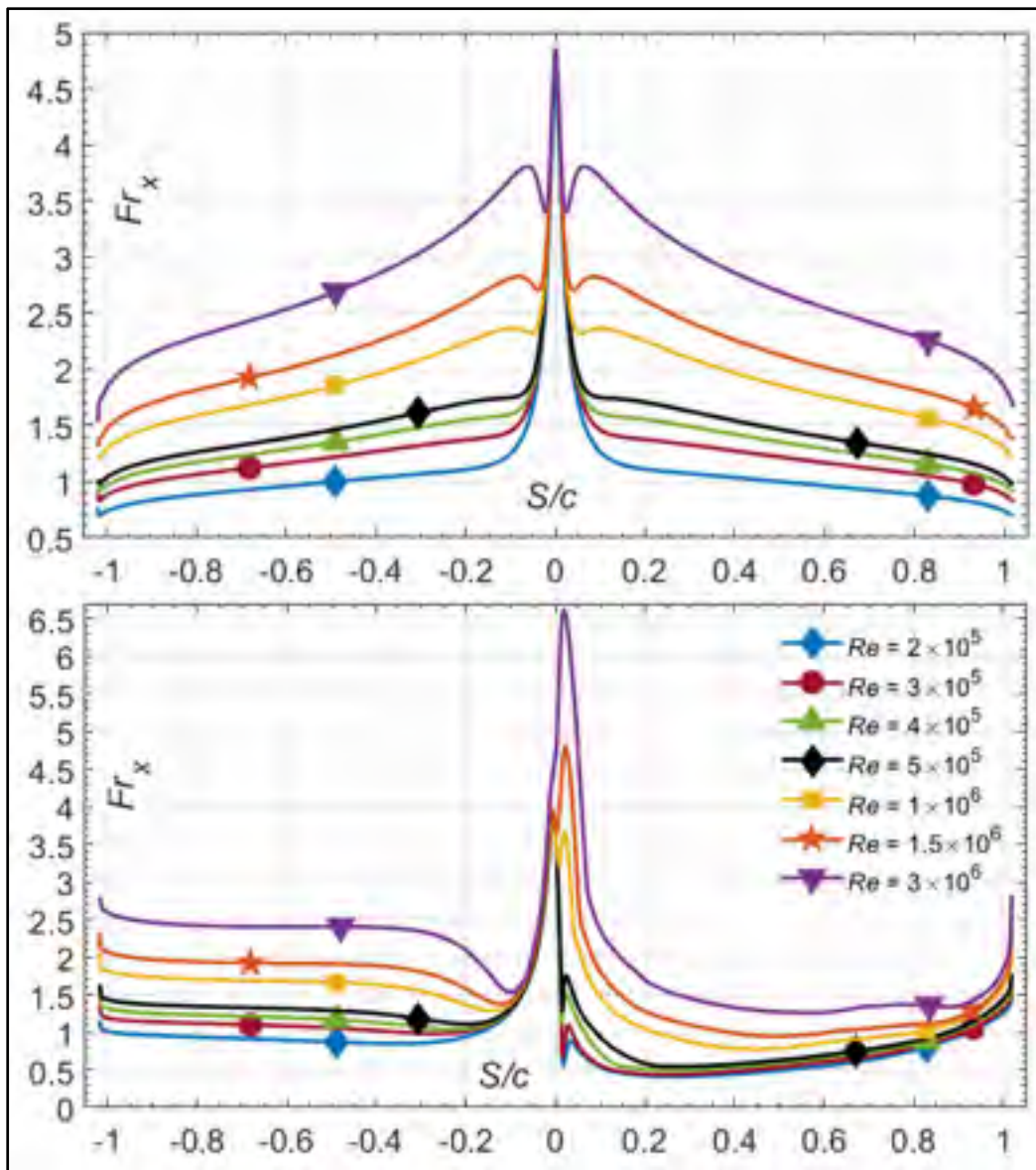
Figure 4.5 Fr_x Variation on NACA 0012 Wall for $\alpha = 0°$ & $\alpha = 20°$ at Various Re

The two examined α correspond to the cases of a symmetric and attached flow ($\alpha = 0°$) from one side as well as an asymmetric and separated flow ($\alpha = 20°$) from the other. While the presented data at $\alpha = 0°$ and $\alpha = 20°$ show that the increasing Re caused the Fr_x to increase at the same S/c, this is true for all other simulated α. It is determined that for any other simulated α, an increase Re causes a direct increase in Fr_x, similar to what was seen for the turbulent correlations of the flat plate.

To quantify the effect of Re on the Fr, the first step of the Fr_{Avg} correlation development for the NACA 0012 (equation (2.4)) is examined here. The literature indicates that for an airfoil at $\alpha = 0°$, the Fr_{Avg} could be fitted in a similar form of the cylinder correlation $Fr_{Avg} = A \times Re^m \times Pr^{1/3}$. Figure 4.6 shows the Fr_{Avg} variation of the NACA 0012 versus the Re as calculated from the CFD simulations. The values correspond to $\alpha = 0°$ and for a range of $2 \times 10^5 \le Re \le 3 \times 10^6$. The figure also the result of curve fitting based on proposed form of the cylinder correlation.
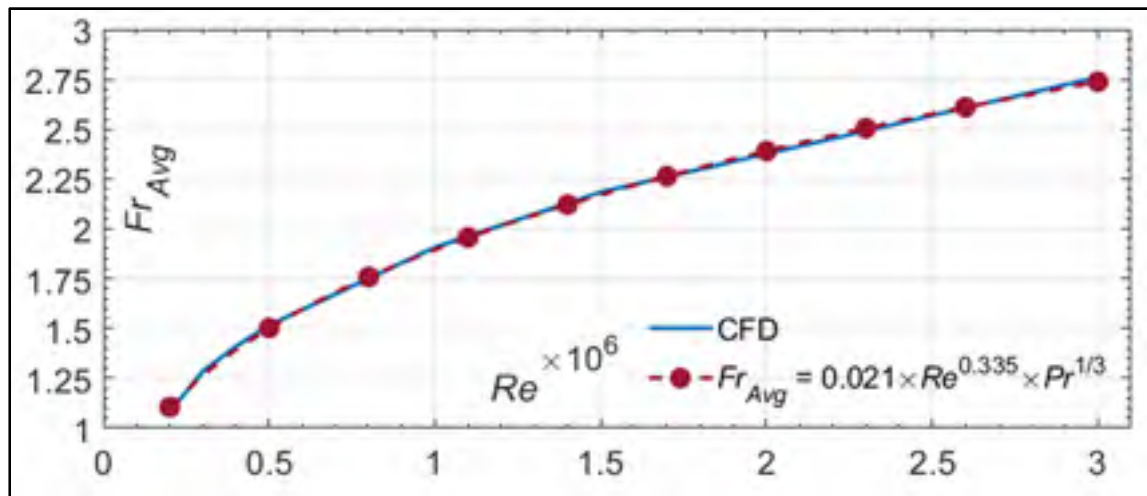
Figure 4.6 Curve Fitting Attempts for Different m of the NACA 0012 Fr_{Avg} at $\alpha = 0°$ and $2 \times 10^5 \le Re \le 3 \times 10^6$

The results of Figure 4.6 indicate that the parameter A is found to be $A = 0.021$ as a best fit to the curve. Moreover, it is determined that $m = 0.335$ would provide the best representation of

the Fr_{Avg} correlation at $\alpha = 0°$ and $2 \times 10^5 \leq Re \leq 3 \times 10^6$. The determined A and m are slightly different than those from the turbulent flat plate correlation equation (4.3) where $A = 0.0296$ and $m = 0.3$. For the NACA 63-241, they are $A = 0.0943$ and $m = 0.136$ (Wang et al., 2008a). This way, the part of the correlation that concerns the variation of Re is developed and the effect of α is examined in the next section.

4.1.2.4   Heat Transfer Effect of Angle of Attack / Stall

The effect of α on the predicted Fr_x variation is investigated in this section. When the CFD simulations are done, the α is incrementally increased until flow separation is observed near the T.E. The observations are made by checking the flow field plots around the simulated airfoil. From top to bottom, the subfigures of Figure 4.7 show the flow field plots around the NACA 0012 at $\alpha = 14°$, $16°$ and $17°$. These plots are for $Re = 1 \times 10^6$.

As seen in Figure 4.7, a separation bubble is first observed near the trailing edge of the suction side at $\alpha = 14°$. Although the bubble is very small at this angle, it is the first encounter with flow separation for $Re = 1 \times 10^6$. At the smaller simulated angles $0° \leq \alpha < 14°$, this phenomenon is not seen. When the higher $\alpha = 16°$ is examined, flow separation becomes more observable and a larger recirculation region within the bubble is seen. The separation point also moves away from the trailing edge and closer towards the leading edge of the airfoil. At $\alpha = 17°$, the separation and corresponding recirculation continue to grow and become more significant. The separation point also continues to move closer towards the leading edge and can be seen around the mid-chord of the airfoil. For higher α up until the highest simulated $\alpha = 30°$, the trend continued. Higher α produced larger recirculation regions and the separation point moved increasingly closer to leading edge, in accordance with what was determined by (Wang et al., 2008a).

To translate the effect of an increasing α and the subsequent flow separation on the heat transfer estimation, the variation of the Fr_x versus the S/c on the suction side of the NACA 0012 is shown in Figure 4.8. The upper subfigure shows the results at $\alpha = 0°$, $5°$, $10°$ and $16°$

while the lower subfigure shows the results $\alpha = 16°$, $20°$, $25°$ and $30°$. All the results are for a simulated $Re = 1 \times 10^6$.
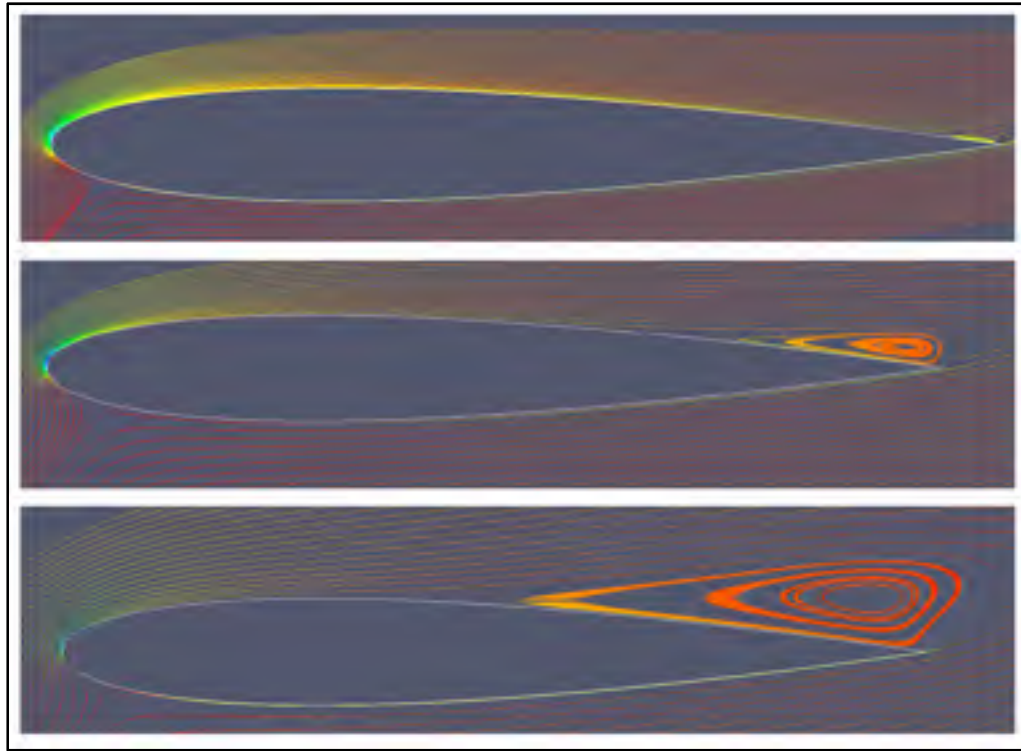
Figure 4.7 Flow Separation formation Near T.E. of NACA 0012 for $\alpha = 14°$, $16°$ & $17°$

For $0° \leq \alpha < 16°$, the Fr_x increases near $S/c \approx 0.04$ when the α is increased. The Fr_x then decreases after $S/c \approx 0.04$ all the way to the trailing edge except for when $\alpha = 16°$. At this angle, the Fr_x is seen to change behavior and started increasing at $S/c \approx 0.9$. This behavior is parallel to the presence of flow separation in Figure 4.7. The recirculation region causes an enhanced turbulent mixing of the flow and causes the heat transfer rate to directly increase on the airfoil. For $16° \leq \alpha < 30°$, flow separation continues to affect the heat transfer on the airfoil. Contrary to the smaller angles near $S/c \approx 0.04$, the Fr_x values drop as the α is increased. The separation point moved closer to the leading edge and the Fr_x decreases until $S/c \approx 0.1$. However, for $S/c \geq 0.1$ it is noted that Fr_x coincided for $\alpha = 20°$, $25°$ and $30°$ and kept

increasing all the way to the T.E. of the airfoil. At those angles, the flow is massively separated and the relative velocity is very low in the recirculation region, leading to a lower heat rate.
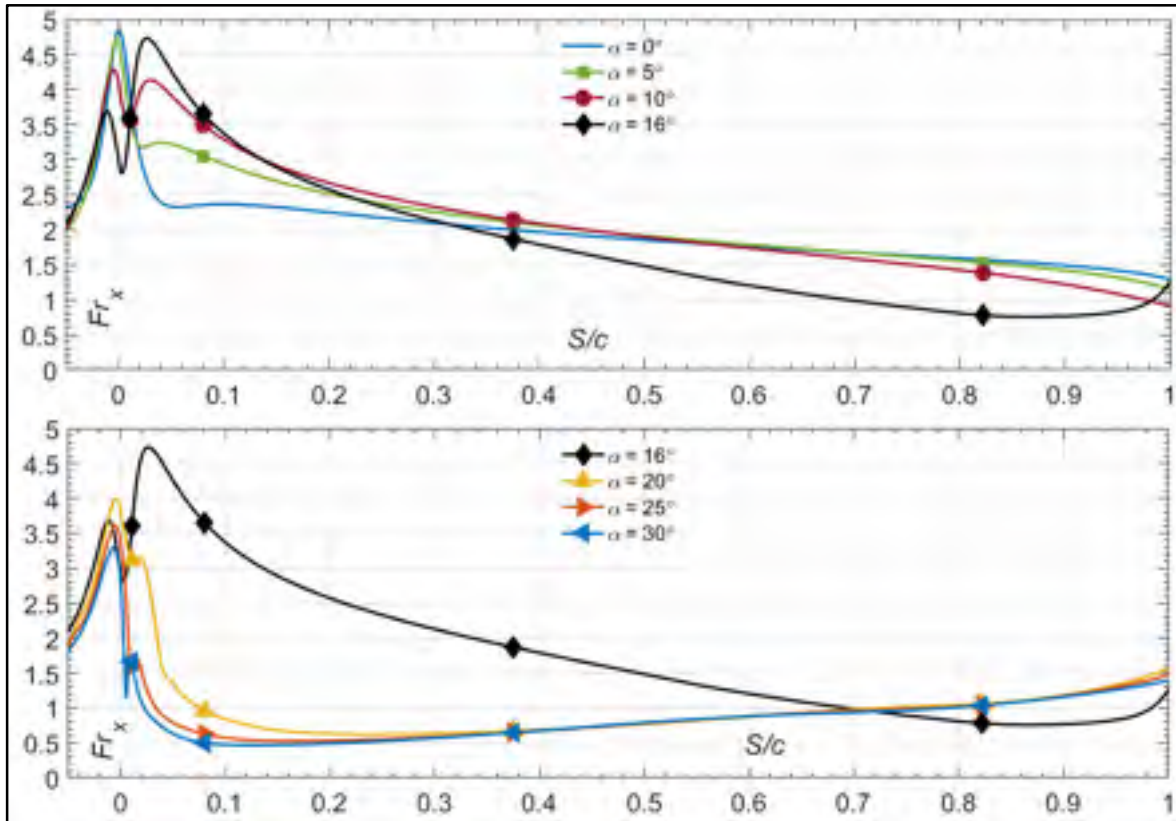
Figure 4.8 Fr_z Variation on NACA 0012 Wall for $Re = 1 \times 10^6$ at Various α

To quantify the effect of α on the Fr, the second attempt of the Fr_{Avg} correlation development for the NACA 0012 (equation (2.4)) is examined here. Specifically, the equation that describes the variation of the Fr_{Avg} (linear, quadratic or cubic) based on a varying α and a fixed Re is investigated. The only comparable form of correlation in the literature is that of (Wang et al., 2008a) (equation (2.3)) who assumed a linear variation of α.

Figure 4.9 shows the Fr_{Avg} variation of the NACA 0012 versus the α as calculated from the CFD simulations. The values correspond to $Re = 1 \times 10^6$ and for a range of $0° \leq \alpha \leq 30°$. The figure also shows three other attempts of curve fittings based on the proposed correlation of

this thesis (equation (2.4)). A linear, quadratic, and cubic variation of α are compared in the figure to the results of the CFD simulations.

The CFD results indicate that the Fr_{Avg} will continuously decrease with an increasing α. Although it had been found that the Fr_x will increase near the L.E. on the upper side of the airfoil as the α increases, the Fr_{Avg} variation indicates that the average value of the Fr over the whole the airfoil will decrease. Also, although stall is seen to occur as early as $\alpha = 14°$, there is no major effect on the Fr_{Avg} before $\alpha = 20°$, where the variation becomes less steep.
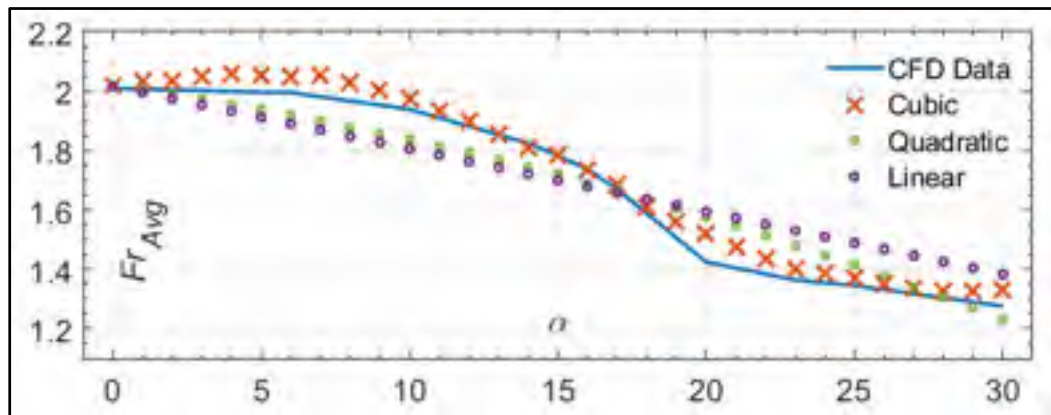
Figure 4.9 Curve Fitting Attempts for Different α Variations of the NACA 0012
Fr_{Avg} at $0° \leq \alpha \leq 30°$ and $Re = 1 \times 10^6$

Now if the different α representations from Figure 4.9 are compared, it can be seen that a linear variation will produce the highest discrepancies compared to the CFD results. A quadratic variation will produce a better agreement however it is deemed that the cubic variation is the best fit. The final form of the correlation will be presented in section 4.1.2.8 when the complete results of all Re and α are examined.

4.1.2.5 Different Thermal Boundary Conditions

In this section, the effect of changing the TBC on the surface on the airfoil is investigated. This is done by running CFD simulations for $Re = 1 \times 10^6$ and for a wide range of angles of attack

$0° \leq \alpha \leq 30°$. The simulated values for α are 0, 5, 7, 10, 14, 15, 16, 17, 20, 23, 25 and 30° and an interpolation is done for the values in between. The only difference with the previously presented results is that the simulations are for a constant Q_S TBC imposed on the wall rather than a constant T_S.

Figure 4.10 shows the results of those simulations in terms of a comparison between the Fr_x values obtained by the two TBCs. The subfigures on the left side show the variation on the whole airfoil wall and the ones on the right side show a zoomed view on the leading edge of the airfoil for $-0.1 \leq S/c \leq 0.1$. The four cases presented are for $\alpha = 0°$, 8°, 16° and 25°.

Starting with the case of $\alpha = 0°$ and by examining the L.E. part first, it is noted that the Fr_x value at the stagnation point $S/c = 0$ for either TBC is not the same. Moreover, for $S/c > 0$ and $S/c < 0$, the Fr_x values from the constant Q_S simulations are lower than those with the constant T_S. By examining the variation from airfoil front to back, the discrepancy varies between 2 to 4%.

When the angle of attack is increased to $\alpha = 8°$, the lower Fr_x from the constant Q_S simulation remain, but are even lower on the suction side than they are on the bottom side of the airfoil. This is also true for the case when $\alpha = 16°$, where not only the discrepancy exists but the variation behavior near the L.E. is also disrupted. For $\alpha = 25°$, it is found that the drop of Fr_x on the upper side of the airfoil after the L.E. is more severe for the constant T_S simulation than it is for the constant Q_S simulation.

To quantify the expected rise in the average Fr values when the TBC is changed, the average Fr_{Avg} is computed for each α of the simulations with the two different TBCs. Figure 4.11 shows the results of Fr_{Avg} as a function of the increasing α for the constant T_S and Q_S simulations. There is no significant change in the behavior of the Fr_{Avg} for different TBCs. However, the constant T_S simulations always overpredict the constant Q_S by 2% to 4%.
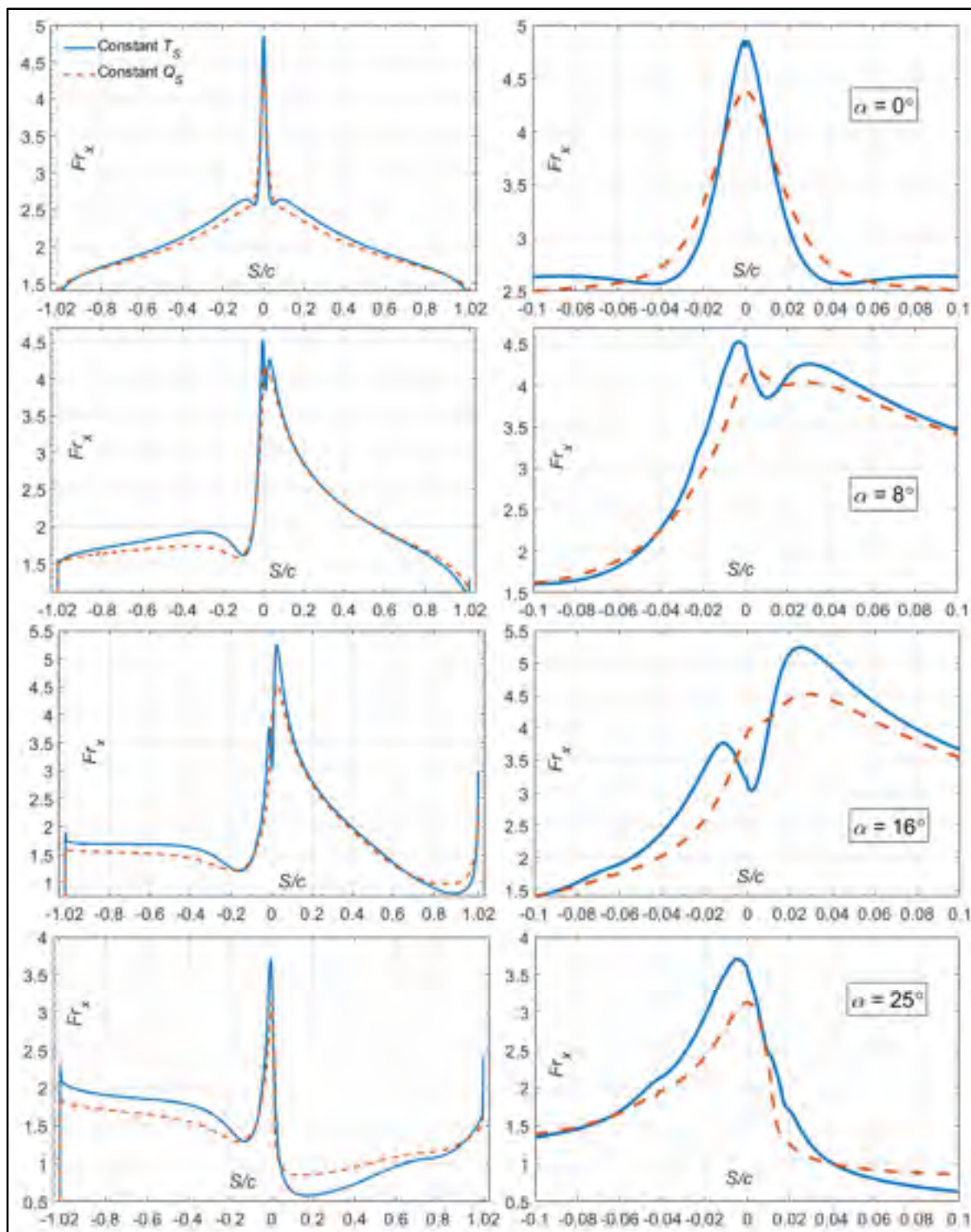
Figure 4.10 Comparison of Fr_x Variation on NACA 0012 for $Re = 1 \times 10^6$ under constant Q_S & T_S TBCs
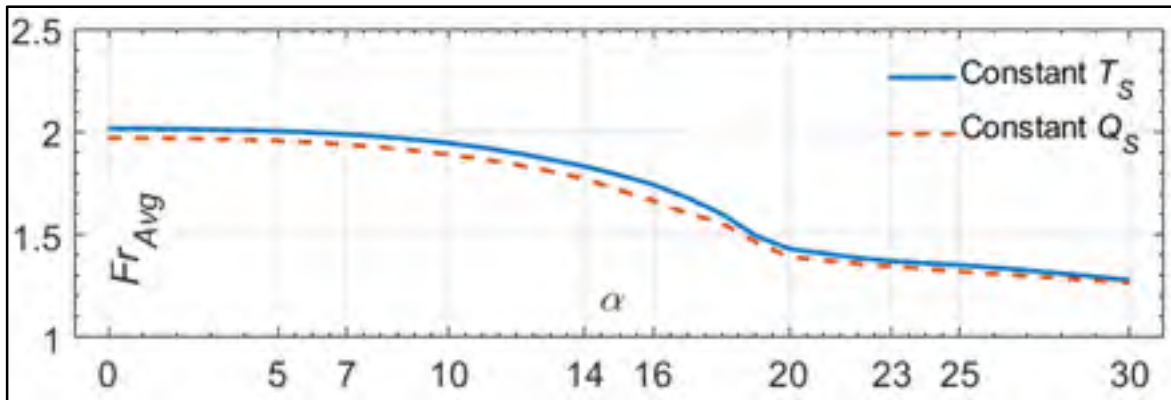
Figure 4.11 Comparison of NACA 0012 Fr_{Avg} under constant Q_S & T_S TBCs for $Re = 1 \times 10^6$

4.1.2.6   Complete Results of Average *Fr*

Each CFD simulation produces Fr_x values at 512 different points on the NACA 0012 wall, but the main interest of this research is the average heat transfer values on different blade radial sections. Therefore, to summarize the results of the database formed by the Fr_x values of each simulation, the Fr_{Avg} of all simulations is calculated. This parameter described the average value of the *Fr* across the entire wall of the airfoil at a unique combination of *Re* & α. Figure 4.12 shows the variation of the calculated Fr_{Avg} between $0° \leq \alpha \leq 30°$ and for a variety of *Re*. Not all the *Re* data are presented to avoid an overfill in the figure but the smallest ($Re = 1 \times 10^5$), largest ($Re = 3 \times 10^6$) and nine other intermediate values ($1 \times 10^5 < Re < 3 \times 10^6$) are shown.

Based on the results of Figure 4.12, the Fr_{Avg} on the NACA 0012 under fully turbulent flow conditions followed a trend. The trend is described by two behaviors : 1 - a direct increase in Fr_{Avg} values as the *Re* is increased, regardless of the α; and 2 – a continuous decrease in Fr_{Avg} values as the α is increased except for $\alpha < 5°$ when $Re = 1 \times 10^5$ and $Re = 2 \times 10^5$.

It was seen in section 4.1.2.3 that at $\alpha = 0°$ and for $2 \times 10^5 \leq Re \leq 3 \times 10^6$, $Fr_{Avg} = A \times \mathrm{Re}^m \times \mathrm{Pr}^{1/3}$ could describe the variation of the Fr_{Avg} with the constants $A = 0.022$

and $m = 0.331$. In section 4.1.2.4, a cubic variation of the α in a correlation of the form of equation (2.4) is also proven to be the best fit to the variation of Fr_{Avg} for $Re = 1 \times 10^6$ and a range of $0° \leq \alpha \leq 30°$. These findings combined with the similarities and trends observed in Figure 4.12 indicate that a correlation that predicts the Fr_{Avg} for all Re and α is possible and will be presented in section 4.1.2.8.
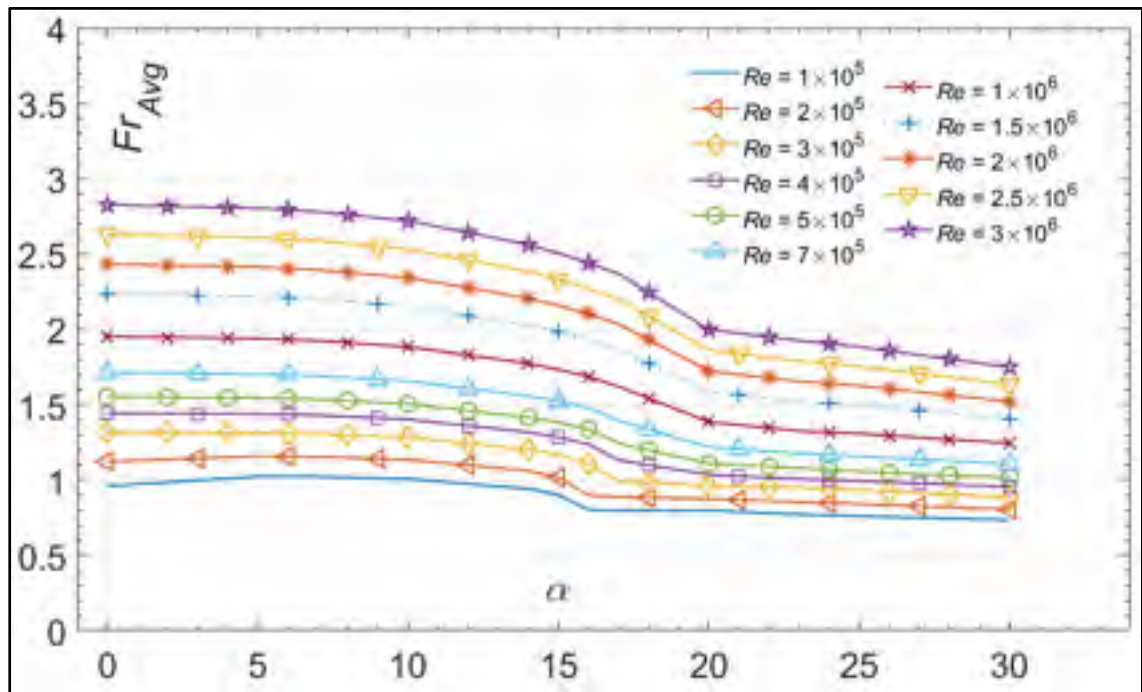
Figure 4.12 NACA 0012 Fr_{Avg} Variation of for $0° \leq \alpha \leq 30°$ & $1 \times 10^5 < Re < 3 \times 10^6$

4.1.2.7 Zone with Maximum *Fr*

In this section, a zone over the airfoil wall that experiences that maximum amounts of heat transfer over the NACA 0012 is sought, based on the airfoil division of section 2.1.4. The correlation is defined only in the pre-stall conditions, it's why the focus for the average *Fr* is given for $0° \leq \alpha \leq 16°$. As was determined from the previous analysis in section 4.1.2.4, stall is assumed to occur at $\alpha_{Stall} = 16°$, based on the CFD simulations under fully turbulent flow conditions and regardless of the *Re*. Following the calculation and averaging of the *Fr* over each of the prescribed zones, the results are plotted in Figure 4.13.

Figure 4.13 shows the variation of the Fr_{Avg} for $0° \leq \alpha \leq 16°$. The depicted Re at each α are $Re = 2 \times 10^5$, 5×10^5, 1×10^6, 1.5×10^6, 2×10^6, 2.5×10^6 and 3×10^6. More Re are simulated but the presented ones cover the whole range of simulations and are selected to avoid a figure overfill. Each subfigure is for one of the corresponding zones described in Figure 2.2. The results of the figure indicate that the highest Fr values are always found on zone 1.
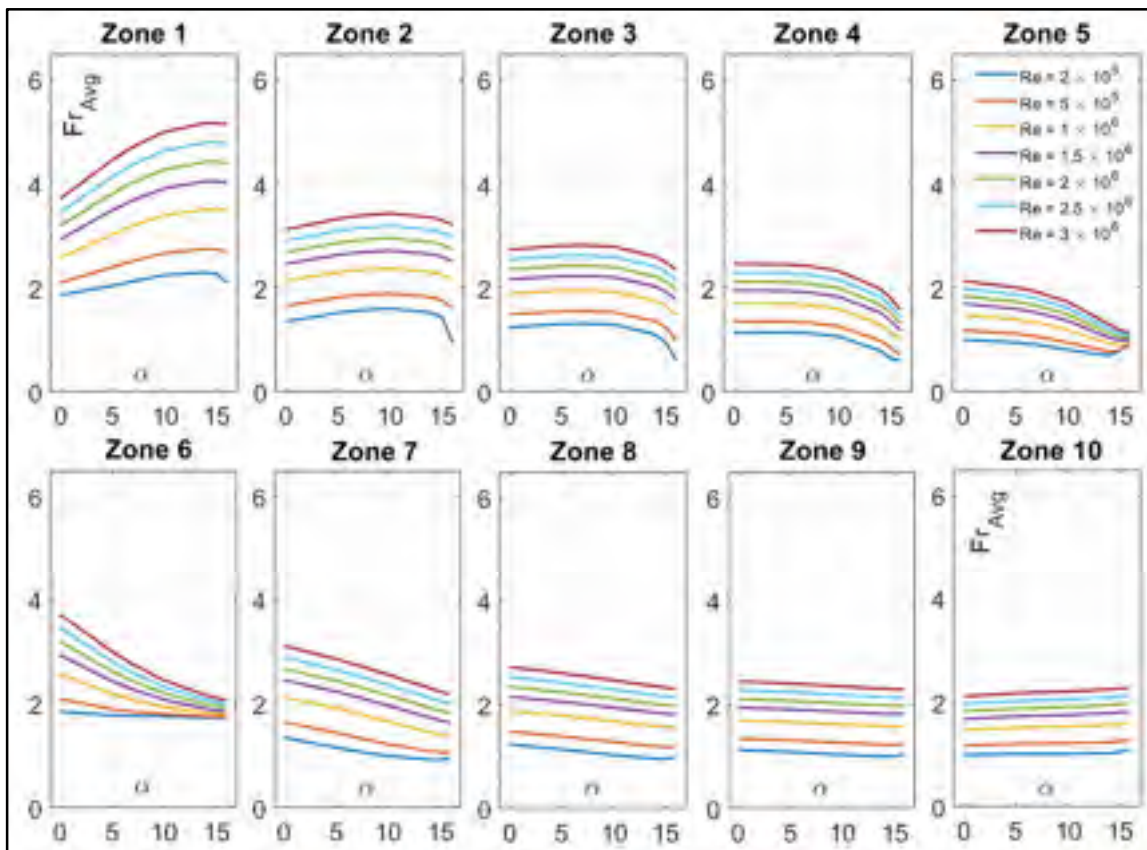
Figure 4.13 Variation of Zone-Specific Fr_{Avg} for $0° \leq \alpha \leq 16°$

In fact, zone 1 is the only zone out of the other nine that shows an increasing Fr for $0° \leq \alpha \leq 16°$ at any Re aside from a slight decline that is seen near $\alpha \approx 16°$. This increase corresponds to the increasing Re as the α is increased. This leads to the conclusion that under fully turbulent flow conditions, zone 1 will be the most vulnerable to icing. Since this is a critical area that the ice-protection system design must take into consideration, the Fr values of zone 1 are

correlated as will be seen in section 4.1.2.8. This way, the correlation could be applied with the BEMT-RHT or the UVLM-RHT.

4.1.2.8   Correlations for *Fr*

In order to simplify the estimation of the *Fr* on the NACA 0012, the data of the Fr_{Avg} and Fr_{Max} are correlated in a similar fashion to the existing flat plate and cylinder correlations. The correlation would be one way to calculate the heat transfer on the airfoil without the need to go through CFD simulations and time-consuming post-processing. The correlation also eliminates the need for database interpolation. As explained in section 2.1.1, the technique was tried before on the NACA 63-421 airfoil as seen in the work of (Wang et al., 2007b, 2008a) and the new correlation of this work would have the form of equation (2.3).

Based on a curve fitting method (MATLAB, 2019b), it is found that a correlation in the form of equation (4.5) is capable of reproducing the CFD results of the *Fr* at $\alpha = 0°$ from Figure 4.12 with an average error of 0.53%. This correlation is valid for a fully turbulent flow condition with a constant T_S TBC and can accommodate a range of $1 \times 10^5 \le Re \le 3 \times 10^6$.

$$Fr_{Avg}\left(\alpha = 0°\right) = 0.021 \mathrm{Re}^{0.335} \mathrm{Pr}^{1/3} \tag{4.5}$$

In a similar analysis, the previous correlation is expanded to accommodate the range of $0° \le \alpha \le 30°$. Equation (4.6) is found to estimate the CFD-determined Fr_{Avg} under fully turbulent flow condition, with a constant T_S TBC and an average error of 2.14%. The correlation is also valid for $1 \times 10^5 \le Re \le 3 \times 10^6$. The α used in the correlation is in radians.

$$Fr_{Avg} = 0.021\left(1 + 1.131\alpha - 8.634\alpha^2 + 10\alpha^3\right)\mathrm{Re}^{0.335} \mathrm{Pr}^{1/3} \tag{4.6}$$

Equation (4.7) is the result of curve fitting the data of Figure 4.13. It describes the Fr_{Max} which corresponds to the *Fr* variation on zone 1 of the airfoil. The correlation is valid for a fully

turbulent flow condition, with a constant T_S TBC and the average error is 2.06%. The range of applicability is $0° \leq \alpha \leq 16°$ (pre-stall) and $1 \times 10^5 \leq Re \leq 3 \times 10^6$.

$$Fr_{Max} = 0.024\left(1 + 2.682\alpha - 4.725\alpha^2\right)Re^{0.345}\,Pr^{1/3} \tag{4.7}$$

From the other hand and if the constant Q_S TBC is examined, the Fr_{Avg} values would be slightly higher than those of the constant T_S, according to the results of section 4.1.2.5. In that section, the Fr_{Avg} values are 2% to 4% higher if a constant Q_S is imposed on the wall of the NACA 0012. While only one Re is studied under the constant Q_S compared to 7 different simulated Re for the constant T_S, the range of simulated α for both TBCs is the same. The trend of variation of the Fr_{Avg} versus α at $Re = 1 \times 10^6$ is also similar for both TBCs (Figure 4.11). Therefore, and as an approximation, it is decided to adopt a 3% decrease of Fr_{Avg} values between the results of constant Q_S and constant T_S TBC. When this approximation is applied to the presented Fr correlations, new parameters are needed, describing the Fr_{Avg} at $\alpha = 0°$ (equation (4.8)), the Fr_{Avg} for $0° \leq \alpha \leq 30°$ (equation (4.9)) and the Fr_{Max} for $0° \leq \alpha \leq 16°$ (equation (4.10)). All of which are for a fully turbulent flow condition.

$$Fr_{Avg}\left(\alpha = 0°\right) = 0.020\,Re^{0.335}\,Pr^{1/3} \tag{4.8}$$

$$Fr_{Avg} = 0.020\left(1 + 1.131\alpha - 8.634\alpha^2 + 10\alpha^3\right)Re^{0.335}\,Pr^{1/3} \tag{4.9}$$

$$Fr_{Max} = 0.023\left(1 + 2.682\alpha - 4.725\alpha^2\right)Re^{0.345}\,Pr^{1/3} \tag{4.10}$$

Finally, this set of correlations is considered comprehensive enough to estimate the heat transfer on a 2D NACA 0012 airfoil section. The effects of varying airspeed (Re), angle of attack (α) and TBC (constant Q_S or T_S) are all represented. Instead of going through CFD simulations or using an airfoil-to-flat-plate approximation, the correlations could be used to

calculate the *Fr*. Another advantage of the correlations is that they provide the average value of the whole airfoil from one side and the maximum from another.

4.2   Aerodynamic Validation of Developed BEMT & UVLM

This section serves to validate the aerodynamic performance of the implemented BEMT and UVLM using 4 experimental test cases from the literature. The first is for a 2-blade hovering rotor with no ground effect and is modeled using both the BEMT and the UVLM. The thrust as well as the sectional lift coefficient C_{Ly} predicted by both methods is compared to experimental data as well as other 2 numerical implementations of the UVLM from the literature. The second test case is for a 4-blade hovering rotor in ground effect and is modeled only using the UVLM at different ground clearances. The validation consists of comparing the predicted tip vortex locations by the UVLM to those measured experimentally. On the other hand, the thrust estimate is also compared based on experimental data as well as another numerical method from the literature. Third, a 2-blade rotor in axial flight test cases is modeled using both the UVLM and the BEMT. The tip vortex locations are compared between the results of the UVLM and those of the experiments at different climb ratios. The figure of merit *FM* estimate by both the BEMT and the UVLM is compared to the experimental data and another numerical method from the literature. The fourth and final test case is for a 2-blade rotor in forward flight and is modeled using the UVLM. The sectional thrust coefficient C_{Ty} predicted by the UVLM is compared to the experimental data as well as to the results of three other numerical implementations from the literature.

4.2.1   Two Blade Hovering Rotor

The experimental setup consisted of two hovering blades having a NACA0012 airfoil section spinning at $\Omega = 1250$ rpm with $Ma_{Tip} = 0.43$. The chord is 0.1905 m (equal to the root cut-out radius) with a radius of 1.143 m and three difference pitch angles are used $\theta = 5°$, $8°$ and $12°$. The BEMT is ran using $n = 200$ radial sections to predict the steady-state value of C_T. For the UVLM, the test case is run for 24 revolutions for $\Delta\Psi = 15°$ using 10×25 vortex panels on

each blade and the first 2 rotor revolutions are used to slow start the rotor. As will be shown in Table 4.2, the discretization of both the UVLM and BEMT is enough to produce stable results that change by less than 3% for finer discretization. The presented UVLM C_{Ly} is the one at the 23rd revolution, when the C_T and C_{Ly} are stabilized and do not change between timesteps.

Figure 4.14 shows the comparison between the results of the UVLM, BEMT and the literature. The left side shows the variation of C_T as function of the rotor revolutions for $\theta = 5°$, $8°$ and $12°$. The data shown are obtained using the viscous UVLM and BEMT and compared to the results of (Colmenares et al., 2015). The right side shows the variation of the C_{Ly} recorded by the experiments of (Caradonna & Tung, 1981) along the length of the blade versus the viscous UVLM and BEMT at the 3 different θ.
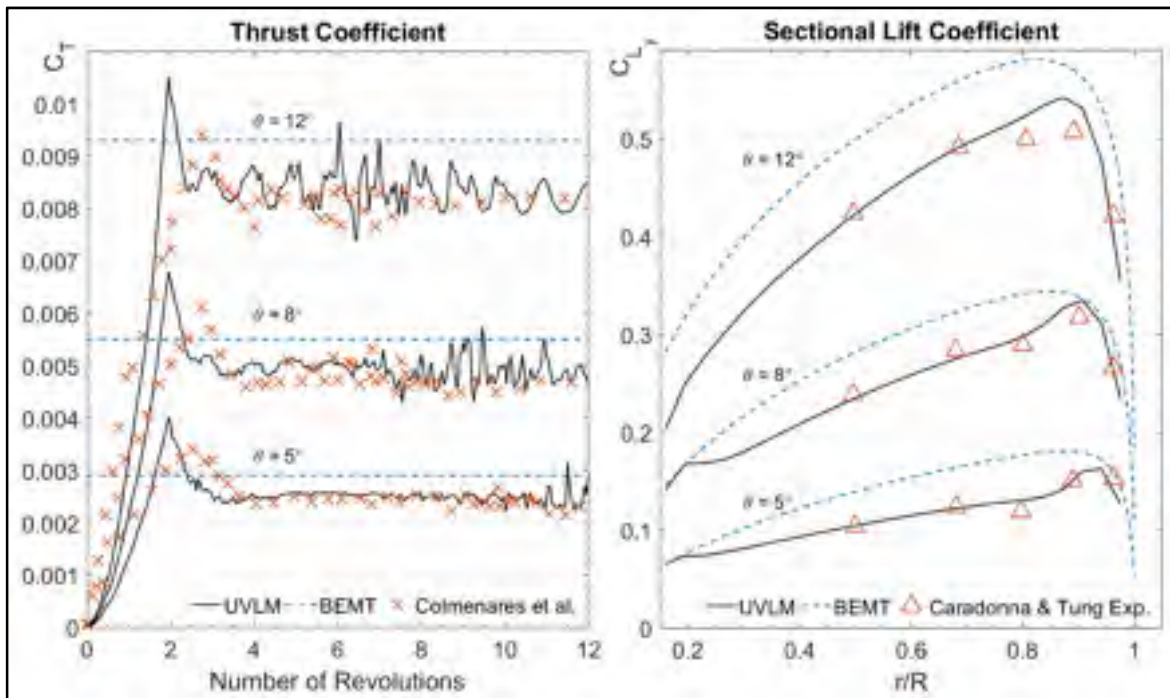
Figure 4.14 Evolution of C_T with Number of Revolutions & C_{Ly} Variation on Blade Radius

For the BEMT, the steady-state C_T is overpredicted by around 15-20% for all θ, perhaps due to the simplified calculation method of the rotor induced velocities. As for the UVLM, the rotor thrust increases from 0 just when the blades commence movement, reaches a maximum

at the second revolution (where maximum rotational speed is reached) and then exhibits a fluctuating behavior ($\pm$ 4%) around an average C_T value. The average C_T predicted by the UVLM and BEMT is compared to the UVLM implementation of (Colmenares et al., 2015) and (Ferlisi, 2018) as well as the experiment in Table 4.1. It is concluded that the UVLM agreed better with the literature results (5% discrepancy) whereas the BEMT overpredicts all other estimations by almost 20%. As for the C_{Ly}, the UVLM agrees within 5% of experimental data whereas the BEMT overestimates the C_{Ly} by almost 20% implying that the α_{eff} predicted by UVLM may also be closer to that of the experiment, although no data to compare with exists.

Table 4.1 Average C_T Values From UVLM, BEMT & Other Numerical & Experimental Data

Average C_T	UVLM	BEMT	Ferlisi	Colmenares et al.	Caradonna & Tung
$\theta = 5°$	0.00243	0.00290	0.00237	0.00221	0.00213
$\theta = 8°$	0.00477	0.00540	0.00460	0.00467	0.00459
$\theta = 12°$	0.00794	0.00910	0.00824	0.00821	0.00796

The hovering test case is also used to study the effect of changing the discretization of the UVLM and the n of the BEMT on the predicted C_T. For the BEMT, changing the n does not have a significant impact on the C_T where for an $n = 1000$, the C_T changes by less than 0.2% compared to $n = 200$. Table 4.2 shows the predicted C_T by the UVLM because of changing the $\Delta\Psi$ for a fixed blade lattice distribution (10 $\times$ 25), as well as changing the blade lattice distribution for a fixed $\Delta\Psi = 15°$. For all cases, a total of 24 revolutions with 2 slow start revolutions are used. The results correspond to the hovering rotor test case with $\theta = 8°$. It is seen that the decrease of $\Delta\Psi$ from $\Delta\Psi = 15°$ to $\Delta\Psi° = 5$ changes the C_T by less than 1.5%, whereas increasing the number of blade lattices from 10 $\times$ 25 up to 20 $\times$ 100 causes the C_T to change by almost 3.2%. Therefore, it is concluded that a BEMT discretization of $n = 200$ and a UVLM discretization of 10 $\times$ 25 blade lattices and $\Delta\Psi = 15°$ are enough to produce stable averaged results and change by less than 3.2%.

Table 4.2 Effect of Changing UVLM Discretization on Predicted Average C_T

$\Delta\Psi$	Blade Lattices	C_T	Blade Lattices	$\Delta\Psi$	C_T
5°		0.00467	10×25		0.00477
10°	10×25	0.00471	15×50	15°	0.00469
15°		0.00477	20×100		0.00462

4.1.2   Four Blade Hovering Rotor in Ground Effect

The Lynx tail rotor experimental setup (Light, 1993) uses a four blade hovering, vertically mounted, rotor with a 0.18 m chord and a 1.108 m total radius (0.425 m root cut) near the ground. The rotor has an NPL 9615 airfoil shape and is spinning at 1660 rpm. For every ground clearance ratio h/R, a set of θ are used to form a test case and the C_T is measured. Four of these tests use a shadowgraph to capture the trailing wake in the axial and radial directions. The BEMT is not implemented here since it does not provide a wake shape nor could model the ground effect.

Figure 4.15 shows the results of the tip vortices axial and radial locations *TVAL* & *TVRL* obtained by UVLM compared to those of the experiments. The *TVAL* & *TVRL* are non-dimensional parameters that describe the location of the shed wake vortex as the rotor is spinning and are calculated according to equation (4.11). They are measured in terms of the wake age that represents the azimuth angle by which the blade had rotated since a specific wake element was shed.

$$TVAL = \frac{Q_{W_z}(\Psi)}{R_{Tip}} \quad TVRL = \frac{Q_{W_x}(\Psi)}{R_{Tip}} \tag{4.11}$$

The subfigure on the upper left is for a test with no ground effect ($h/R = \infty$) and every other subfigure shows the tip locations for a test with a smaller h/R. The idea is to determine if the

UVLM could be validated even at small h/R. For $h/R = \infty$ and $h/R = 0.84$, the axial and radial tip locations are captured with around 92% agreement. Discrepancies exist but the overall wake behavior is well captured. However, as the h/R is decreased to 0.52 and 0.32 respectively, the radial positions by the UVLM slightly deviate from the experimental data although the axial locations are well predicted.
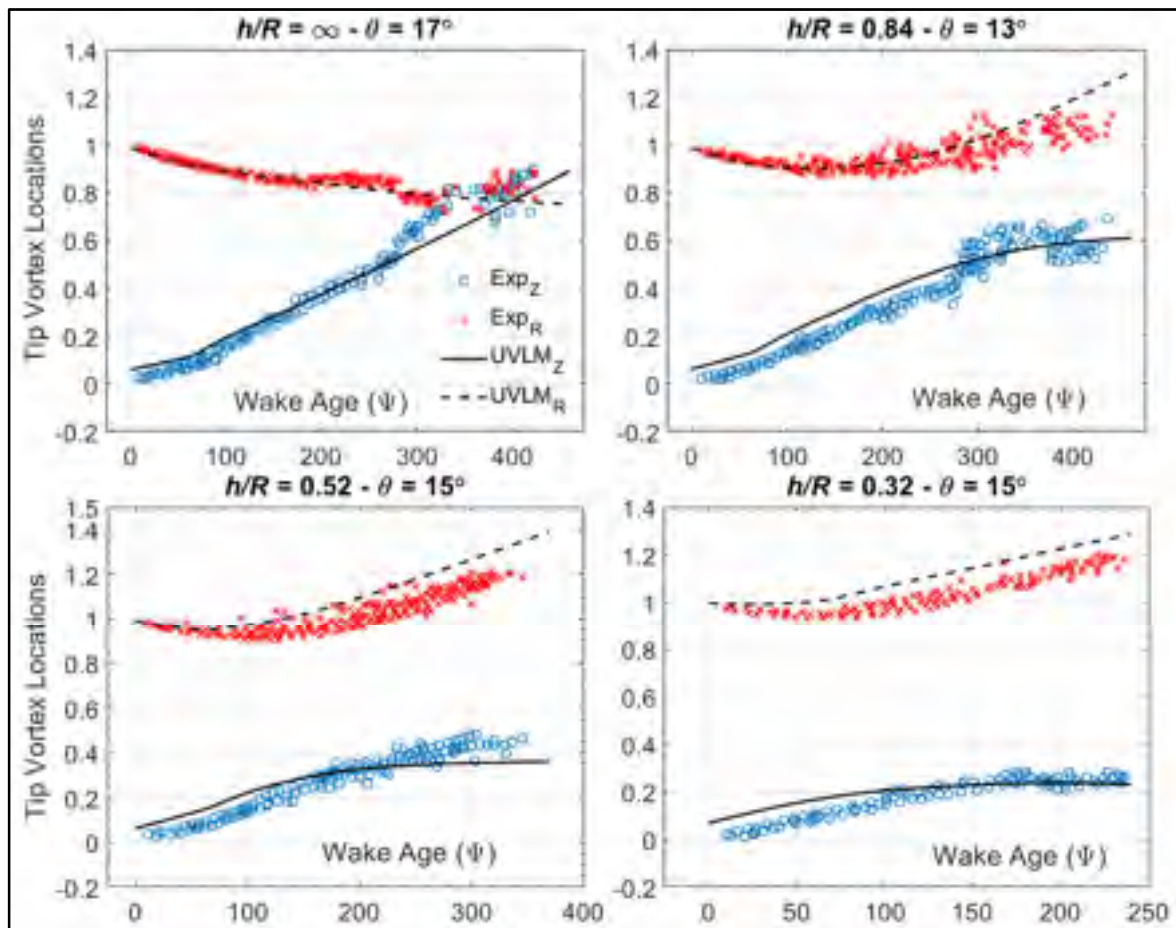
Figure 4.15 Comparison of UVLM Axial & Radial Tip Vortex Locations with Experimental Data (IGE)

For C_T predictions, Figure 4.16 shows the variation of the C_T versus h/R predicted by the UVLM compared to those recorded from the experiments. The predictions of the numerical method of (Cheeseman & Bennett, 1955) are also presented to check how the UVLM compared to other numerical calculations. Existence of two data points for the same h/R indicate a

different θ for each. For $h/R >= 0.52$, the UVLM predicts C_T values within 8% of the experimental and numerical results of the literature. The results from the UVLM are closer to the numerical values of (Cheeseman & Bennett, 1955) than they are to those of the experiments. The highest discrepancy of the C_T predicted by the UVLM was for the case of extreme ground effect ($h/R <= 0.32$), up to 25% different than experiments.
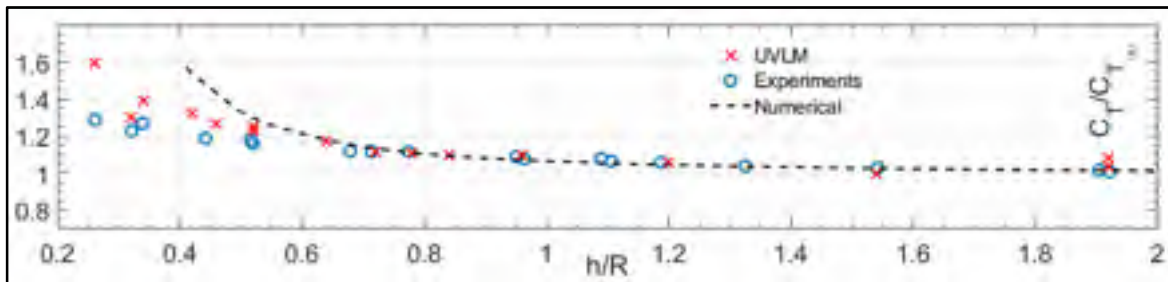
Figure 4.16 Comparison of UVLM C_T Predictions at Different Height Ratios with Numerical & Experimental Data

It is believed that the larger discrepancy of the implemented UVLM in extreme ground effect may have been either the results of discretization or the induced velocities calculations. It is observed that when the h/R is decreased, the wake lattices near the ground become very condensed and got much closer together. This may result with the vortex segment distances being very small and with the induced velocities not calculated properly. For the implemented UVLM in the work of (Ferlisi, 2018), the comparison of the predicted $TVRL$ matched the experimental results but his predicted $TVAL$ did not provide a good agreement.

4.2.3   Two Blade Rotor in Axial Flight

(Caradonna, 1999) conducted a two-blade rotor experiment for a rotor in axial flight. The rotor radius is 1.067 m and the aspect ratio is 13.67. The blades are not tapered nor twisted. The sectional airfoil is a symmetric Bell Profile. The root cutout is approximately equal to one chord. The rotor speed is 1800 rpm, the Ma_{Tip} is around 0.46 and the climb ratios CR are varied. The goal in this section is to validate the wake shape and blade loading predicted by the UVLM, so the $TVAL$ & $TVRL$ predicted by the UVLM using equation (4.11) are compared to the ones

recorded by the experiments. The numerical model consisted of 10×25 vortex lattices on each blade and is run for 24 revolutions with $\Delta\Psi = 10°$.
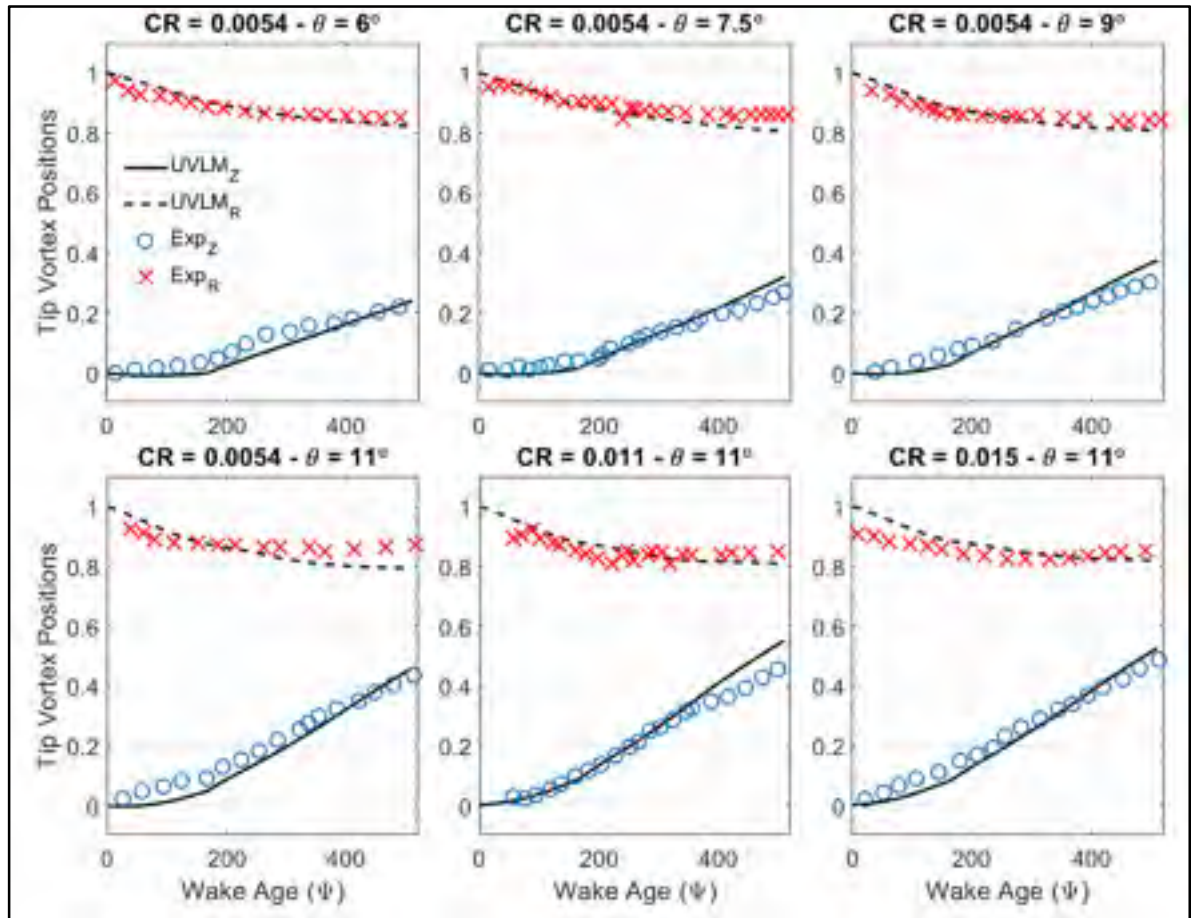
Figure 4.17 Comparison of UVLM Axial & Radial Tip Vortex Locations with
Experimental Data for a Rotor in Axial Flight

Figure 4.17 shows the *TVAL & TVRL* obtained by the UVLM compared to those of the experiments for a length of 1.5 revolutions. The cases presented involve a rotor with $\theta = 6°$, 7.5°, 9° and 11° whereas $CR = 0.0054$, 0.011 and 0.015. The UVLM results are recorded at the 20th turn after a steady-state wake shape is observed. In fact, the *TVAL & TVRL* changed by less than 2% since the 15th revolution. It can be seen from Figure 4.17 that the tip vortex locations predicted by the UVLM agree with those of the experiments within 90% although

some discrepancies exist for the axial data, especially for $CR = 0.011$. The implementation of the UVLM is therefore capable of reproducing the wake shape from the experiments.

To validate the blade loading however, the Figure of Merit FM is computed and shown in Figure 4.18. This is done for $0.002 < CR < 0.04$. Results from the experiments as well as the viscous UVLM implementation of (Ferlisi, 2018) are used to validate the results from the UVLM and BEMT of this work. The viscous corrections of *Ferlisi* are obtained using XFOIL whereas this work uses CFD based viscous corrections.
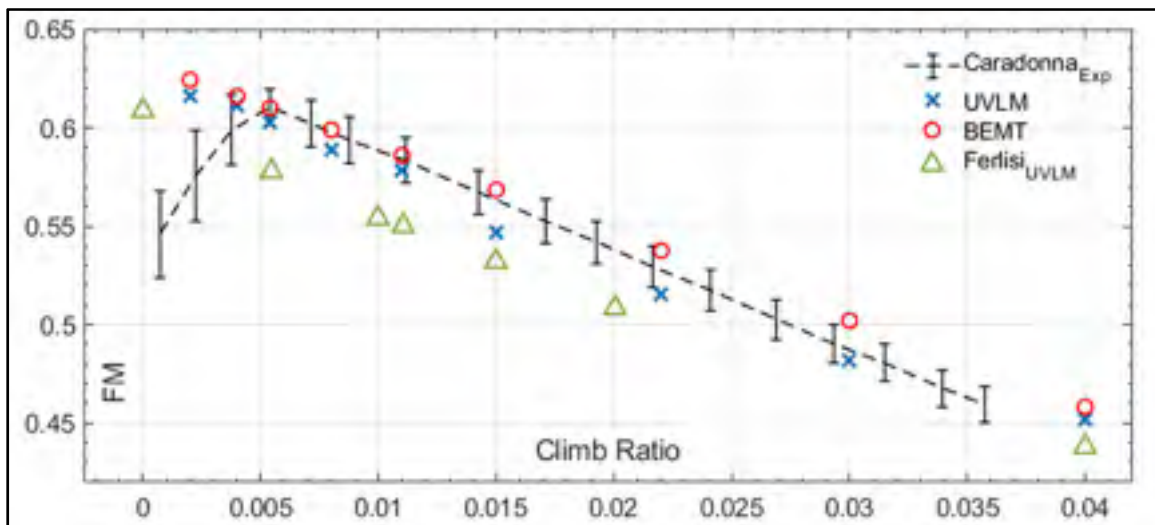
Figure 4.18 Comparison of Predicted *FM* by the UVLM & BEMT with Numerical & Experimental Data

The results of Figure 4.18 show that the viscous BEMT and UVLM implemented in this work well predict the variation of the *FM* compared to the numerical method from the literature as well as the experiments, with a discrepancy for $CR < 0.005$. The results of the BEMT and UVLM agree within ± 7% of the experiments, a closer agreement than the UVLM method from the literature. All the numerical methods shown in Figure 4.18 showed a discrepancy with the experiments for $CR < 0.005$. According to (Caradonna, 1999), this may be due to experimental errors where a linear variation of *FM* down to $CR = 0$ is more likely expected.

4.2.4   Two Blade Rotor in Forward Flight

The AH-1G 2-blade rotor experiment by (Cross, 1988) is also analyzed for a rotor in forward flight. The goal in this section is to validate the blade loading calculated by the UVLM for a rotor in forward flight. The blades have an OLS/TAAT airfoil shape and its characteristics are obtained from (Watts, Cross, & Noonan, 1988). The rotor radius is 6.7 m and the aspect ratio is 9.2 with a linear twist ratio of -10°. The rotor operates at $Ma_{Tip} = 0.68$ and the advance ratio is 0.19. The numerically modeled blade with the UVLM consist of 20×60 vortex lattices ran for 12 revolutions at $\Delta \Psi = 10°$. A finer discretization is used in this test case to better capture the r/R and get similar ones to those of experiments. The calculated sectional C_T is compared to the experiments, the unsteady potential method of (Tan & Wang, 2013a), the free wake method of (Kim, Park, & Yu, 2009) and the CFD calculations of (Lee, Yee, Oh, & Kim, 2009).

Figure 4.19 shows the variation of sectional C_{Ty} on the blade versus the wake age. Each subfigure corresponds to a specific radial section located at $r/R = 0.87$, $r/R = 0.91$ and $r/R = 0.97$. The results of the UVLM and those of the experiment are compared in every subfigure whereas the results of the numerical methods from the literature are shown as follows: the potential method at $r/R = 0.87$, the free wake at $r/R = 0.91$ and CFD at $r/R = 0.97$. This is done to avoid a data overfill in the figures.

The variation of the C_{Ty} versus Ψ corresponded with the movement of the blade from an advancing side to a retreating side. The point of minimum tip local velocity is at $\Psi = 90°$ and the maximum velocity is reached half a revolution after at $\Psi = 270°$. Relating to Figure 4.19 and for all shown r/R, the C_{Ty} increases starting at $\Psi = 90°$ until a maximum value around $\Psi = 270°$ before decreasing when the blade is in the retreating side and the velocity decreases. This effect is captured well by the UVLM and all other shown data from the literature compared to the experimental results.

The UVLM agrees within 80% to the results of the experiments for all r/R. However, at $r/R = 0.87$, the discrepancy of the UVLM compared to the Potential Method was around 20%. At

$r/R = 0.91$, the UVLM shows a discrepancy as low as 5% with the results of the Free Wake method before $\varPsi = 270°$ and around 20% for $270° < \varPsi < 360°$. The discrepancy with the CFD results at $r/R = 0.97$ is around 10% but the C_T is overpredicted at $\varPsi < 90°$.
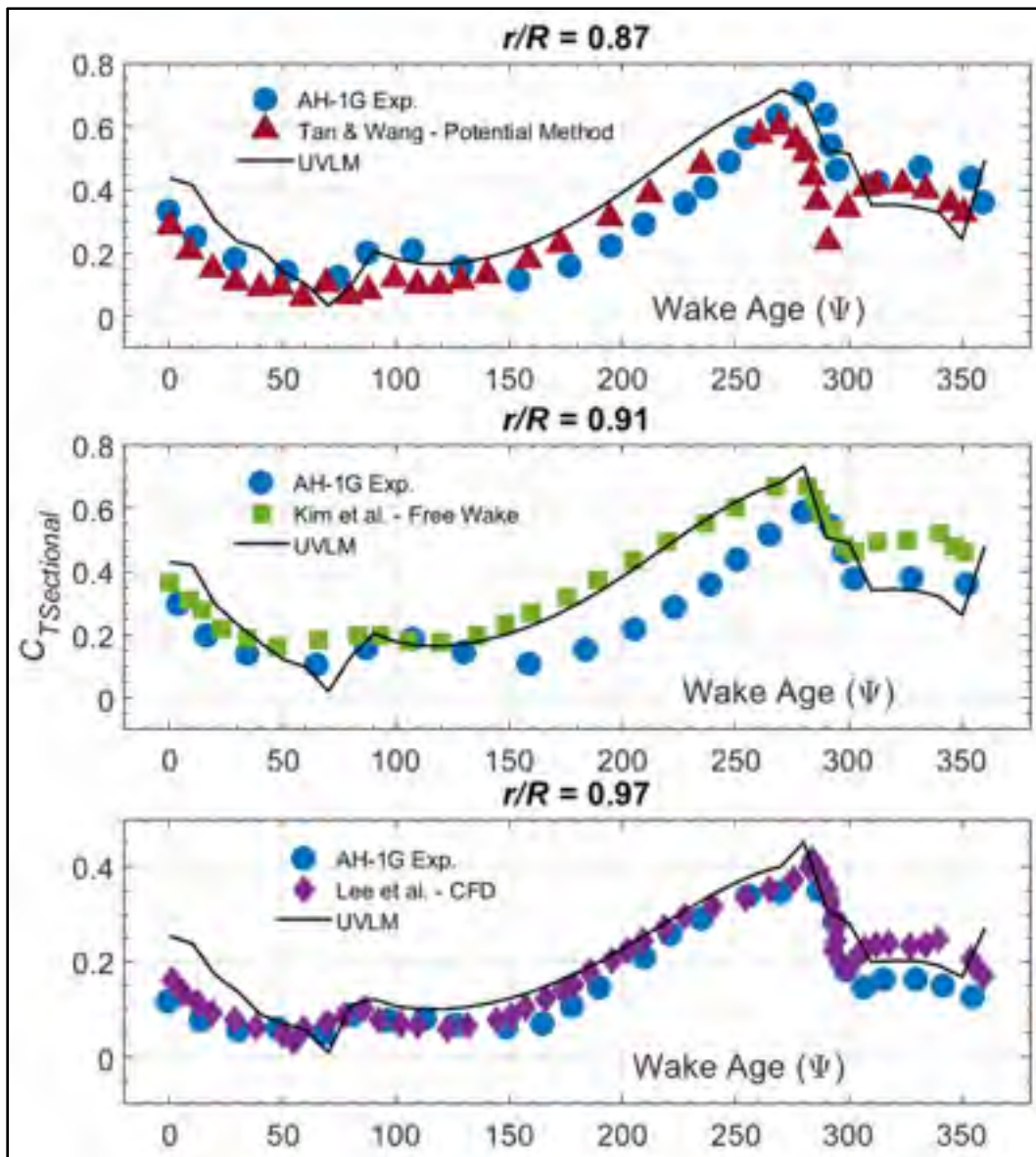
Figure 4.19 Comparison of Predicted C_{Ty} by the UVLM versus Numerical & Experimental Data for a Rotor in Forward Flight

Although the discrepancy varies when comparing the UVLM to the other numerical methods in the literature, the predicted C_{Ty} by the UVLM is acceptable considering the original purpose of the tool. The CFD results are the best in terms of numerical results, showing a match with experimental data except for a maximum 25% error between $300° \leq \Psi \leq 350°$, mainly due to high fidelity approach and detailed calculations. Unlike the UVLM, the potential method models the thickness of the blades, so this perhaps explains the better agreement with experimental results. The UVLM of this work behaves similarly to the other free wake method.

4.3 Modified Bell 429 Tail Rotor Heat Transfer Results

To present the results of the heat transfer distribution on a rotor using the BEMT-RHT and UVLM-RHT, a modified version of the Bell 429 tail rotor is chosen. For this work, the airfoil profile considered is a NACA 0012 to relate the calculations to the proposed Fr correlations. The 4-blade rotor has a chord of $c = 0.1752$ m with a diameter of 1.652 m. It operates at a speed of $\Omega = 2292$ rpm with a $Ma_{Tip} = 0.6$ at hover. The blades are not twisted, and the simulated pitch angle is $\theta = 8°$. The blade surfaces are assumed to be maintained at a constant T_S to match the boundary condition imposed on the 2D CFD simulations. The BEMT-RHT is used to model the rotor in hover and axial flight whereas the UVLM-RHT is used in hover, axial, forward flight as well as hover in ground effect. Based on the discretization study of each method in section 4.2.1, the UVLM-RHT is used with 10×25 vortex lattices and $\Delta\Psi = 10°$ while the BEMT-RHT is used with $n = 200$ blade elements. The objective is to quantify the heat transfer predicted by each of the BEMT-RHT and the UVLM-RHT using the correlations for Fr_{Avg} and the Fr_{Max} in equations (4.6) and (4.7) for basic rotor operations under typical flight conditions. The air properties are evaluated at $T_\infty = 268.15$ K.

4.3.1 Hovering Out-of-Ground-Effect (OGE) Rotor

To estimate the Fr on the rotor, the hovering test case is ran once using the UVLM-RHT for 20 revolutions and another time using the BEMT-RHT. The BEMT directly provided the steady-state solution for the loads and heat transfer. The solution from the UVLM-RHT is time

dependent, but it is observed that steady state variations of the wake shape and loads are attained after 20 revolutions as seen in Figure 4.20. In the figure, the wake contraction below the rotor plane is well observed and the wake propagates in the negative Z axis direction freely without restriction, similar to results of (Colmenares et al., 2015). The pure rotational movement of the rotor produces a symmetric wake. Eventually, the wake rolled-up and an inverted mushroom shape is formed.

For the case of the hovering rotor, the velocity distribution as the rotor spins only varies from hub to tip and remains constant at any Ψ, thus the Re varies only in the radial direction. At the 20th revolution of the UVLM-RHT, the computed Re and α_{Eff} at every radial position and at every blade $\Delta\Psi$ are used to calculate the Fr_{Avg} and Fr_{Max} using the proposed correlations. As for the BEMT-RHT, the results of Re and α_{Eff} are already in their steady-state form with a single value corresponding to each blade element n. Equations (4.6) and (4.7) are again applied to obtain the Fr_{Avg} and Fr_{Max} across the blade length.
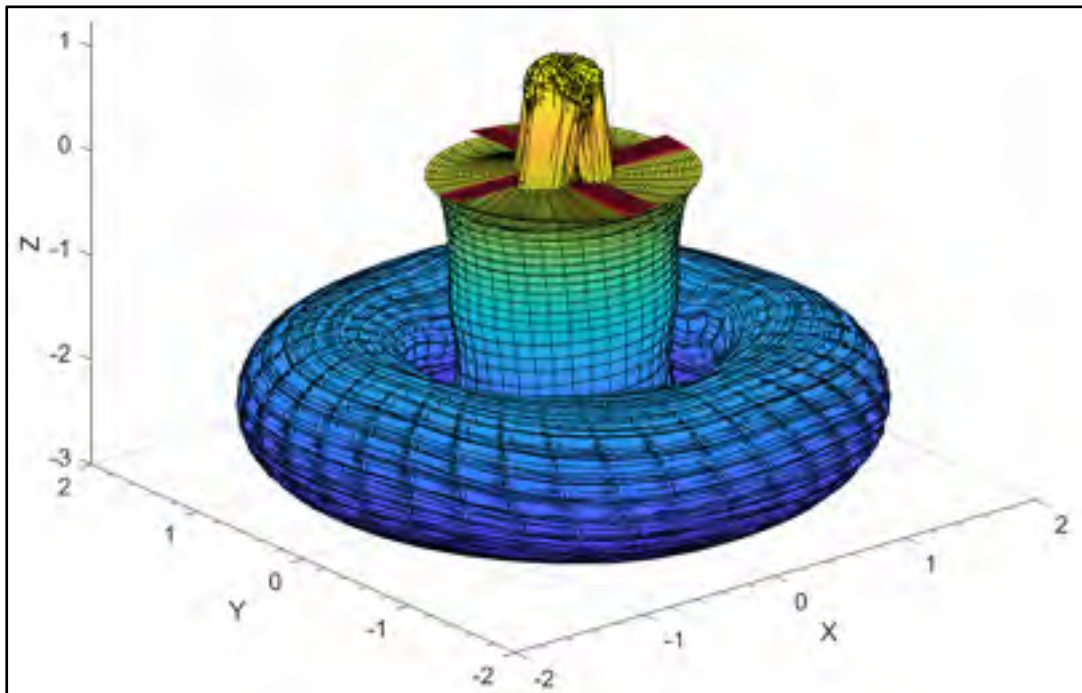
Figure 4.20 Wake Shape Produced by UVLM for the Hovering Four Blade Rotor

Figure 4.21 shows the contours of the steady state Fr_{Avg} for one steady state rotor revolution. The contours represent the value of the Fr_{Avg} at the different radial positions and azimuth angles. The upper subfigure shows the results predicted by the UVLM-RHT and the lower subfigure shows the predicted results of the BEMT-RHT. The color bar representation is used where the blue to red scale represents lower to higher Fr values.

The predicted values of each numerical tool are symmetric across the rotation plane. The predicted values of Fr_{Avg} from the UVLM-RHT varies between a minimum of 1.4 near the hub and a maximum of 2.7 on the tip. This is associated with the linear variation of the Re from hub to tip and indicates that the computed α_{Eff} had no significant impact on results. The results of the BEMT-RHT shows excellent agreement with those of the UVLM-RHT. By comparing the values from the upper subfigure to the lower one, it is found that the discrepancy between the Fr_{Avg} values of each numerical tool is no more than 3%.

In a similar analysis, Figure 4.22 shows the contours of the steady state Fr_{Max} for one steady state rotor revolution. The values predicted by the UVLM-RHT are shown in the upper subfigure while the lower subfigure is for the BEMT-RHT. The Fr_{Max} varies between 1.9 and 3.8 from hub to tip based on the UVLM-RHT calculations. This corresponds to an increase of 32% and 27% more than the Fr_{Avg} values at the same locations.

By comparing the Fr_{Max} values predicted by the BEMT-RHT to those by the UVLM-RHT, an increase of discrepancy is noted. It is found that the results of the former overpredicted those of the latter by almost 7%. This discrepancy is due to the α_{Eff} predicted by each method as the Re calculated by each method is practically the same. As was determined previously, the Fr_{Max} is more sensitive to the α_{Eff} than the Fr_{Avg}. The overpredicted α_{Eff} by the BEMT-RHT compared to that determined by a viscous coupling algorithm in the UVLM-RHT translates into a direct overprediction in Fr_{Max}. However, for the case of the hovering rotor, the two different methods provide similar results in terms of heat transfer.
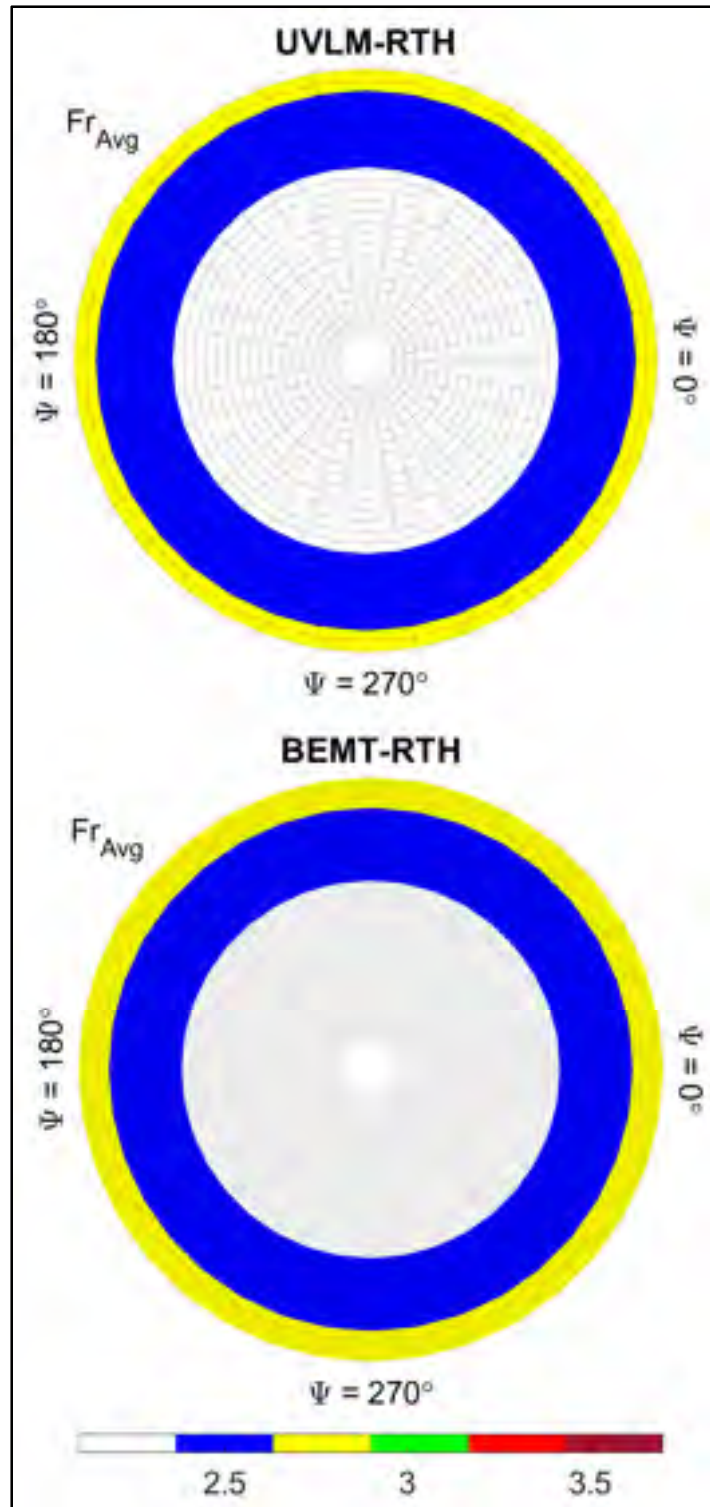
Figure 4.21 Contours of Fr_{Avg} Obtained Using UVLM-RHT & BEMT-RHT for Hovering Rotor
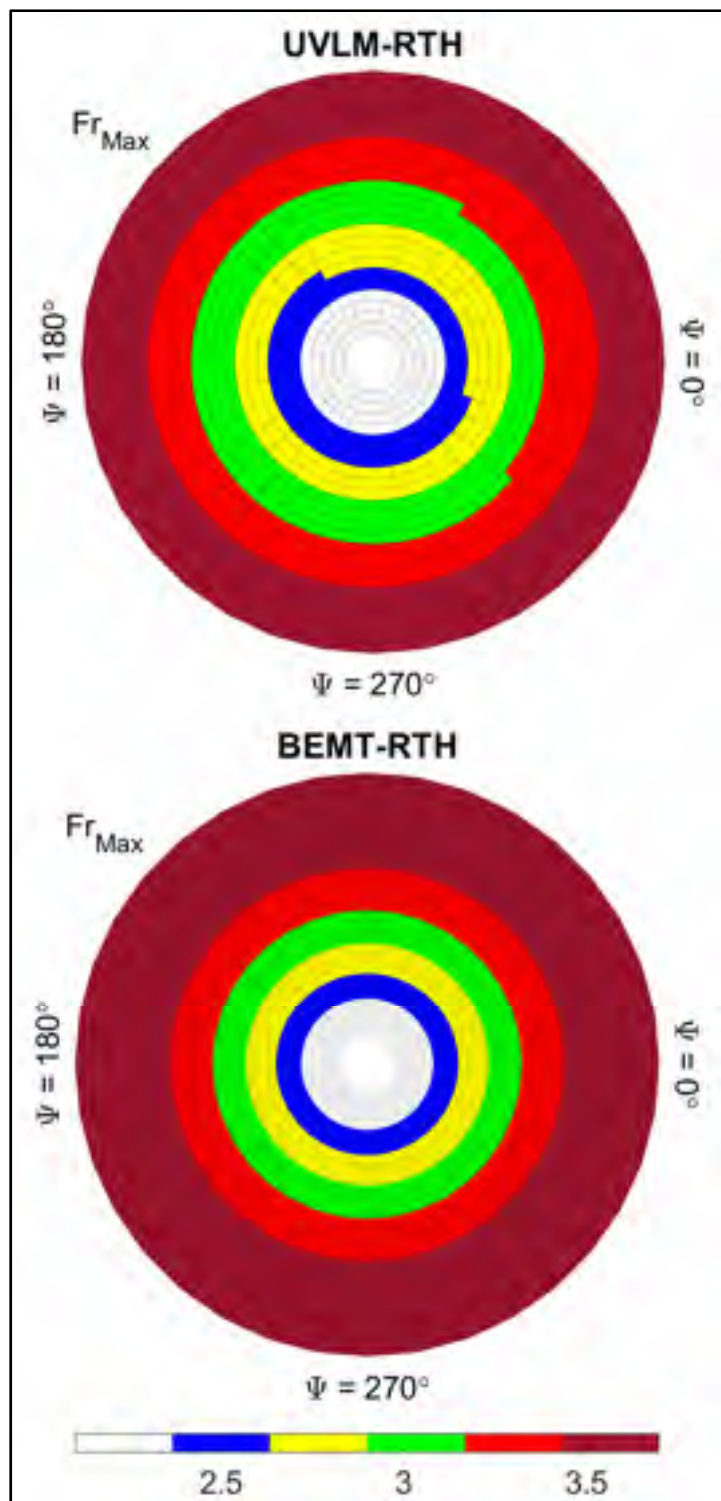
Figure 4.22 Contours of Fr_{Max} Obtained Using UVLM-RHT & BEMT-RHT for Hovering Rotor

4.3.2   Hovering In-Ground-Effect (IGE) Rotor

To understand the changes on blade heat transfer prediction for a rotor close to the ground, the Fr_{Avg} and Fr_{Max} predicted by the UVLM-RHT in ground effect are investigated in this section. The implementation of the BEMT-RHT in this thesis could not account for the ground. The same hovering test case of the modified Bell 429 tail rotor is modeled but with a ground clearance $h/R = 0.52$ to avoid being in extreme ground effect, based on the validation test case of section 4.2.2. Similar to the hovering test case, steady state variations of the wake and C_T are obtained after 20 revolutions, and the computed Re and α_{Eff} at every radial position are used once to calculate the Fr_{Avg} and another time for the Fr_{Max} using the proposed correlations.

Figure 4.23 shows the wake shape obtained by the UVLM-RHT for the four-blade rotor near the ground after 20 revolutions. It is seen that the symmetry of the wake propagation is conserved and the wake shape agrees with the results of (Ferlisi, 2018). However, due to the limited ground clearance below the rotor plane, the wake is seen to stop propagating at $z = 0$ (where the rotor is at $z = h/R = 0.52$) and expands in the X and Y directions while still rolling up into a flattened inverted mushroom shape. A notable difference with the case of the hovering OGE rotor is the greater expansion of the hub wake lattices. It is observed from Figure 4.23 that near the hub of the rotor, the wake lattices grew more than their counterparts when no ground is modeled, also confirmed by the results of (Ferlisi, 2018).

Figure 4.24 shows the contours of the steady state Fr_{Avg} and Fr_{Max} for one steady state rotor revolution of the hovering rotor in ground effect predicted by the UVLM-RHT. At the simulated case of $h/R = 0.52$, the predicted Fr_{Avg} is within 1% discrepancy of that of the hovering OGE rotor from the previous section. The discrepancy for the Fr_{Max} is higher at around 9%. More specifically, the Fr_{Avg} is higher in the OGE test case than it is for the IGE. The inverse is true for the Fr_{Max} where it is higher in the IGE test case than it is for the OGE. For both test cases, the Re is the same since the rotor operates at the speed and temperature. It is suspected that the discrepancy originates from the calculated α_{Eff}.
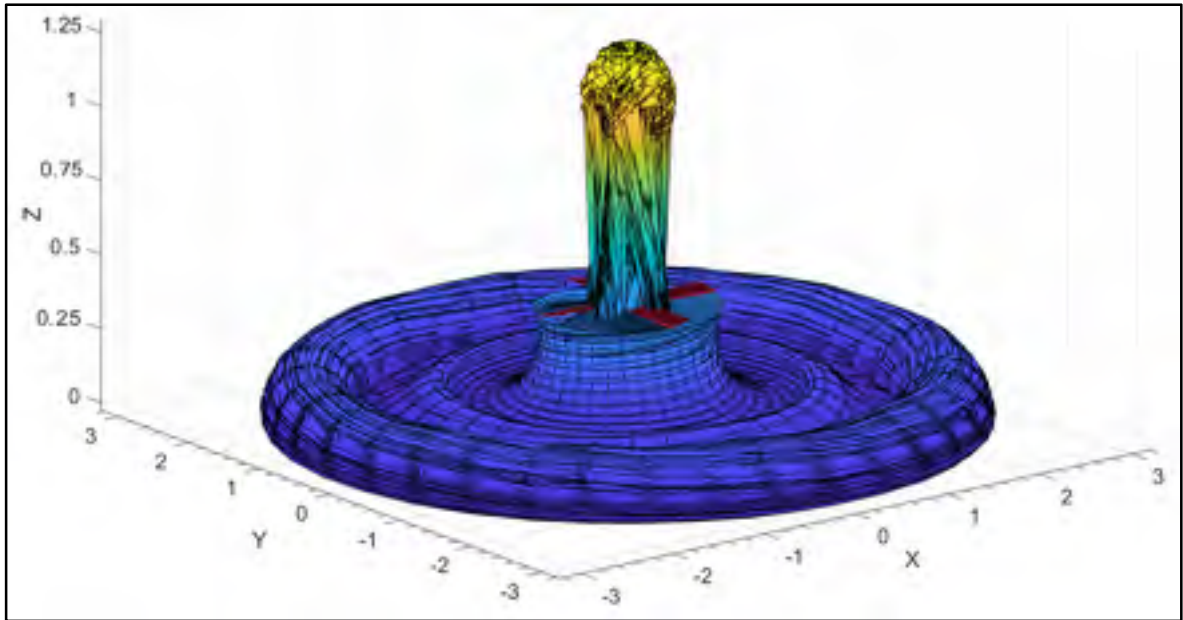
Figure 4.23 Wake Shape Produced by UVLM for the Hovering Four Blade Rotor In
Ground Effect ($h/R = 0.52$)

To verify, the α_{Eff} predicted by the hovering rotor OGE vs. IGE test cases is shown in Figure 4.25. The upper subfigure is for the OGE test case and the lower one is for the rotor IGE. It is determined that the imposed ground clearance causes the α_{Eff} to increase compared to the case when no ground is modeled. It increases by 70% near the tips up to 300% near the hub. This is caused by the stronger wake vortices that originate near the hub for the OGE rotor as is shown in the wake shape figure.

Based on the variations of the Fr_{Avg} and Fr_{Max} presented earlier in the chapter, a higher α_{Eff} will cause the Fr_{Avg} to decrease at the same Re while the Fr on zone 1 (Fr_{Max}) increased. This is clearly translated into the results where the IGE vs. OGE rotors are compared. It is therefore determined that a rotor closer to the ground will cause the heat transfer to decrease overall on the blade sections, but to increase specifically on zone 1 near the L.E..
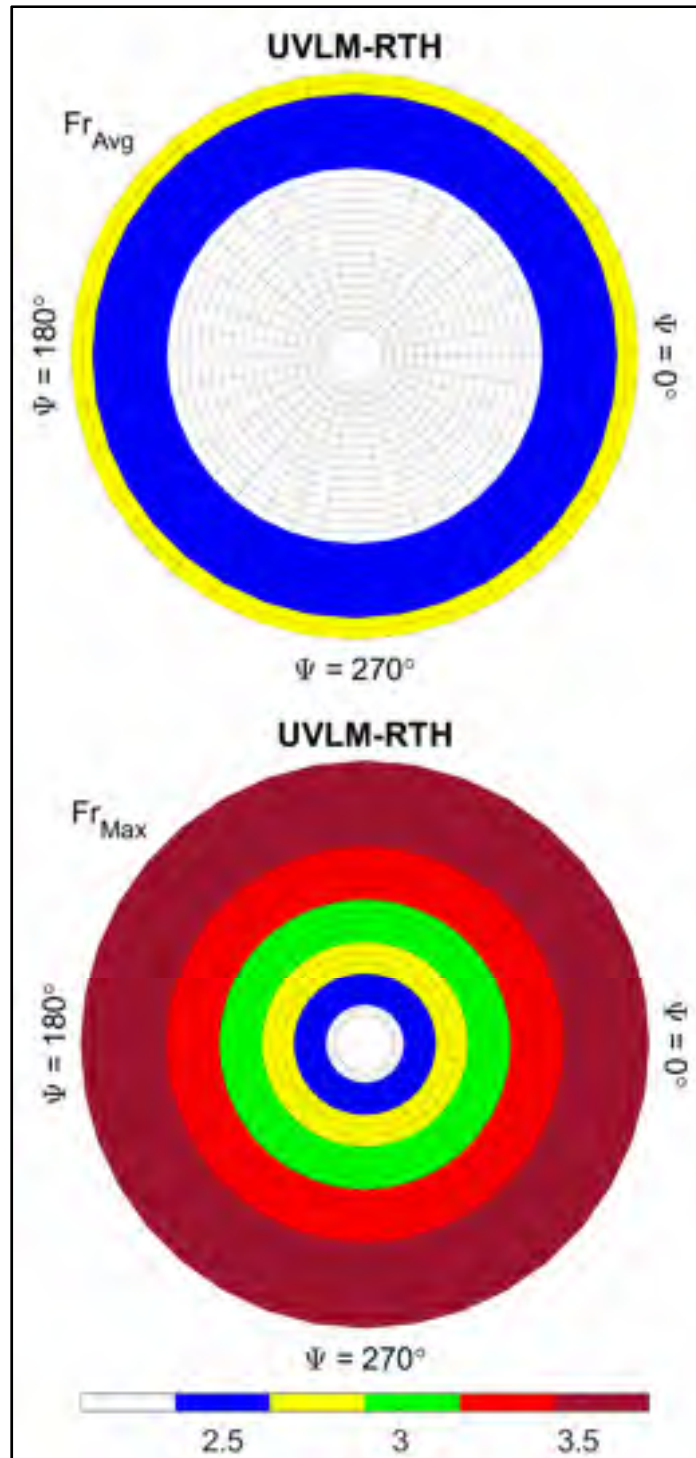
Figure 4.24 Contours of Fr_{Avg} & Fr_{Max} Obtained Using
UVLM-RHT for Hovering Rotor In Ground Effect
($h/R = 0.52$)
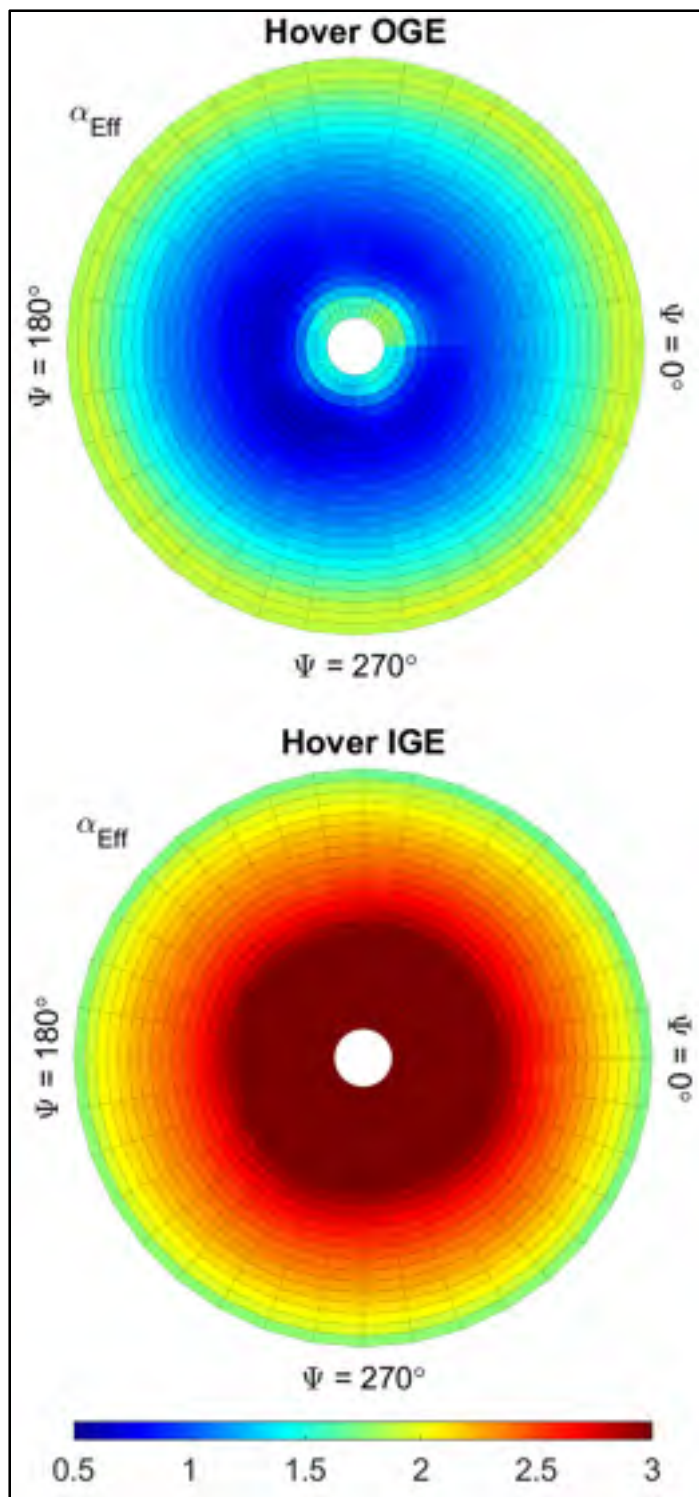
Figure 4.25 Contours of α_{Eff} Obtained Using UVLM-RHT for Hovering Rotor OGE & IGE

4.3.3   Rotor in Axial Flight

The axial flight for a horizontally mounted rotor corresponds to the lateral maneuver of a vertically mounted tail rotor. In both cases, there exists a velocity component perpendicular to the rotor plane that causes a drop in the local blade velocity. The climb ratio is used to determine the ratio of the vertical velocity component W_∞ to the tip speed of the rotor $\Omega \times R_{Tip}$. In this section, the modified Bell 429 tail rotor is modeled with $CR = 5\%$ with the UVLM-RHT. The same climb ratio is used for the BEMT-RHT. The same methodology as the previous test cases is followed to calculate the Fr using equations (4.6) and (4.7).

Figure 4.26 shows the wake shape produced by the UVLM-RHT for the four-blade rotor in axial flight, similar to the one in (Caradonna, 1999). The presented shape is the one corresponding to 18 rotor revolutions. The rotor starts its movement at $z = 0$ and travels to a higher altitude due to the shown vertical freestream velocity W_∞. This also causes the root vortices to be entirely pushed below the rotor plane. As the rotor is climbing, wake elements are produced and shed from the T.E. of the rotating blades. The combination of the translational and rotational velocities of the rotor causes the wake to be elongated yet preserve its symmetry.

Figure 4.27 shows the contours of the steady state Fr_{Avg} predicted by the UVLM-RHT and the BEMT-RHT for the rotor in axial flight. The upper subfigure is for the former and the lower subfigure is for the latter. The vertical velocity component acts perpendicularly to the presented contour and in the out-of-the-page direction.

A symmetric profile of Fr variation is maintained due to the constant W_∞ applied equally at all blade locations. For the UVLM-RHT, the predicted Fr_{Avg} varies between 1.3 and 2.6 from hub to tip. Similar results are obtained by the BEMT-RHT with a 6% discrepancy. Although the wake produced is larger in size than that of the hovering rotor, its effect is diminished as it gets farther from the rotor blades.
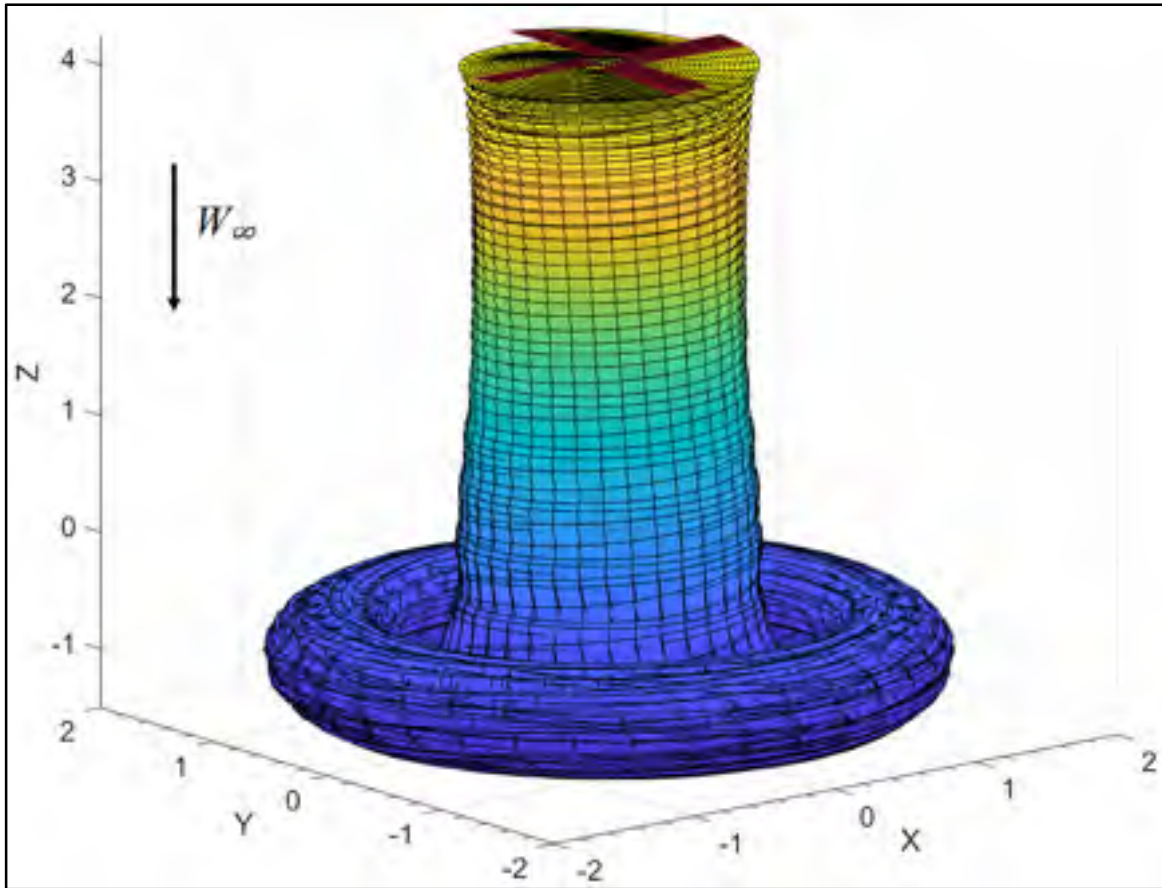
Figure 4.26 Wake Shape Produced by UVLM for the Four Blade Rotor in Axial Flight

For the Fr_{Max} predictions shown in Figure 4.28, the values predicted by the UVLM-RHT are 37% to 42% higher than the Fr_{Avg} of the same method. The BEMT-RHT also predicted heat transfer rates that are within 8% of those of the UVLM-RHT. Comparing these results to those of the hovering test case, the Fr values in axial flight are lower than the hovering rotor at the same Ω. Mainly due to the lower Re associated with the drop by W_{∞}..
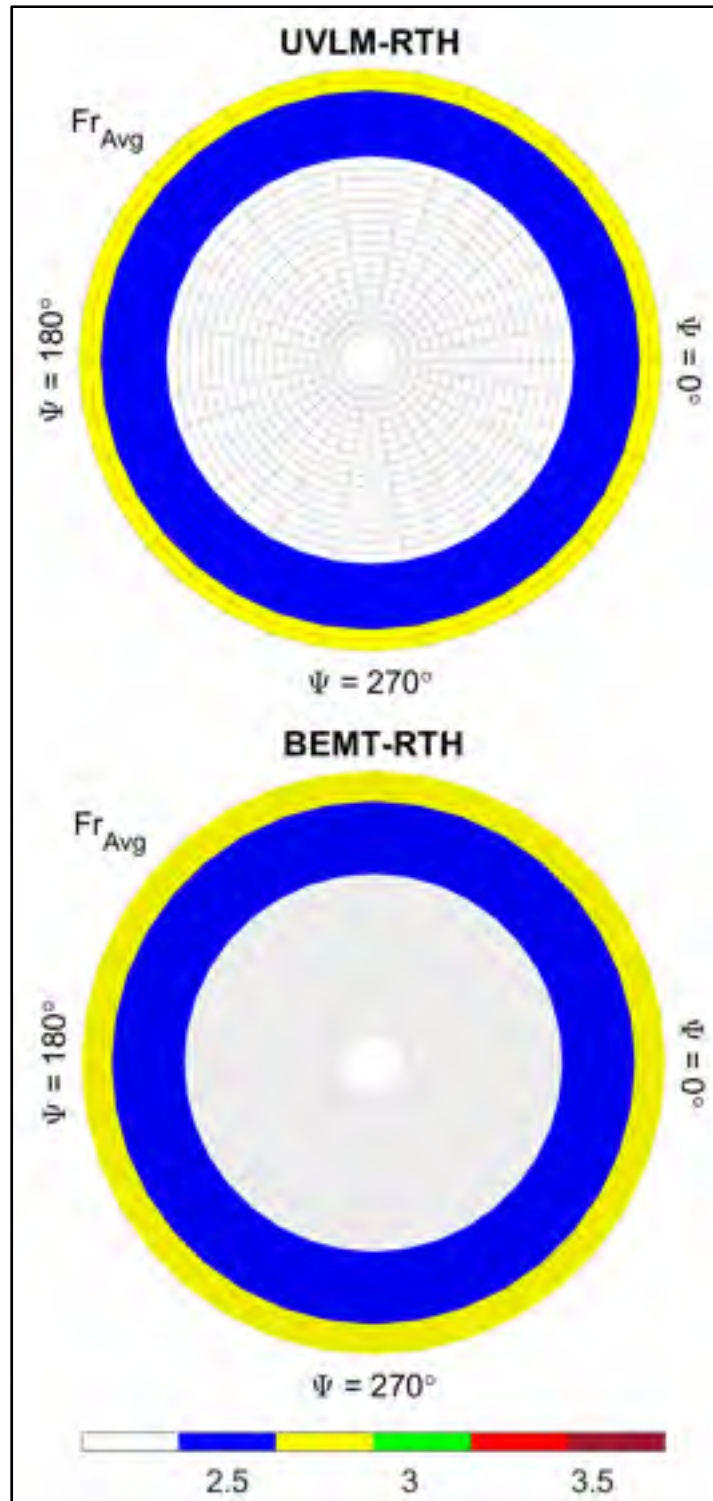
Figure 4.27 Contours of Fr_{Avg} Obtained Using UVLM-RHT & BEMT-RHT for Rotor in Axial Flight (CR = 0.05)
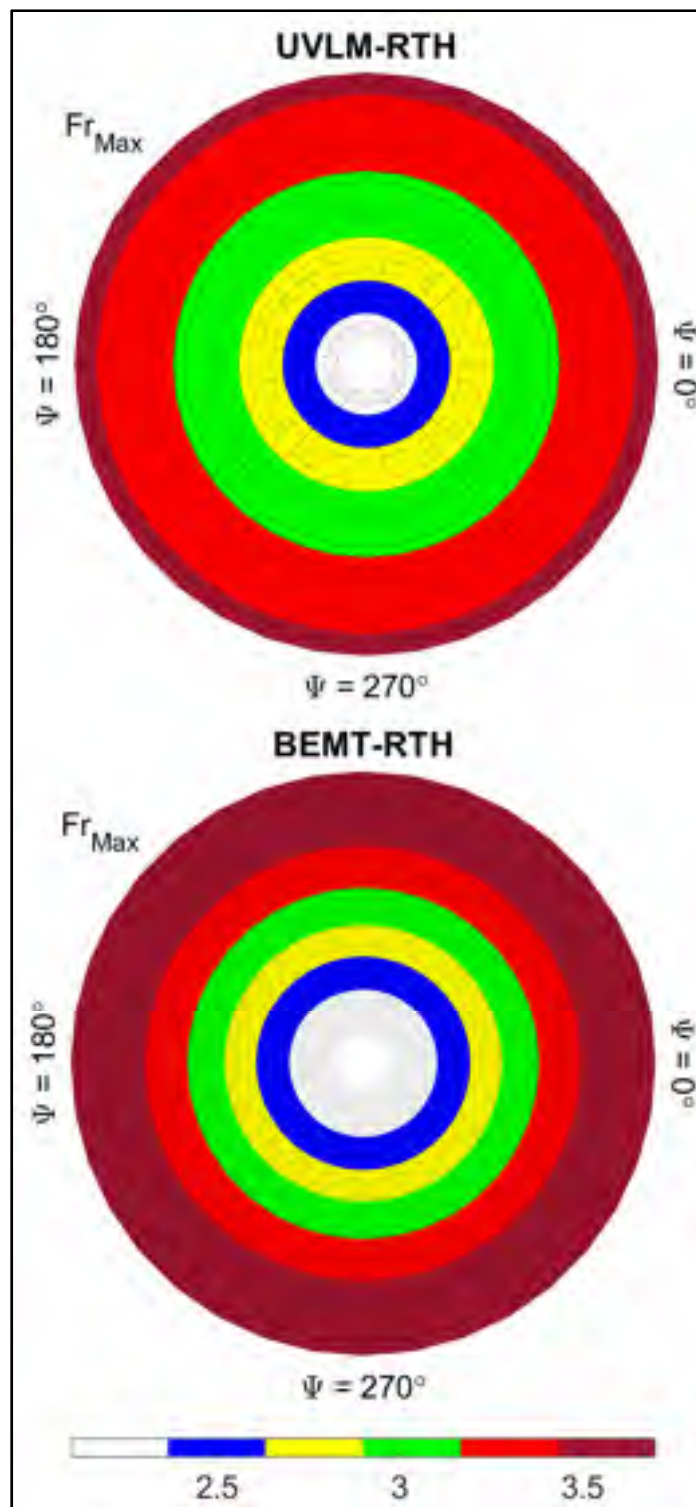
Figure 4.28 Contours of Fr_{Max} Obtained Using UVLM-RHT & BEMT-RHT for Rotor in Axial Flight ($CR = 0.05$)

4.3.4 Rotor in Forward Flight

For the case of forward flight, the rotor is spinning at $\Omega = 2292$ rpm and the advance ratio AR is 10%. The AR is used to determine the ratio of the lateral velocity component U_∞ to the tip speed of the rotor $\Omega \times R_{Tip}$. The modeled AR maintained the maximum Re below 3×10^6 for the sake of validity of Fr correlations. Blade flapping is not modeled for simplicity, so a reverse flow region is expected. The UVLM-RHT is run for 12 revolutions until a steady wake shape is obtained and the steady-state C_T value is reached (changes within $\pm$ 3% between revolutions). For a rotor in forward flight without trim and flapping blades, a dissymmetry of lift exists across the rotor disk due to the presence of advancing and retreating blade regions. More specifically, the local velocity across the blade radius is not only a function of the radius due to rotation but also depends on the Ψ.

Figure 4.29 shows the wake shape produced by the simulated four-blade rotor in forward flight. The wake shown is the one obtained for the 12 revolutions of the simulation. The direction of the freestream velocity U_∞ due to the forward motion of the rotor is indicated by the arrow in the figure and the positions of the reference angles of Ψ are indicated. The wake shape agrees with what is expected of a rotor in forward flight, compared to the literature of similar geometries and analyses (Gennaretti, Bernardini, Serafini, & Romani, 2018; Tan & Wang, 2013a). The roll on the edges of the wake as well as the descent of the wake due to the rotor downwash are noted, which is expected in similar flight conditions. The trailing wake behind the advancing blade is seen expanding more than that produced by the retreating blade, producing an asymmetric wake. There is also an instance where the blade and the wake interact, this is seen at $\Psi = 270°$ when the advancing blade comes into contact with the wake of the other blade.

Figure 4.30 shows the steady state contours of the Re and α_{eff} for the simulated rotor. The direction of the incoming freestream velocity due to the forward motion of the rotor is indicated by the arrow in the figure. The Re contour of Figure 4.30 showed that the retreating side of the blade, where the local blade velocity decreased, is between for $90° < \Psi < 270°$ and the

advancing side, associated with an increase in the local blade velocity, is between $270° < \Psi < 90°$. The maximum Re is at $\Psi = 0°$ (where the tip velocity is maximum) and the minimum is at $\Psi = 180°$. The tip velocity is exactly equal to $\Omega \times R_{Tip}$ at $\Psi = 90°$ and $\Psi = 270°$.
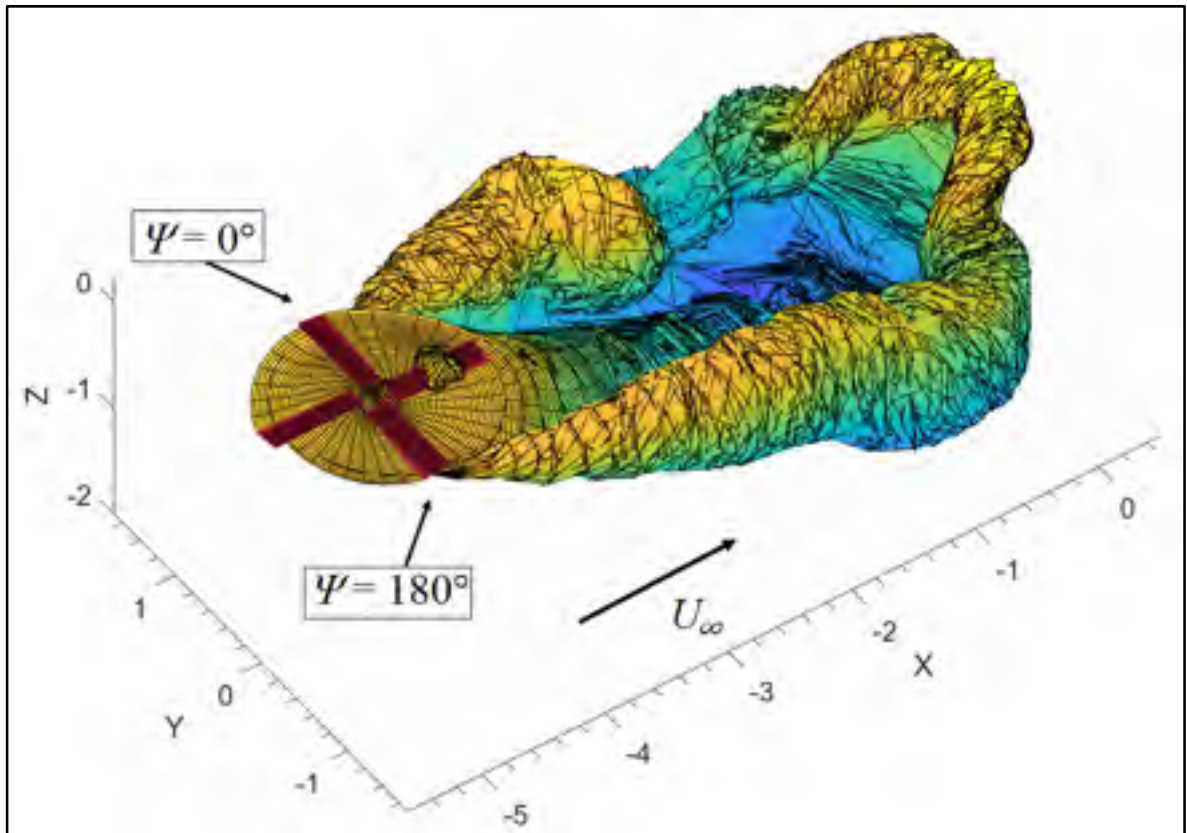
Figure 4.29 Wake Shape Produced by UVLM for the Four Blade Rotor in Forward Flight

The α_{Eff} on the upper side of Figure 4.30 is determined using the viscous coupling algorithm. The highest values are seen in the quadrant between $270° < \Psi < 0°$ in the advancing blade region that moves away from the trailing wake. Considering the very low values of α_{eff} ($\approx 0°$) at the other Ψ, the symmetric airfoil profile used indicates that the majority of the rotor forces will be generated in the quadrant where α_{Eff} is maximum, representing a dissymmetry of lift.
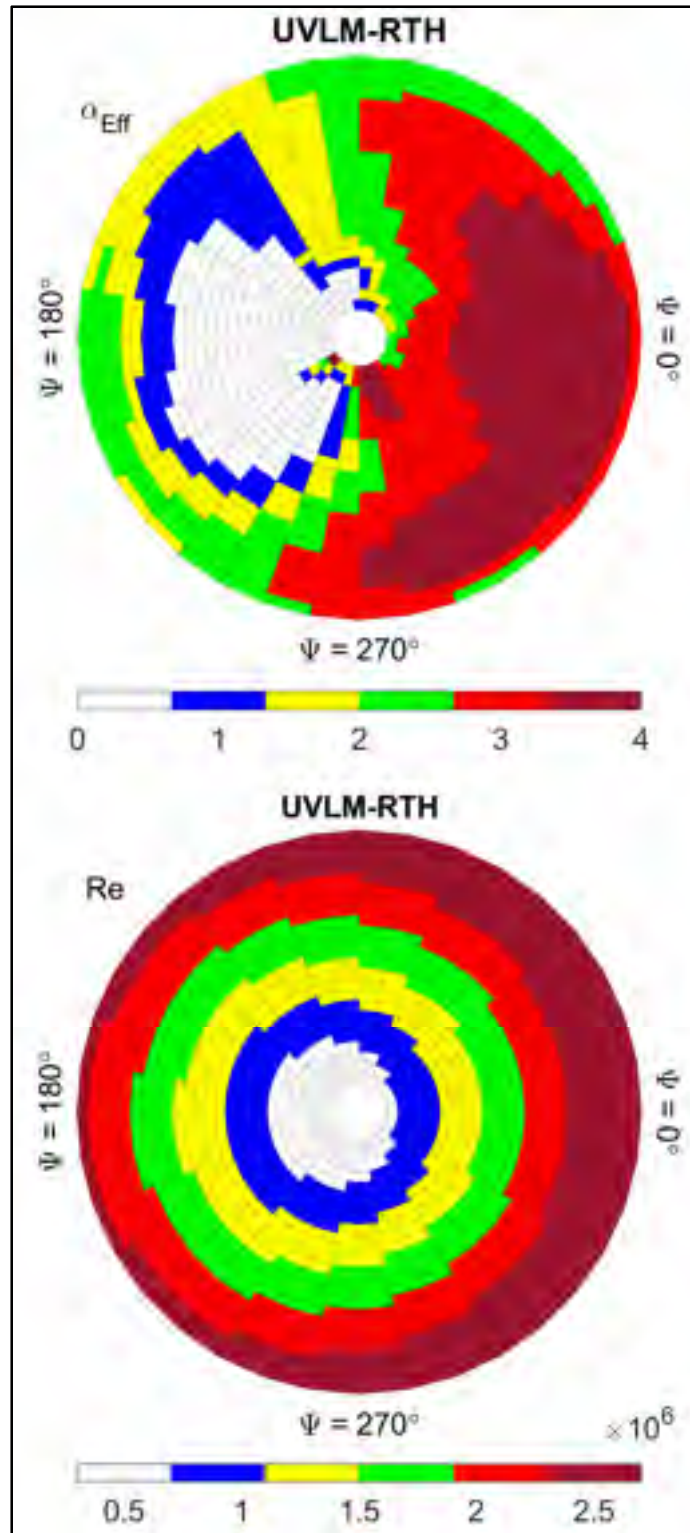
Figure 4.30 Contours of α_{Eff} & Re Obtained Using
UVLM-RHT for Rotor in Forward Flight ($AR = 0.1$)

Finally, Figure 4.31 shows the steady state contours of the Fr_{Avg} and Fr_{Max} for the simulated rotor in forward flight. The two shown azimuth angles, $\Psi = 0°$ and $\Psi = 180°$, correspond to the points where the local tip blade velocity is respectively at a maximum and a minimum. The blades are rotating in the counterclockwise direction from $\Psi = 0°$ to $\Psi = 180°$.

In the upper side of the figure, the predicted values of Fr_{Avg} varied between a minimum of 0.85 near the hub on the retreating blade ($\Psi = 180°$) and a maximum of 2.8 on the tip of the advancing blade ($\Psi = 0°$). In general, the contour of Fr_{Avg} values in forward flight is shifted to the side of the retreating blade compared to the symmetric Fr_{Avg} contours predicted for the case of the hovering rotor. The highest Fr_{Avg} values are seen in the region of the advancing side mainly due to the higher velocities compared to the retreating side, indicating that the Re has a stronger influence than the α_{Eff} on the Fr_{Avg}.

On the contrary, the Fr_{Max} seems to be more influenced by the α_{Eff} than the Re. This is shown in the lower side of Figure 4.31, the highest values are also predicted in the advancing side of the blade. However, they are more concentrated to the quadrant between $270° < \Psi < 0°$, in accordance with the α_{Eff} values from Figure 4.30. Although the influence of the Re on the Fr calculation is more significant, the higher α_{Eff} in that quadrant along with the varying local blade speed due to the forward motion causes a significant change in the Fr_{Max}. The Fr_{Max} values varies between a minimum of 1.25 near the hub on the retreating blade ($\Psi = 180°$) and a maximum of 4.2 on the tip of the quarter revolution quadrant. This corresponds to a 47% to 50% increase compared to the Fr_{Avg} values at the same locations.
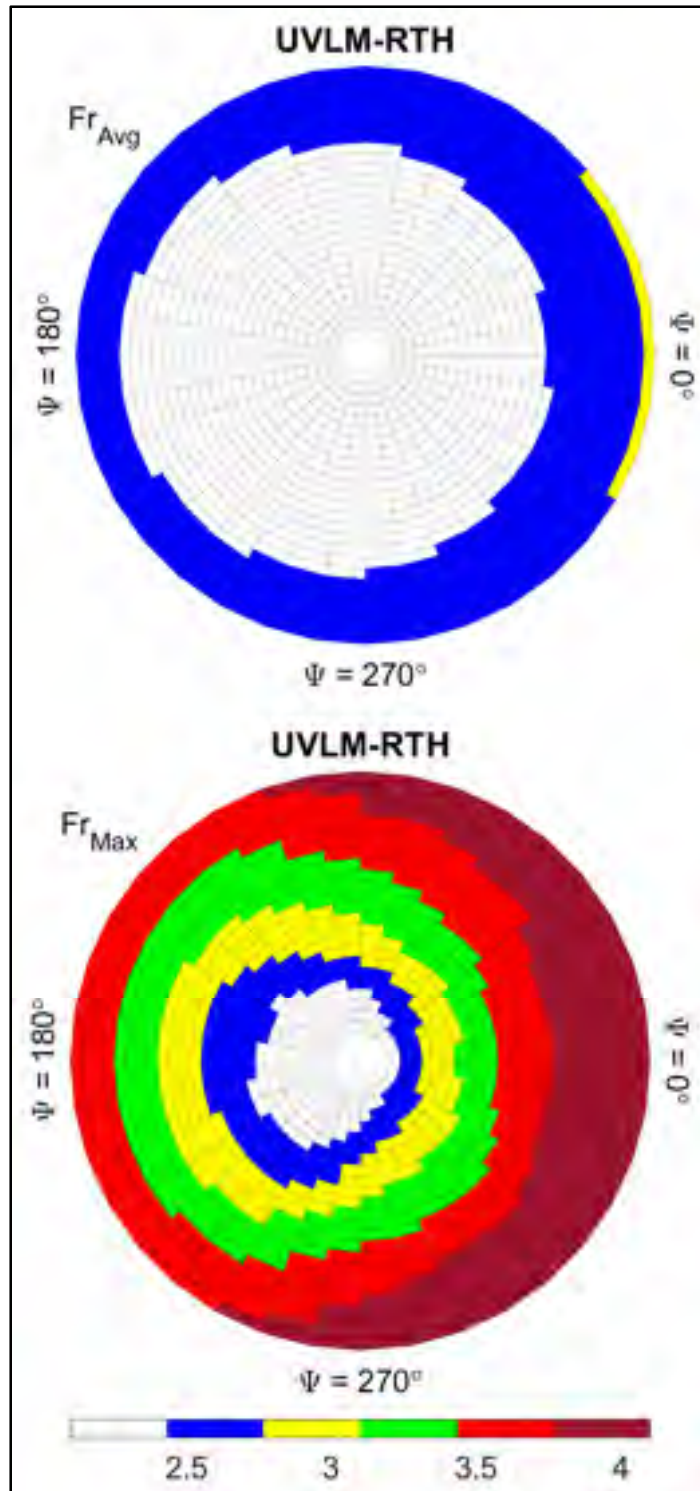
Figure 4.31 Contours of Fr_{Avg} & Fr_{Max} Obtained Using
UVLM-RHT for Rotor in Forward Flight ($AR = 0.1$)

4.3.5   Discussion

In order to directly compare the Fr_{Avg} and Fr_{Max} values predicted by the UVLM-RHT and BEMT-RHT, the heat transfer variation with r/R is compared here based on the results of the sections 4.2.1 and 4.2.3. Figure 4.32 shows a comparison between the predictions of the two methods, in terms of the calculated Fr_{Avg} and Fr_{Max} versus r/R. The upper subfigure is the hovering rotor test case while the lower one is for the axial flight test case.

For the case of the hovering rotor, the BEMT-RHT and UVLM-RHT predicted similar results for the Fr_{Avg} and Fr_{Max}, within $\pm 1.5\%$ discrepancy for the former and $\pm 4\%$ for the latter. Since the Re predicted by each method is the same, the source of the discrepancy comes from the α_{Eff} calculation by each method. A similar finding was seen when the axial flight test case is examined. Both methods predict Fr_{Avg} values that are within $\pm 1\%$ of each other, but a larger discrepancy is seen for the Fr_{Max}. The BEMT-RHT shows Fr_{Max} values up to 7% lower before $r/R = 0.5$, compared to the UVLM-RHT, and up to 8% higher afterwards.

The BEMT-RHT showed better agreement with the UVLM-RHT in terms of the heat transfer predictions than it did when the aerodynamic performance was modeled in sections 4.2.1 and 4.2.3. The hovering and axial rotor test cases showed discrepancies up to 15% in the calculated C_T and FM between the BEMT and UVLM. This was not the case for the Fr_{Avg} and Fr_{Max}. Although the UVLM-RHT is more complicated to solve and takes longer computing time than the BEMT-RHT, the similarity of heat transfer results is remarkable.

To get another view on the heat transfer variation on the rotor in different flight modes, the Fr_{Avg} and Fr_{Max} on specific r/R and Ψ are now compared based on the results of the sections 4.2.1, 4.2.2, 4.2.3 and 4.3.4. Since the BEMT-RHT and UVLM-RHT have previously been compared, and since only the UVLM-RHT could model the four different flight modes, only the results of the latter are investigated.
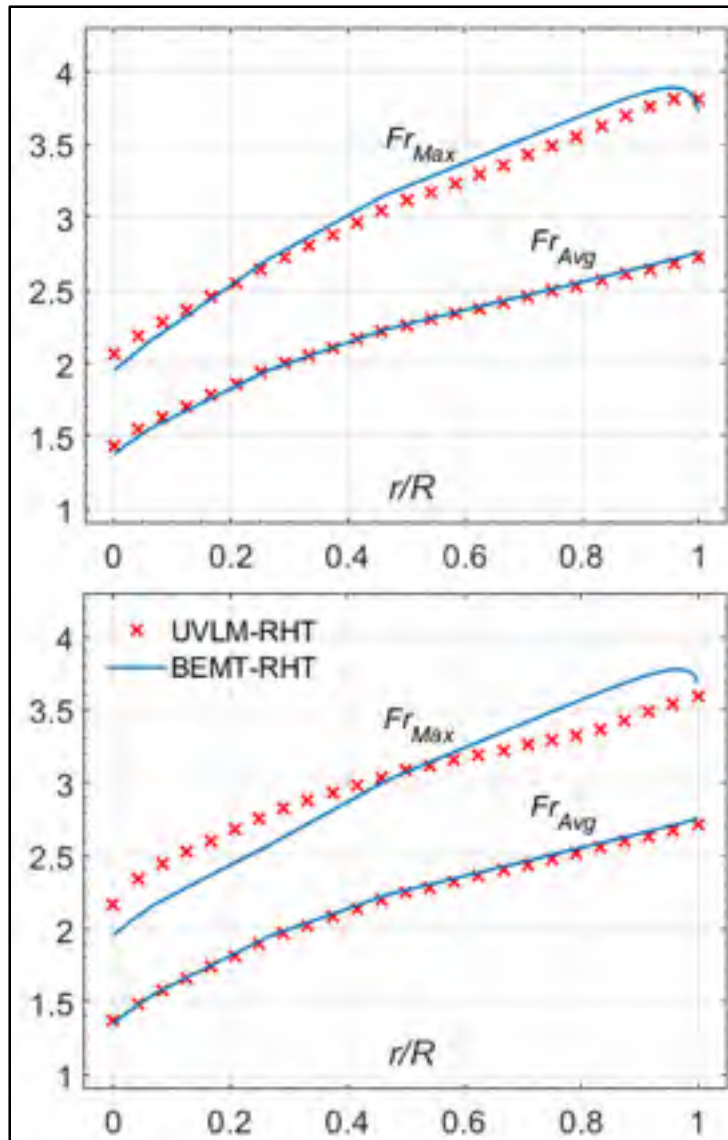
Figure 4.32 Comparison of the Fr_{Avg} & Fr_{Max} Calculated
by the BEMT-RHT & UVLM-RHT for Hovering Rotor
(Upper) or Axial Flight (Lower)

Figure 4.33 shows a comparison of the variation of the Fr_{Avg} and Fr_{Max} calculated across the blade radius r/R for the modified Bell 429 rotor. The upper subfigure compares the Fr_{Avg} from the four flight conditions presented earlier while the bottom one shows a similar representation of the Fr_{Max}. For simplicity and throughout this section, the term "hovering rotor" will refer to the OGE hovering test case and "IGE" will refer to the hovering rotor in ground effect.
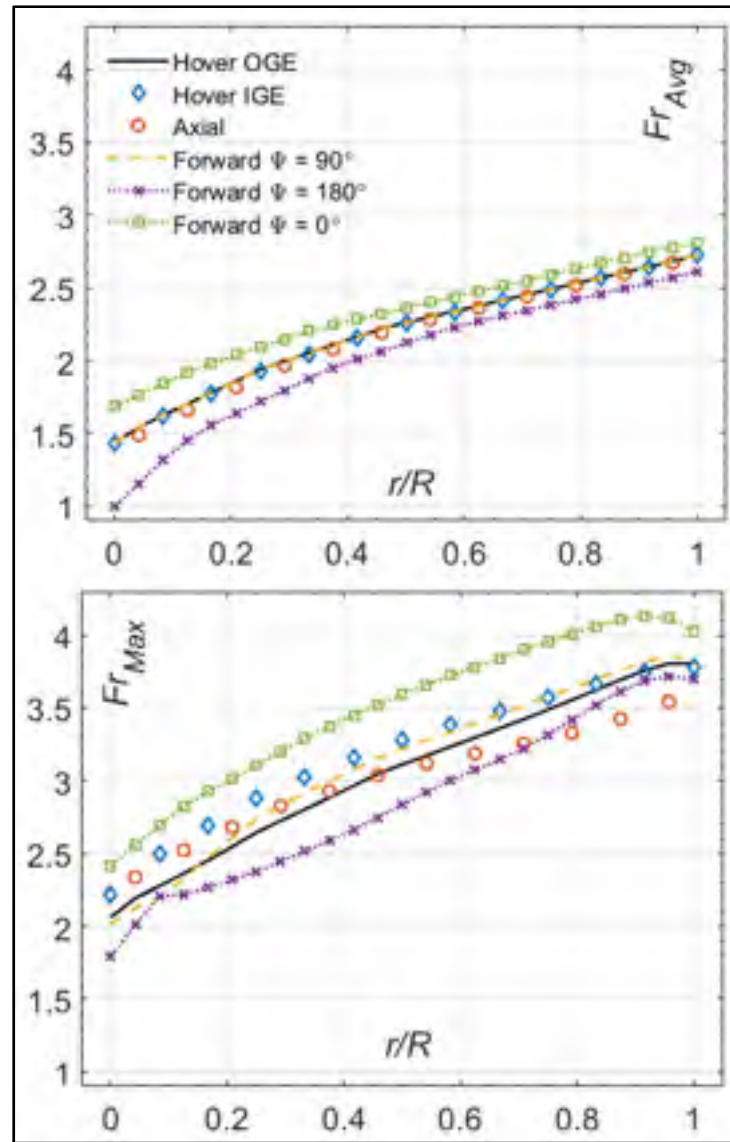
Figure 4.33 Comparison of the Fr_{Avg} & Fr_{Max} Calculated
by the UVLM-RHT for Hovering Rotor, IGE Rotor, Axial
Flight and Forward Flight at Three Different Ψ

Based on the results of Figure 4.21, Figure 4.24 and Figure 4.27, the Fr_{Avg} did not change between the different Ψ for the rotor in hover, IGE or axial flight. A similar conclusion can be drawn for the Fr_{Max} based on Figure 4.22, Figure 4.24 and Figure 4.28. Therefore, only the values at $\Psi = 0°$ are plotted in Figure 4.33 for the rotor in hover, IGE or axial flight. The case of forward flight at $\Psi = 90°$ is also added for comparison. At that Ψ, the local velocity of the blade is only due to rotation and the forward speed has no impact.

The results of Figure 4.33 show that the Fr_{Avg} is almost the same regardless of the flight condition, a discrepancy up to 5% however is found. Compared to the hovering test case, the IGE test case had lower Fr_{Avg} within 1% for all r/R. The IGE introduces no changes to the Re on the blade, so the discrepancy between the OGE and IGE rotors is mainly due to the higher α_{Eff}. This originates from the proximity to the ground as is shown in Figure 4.25. The higher α_{Eff} is also responsible for the 9% higher Fr_{Max} for the IGE compared to the hovering rotor, as seen in Figure 4.33. In the previous analysis, Figure 4.13 showed that the Fr_{Max} increases with an increasing α_{Eff} while Figure 4.12 showed that the Fr_{Avg} decreases. Therefore, although the Re between the IGE and hovering rotor is the same, the Fr_{Max} at the L.E. of the blade is 9% different due to a different α_{Eff}. The Fr_{Avg} is less influenced by the α_{Eff} and is almost the same.

The axial flight with $CR = 5\%$ shows Fr_{Avg} up to 5% lower than the hovering rotor, especially near the hub, as shown in Figure 4.33. The axial motion of the rotor causes the blade Re to drop, thus explaining the higher discrepancy to hovering rotor compared to the IGE. The Fr_{Max} in axial flight is up to 7% higher than that in OGE hover before $r/R = 0.5$ and up to 7% lower afterwards. While the lower Re is to blame for the reduction in Fr_{Max} for $r/R \geq 0.5$, the higher values for $r/R \leq 0.5$ are a direct result of an increased α_{Eff}.

When the blade of the rotor in forward flight is at $\Psi = 90°$ (or $\Psi = 270°$), the forward speed had no effect on the Re. This translates to a match between the Fr_{Avg} in hover and that in forward flight at the considered Ψ, as seen in Figure 4.33. The Fr_{Max} is also slightly higher, up to 5%, mainly due to a slightly higher α_{Eff} as seen in Figure 4.30. There is more to consider for the rotor in forward flight, especially when other Ψ are examined. When the blade is at $\Psi = 180°$ and the local blade velocity is minimum, the Fr_{Avg} drops by as much as 25% compared to the hovering rotor and by around 14% for the Fr_{Max}. In the advancing region of the blade and at $\Psi = 0°$, the inverse is true and the Fr_{Avg} and Fr_{Max} are up to 17% and 19% higher than the corresponding values for the hovering rotor.

Based on the previous analysis, it is determined that the Fr_{Avg} varied slightly between the studied test cases of the hovering rotor, ground effect and axial flight with $CR = 5\%$. When examined based on the variation with Ψ (sections 4.2.1, 4.2.2, 4.2.3 and 4.3.4), the Fr_{Avg} for each the three mentioned flight conditions showed consistent values between the different azimuthal angles. Moreover, when the variation of the Fr_{Avg} in the radial direction is compared between the different flight conditions, similar results are obtained, and the largest discrepancy is around 5%. The only significant change in Fr_{Avg} values is seen in the case of forward flight, where the heat transfer rates varied with both the radial direction and the azimuth angle.

While calculating the Fr_{Avg} on each blade element is helpful in determining the average heat transfer rates, it has also proven somewhat misleading. While the Fr_{Avg} showed little changes between the different flight conditions, the latter have a significant effect on the Fr_{Max}. The IGE rotor showed Fr_{Max} values 9% higher than those of the hovering rotor, compared to less than 1% change in Fr_{Avg}. Similarly, the Fr_{Avg} and Fr_{Max} on the blade of the vertically travelling rotor are 5% and $\pm$ 7% different than the hovering test case. Finally, for the rotor in forward flight, the Fr_{Max} values are $\pm$ 19% those in hover compared to $\pm$ 5% for the Fr_{Avg}.

4.4   Conclusion

This chapter presented the results corresponding to the numerical component of this thesis. Regarding airfoil heat transfer, CFD simulations using *SU2* on a flat plate test case verified the predicted C_f and Fr are within 92% to 98% agreement with correlations from the literature. When the Fr from CFD is compared to similar implementations of the *S-A* turbulence model from the literature, the discrepancy was around 2%. Comparisons of NACA 0012 CFD results to flat plate correlations indicated an agreement within 80% to 95% in Fr values up to a $Re = 1 \times 10^6$. The Fr values of the NACA 0012 CFD at the stagnation point agreed within 8% of experimental cylinder and NACA 0012 data. The main finding however is the correlations of section 4.1.2.8 that calculate the Fr_{Avg} and Fr_{Max} based only on the Re, α_{Eff} and the Pr.

The implemented BEMT and UVLM are validated against rotor aerodynamic performance experiments from the literature. The implemented BEMT predicted C_T and C_{Ly} values 15% to 20% higher than experiments for a hovering rotor, typical to the BEMT whereas the UVLM provided 98% agreement. The *TVAL* & *TVRL* by the UVLM agreed within 90% a rotor in ground effect and axial flight, although a larger discrepancy was seen in extreme ground effect. The UVLM is also validated within 75% compared to experiments results of a forward flight test case although 87% agreement with a free wake method from the literature is noted.

The main contribution of this research, the BEMT-RHT and UVLM-RHT, are used to quantify the steady state radial distribution of the Fr_{Avg} and Fr_{Max} on a modified version of the Bell 429 tail rotor. The rotor is modeled in four different flight conditions. It is found that the Fr_{Avg} predicted by the BEMT-RHT and the UVLM-RHT is within 1% for both the hovering test case and axial flight. The Fr_{Max} shows a higher discrepancy between 4% to 8% due to a difference in the computation of α_{Eff} by each method. Although both methods provided relatively quick results, the BEMT-RHT takes a fraction of the simulation time compared to the UVLM-RHT.

The Fr_{Avg} variation in the radial direction was almost the same for the rotor in hover, IGE, axial flight or when the blade is at $\Psi = 90°$ or $\Psi = 270°$ in forward flight. The highest discrepancy is 5%, found for the case of axial flight near the rotor hub. When the blades of the rotor in forward flight hit the maximum velocity of the advancing region, the Fr_{Avg} increases by around 17%. Similarly, when the minimum velocity of the retreating region acts on the blade, the Fr_{Avg} decreases by as much as 25%.

The differences in the calculated Fr_{Max} are more remarkable. The proximity to the ground increased the α_{Eff} of the hovering rotor, causing the Fr_{Max} to increase up to 9% compared to the hovering rotor with no ground effect. Similarly, the rotor in axial flight showed a different α_{Eff}, leading to a difference of $\pm$ 8% in Fr_{Max}. Finally, as the blades of the rotor in forward flight change their azimuthal positions, the Fr_{Max} is impacted by a range of 14% decrease and 19% increase in values, compared to the hovering rotor.

CHAPTER 5

EXPERIMENTAL RESULTS

This chapter presents the results of the experimental component of this thesis, based on the methodology of Chapter 3. The first objective of the chapter is to verify the results of experimental work that measured the heat transfer on a fixed wing with a NACA 0012 profile. The second objective is regarding the experimental work that measured the heat transfer on a 2-blade rotor with a NACA 0012 blade shape and the verification of its results. The final objective is to validate the results of the BEMT-RHT and the UVLM-RHT to those measured experimentally on the 2-blade rotor.

Starting with the fixed wing experiments, the section begins with a quantification of the total experimental error based on the analysis of (Moffat, 1988) as well as based on the randomness error of test repetitions. The validation process is done first on the measured Fr_x values on the stagnation point at $\alpha = 0°$. These are compared to previous experimental data for a NACA 0012 as well as the CFD simulations. Next, the variation of the Fr_x in the chordwise direction of the NACA 0012 is compared to that predicted by CFD as well as similar measurements from the literature for a BO 28 airfoil. In order to numerically compare the variation of the measured Fr_x to CFD results, the data from either method are correlated based on an Fr_x variation with Re^m, where m is determined by curve fitting. Finally, the limitations of the experiments as well as a discussion are laid out.

The other half of the chapter is dedicated for the rotor heat transfer experiments. The section begins with an estimate of the total experimental error based on the same method used for the fixed wing experiments. Results of the experiments are then verified in terms of the variation of the Fr_x in the radial as well as the chordwise direction. This is done for both cases of a non-lifting ($\theta = 0°$) and lifting ($\theta = 6°$) rotor. Later, the 2-blade rotor is replicated in the BEMT-RHT and the UVLM-RHT and the heat transfer predicted by the two numerical tools is compared to the results of the experiments.

5.1 Fixed Wing Heat Transfer Experimental Results

The fixed wing experiments (Figure 3.3) are done on a NACA 0012 profile whose wall is almost 90% covered with heating elements that operated at a constant Q_S TBC. Four angles of attack are tested, and they are $\alpha = 0°$, $\alpha = 5°$, $\alpha = 10°$ and $\alpha = 15°$. The windspeeds are adjusted to provide a range of Re between $1 \times 10^5 \leq Re \leq 1.4 \times 10^6$. 10 RTDs are distributed on the surface to provide measurements at different locations across the chord.

The results of those tests are presented in the form of the Fr_x as well as the Fr_{Avg}. The 10 datapoints across the surface made the calculation of the average value of heat transfer possible. It also made it possible to compare the predictions from the fully turbulent CFD simulations in both its local and average values. As will be seen in the following sections, it is suspected that transitional effects strongly influenced the behavior of the flow and the subsequent calculation of the heat transfer.

The results of the Fr_x variation are also supported by the figures of APPENDIX II. The latter show the steady-state results of the difference between the temperature of the air in the IWT and the temperatures measured by the RTDs, the temperature difference is referred to as ΔT_x. With the same range of Re of Figure 5.7 and Figure 5.8, the ΔT_x is presented at $\alpha = 0°$ (Figure II-1), $\alpha = 5°$ (Figure II-2), $\alpha = 10°$ (Figure II-3) and $\alpha = 15°$ (Figure II-4).

5.1.1 Experimental Error

Based on the methodology of section 3.4.5, the measurements error due to temperature measurements, voltage fluctuations and current fluctuations is determined by equation (3.16) and is found to be 5.3%. On the other hand and for the randomness error calculation, most of the tests at $\alpha = 0°$, $\alpha = 5°$ and $\alpha = 10°$ are repeated at least twice for all Re, whereas only 3 tests at $\alpha = 15°$ are repeated. For $\alpha = 0°$, the repeated tests have different T_∞ where one set had $T_\infty = 263.15$ K and another set had $T_\infty = 273.15$ K. At all other α, the same conditions are set between

repeated runs. Some tests had three runs to avoid the phenomenon of tunnel heating that is encountered during some tests.

At wind speeds around and higher than 60 m/s, in the range of $Re \approx 9 \times 10^5$ and more, the IWT is incapable of maintaining a constant freestream T_∞. This caused the T_∞ to increase during the test ending up for some tests at 6 K to 7 K higher than the start of the test. By analyzing the results found in terms of the Fr calculations, it is found that tunnel heating is the major contributor for large discrepancies (up to 40%) between repeated runs. To overcome this problem, two steps are taken. First, the tunnel compressor is set to a much lower operating temperature to try to maintain the circulating air at the desired T_∞. Second, the test duration at high speeds ($Re \geq 9 \times 10^5$) is shortened. When the results of all tests are examined, it is found that the Fr values usually reached their steady-state values at the 300 seconds mark and a test of 600 or 900 seconds is unnecessary especially at high speeds.

The results of the randomness error are shown in Figure 5.1. The figure shows the variation of the error percentage between one test and the other as a function of the test calculated Re. In the figure, the comparison is made between two repeated tests from Table 3.4. In the case when tunnel heating is encountered and a test is repeated three times, the figure only shows the results of repeated tests with shortened test duration (with no tunnel heating).

Figure 5.1 shows that the discrepancy between the different runs of the same tests generally increased as the Re is increased up to $Re = 9 \times 10^5$. The randomness error varies between 2% at the lowest Re and the maximum is 12.3% at $\alpha = 0°$ and $Re = 9 \times 10^5$. Keeping in mind that the tests are at $\alpha = 0°$ had different T_∞, the discrepancies of those tests are consistent with the results of the repeated tests with the same T_∞ at $\alpha > 0°$. It is concluded that there is no significant effect on the randomness error caused by a change of T_∞, confirming that the T_∞ did not have an effect on the non-dimensional calculation of the Fr.

There is one more source of error that is found for the tests at $Re \geq 6 \times 10^5$. As will be explained in the next section, the lack of conduction tests for those Re gives an added uncertainty of 5%

to the tests with $Re \geq 6 \times 10^5$. Between the measurement error and the randomness error, the total experimental error of the fixed wing experiments with $Re \leq 6 \times 10^5$ is set at 17.5%. For the tests with $Re \geq 6 \times 10^5$, the total experimental error is 22.5%.
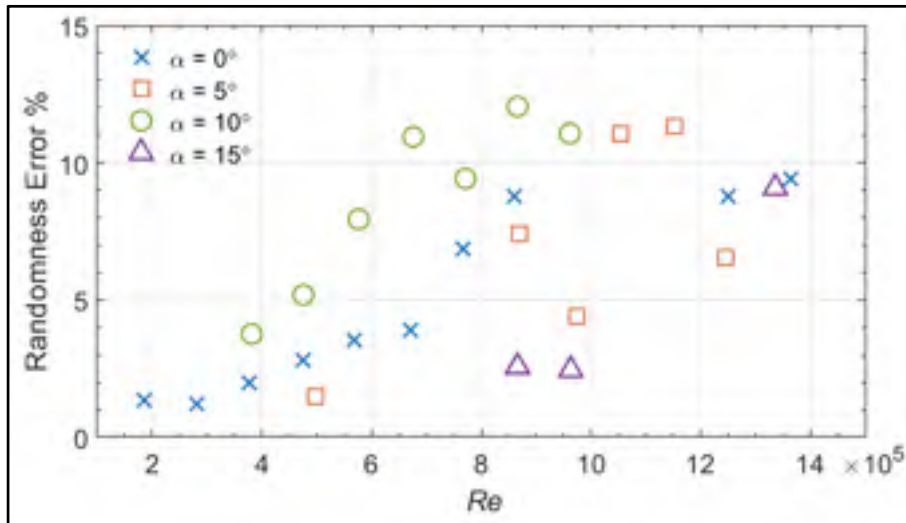
Figure 5.1 Fixed Wing Randomness Error for Tests at Different α and Re

5.1.2   Conduction Losses

This section investigates the results of the tests done on the fixed NACA 0012 to determine the amount of heat lost to conduction inside the wing aluminum body. By measuring the temperature difference between the outer and inner sides of the airfoil skin, the conductive heat transfer is determined based on the thickness of the aluminum and heating elements. Data from the literature indicate that the average conduction loss was between 2% and 13% of the electrical power supplied in the work of (Poinsatte, 1990) and around 2% in the work of (Li et al., 2009). Both works used polished heated tiles embedded in the airfoil surface surrounded by insulating material to prevent heat from dissipating into the rest of the wing that is not heated. Whereas the experiments of this work used a hollow, closed edges, NACA 0012 whose surface is almost completely covered with heating elements, except a small portion almost 6% of the chord long that is left unheated but covered with insulating tape.

Figure 5.2 shows the results of the conduction tests done on the NACA 0012 corresponding the RTD locations as described in Figure 3.5. The results are presented in the form of the ratio of the calculated conduction Q_{Cond} to the supplied electrical heating power Q_{Elec}. The conduction here represents the heat lost in the wing inner aluminum material. The upper subfigure is for the test at $\alpha = 0°$ whereas the lower subfigure is for $\alpha = 10°$. The data are shown for each RTD location S/c and with the varying Re.
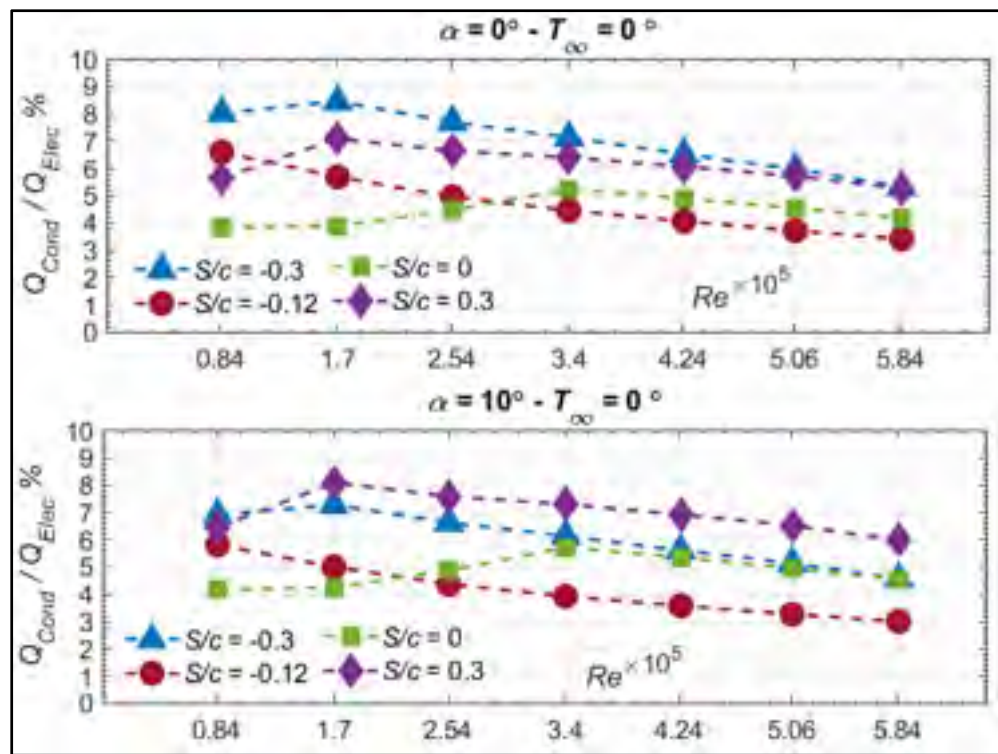
Figure 5.2 Ratio of Heat Lost in Conduction to Electrical Heat Supplied at Different α and RTD Locations S/c

Based on the results of Figure 5.2, the conduction losses decrease with an increasing Re regardless of the S/c. This means that the convective heat transfer becomes more dominant as the Re is increased whereas less losses are transferred by conduction. Since the data for conduction losses only cover some of the outer RTD locations, two assumptions are made. First, for $Re < 6 \times 10^5$ the RTDs of the convection tests at $S/c \geq + 0.2$ and $S/c \leq - 0.2$ have conduction losses equal to those found at $S/c = + 0.3$ and $S/c = - 0.3$. Second and for $Re > 6 \times$

158

10^5 where no conduction measurement tests are made, the conduction losses are assumed to be at an average of 5%. Based on the observations of Figure 5.2, the increase of Re directly decreases the conduction losses, so for $Re \geq 6 \times 10^5$ the losses should be less than 5%. This assumption however could present an additional error of 5% to the experimental data for $Re > 6 \times 10^5$ since no exact measurements are made.

5.1.3 Stagnation Point Measurements

The first verification process of the experiments is done on the Fr_x measurements of the stagnation point ($S/c = 0$) corresponding to the tests at $\alpha = 0°$. Similar to what is done previously in section 4.1.2.2, the experimental data are compared to the NACA 0012 CFD determined values as well as the results of the NACA 0012 experimental measurements of (Poinsatte, 1990). Figure 5.3 shows the results of the Fr_x comparison on the stagnation point of the three previously described sets of data. Specifically, the comparison is done for the range of $1.86 \times 10^5 \leq Re \leq 1.36 \times 10^6$ for the current experiments, $2 \times 10^5 \leq Re \leq 3 \times 10^6$ for CFD and $1.29 \times 10^6 \leq Re \leq 2.48 \times 10^6$ for the experiments of (Poinsatte, 1990). For the experiments of this work, the total experimental error (from section 5.1.1) are also included with the error bars.

According to Figure 5.3, the CFD data show that the Fr_x at the stagnation point is constant at $Fr_x = 4.93$ for all Re except for $Re = 2 \times 10^5$, where a slightly smaller value ($Fr_x = 4.75$) is seen. The experiments of (Poinsatte, 1990) showed that between $Re = 1.29 \times 10^6$ and $Re = 2.48 \times 10^6$, the Fr_x varies slightly between $Fr_x = 4.2$ and $Fr_x = 4.5$. In the present experiments, the Fr_x at the stagnation point increases starting from $Fr_x = 2.5$ at $Re = 1.86 \times 10^5$ before stabilizing at around $Fr_x \approx 4$ at $Re = 6 \times 10^5$. If the error bars are also accounted for, it can be determined that the Fr_x stabilized at $Re < 4 \times 10^5$. This leaves out the $Re < 4 \times 10^5$ showing lower values for the Fr_x at $S/c = 0$.

c
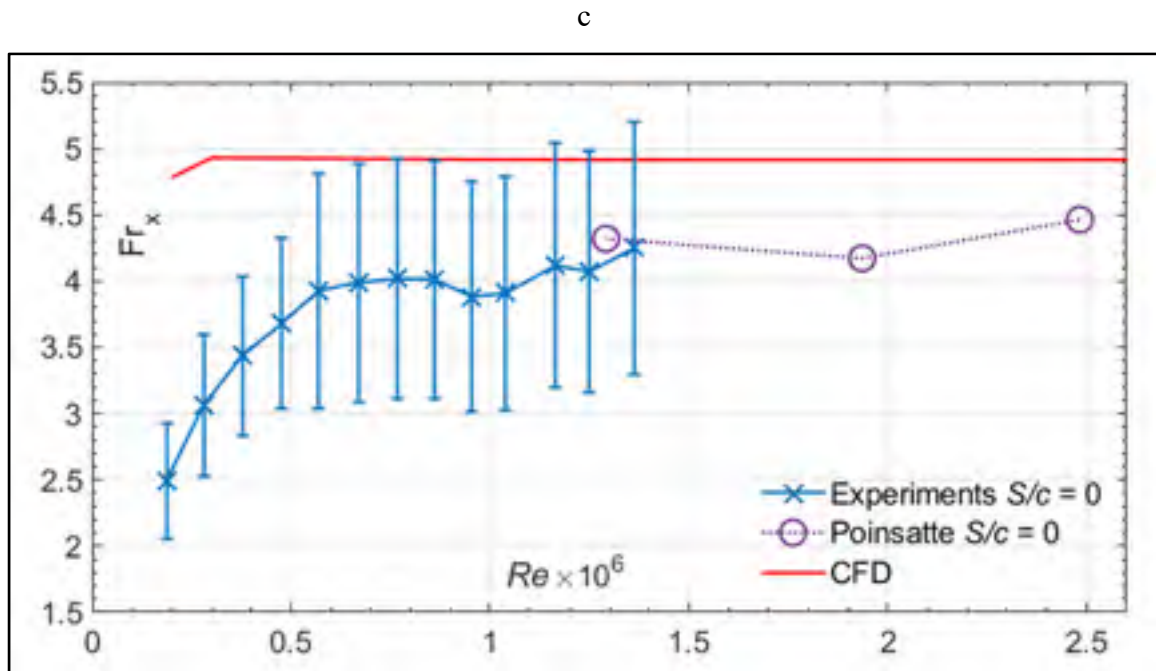
Figure 5.3 Comparison of Stagnation Point ($S/c = 0$) Measurements at $\alpha = 0°$ Versus CFD & NACA 0012 Experimental Data

The comparison of values between the current experiments and the results of CFD indicate a minimum discrepancy of 1% for $Re = 1.36 \times 10^6$ and with the highest extremity of the error bar, as well as a maximum discrepancy of 60% at $Re = 1.86 \times 10^5$ with the lowest extremity of the error bar. Similarly, the values from the measurements of (Poinsatte, 1990) are in the range of the present experiments, especially for the tests with $Re \geq 4 \times 10^5$. Between $1.1 \times 10^6 \leq Re \leq 1.4 \times 10^6$, the Fr_x from both experiments almost matches within 3% discrepancy. If the experimental error is accounted for, the discrepancy could be as high as 36.9%. There are no measurements at lower Re in the work of (Poinsatte, 1990).

This way, the experiments done for $4 \times 10^5 \leq Re \leq 1.36 \times 10^6$ all agree with the stagnation point measurements of (Poinsatte, 1990) within the ranges previously specified. Neither the experiments of this work nor those of the literature could match the values predicted by CFD, with both underpredicting the CFD values unless the highest extremity of the error is accounted

for. Concluding, the present measurements gave Fr_x values at the stagnation point in the range of the measurements of (Poinsatte, 1990) and CFD simulations. At the lowest Re ($< 4 \times 10^5$), an unexpected increase of the Fr_x is noted and will be addressed later on in section 5.1.9.

5.1.4 Chordwise Variation of the Fr_x

This section presents the second verification process of the measured Fr_x on the NACA 0012. Here, the experimental measurements are compared to the results of the fully turbulent NACA 0012 CFD simulations presented earlier in Chapter 4. On the other hand, and since the experiments are not for a fully turbulent flow, the results of a similar experimental work are also included for comparison. The other work is that of (Li et al., 2009) who measured the Fr_x on the surface of a BO 28 airfoil. The aerodynamic data of the BO 28 are not found, so a direct comparison between the two airfoils is difficult. The only known detail of the BO 28 is that it has a 28% thickness ratio, 2.5 times thicker than the NACA 0012.

Figure 5.4 shows the results of the Fr_x comparison between the NACA 0012 experiments of this work, the BO 28 experiments and the NACA 0012 fully turbulent CFD simulations. In the upper subfigure, the Re is $Re = 2.81 \times 10^5$ for the NACA 0012 experiments, $Re = 2.5 \times 10^5$ for the BO 28 experiments and $Re = 3 \times 10^5$ for the CFD simulations. In the same order, the lower subfigure's Re are $Re = 5.69 \times 10^5$, $Re = 5.82 \times 10^5$ and $Re = 6 \times 10^5$. The NACA 0012 experiments as well as the CFD data are for $\alpha = 0°$ whereas the BO 28 data are for $\alpha = -1.5°$. The Fr_x is plotted versus the non-dimensional chord distance x/c.

With only 10 RTDs distributed on the experimented NACA 0012 wall, the Fr_x readings between the points are joined by a Modified Akima Cubic Hermite interpolation defined in MATLAB toolbox (MATLAB, 2019a) as shown in the figures. According to MATLAB, it produces fewer undulations than a spline interpolation, but does not flatten as aggressively. The use of such non-linear joining of points is common and is used in the works of (Wang et al., 2007b, 2008a). Similar to the previous section, the error bars are included to account for the total experimental error.
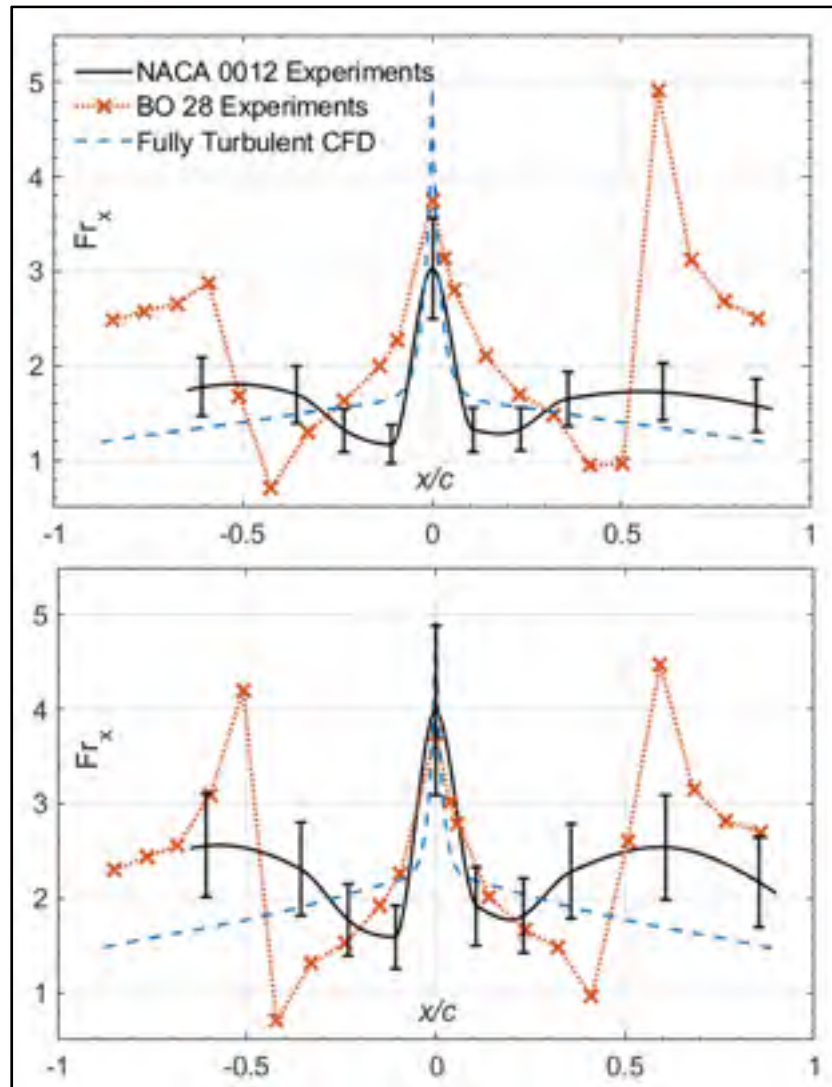
Figure 5.4 Comparison of Fr_x Variation Measured by NACA
0012 & BO 28 Experiments and NACA 0012 Fully Turbulent
CFD at Low Re (Upper) and High Re (Lower)

The main interest of Figure 5.4 is the comparison between the experimental and numerical data
of the NACA 0012. The CFD data indicate that the Fr_x decreases starting from the L.E. all the
way to the T.E., for both presented Re. The experimental data also show a decrease after the
stagnation point at $x/c = 0$ but in contrast to CFD, is followed by an increase of Fr_x on both
sides of the airfoil all the way to $x/c \approx \pm 0.6$. There are no measurements further than that on

the bottom side of the airfoil since there are no RTDs placed there, however on the upper side it is seen that the Fr_x will decrease again after reaching the peak at $x/c \approx + 0.6$.

For the case with the lower Re, the experimental Fr_x is lower than that predicted by CFD by up to 25% before the two curves intersect at $x/c \approx \pm 0.3$. At higher x/c, the Fr_x is almost 27% higher than that from CFD. Similarly, and for the higher Re, the experimental Fr_x is 31% lower before the two curves intersect at $x/c \approx \pm 0.25$ and 35.5% higher than CFD downstream.

The contradiction between the results of experiments and those of CFD could be explained by the examination of the Fr_x from the BO 28 experiments. Although a large discrepancy exists between the Fr_x values of the NACA 0012 and BO 28 experiments, the behavior is somewhat similar. Flow and pressure measurements from the latter experiments attribute the initial decrease of the Fr_x to the laminar flow region, the subsequent increase to the transitional flow behavior and the final decrease after the peak to a fully developed flow (Li et al., 2009).

With that in mind, it can be concluded that the flow in those experiments followed the same three flow behaviors described for the BO 28. A laminar flow region could explain the lower Fr_x for $x/c \leq \pm 0.3$ at $Re = 2.81 \times 10^5$ and for $x/c \leq \pm 0.25$ at $Re = 5.82 \times 10^5$. The flow transition could also explain the increase of Fr_x to values 27% and 35.5% higher than CFD and finally, the decline of the Fr_x after the transition peak could be the result of a fully turbulent flow. This way, it is suspected that the Fr_x values that are predicted by the CFD simulations, will be reached only after the decline of Fr_x values following the transitional flow peak.

The intersection between the Fr_x curves of the experimental and numerical data occur earlier at $Re = 5.82 \times 10^5$ than it did at $Re = 2.81 \times 10^5$. Although no flow or pressure measurements are employed in the experiments, this could also be linked to an earlier flow transition point. As shown by (Li et al., 2009), an increase of Re is consistent with an earlier location of the transition point and a corresponding increase of Fr_x.

On a final note for the comparison between the NACA 0012 experimental and fully turbulent CFD results, the numerically calculated Fr_{Avg} is within 5% of that calculated through the experiments and for either of the two presented Re in Figure 5.4. This indicates that although the laminar and transitional flow behaviors are not modeled in CFD, the averaging of the Fr_x could result in evening out the differences between the two curves. This will be discussed in the more detail later in section 5.1.8 when the Fr_{Avg} from all the tests are compared.

To further examine the experimental results, Figure 5.5 shows a comparison with CFD results of the Fr_x for a NACA 0012 obtained using a transitional flow model and a constant Q_S TBC. The turbulence model is either the S-A model or the transitional S-A with the B-C transitional model (Cakmakcioglu, Bas, & Kaynak, 2018), with the free stream turbulence intensity parameter $T_{u,\infty}$ = 4.0. Both curves in the figure correspond to Re = 1.25 × 10⁶ and α = 0°. It should be noted that the $T_{u,\infty}$ in the CFD results of the figure may have a different outcome on the Fr_x variation, specifically at the transition point location, but the set value was chosen because it caused the increase of Fr_x to start at a similar point as the experiments (S/c = 0.12).

Starting with the stagnation point, it is seen that the CFD results are within the range of the experimental value of Fr_x. Further downstream, both curves exhibit a decrease of Fr_x after S/c = 0 with the CFD results clearly changing to an increasing behavior around S/c = ± 0.12 where the transition point occurs. It is known from the CFD simulation that the flow between those two points is laminar. It should be noted that the decrease of the Fr_x in the laminar region is steeper for the numerical data compared to the experimental values in the same points range. The experimental data also show an increasing Fr_x between ± 0.12 ≤ S/c ≤ ± 0.25. On a best estimate, when the lower ends of the error bars are considered, the curves differ by around 25% at S/c = + 0.12, 5% at S/c = - 0.12 and the CFD data are in range of the experiments at S/c = ± 0.25. At S/c = ± 0.37, the discrepancy can be as low as 2%.
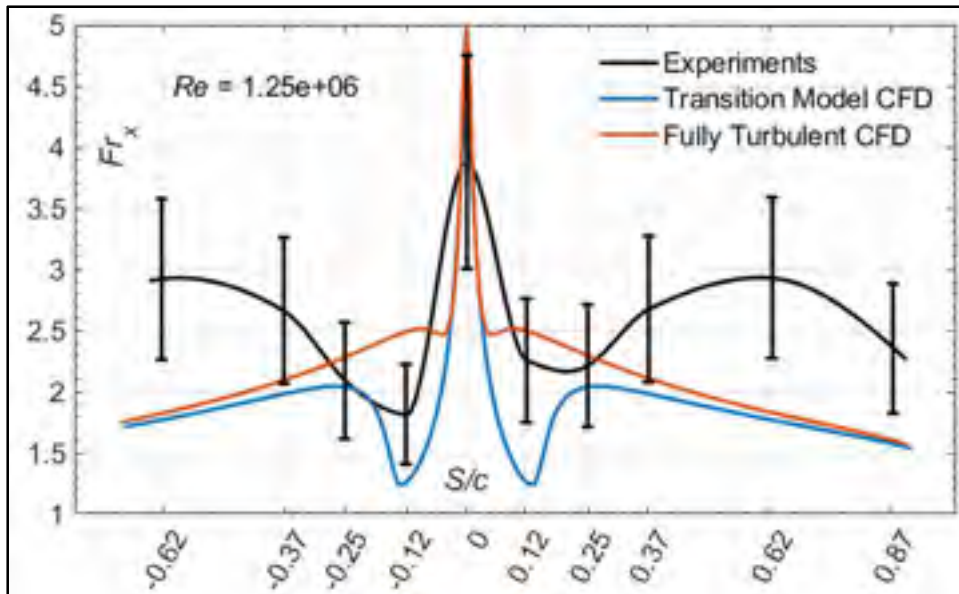
Figure 5.5 Comparison of Fr_x Variation Measured by NACA 0012
Experiments and NACA 0012 Transition Model CFD at $Re = 1.25 \times 10^6$
and $\alpha = 0°$

The discrepancy is larger at the other S/c. While the CFD results decrease all the way to the T.E. after $S/c = \pm 0.25$, the experimental data show an increase up until $S/c = \pm 0.62$. The increase could have stopped earlier however, due to the lack of RTDs between $\pm 0.37 \leq S/c \leq \pm 0.62$. At $S/c = \pm 0.62$ and $S/c = +0.87$, the discrepancy varies between 18% and 50%.

In conclusion, the CFD transition model and experimental results show a similar behavior between the Fr_x variations. Similar to the BO 28 experiments, the CFD transition model shows a decreasing Fr_x in the laminar region which increases after the transition point followed by a continuous decrease in the developed flow region all the way towards the T.E. The behavior of the experimental results somewhat agrees with those of CFD with an obvious difference in the transition location and a maximum discrepancy of 50% between the two.

5.1.5   Effect of Angle of Attack

This section investigates the effect of α on the measured Fr_x at different Re, recorded at the different locations S/c. Figure 5.6 shows the measured Fr_x versus the S/c for the four tested

angles of attack $\alpha = 0°$, $\alpha = 5°$, $\alpha = 10°$ and $\alpha = 15°$. The upper subfigure corresponds to tests at $Re = 2.81 \times 10^5$ while the lower subfigure corresponds to tests at $Re = 1.04 \times 10^6$. The points of measurement with the RTD are marked with the symbols while the data are joined in a similar interpolation to the one described earlier.
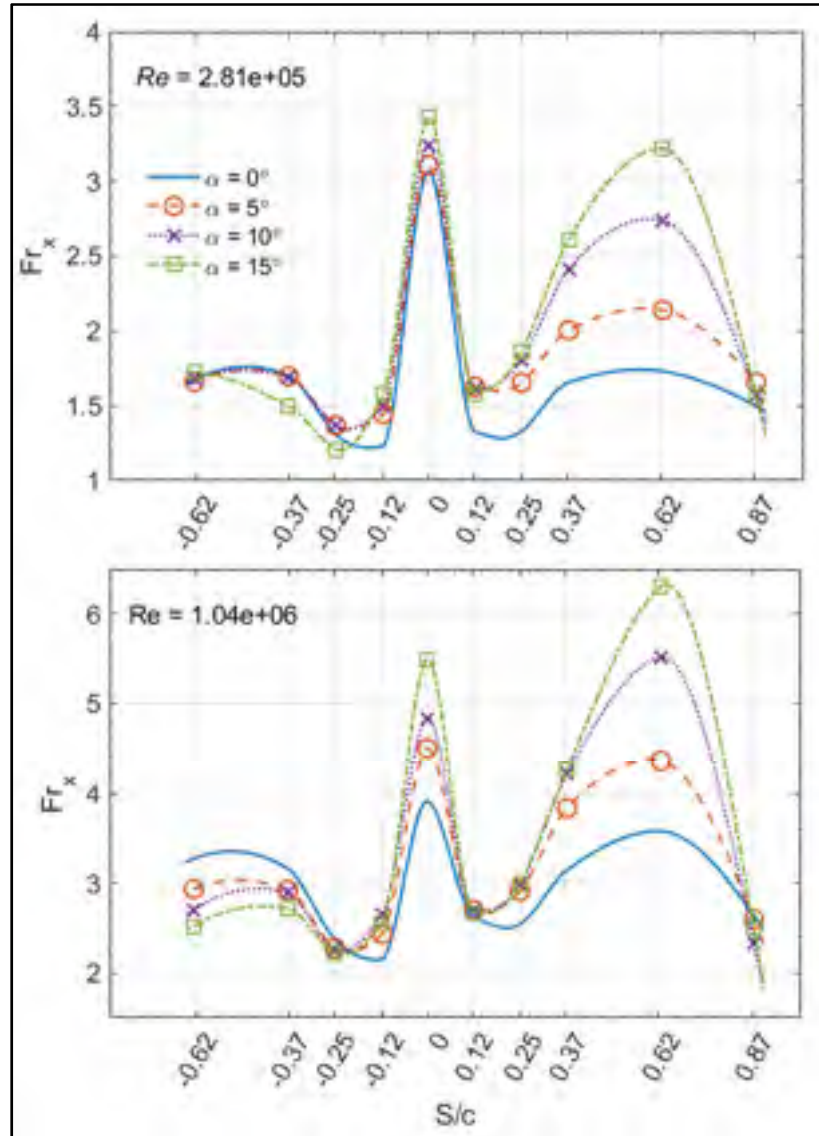
Figure 5.6 Comparison of Fr_x Variation Measured by the
NACA 0012 Experiments Due to an Increase of α at Low Re
(Upper) and High Re (Lower)

Starting at $S/c = 0$, the stagnation point moves on the bottom side of the airfoil when the α is increased. Different α showed similar but increasing values of the Fr_x at that point for the case at $Re = 2.81 \times 10^5$. As the α is increased, the Fr_x increases at $S/c = 0$ between $Fr_x = 3.02$ at $\alpha = 0°$ and $Fr_x = 3.47$ at $\alpha = 15°$. For $Re = 1.04 \times 10^6$ however, the increase of Fr_x is more significant at $S/c = 0$ as the α is increased. At $\alpha = 15°$, the measured Fr_x is 27% higher than the one recorded at $\alpha = 0°$ and at the same point. (Wang et al., 2007b, 2008a) had similar observations and concluded that the changes in the local Fr_x at the same point became more important when the Re is greater than 5×10^5. In their experiments, the Fr_x at $S/c = 0$ changes by less than 10% when $Re = 1.6 \times 10^5$ and changes by 21% between $\alpha = 0°$ and $\alpha = 15°$ for the NACA 63-421, similar to what's seen in Figure 5.6.

Between $- 0.12 \leq S/c \leq + 0.12$, the variation remains relatively unchanged between the different α, the unchanging behavior is also extended to $S/c = - 0.25$ for the higher α. On the upper side of the airfoil, the higher α shows higher Fr_x values than those measured at $\alpha = 0°$. Also, the increasing α shows higher Fr_x values at $S/c = + 0.25$, $S/c = + 0.37$ and $S/c = + 0.62$. This is consistent for both $Re = 2.81 \times 10^5$ and $Re = 1.04 \times 10^6$. For higher Re however, the Fr_x at $\alpha = 10°$ and $\alpha = 15°$ for $S/c = + 0.62$ is higher than that recorded at $S/c = 0$. Similar results are obtained by (Li et al., 2009) who concluded that the Fr_x in the transition region consistently shows higher values than those at $S/c = 0$, as shown previously in Figure 5.4.

On the bottom side of the airfoil, the Fr_x values are almost the same for $\alpha = 0°$, $\alpha = 5°$ and $\alpha = 10°$ when $Re = 2.81 \times 10^5$. For $\alpha = 15°$ at the same Re, the Fr_x are lower than the other angles. When the Re is increased to $Re = 1.04 \times 10^6$, the increasing α consistently shows lower Fr_x values all the way to the T.E., except for $\alpha = 0°$ at $S/c = - 0.12$, which also shows lower Fr_x.

The overall Fr_x behavior on both sides of the experimented airfoil are not strange and could be explained by examining the works of (Li et al., 2009) and (Wang et al., 2007b, 2008a). The former concluded that a higher α causes transition to occur earlier on the upper side of the airfoil and to delay it on the bottom side. This could explain the increase of Fr_x on the upper

side of the NACA 0012 and the decrease on its bottom side. Moreover, (Wang et al., 2007b, 2008a) showed that an increasing α for $Re = 1.6 \times 10^5$ causes little change to the Fr_x except for an initial increase near the L.E. compared to $\alpha = 0°$, similar to the results of Figure 5.6.

5.1.6 Complete Test Results

In this section, the results of the measured Fr_x at all S/c for all tests are investigated. The measured Fr_x of all Re at a specific α are examined separately. The attention here will be regarding the effect of the Re on the Fr_x. The upper subfigure of Figure 5.7 shows the Fr_x variation for $1.86 \times 10^5 \le Re \le 1.36 \times 10^6$ at $\alpha = 0°$ while the lower subfigure is for $8.88 \times 10^4 \le Re \le 1.35 \times 10^6$ at $\alpha = 5°$. Similarly, the upper subfigure shows the Fr_x variation for $9.28 \times 10^4 \le Re \le 1.36 \times 10^6$ at $\alpha = 10°$ while the lower subfigure is for $9.07 \times 10^4 \le Re \le 1.34 \times 10^6$ at $\alpha = 15°$. With only 10 RTDs distributed on the NACA 0012 wall, the RTD points of measurement are marked with the symbols while the data are joined by interpolation.

Generally, there are two obvious trends in the results of the presented figures. First, an increase of Re causes an increase of the Fr_x throughout the airfoil wall and second, an increase of α causes the Fr_x to increase more on the upper side of the airfoil than it does on the bottom side. The curves corresponding to the tests at $\alpha = 0°$ are mostly symmetrical due to the airfoil symmetry. The symmetry is lost and Fr_x deviate when α is increased, this also occurs together with the stagnation point moving on the bottom side of the airfoil.

Moreover, three regions of interest could be identified by examining Figure 5.7 and Figure 5.8. The first includes the stagnation point and is governed by the decreasing Fr_x, generally between - 0.25 $\le S/c \le$ + 0.25 although it varies depending on the Re and α. The second is located downstream of the first and is marked by the increase of Fr_x. It occurs on either airfoil sides and is seen to extend up to $S/c = \pm 0.65$. A distinguishing feature of this region is a "peak" of Fr_x values that generally occurs at $S/c = \pm 0.65$, after which a rapid decrease is observed. The decrease of Fr_x values following the peak marks the final region.
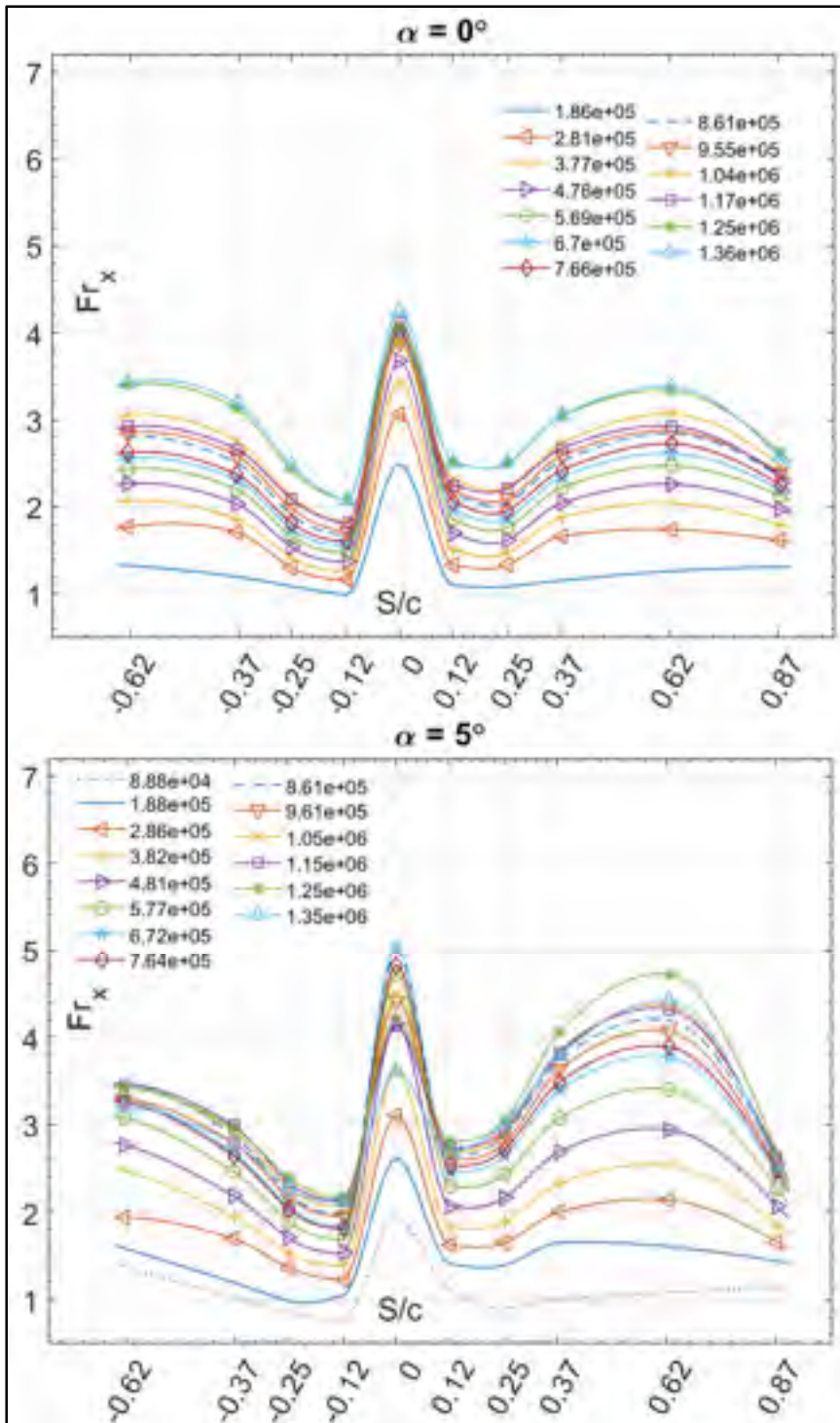
Figure 5.7 Measured Fr_x Variation on NACA 0012 wall for *a*) 1.86 $\times 10^5 \leq Re \leq 1.36 \times 10^6$ at $\alpha = 0°$ and *b*) for $8.88 \times 10^4 \leq Re \leq 1.35 \times 10^6$ at $\alpha = 5°$
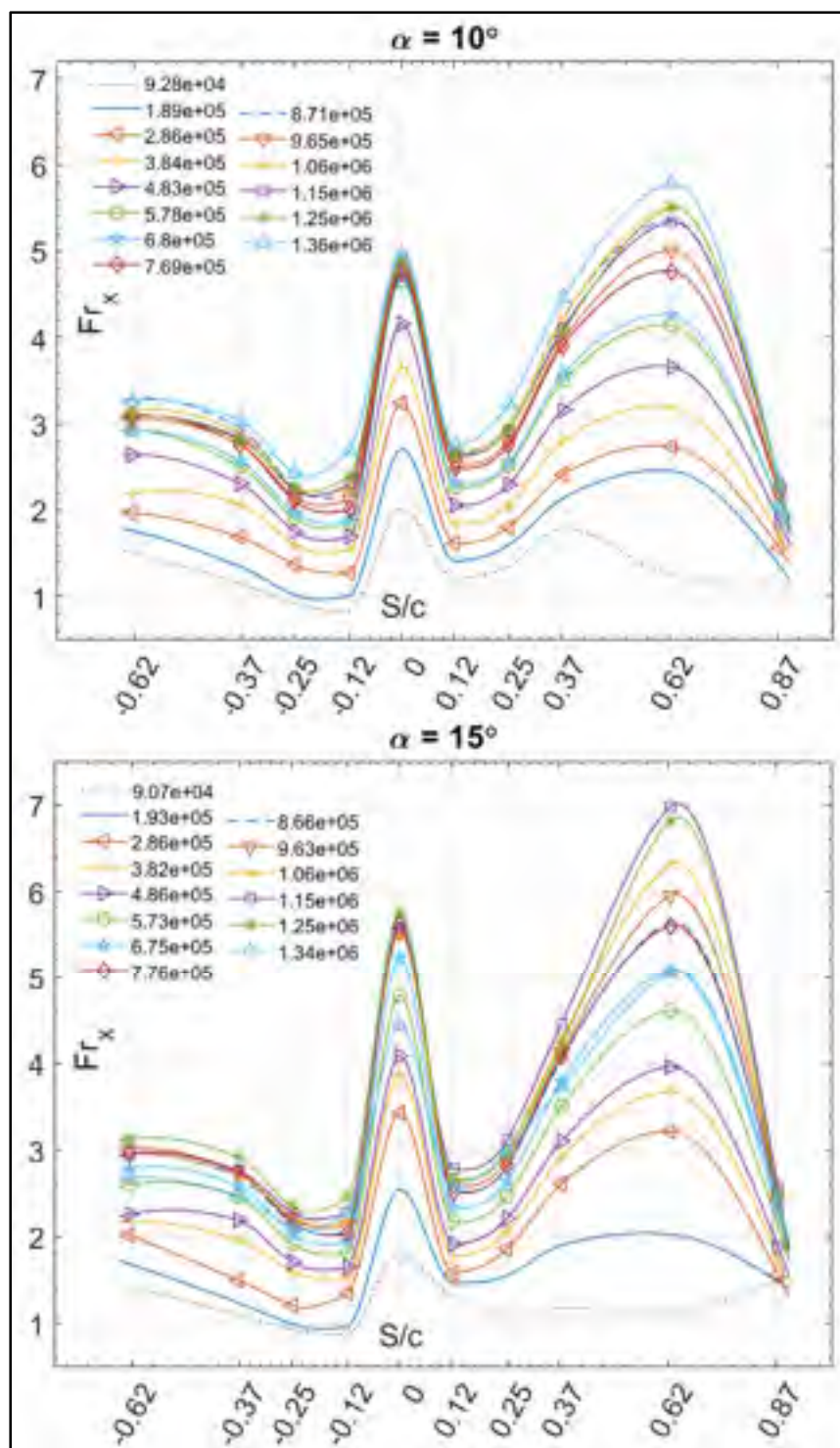
Figure 5.8 Measured Fr_x Variation on NACA 0012 wall for *a*) 9.28 $\times 10^4 \leq Re \leq 1.34 \times 10^6$ at $\alpha = 10°$ and *b*) for $9.07 \times 10^4 \leq Re \leq 1.34 \times 10^6$ at $\alpha = 15°$

The identified three regions of interest based on the results of Figure 5.7 and Figure 5.8 agree with what is previously seen in section 5.1.4. In that section, two *Re* test cases of the NACA 0012 experiments at $\alpha = 0\,°$ showed similar Fr_x behavior to the results of the BO 28 experiments who had evidenced transition effects. When the results of Figure 5.7 and Figure 5.8 are examined, they show a consistent variation with the different tested *Re* and α. Since the present experiments lacked flow measurements, it is the difficult to be sure about the flow condition.

One way to check is by quantifying the variation of the Fr_x with Re^m. In other words, determining the power of *Re* by which the Fr_x varies. As will be seen in the next section, previous works correlated the data in a similar way and linked the flow condition to the parameter *m*. If the correlation can be successfully applied based on the results of the present experiments, then another degree of certainty could be added to the measured Fr_x and its respective flow condition.

5.1.7   Local Frossling Correlation with Reynolds Number

To quantify the variation of Fr_x with *Re*, a curve fitting is done based on the equation $Fr_x = A \times Re^m \times Pr^{1/3}$. *A* and *m* are the constants determined by the curve fitting, *m* is more interesting to determine since it describes that power by which the Fr_x with *Re*, while the *A* scales the the overall results linearly. This procedure is done on the results of Figure 5.7 and Figure 5.8. The Fr_x and *Re* are correlated for each α and at every RTD location separately.

Previous correlating attempts show that $m = 0$ in the laminar region near the L.E. of the NACA 0012 (Poinsatte, 1990) as well as for a laminar flow on flat plates (Kays & Crawford, 1993). For a turbulent flow on the NACA 0012, it was determined back in section 4.1.2.8 of Chapter 4 that the Fr_{Avg} and Fr_{Max} correlate with Re^m by $m = 0.331$ and $m = 0.345$ respectively. While turbulent flows on a flat plate correlate with $m = 0.3$ (Kays & Crawford, 1993).

The Fr_x from NACA 0012 fully turbulent CFD simulations is correlated first, based on the same S/c of the experiments. The results for A and m are presented for each S/c and α in Table 5.1 where R^2 is the correlation coefficient. As expected from a turbulent flow, the m values range mostly between $0.3 \leq m \leq 0.4$, although some points show m values as low as $m = 0.094$ and as high as $m = 0.454$. To get a better comparison between CFD and experimental data, the A constants from CFD are used in the curve fitting of the experimental data, this way the only difference between experiments and CFD would be m.

If the m values from the experiments are compared to those obtained from CFD simulations, two points can be remarked. First, the majority of the m values predicted by CFD fall in the range of those determined experimentally. Second, the technique of fixing the A constant from CFD and using it in the determination of the m based on the experimental data is successful based on the obtained R^2 values.

According to the results of Table 5.1, the similarity between the m values determined through the curve fitting of both the numerical and experimental data is noticeable. Most of the points from either set of data show m values between $0.3 \leq m \leq 0.4$. Moreover, the highest m values are found at $S/c = + 0.374$ and $S/c = + 0.625$ when $\alpha = 15°$. Similarly, the lowest m values are also predicted by both CFD and experiments to be at $S/c = - 0.124$ when $\alpha = 15°$. On average, the m values from either set are within 7% of each other.

What this means from a numerical point of view, is that the variation with Re^m of the majority of the measured Fr_x from the experiments agree with what's expected from the CFD simulations. Recalling that the expected value of m is $m = 0$ for a laminar flow and between $0.3 \leq m \leq 0.4$ under turbulent conditions then in consequence, the experimental data agree resemble what's expected in a turbulent flow condition.

Table 5.1 Constants for Curve Fit $Fr_x = A \times Re^m \times Pr^{(1/3)}$ of NACA 0012 Fixed Wing Fully Turbulent CFD & Experimental Data

α	S/c	A	CFD		Experiments	
			m	R^2	m	R^2
0°	+ 0.124	0.013	0.392	0.945	0.382	0.951
	+ 0.248	0.017	0.369	0.979	0.364	0.963
	+ 0.374	0.020	0.352	0.972	0.366	0.981
	+ 0.625	0.022	0.335	0.980	0.366	0.977
	+ 0.874	0.021	0.328	0.993	0.350	0.976
	− 0.124	0.013	0.392	0.981	0.371	0.995
	− 0.248	0.017	0.369	0.981	0.361	0.928
	− 0.374	0.020	0.352	0.987	0.367	0.964
	− 0.625	0.022	0.335	0.981	0.363	0.970
5°	+ 0.124	0.030	0.347	0.987	0.331	0.991
	+ 0.248	0.032	0.330	0.928	0.328	0.993
	+ 0.374	0.032	0.323	0.908	0.346	0.981
	+ 0.625	0.029	0.318	0.928	0.360	0.987
	+ 0.874	0.025	0.315	0.945	0.343	0.976
	− 0.124	0.015	0.367	0.979	0.373	0.995
	− 0.248	0.011	0.387	0.924	0.392	0.988
	− 0.374	0.014	0.366	0.987	0.389	0.984
	− 0.625	0.020	0.338	0.976	0.368	0.990
10°	+ 0.124	0.050	0.318	0.979	0.293	0.976
	+ 0.248	0.041	0.317	0.924	0.315	0.975
	+ 0.374	0.035	0.318	0.981	0.351	0.972
	+ 0.625	0.026	0.322	0.993	0.384	0.980
	+ 0.874	0.018	0.331	0.991	0.360	0.964
	− 0.124	0.056	0.256	0.993	0.279	0.991
	− 0.248	0.009	0.391	0.981	0.409	0.967
	− 0.374	0.009	0.387	0.987	0.422	0.950
	− 0.625	0.015	0.353	0.928	0.385	0.916
15°	+ 0.124	0.039	0.335	0.958	0.311	0.945
	+ 0.248	0.017	0.376	0.956	0.381	0.979
	+ 0.374	0.005	0.451	0.936	0.499	0.924
	+ 0.625	0.003	0.454	0.955	0.551	0.935
	+ 0.874	0.048	0.234	0.916	0.292	0.884
	− 0.124	0.437	0.094	0.950	0.119	0.968
	− 0.248	0.013	0.352	0.916	0.378	0.928
	− 0.374	0.009	0.381	0.945	0.420	0.908
	− 0.625	0.014	0.352	0.955	0.384	0.928

Although an agreement with CFD data is found, the only thing the results confirm is that the laminar flow behavior is not seen. This is not to say that a fully turbulent flow over the experimented airfoil definitely occurs. While there are no indications of a laminar flow behavior where a constant Fr_x with Re is expected, nor did the stagnation point show constant

Fr$_x$ values, the variation of the *Fr$_x$* in the *S/c* direction does not agree with the fully turbulent CFD simulations and resembles more what's expected from a transitional flow (as is seen in Figure 5.4). As will be seen later on in section 5.1.9, turbulence intensity is suspected to play a role in the overall *Fr$_x$* values and behavior.

5.1.8   Average Frossling Correlation with Reynolds Number

As a final analysis, the *Fr$_{Avg}$* is calculated based on the results of testing and those presented in Figure 5.7 and Figure 5.8. The *Fr$_{Avg}$* is based on the tests *Re* and *α*, the results are presented in Figure 5.9. This figure shows the variation of the *Fr$_{Avg}$* as a function of the *Re* and *α* obtained through the wind tunnel experiments as well as the fully turbulent CFD simulations. Both subfigures represent the *Fr$_{Avg}$* obtained under a constant *Q$_S$* TBC.
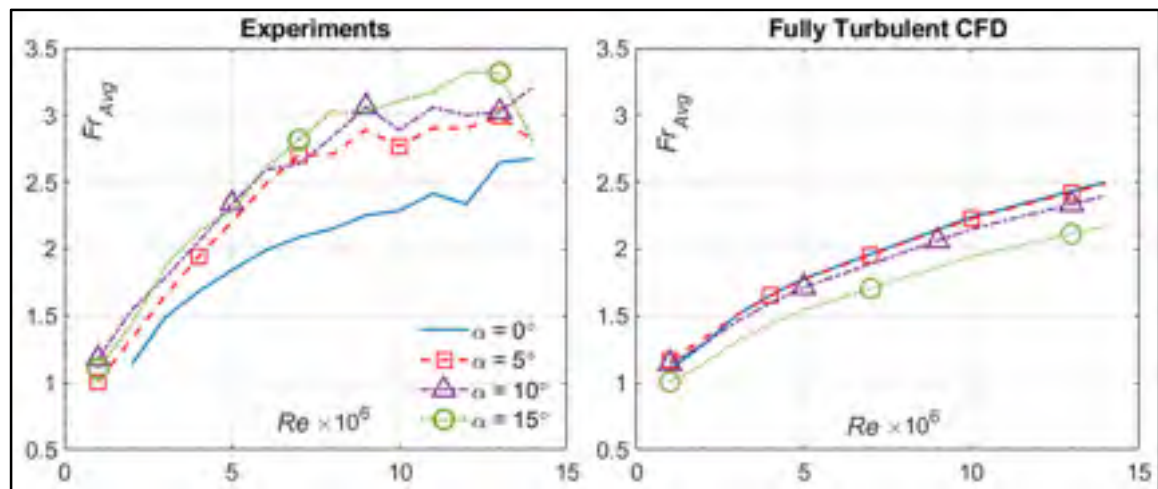
Figure 5.9 NACA 0012 *Fr$_{Avg}$* Variation as a function of the *Re* and *α* Obtained Through Experimental and Fully Turbulent CFD Simulations

As was discussed earlier in Chapter 4, the CFD results showed that the *Fr$_{Avg}$* increased with an increasing *Re* and decreased as the *α* is increased. This is clearly shown in the variations of Figure 5.9. However, the results of the wind tunnel experiments showed a contradicting behavior when an increase of either the *Re* or *α* caused the *Fr$_{Avg}$* to increase. This trend however is also observed by (Li et al., 2009) and (Wang et al., 2007b, 2008a). The average discrepancy

between the experimentally and numerically determined Fr_{Avg} is 4.44% for $\alpha = 0°$, 18.02% for $\alpha = 5°$, 23.90% for $\alpha = 10°$ and 32.3% for $\alpha = 15°$ with the experimental data always overpredicting the Fr_{Avg}. The increasing α would still cause a higher Fr_{Avg} than that of the CFD.

On the other hand, Table 5.2 shows the results of the curve fitting for the Fr_{Avg} as a function of the Re for each α separately. In a similar procedure to what is done for the Fr_x, the Fr_{Avg} is now correlated with Re by the equation $Fr_{Avg} = A \times \mathrm{Re}^m \times \mathrm{Pr}^{1/3}$. The data from CFD are fit first to determine the corresponding A and m constant and the experimental data are then fit based on the constant A found from CFD. Therefore, the A constant is the same between fitting of CFD and experiments and the m is determined separately and can then be compared.

The results in the table indicate that CFD predictions for m vary between $0.295 \le m \le 0.319$ while the experiments show values up to 12% higher, between $0.322 \le m \le 0.336$. Therefore, based on a variation of the Re and similar to what is found previously for the Fr_x, the Fr_{Avg} from experiments shows agreement with the results of the CFD.

Table 5.2 Constants for Curve Fit $Fr_{Avg} = A \times Re^m \times Pr^{(1/3)}$ of Experimental & CFD Data

		$\alpha = 0°$	$\alpha = 5°$	$\alpha = 10°$	$\alpha = 15°$
Experiments	A	0.030	0.039	0.040	0.031
	m	0.322	0.313	0.317	0.336
	R^2	0.924	0.933	0.914	0.931
CFD	A	0.030	0.039	0.040	0.031
	m	0.319	0.299	0.295	0.305
	R^2	0.991	0.986	0.992	0.985

5.1.9   Discussion

The present experiments aim to measure the variation of the Fr_x on different S/c locations of the NACA 0012 for different Re and α. While a review of the literature as well as comparison with data from CFD simulations show good agreement in terms of the Fr_x variation with the Re, there are a few limitations to the presented results. These are discussed in the following paragraphs.

Based on heat transfer variations in laminar flow regions, it was expected that the Fr_x values would remain unchanged with the increasing Re at the stagnation point and near the L.E.. This behavior is evidenced on flat plates in the work of (Lienhard, 2020) as well as (Poinsatte, 1990) and (Li et al., 2009) for airfoils. While Figure 5.7 and Figure 5.8 show that some of the Fr_x curves between $-0.12 < S/c < +0.12$ coincide especially when the $Re \geq 5 \times 10^5$, it is also observed that there are significant variations in the magnitude of the Fr_x at $S/c = 0$ especially for $\alpha > 0°$. Moreover, the length of the laminar region was expected to be longer and similar to what's seen in Figure 5.4 for the BO 28 experiments. In the latter, the Fr_x curves collapsed into one up to $x/c = \pm 0.4$, while the examination of Figure 5.7 and Figure 5.8 consistently showed that the Fr_x curves had an increasing trend and deviated from each other between $S/c = \pm 0.12$ and $S/c = \pm 0.25$.

The total experimental error may be responsible for a misrepresentation of the Fr_x at the stagnation point, but it is not thought to be the only factor. There is evidence in (Ames, 2017) relating the changes the turbulence intensity TI to increases of heat transfer at the stagnation point and in laminar flow regions in what is known as turbulence augmentation of heat transfer. Moreover, the same source indicates that the TI is a factor that affects the flow transition location and also increases the heat transfer rates in transitional and even turbulent flows.

Correlation (3.14) is used based on the TI and Re_d of the present experiments. The aim is to check if the TI of the experiments would have an impact on the calculated Fr_0, which could in turn explain the increasing values at the stagnation point and supposed laminar region seen in

the experiments. Thus, the *TI* as well as the Re_d are calculated using equation (3.13) and (3.15) for each of the tests. They are then used in the Fr_0 correlation and the results are shown in Figure 5.10. Since the correlation provides the Fr_0 based on the L.E. diameter, the values in the figure are converted to their chord-based counterparts based on equation (3.15). The results are for all the tests at $\alpha = 0°$, $\alpha = 5°$, $\alpha = 10°$ and $\alpha = 15°$.

What Figure 5.10 says is that based on the *TI* and *Re* of the experiments, the Fr_0 is expected to increase. In fact, an increase between the lowest and highest tested *Re* can be by as much as 12%. Therefore, it is not strange to see an increase of the Fr_x at $S/c = 0$ in Figure 5.7 and Figure 5.8. If the experimental error is also considered, then the experiments could have misrepresented the stagnation point Fr_x by up to 35% of its true value.
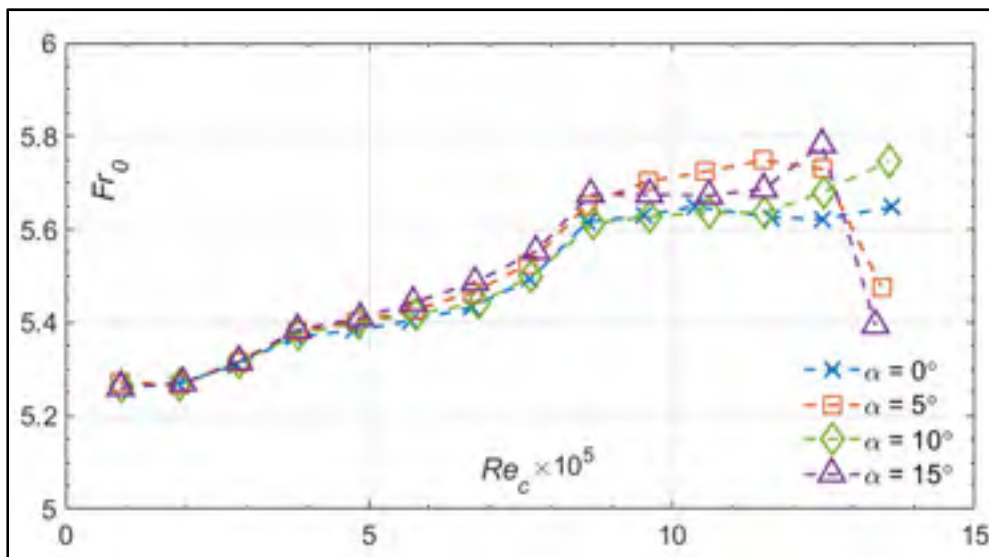
Figure 5.10 Stagnation Point Fr_0 versus Re_c Obtained Through (Van Fossen et al., 1995) Correlation for $8.88 \times 10^4 \le Re \le 1.36 \times 10^6$ and at $\alpha = 0°$, $\alpha = 5°$, $\alpha = 10°$ and $\alpha = 15°$

On a separate note, Figure 5.10 shows that when the least turbulence is involved, the Fr_0 had a value of around 5.25 and increased up to 5.8 at its maximum. These values are higher than those predicted by CFD or by the experiments of (Poinsatte, 1990) and are likely due to differences in geometries between the cylinder and the NACA 0012, as was seen previously in

Figure 4.4. So while the correlation may not represent the true values of the NACA 0012 Fr_0, it shows that the turbulence level has an increasing effect on the measured heat transfer.

Another note of interest is for the tests for $Re = 1.35 \times 10^6$ at $\alpha = 5°$ and $\alpha = 15°$. Figure 5.7 and Figure 5.8 show that the Fr_x variation increased with Re, except for the two aforementioned cases. For those tests, Figure 5.10 show that the effect of TI is low compared to the other Re, thus explaining the decrease of Fr_x at those Re.

The effect of the TI also extends to the laminar region heat transfer. (Van Fossen et al., 1995) also linked the turbulence induced heat transfer at the stagnation point to a corresponding augmentation of heat transfer in the laminar region near the L.E. Specifically, this means that the true values of Fr in the laminar region is directly proportional to changes brought by the turbulence level at the stagnation point. By examining the results of Figure 5.7 and Figure 5.8, it is seen that the Fr_x values at $S/c = \pm 0.12$ increase with the Re in a similar way of the values at $S/c = 0$. The supposed laminar flow in that region could then be experiencing a turbulence augmentation of heat transfer, explaining the non-uniformity of the Fr_x values.

On the other hand, there is a peak of the Fr_x values that is consistently seen at $S/c = + 0.62$ regardless of the Re and α in the results of Figure 5.7 and Figure 5.8. A comparison to similar heat transfer behavior on airfoils show that this could be attributed to flow transition (Li et al., 2009). It is believed that the lack of RTD for Fr_x measurements between $+ 0.37 \leq S/c \leq + 0.62$ may have misrepresented the heat transfer variation in the region. (Li et al., 2009) showed that the increase of Fr_x values occurs earlier if either the Re or α are increased, a behavior that is not clearly visible in the results of the present experiments. Therefore, the constant increase between $+ 0.37 \leq S/c \leq + 0.62$ is not expected and a different behavior of the Fr_x in that region is more realistic.

Finally, in terms of the Fr_x variation with the Re at a specific S/c, the results of the experiments show that a similar variation is obtained between experiments and CFD. This is based on a comparison of the curve fitting of data at the different S/c under the form of

$Fr_{Avg} = A \times \mathrm{Re}^{m} \times \mathrm{Pr}^{1/3}$, where the A is fixed and m is determined and compared. Results from the data averaging of both the CFD and experiments also showed that the experiments predicted similar variation of the Fr_{Avg} with the Re compared to the results of CFD. This however is not the case for a variation with α where an agreement between 4.44 % and 32.3% is found when the Fr_{Avg} from CFD is compared to that of the experiments. This could be due to the drawback of the experiments where a laminar flow region, where lower Fr_x are expected, is not well represented. A combination of the experimental error plus the turbulence intensity augmentation of heat transfer caused the experimental data to be within 35% of their true values.

5.2   Rotor Heat Transfer Experimental Results

The rotor tests are done on 2-blade rotor with a NACA 0012 profile, the blades are more than 95% covered with heating elements that operated at a constant Q_S TBC. Two pitch angles are tested and they are $\theta = 0°$ and $\theta = 6°$. The rotor speeds are varied between 500 RPM and 1500 RPM, the range of Re between the different r/R and Ω is $1 \times 10^5 \leq Re \leq 4 \times 10^5$. The RTDs are distributed across the radius to provide measurements at different locations across the radius as well as the chord.

The results of those tests are presented in the form of the Fr_x in this chapter, while the results in terms of the temperature difference between the air and RTDs are supplied in APPENDIX III. There are not enough datapoints across the surface to predict an average value of heat transfer due to complexity of setup and wiring limitations. Therefore, the results could only be compared in their local form to those of the UVLM-RHT and BEMT-RHT.

Similar to the results of the fixed wing experiments, it is suspected that transitional flow effects influenced the behavior of the flow and the subsequent calculation of the heat transfer. These effects are more important in the case of the non-lifting rotor compared to the rotor with a positive pitch angle. Transitional effects are also suspected to be the main source of the discrepancy obtained between numerical predictions and experiments.

5.2.1   Experimental Error

Based on the methodology of section 3.4.5, the experimental error due to measurements is determined by equation (3.16) and is found to be 3.4%. On the other hand, for the randomness error, Figure 5.11 shows the results of the calculated randomness error between the repeated tests. Results are shown for tests from different Ω and with the error at each measured r/R. Unlike the fixed wing tests, no tunnel heating is encountered during the tests since the freestream is always at V_∞ = 5 m/s and the T_∞ = 248.15 K is always maintained. The randomness error ranged between 2% and 9.7% and is similar to that obtained for the fixed wing experiments.
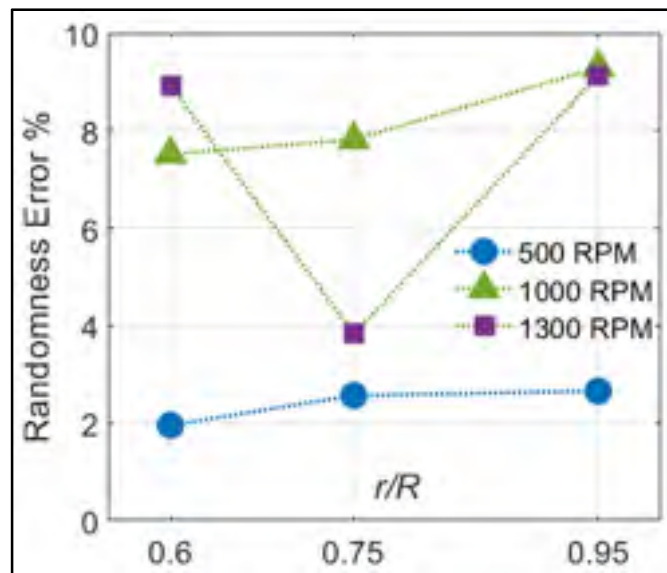
Figure 5.11 Rotor Randomness Error for Tests at Different θ & Re

Another source of error is due to the assumption of the rotor being in a hovering condition whereas a freestream of circulated at V_∞ = 5 m/s. Although the air velocity is small, it becomes somewhat significant especially at lowest tested RPM. To take this error into account, UVLM calculations indicate that the difference in heat transfer between the hovering rotor and the rotor in forward flight could show a maximum discrepancy of ± 4% for Ω = 500 RPM, ± 3.2% for Ω = 1000 RPM , ± 2.8% for Ω = 1300 RPM and ± 2.6% for Ω = 1500 RPM.

The last source of error comes from the assumption taken on the conduction losses in the rotor blades discussed in section 3.4.1. For the rotor tests, the range of Re tested is between 1×10^5 $\leq Re \leq 4 \times 10^5$. Moreover, according to the fixed wing conduction tests of section 5.1.2, the conduction losses for that range of Re are between 4% and 8% of Q_{Elec}. The assumption is to equate the conduction losses from the fixed wing to those of the rotor tests at similar Re. A reduction of the Q_{Cond} from the Q_{Elec} will directly reduce the measured Fr by the same percentage. Since this is an approximation and not based on direct measurements of the conduction in the blades, an uncertainty between 4% and 8% is added to the total experimental error of the rotor tests. Summarizing, Table 5.3 shows the previously discussed sources of error along their calculated values. The total experimental error is then a sum of all sources of error and is set at $\pm 25.1\%$ for presented results.

Table 5.3 Different Sources of Error in the Rotor Tests with Corresponding Percentages

Type	Measurement	Randomness	Hovering Approximation	Conduction Losses	Total
Value	3.4%	9.7%	4%	8%	25.1%

5.1.2 Turbulence Intensities

The turbulence intensity TI is calculated for each of the rotor tests. The local velocity V_{local} at each blade section is first calculated using equation (3.12), based on the velocity due to rotation $\Omega \times r$ plus the velocity due to the freestream of air V_∞. The results of the calculated TI using equation (3.13) for each test done at $S/c = 0$ is then shown in Figure 5.12. The figure shows the results for the tests at the two angles θ and their three tested rotor speeds Ω, at the corresponding radial location r/R.

The V_∞ had a major effect on the *TI*, although the lowest possible V_∞ to operate the IWT is imposed. Despite being necessary to maintain the temperature in the IWT, it also caused fluctuations in the blade local velocity as the rotor is spinning. In fact, this is evidenced in Figure 5.12 where the *TI* is seen to decrease with an increasing Ω and *r/R*. At low Ω and *r/R*, the rotation speed is largely affected by the V_∞ and has large fluctuations. When the Ω is increased, the effect of the V_∞ is minimized.
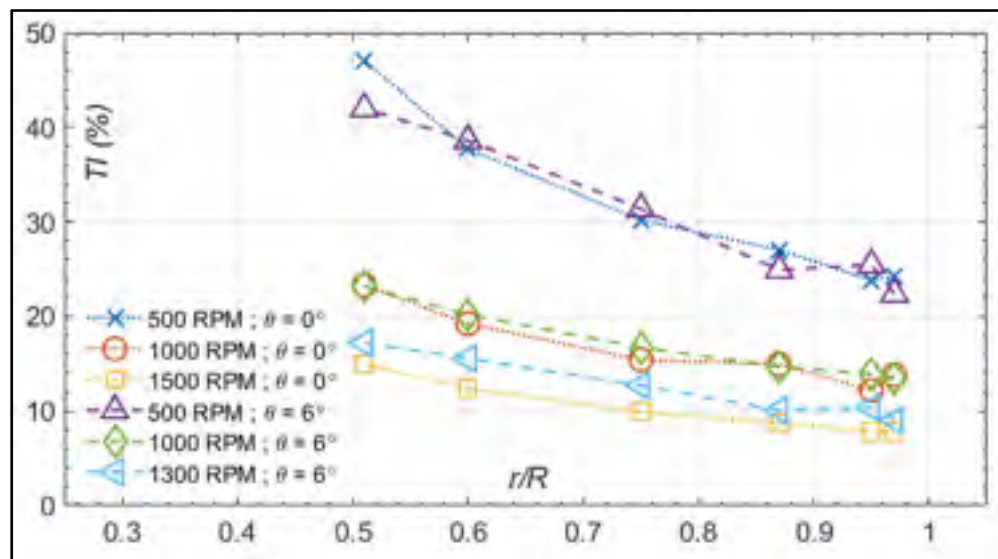
Figure 5.12 Calculated Turbulence Intensity Percentage for Rotor Tests at *S/c* = 0 for Different θ, Ω and *r/R*

The *TI* for the other tests at the other locations *S/c* is not shown in Figure 5.12 since the chordwise location has minimal to no effect on the local velocity. This is also verified by calculations and the *TI* at the other *S/c* is almost identical to that at *S/c* = 0 in the figure. For Ω = 500 RPM, the *TI* varied between 48% at *r/R* = 0.51 and 23% at *r/R* = 0.97. For Ω = 1000 RPM, the *TI* values are between 23% and 12% while for the highest Ω, the range is between 18% and 9%.

5.2.3   Radial Variation of the Fr_x

The results of the rotor tests are first examined as a function of the variation of the measured heat transfer rates in the radial direction of the blade. To do this, the calculated Fr_x is plotted versus the non-dimensional radial distance r/R for each chordwise location S/c separately. Figure 5.13 shows the results for the tests when the rotor is at $\theta = 0°$ and operated at $\Omega = 500$ RPM, 1000 RPM and 1500 RPM. Similarly, Figure 5.14 shows the results at $\theta = 6°$ for $\Omega = 500$ RPM, 1000 RPM and 1300 RPM. It should be noted that for both θ, six radial positions are tested for $S/c = 0$ while all other S/c had three radial positions tested.

5.2.3.1   Non-Lifting Rotor ($\theta = 0°$)

In general, Figure 5.13 shows that the Fr_x increases with an increasing Ω and r/R. An exception is at $r/R = 0.95$ for $S/c = 0.3$ and $S/c = 0.44$ where the Fr_x decreases at those points. On a first observation, the increase of Fr_x could be explained by the increase of Re and the decrease is suspected to be due to a movement of the transition point.

The locations at $S/c = 0.3$ and $S/c = 0.44$ show a different behavior than the previously discussed locations and this may be the result of a transition point movement. Previous work show that the increase of the Re will cause the transition point to move closer to the L.E. (Li et al., 2009). The same source also shows that the transition point will show elevated Fr_x values, higher than those in the laminar region and even in the turbulent region. Therefore, the transition could have occurred earlier or later than $S/c = 0.3$ and $S/c = 0.44$, explaining the different behavior at those points. While this might be the case, this will be analyzed in more detail in the next section when the chordwise variation of the Fr_x will be examined.

All in all, the variations of the Fr_x in Figure 5.13 indicate somewhat of a consistent behavior between the different r/R and Ω, except at the tip of tests at $S/c = 0.3$ and $S/c = 0.44$. The only major change brought about originated from the different Re. An effect of transition may also be suspected but will be examined later on with more detail.

Figure 5.13 Radial Variation of Fr_x at Four Different Chord Locations ($S/c = 0$, 1/7, 2/7 & 3/7), for Three Rotor Speeds ($\Omega = 500$ RPM, 1000 RPM and 1500 RPM) & $\theta = 0°$

5.2.3.2   Lifting Rotor ($\theta = 6°$)

In this section, the results of the tests done at $\theta = 6°$ are examined. Figure 5.14 shows the variation of the Fr_x versus the radial location r/R and at the three different rotor speeds. Each of the subfigures correspond to a different S/c, with the first three being the same as the tests for $\theta = 0°$. The last subfigure in the bottom right corner is for $S/c = 0.58$. For the case of $S/c = 0$, there is no significant change compared to the case of the non-lifting rotor. The Fr_x generally increases with the Ω as well as with the r/R.

The variation of the Fr_x for positions $S/c \neq 0$ is different than that seen for the case of $\theta = 0°$. For instance, at $S/c = 0.15$, the Fr_x decreased for all Ω going from $r/R = 0.6$ to $r/R = 0.95$ for $\theta = 6°$ with a high of $Fr_x = 3.45$. Whereas the highest values at that point for $\theta = 0°$ are around $Fr_x = 1.4$. There is a significant drop in values near $r/R = 0.95$ at $S/c = 0.3$ at $\theta = 6°$ compared to an almost unchanged behavior at $\theta = 0°$. The Fr_x at $S/c = 0.58$ showed a continuously decreasing Fr_x from $r/R = 0.6$ all the way to the blade tips. Also, no drop of Fr_x at $r/R = 0.95$ similar to the case of $\theta = 0°$ is seen.
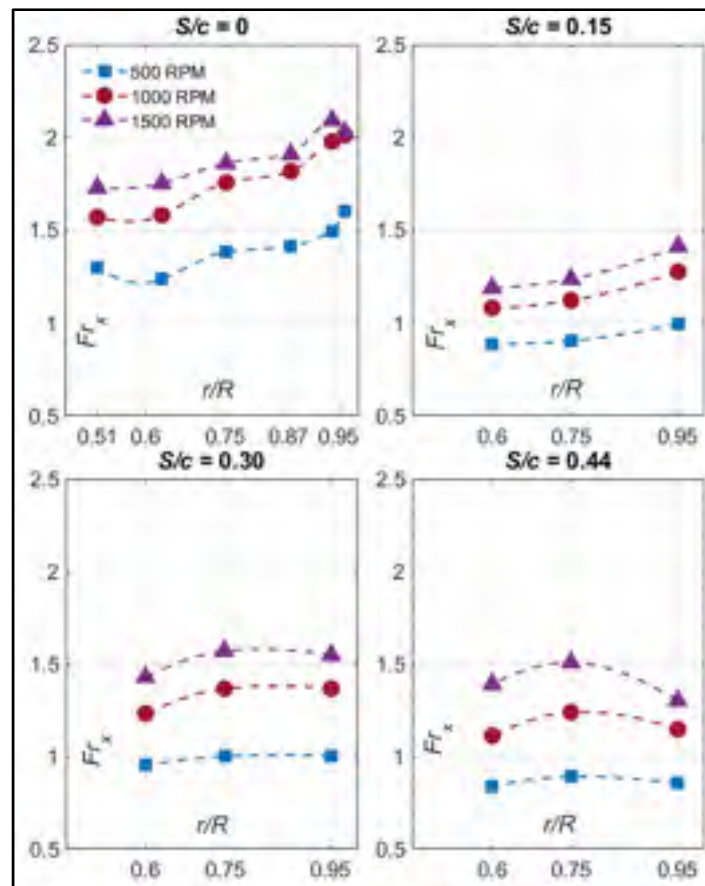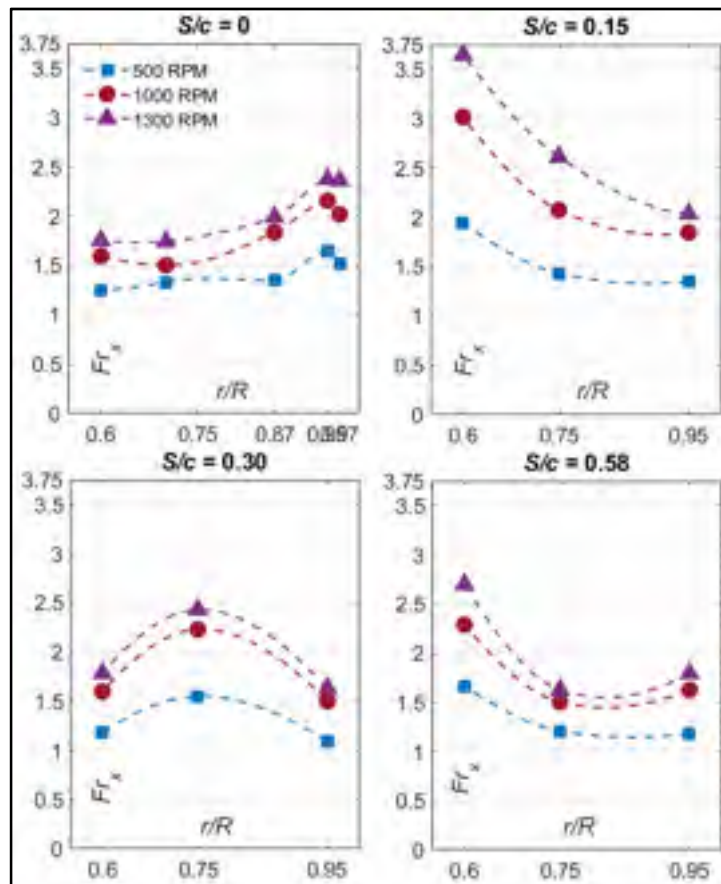

Figure 5.14 Radial Variation of Fr_x at Five Different Chord Locations ($S/c = -1/7, 0, 1/7, 2/7$ & $4/7$), for Three Rotor Speeds ($\Omega = 500$ RPM, 1000 RPM and 1300 RPM) & $\theta = 6°$

While the results shown in Figure 5.13 and Figure 5.14 do not provide enough analysis to build upon, they serve to show how the heat transfer on the rotor will change significantly with three parameters: the Re, θ as well as the r/R. Tip vortex losses, induced velocities and the variation

of the α_{Eff} with the r/R are all related to the heat transfer, but to perform a thorough analysis on the variation of the Fr_x, flow measurements and more datapoints are needed. Having that said, the present analysis discusses the obtained results but serves ultimately to numerically validate the BEMT-RHT and UVLM-RHT, not to conduct a thorough investigation of heat transfer on rotor blades.

5.2.4 Chordwise Variation of the Fr_x

In the current and following sections, another look is taken at the results of the tests but with a different arrangement. The heat transfer rates are now compared based on their chordwise variations at individual blade sections. Since the Re varied on the rotor blade in two ways, so it is important to differentiate between the two. The first is with an increasing Ω and another time with the r/R due to the linearly increasing blade local velocity due to rotation.

5.2.4.1 Non-Lifting Rotor ($\theta = 0°$)

Figure 5.15 and Figure 5.16 show the variation of the measured Fr_x in the chordwise direction of the blade represented by S/c when the rotor is at $\theta = 0°$. Figure 5.15 shows the variation of the Fr_x at a specific r/R for $\Omega = 500$ RPM, 1000 RPM and 1500 RPM while Figure 5.16 is for a specific Ω at $r/R = 0.95$, 0.75 and 0.6.

On a general observation, the results of Figure 5.15 show a repetitive trend between all the plots. The Fr_x first decreases starting from the stagnation point at $S/c = 0$ until $S/c = 0.15$, it then increases between $0.15 \leq S/c \leq 0.3$. Finally, and for $S/c \geq 0.3$, all the presented graphs for all r/R and Ω, the Fr_x decrease all the way to the last measured point at $S/c = 0.44$.

Figure 5.15 Chord-Wise Variation of Fr_x at Three Different Radial Locations (r/R = 0.95, 0.75 & 0.6), for Three Rotor Speeds (Ω = 500 RPM, 1000 RPM and 1500 RPM) & θ = 0°

It is found that the increases of Fr_x with Re are consistent between the presented results. For the case of the varying Ω, Figure 5.15, the increase of Ω from 500 RPM to 1000 RPM causes the Fr_x to increase by 29% while an increase from 500 RPM to 1500 RPM causes the Fr_x to increase by 48% at any r/R. This means that when the Re is doubled and tripled due to an increase in Ω, the Fr_x increases by 29% and 48% respectively. From the other hand and for any of the presented Ω, between r/R = 0.6 and r/R = 0.75, the Re increases by 19% and the Fr_x by 8%. Similarly, between r/R = 0.6 and r/R = 0.95, the Re increases by 45% and the Fr_x by 11%. The range of Re is between $9.5 \times 10^4 \leq Re \leq 3.71 \times 10^5$ corresponding to the lowest Re at r/R = 0.6 for Ω = 500 RPM and the highest at r/R = 0.95 for Ω = 1500 RPM.

There is a noticeable effect of the Re on the Fr_x behavior especially seen between $0.15 \leq S/c \leq$ 0.3 for Ω = 1000 RPM where the increase of the Fr_x is steeper than the other rotor speeds. Another effect is seen between $0.3 \leq S/c \leq 0.44$ for Ω = 1500 RPM where a steeper decline of Fr_x is seen compared to the other Ω at the same S/c. As a conclusion, there is consistency between the changes of the Fr_x as well as a minor difference of the Fr_x behavior for a non-lifting rotor at θ = 0°. Therefore, the heat transfer rates on the rotor blades are largely governed by the changes of Re due to a changing Ω. In other words, for the non-lifting rotor, the Ω had a greater impact on the values of Fr_x than the location on the blade radius r/R.
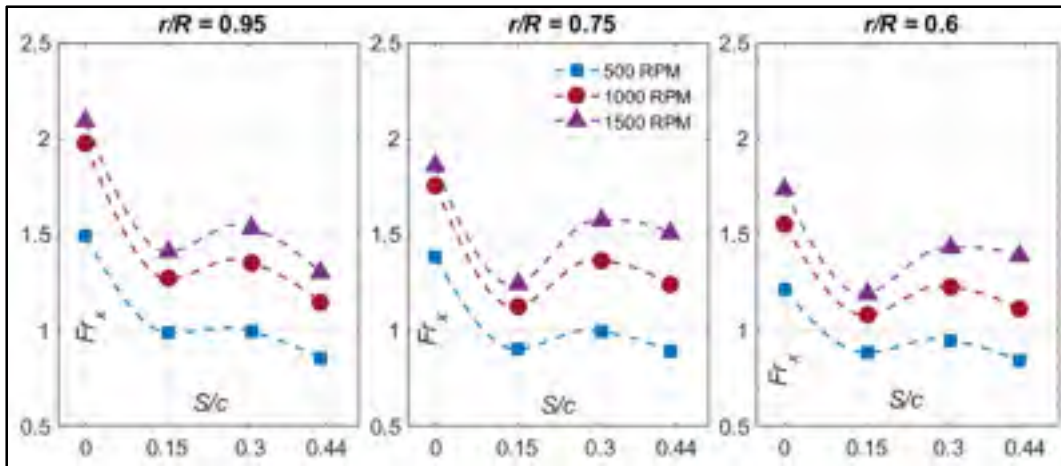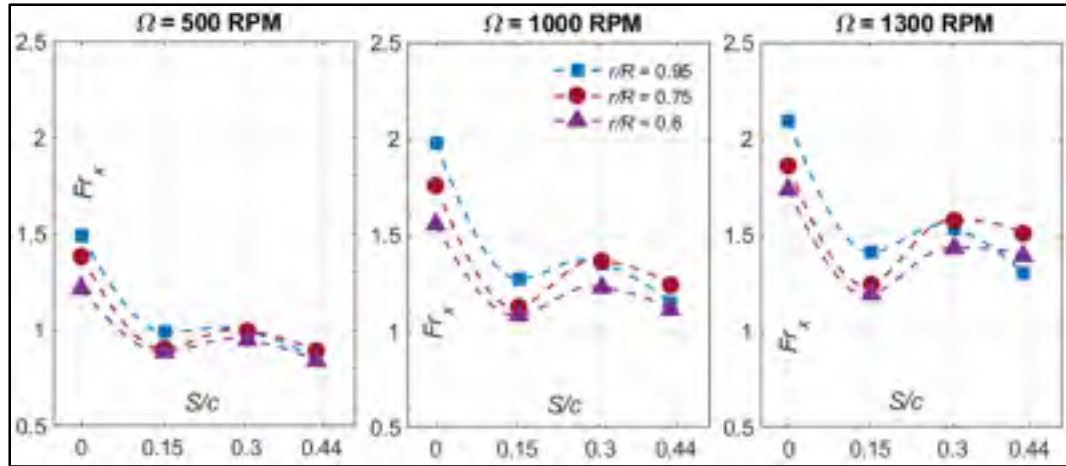
Figure 5.16 Chord-Wise Variation of Fr_x at Three Different Radial Locations (r/R = 0.95, 0.75 & 0.6), for Three Rotor Speeds (Ω = 500 RPM, 1000 RPM and 1500 RPM) & θ = 0°

If the Fr_x are correlated in a similar way to the fixed wing data in section 5.1.6 based on the equation $Fr_x = A \times \mathrm{Re}^m \times \mathrm{Pr}^{1/3}$, the A and m values would be those presented in Table 5.4 where R^2 is the correlation coefficient. The variation of Re used to correlate the data is based on a changing Ω and not r/R. These correspond to the subfigures on the left of Figure 5.16. The Fr_x based on a changing r/R could not be correlated with the same equation due to a poor R^2 (R^2 < 0.5) and large errors (up to 70%). The correlated data correspond to all the RTDs except the one at the supposed stagnation point S/c = 0.

To compare the predicted m values to those from the NACA 0012 CFD simulations, the Fr_x from fully turbulent CFD are correlated at similar S/c at α = 0°. The results for A, m and R^2 are also shown in Table 5.4. The A values from CFD are then used in the curve fitting of the rotor experimental data depending on the S/c, this way the m values are the only different parameters between the two.

The results of Table 5.4 first show that the rotor Fr_x data could be succesfully correlated based on the presented equation, judged by the relatively high R^2. What the table also shows is that

the m values don't change by more than 5% between the different r/R, so the power of Re by which the Fr_x varies is maintained.

Table 5.4 Constants for Curve Fit $Fr_x = A \times Re^m \times Pr^{(1/3)}$ of Rotor Experimental Data at $\theta = 0°$ & NACA 0012 Fixed Wing Fully Turbulent CFD at $\alpha = 0°$

θ	r/R	S/c	A	CFD ($\alpha = 0°$)		Experiments	
				m	R^2	m	R^2
0°	0.95	0.155	0.014	0.387	0.996	0.371	0.976
		0.300	0.018	0.361	0.991	0.360	0.981
		0.443	0.021	0.345	0.995	0.342	0.993
	0.75	0.155	0.014	0.387	0.996	0.368	0.983
		0.300	0.018	0.361	0.991	0.362	0.984
		0.443	0.021	0.345	0.995	0.344	0.986
	0.6	0.155	0.014	0.387	0.996	0.372	0.994
		0.300	0.018	0.361	0.991	0.355	0.981
		0.443	0.021	0.345	0.995	0.331	0.986

When compared to the values of m from CFD, a similarity between the rotor correlation parameters and NACA 0012 simulations is also found within 5%. From a flow behavior point of view, this means that the rotor Fr_x data at the tested S/c do not agree those of a laminar flow condition where $m = 0$ is expected (Poinsatte, 1990). The values correspond more to either a transitional or a turbulent flow condition. However, given the overall behavior of the Fr_x in Figure 5.16, the decrease of Fr_x between $0 \leq S/c \leq 0.15$ and subsequent increase between 0.15 $\leq S/c \leq 0.3$, a flow transition is suspected at $S/c = 0.15$ as evidenced by (Li et al., 2009).

5.2.4.2   Lifting Rotor ($\theta = 6°$)

Similar to the previous section, the results of the heat transfer measurements, in the chordwise direction, on the rotor with the blades at $\theta = 6°$ are investigated here. Figure 5.17 and Figure 5.18 show the variation of measured Fr_x versus the S/c when the rotor is at $\theta = 6°$. Figure 5.17 shows the variation of the Fr_x at a specific r/R for $\Omega = 500$ RPM, 1000 RPM and 1300 RPM while Figure 5.18 is for a specific Ω at $r/R = 0.95$, 0.75 and 0.6.
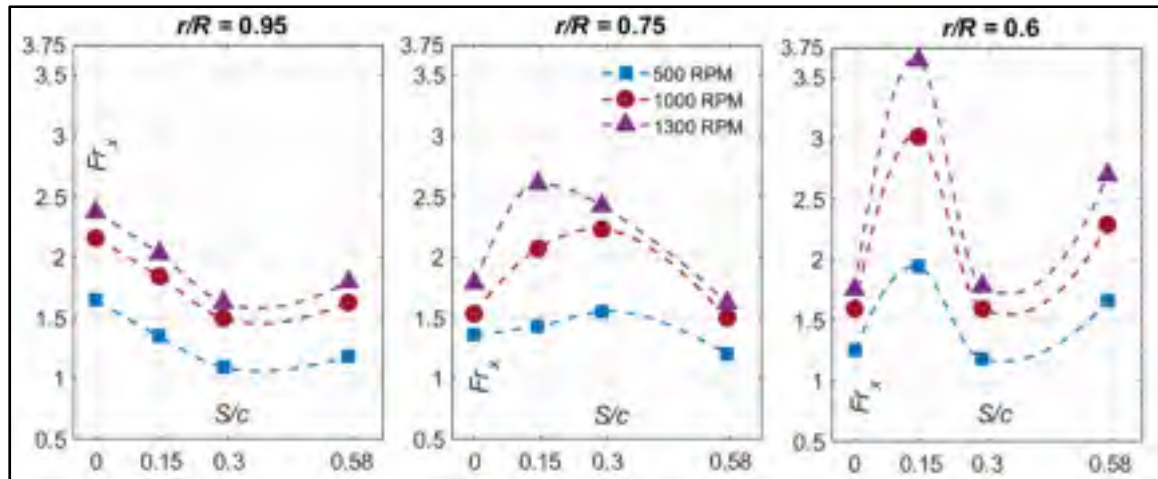
Figure 5.17 Chord-Wise Variation of Fr_x at Three Different Radial Locations (r/R = 0.95, 0.75 & 0.6), for Three Rotor Speeds (Ω = 500 RPM, 1000 RPM and 1300 RPM) & θ = 6°

The inspection of the results of Figure 5.17 indicate that significant changes are brought when the pitch is increased to θ = 6° compared to the non-lifting rotor test case. While no major changes are the result of increasing the Ω from 500 RPM to 1300 RPM other than the magnitude of the Fr_x, they are the different r/R that show different Fr_x behaviors.

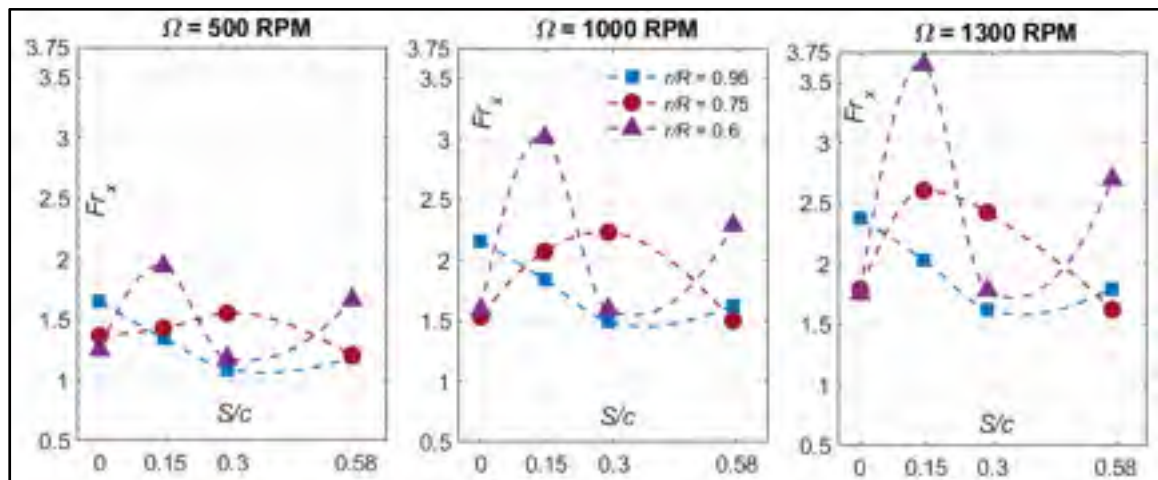Figure 5.18 Chord-Wise Variation of Fr_x for Three Rotor Speeds (Ω = 500 RPM, 1000 RPM and 1300 RPM) at Three Different Radial Locations (r/R = 0.95, 0.75 & 0.6) & θ = 6°

By examining Figure 5.17, it is found that on average, the increase of Ω from 500 RPM to 1000 RPM causes the Fr_x to increase by 32%, while an increase from 500 RPM to 1300 RPM causes the Fr_x to increase by 46% at any r/R. The range of Re is between $9.5 \times 10^4 \le Re \le 3.35 \times 10^5$ corresponding to the lowest Re at $r/R = 0.6$ for $\Omega = 500$ RPM and the highest at $r/R = 0.95$ for $\Omega = 1300$ RPM. The rates of increase of the Fr_x are almost similar to the case of the non-lifting rotor. However, the point at $S/c = 0.15$ at $r/R = 0.6$ shows significant increase, up to 75%, when the rotor speed is changed from 500 to 1300 RPM.

In Figure 5.18, the change in r/R shows how the Fr_x behavior is impacted. Each of the three presented r/R show a different behavior. At $r/R = 0.95$ and for any Ω, the Fr_x are generally the lowest compared to the other r/R and a decrease of values is seen between $0 \le S/c \le 0.3$. Also, the point at $S/c = 0.58$ shows an increase of Fr_x. At $r/R = 0.75$, the Fr_x increases between $0 \le S/c \le 0.3$ for both $\Omega = 500$ RPM and $\Omega = 1000$ RPM and between $0 \le S/c \le 0.15$ for $\Omega = 1300$ RPM. A decrease of values is then noted till the last measurement point at $S/c = 0.58$. Finally, and at $r/R = 0.6$, a rapid increase of values before $S/c = 0.15$ followed by rapid decrease afterwards is seen for all Ω. Also, between $0.3 \le S/c \le 0.58$ an increase of Fr_x is also noted for all Ω.

Similar to the analysis done in the previous section, the Fr_x data from Figure 5.17 are correlated based on the equation $Fr_x = A \times Re^m \times Pr^{1/3}$. The Re in the correlation is also based on a change of Ω since the r/R changes to the Re failed to provide a satisfactory correlation with a $R^2 > 0.5$. Table 5.5 shows the A and m values determined by the curve fitting process, with the A values used being the same from Table 5.4.

The results of Table 5.5 first show that the m values corresponding to the rotor at $\theta = 6°$ are 5% to 21% higher than those of the rotor at $\theta = 0°$. What this means is that for the rotor with the positive pitch, the Fr_x values are more influenced by the Re than the non-lifting rotor case. Moreover, the m could provide an idea about the flow condition although no flow measurements are made. As discussed in the previous section, in the case of a laminar flow the

$m = 0$. With the data from Table 5.5 showing $0.355 \leq m \leq 0.449$, the flow does not agree with laminar flow correlation parameters and is more suspected to have transitional or turbulent behaviors.

Table 5.5 Constants for Curve Fit $Fr_x = A \times Re^m \times Pr^{(1/3)}$ of Rotor Experimental Data at $\theta = 6°$

θ	r/R	S/c	A	m	R^2
		0.155	0.014	0.449	0.981
	0.95	0.300	0.018	0.379	0.976
		0.586	0.021	0.398	0.985
		0.155	0.014	0.414	0.986
6°	0.75	0.300	0.018	0.397	0.986
		0.586	0.021	0.357	0.983
		0.155	0.014	0.396	0.977
	0.6	0.300	0.018	0.359	0.962
		0.586	0.021	0.355	0.981

The latter conclusion goes in parallel with the behavior of the Fr_x seen in Figure 5.17. The continuous decrease seen at $r/R = 0.6$, followed by a rise of values near $S/c = 0.15$ at $r/R = 0.75$, and increase of Fr_x magnitude at $r/R = 0.95$ could be the result of the transition point movement. (Li et al., 2009) showed that the increase in α brings the transition point closer to the L.E. accompanied by a significant rise of Fr_x values. The fixed wing experiments from section 5.1.6 also showed that the magnitude of the Fr_x is increased with the increasing Re and α. Both these findings confirm with the results of Figure 5.17, but without flow measurements, this could not be ascertained.

5.2.5 Validation with UVLM-RHT & BEMT-RHT

To validate the BEMT-RHT & the UVLM-RHT, the experimented rotor is numerically modeled with each tool. The UVLM-RHT is ran, in forward flight mode, with 10×25 vortex lattices at $\Delta\Psi = 10°$ for 20 revolutions and the AR corresponding to the freestream velocity V_∞.

in the tunnel is adjusted in each UVLM simulation based on the ratio between Ω and V_∞. The BEMT-RHT is ran with n = 200 blade elements in hover mode without considering the V_∞. Each numerical tool is used to simulate the rotor for Ω = 500, 1000 and 1500 RPM at θ = 0° and Ω = 500, 1000 and 1300 RPM at θ = 6°. Both the BEMT and the UVLM predicted a C_T = 0 at θ = 0° whereas at θ = 6°, it is C_T = 0.0015 for the BEMT and C_T = 0.0017 for the UVLM. The disagreement between the C_T of each tool is 16.67%, similar to what is obtained in the validation test case of section 4.2.1.

Since the RTDs placed on the rotor blade wall are not enough to calculate the Fr_{Avg} on each blade section, the CFD-determined NACA 0012 heat transfer database is used differently. Instead of using the Re and α_{Eff} with the Fr_{Avg} correlation ((4.6) or (4.9) depending on the TBC), they are used to interpolate the Fr_x database based on each S/c of the NACA 0012 wall. This way, a comparison between the numerical and the experimental data can be done based on the local RTD measurements.

The Re and α_{Eff} predicted by the BEMT-RHT, at each r/R, are fed into the Fr_x database and interpolated to obtain a chordwise variation of the heat transfer at each of the 200 modeled blade elements. Similarly, for the UVLM, the viscous coupling algorithm is used to predict the α_{Eff} at each of the 25 modeled blade radial locations. Together with the corresponding calculated Re, an interpolation in the Fr_x database is performed.

5.2.5.1   Non-Lifting Rotor (θ = 0°)

Figure 5.19 shows the results of the comparisons between the BEMT-RHT and UVLM-RHT from one side and the measured experimental data from another, all for the rotor at θ = 0°. From top to bottom, the rows of subfigures represent the cases of Ω = 500, 1000 and 1500 RPM respectively. From left to right, the columns of subfigures are for r/R = 0.95, 0.75 and 0.6. Each of the subfigures also shows its corresponding Re. The error bars shown on the experimental datapoints correspond to the accounted total experimental error of 25.1% determined in section 5.2.1.

The predictions of each numerical tool are strikingly similar, and the discrepancy is not more than 6% for all the presented r/R and Ω. This is in accordance to the conclusion found based on the Fr_{Avg} & Fr_{Max} predictions for the modified Bell 429 tail rotor in sections 4.2 and 4.3. Although the numerical tools are seen to predict C_T values that are up to 20% different, the Fr_x predictions are almost similar.

From a strictly numerical point of view, the results of the BEMT-RHT and the UVLM-RHT agree with the experimental data, except for a large discrepancy at $S/c = 0$. There is also a consistency between the numerical and experimental data. In others words, the points at $S/c = 0$ and $S/c = 0.15$ showed lower Fr_x values regardless of the r/R and Ω, and the points at $S/c = 0.3$ and $S/c = 0.44$ always matched or are slightly different than the numerical data.

The numerical predictions at $S/c = 0$ are considerably higher than those recorded experimentally as shown in Figure 5.19. The Fr_x at that point is between 2 to 2.5 times greater than the experimental value for any r/R and Ω. This effect is previously encountered, with a smaller discrepancy, in the fixed wing experiments (section 5.1.9). In the latter, the turbulence intensity was found to be the factor for the discrepancy, which will be discussed later in section 5.2.6 for the rotor tests.

At $S/c = 0.15$, the experimental data are 5% to 43% lower than the numerical prediction. If the highest discrepancy is considered (corresponding to the maximum experimental error), then the experimental data would likely be attributed to a laminar flow at that point. Laminar flows are known to generate lower Fr_x values compared to the fully turbulent CFD simulations through which the numerical data of this work are obtained (Poinsatte, 1990).

The points at $S/c = 0.3$ and $S/c = 0.44$ matched the numerical data but had a maximum discrepancy of 12%, even when the total experimental error is accounted for. This could imply that the flow at that point follows the same behavior as the CFD simulations and is suspected to be turbulent. Moreover, the point at $S/c = 0.3$ is believed to be a point of transition from

laminar flow to turbulence in experiments, as evidenced by the increase of Fr_x. Although no transition effects are modeled in CFD, it is seen through the fixed wing experiments that at relatively low Re ($\leq 4 \times 10^5$) and $\alpha = 0°$ the Fr_x values in the suspected transition region are within 10% of the CFD values.
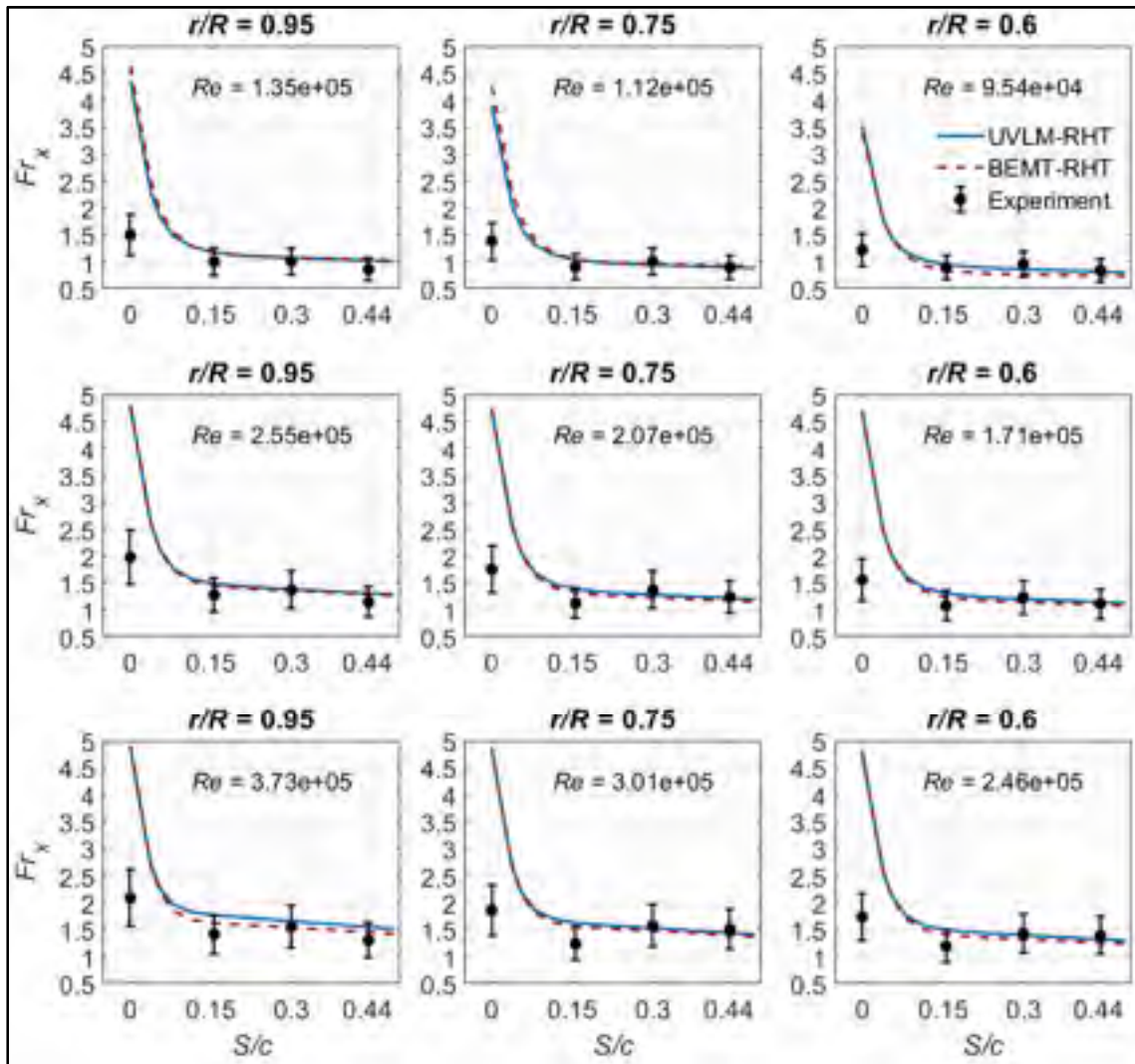

Figure 5.19 Comparison Between the Fr_x Predicted Numerically by the UVLM-RHT & BEMT-RHT and Measured Experimentally at $\theta = 0°$ for different r/R and Ω

5.2.5.2   Lifting Rotor ($\theta = 6°$)

For the case when the blades are at $\theta = 6°$, Figure 5.20 shows the results of the comparisons between the BEMT-RHT and UVLM-RHT from one side and the measured experimental data from another, the rows of subfigures represent the cases of $\Omega = 500$, 1000 and 1300 RPM respectively. From left to right, the columns of subfigures are for $r/R = 0.95$, 0.75 and 0.6. Each of the subfigures also shows its corresponding Re. The experimental data are also shown with the total experimental error of 25.1% determined in section 5.2.1, represented by the error bars.

Similar to what is seen in the previous section, the use of the different numerical tools did not affect the Fr_x predictions significantly. Disagreements up to 10% existed however and are mostly seen in cases with the lowest Re of Figure 5.20. Both numerical tools are verified to have predicted the same Re, so the disagreement in the predicted Fr_x is the result of a disagreement in the computation of α_{Eff} since the Fr_x is interpolated based only on the Re and α_{Eff}.

When compared to the experimental values, the results of the BEMT-RHT and the UVLM-RHT are less consistent with the measured Fr_x values, compared to the non-lifting rotor test case. As previously explained in section 5.2.4.2, the behavior of the Fr_x variations changed significantly between one r/R and the other. This is directly translated in varying agreement and disagreement with the numerical predictions.

To begin with, the point at $S/c = 0$ shows experimental Fr_x values that are lower than those predicted numerically, regardless of the r/R and Ω examined. Similar to the test cases at $\theta = 0°$ of the previous section, the numerical values are 2 to 2.5 times greater than their experimental counterparts. The discrepancy found at the supposed stagnation point at both tested θ is thought to be due to the reason that will be discussed later in section 5.2.6.

At $r/R = 0.95$ the numerical data generally matched those from the experiments. The maximum discrepancy (aside from $S/c = 0$) of 10% is found at $S/c = 0.15$. At $r/R = 0.75$, all of the

measured Fr_x showed higher values than those predicted by either the BEMT-RHT or the UVLM-RHT, except at $S/c = 0$. The discrepancy at that r/R varied between 5% at $S/c = 0.58$ and 55% at $S/c = 0.15$. Finally, the greatest discrepancy is found at $r/R = 0.6$ where the points at $S/c = 0.15$ and $S/c = 0.58$ show up to 80% discrepancy. The point at $S/c = 0.3$ agrees with the numerical data however within 14%.
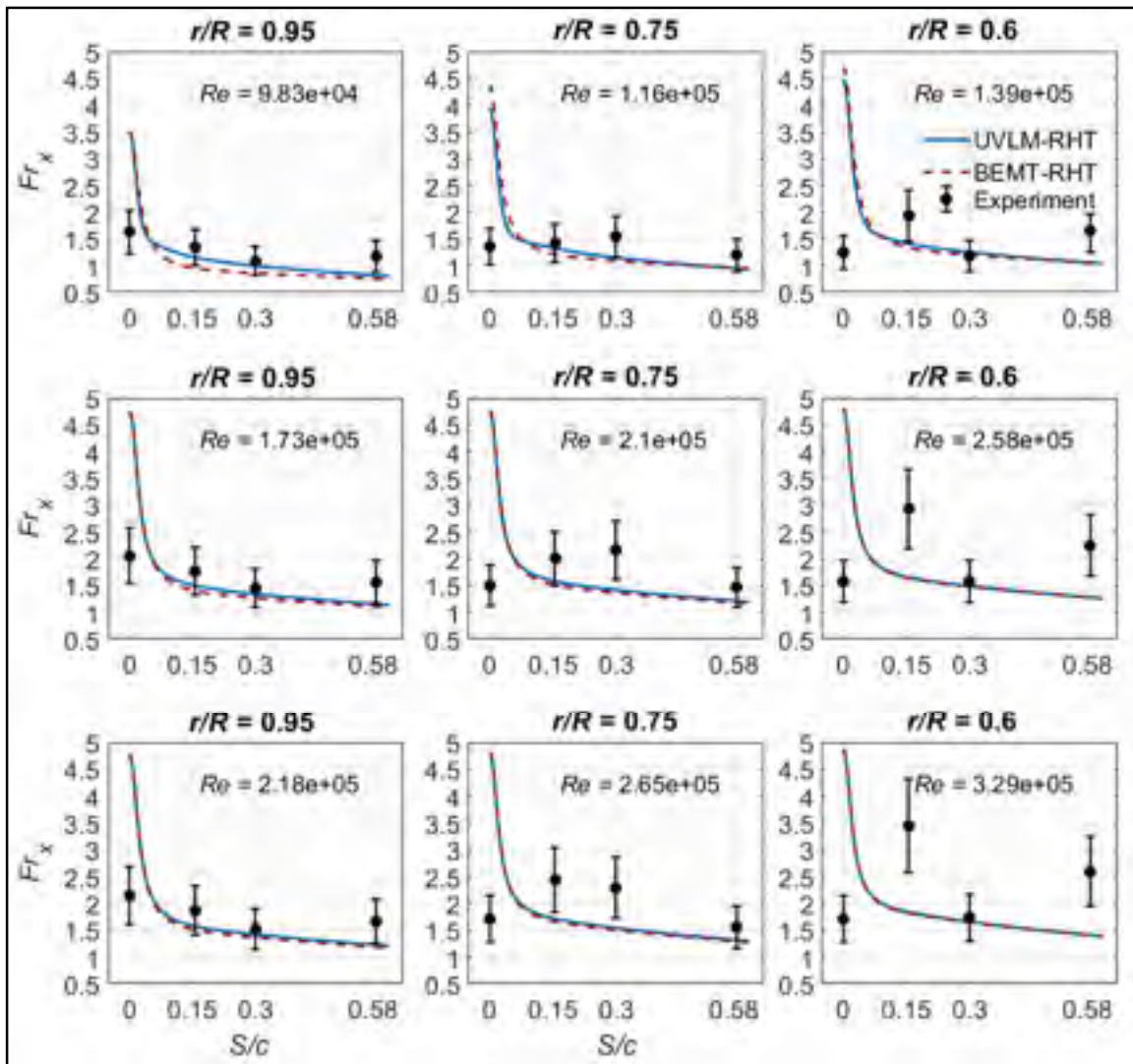

Figure 5.20 Comparison Between the Fr_x Predicted Numerically by the UVLM-RHT & BEMT-RHT and Measured Experimentally at $\theta = 6°$ for different r/R and Ω

5.2.6   Discussion

The rotor experiments measured the heat transfer in terms of the Fr_x on different locations of the blade, measurements are taken in the radial direction r/R and in the chord direction S/c, two angles are tested and three different rotor speeds. The aim of the experiments is to validate the developed numerical tools of this thesis, the BEMT-RHT and the UVLM-RHT. While a review of the literature as well as comparison with data from the numerical tools showed agreement in terms of the measured Fr_x (5% to 80% discrepancy depending on the test conditions), there are a few limitations to the presented results. These are discussed in the following paragraphs.

Based on heat transfer meassruements in laminar flows conducted on flat plates in the work of (Lienhard, 2020) as well as (Poinsatte, 1990) and (Li et al., 2009) on airfoils, it was expected that the Fr_x values would remain unchanged with the increasing Re at the stagnation point and near the L.E. Particularly, this would apply to meassruements at the supposed stagnation point $S/c = 0$ in both Figure 5.13 and Figure 5.14 as well as the supposed laminar region which is at least between $0 \leq S/c \leq 0.15$ in Figure 5.16 and Figure 5.17. Based on all those figures, the stagnation point did not show a constant Fr_x and the point at $S/c = 0.15$ showed varying values. Moreover, the data near the L.E. satisfied the correlation with Re^m with values of m similar to those found in turbulent data correlations.

Relating to the previous paragraph but from another perspective, flow transition on airfoils is seen to occur at low velocities such as $Re = 2.5 \times 10^5$ in the work of (Li et al., 2009), so it should not be strange to occur in rotor tests with the higher $\Omega \geq 1000$ RPM. However, for the low speed tests $\Omega = 1000$ RPM, the Re is consistently lower than 2×10^5 and as low as 9×10^4. Therefore, a transition or turbulent flow at those Re is unlikely to occur naturally, and heat transfer measurements should be those expected from a laminar boundary layer. An agreement of experimental data with the fully turbulent results of the numerical tools, as seen in Figure 5.16 and Figure 5.17, is surprising.

It should be remembered that the fixed wing experiments showed similar Fr_x behaviors at the stagnation point and supposed laminar region. In those experiments, the TI is deemed responsible via the turbulence augmentation of heat transfer (section 5.1.9). The rotor tests also showed elevated TI values that are the direct result of rotation plus freestream velocity of the IWT.

Recall that there is evidence in (Ames, 2017) relating the changes in TI to increases of heat transfer values at the stagnation point and in laminar flow regions in what is known as turbulence augmentation of heat transfer. Moreover, the same source indicates that the TI is a factor that affects the flow transition location and also increases the heat transfer rates in transitional and even turbulent flows. The works (Van Fossen et al., 1995) and of (Yeh et al., 1993) indicate however that the rates of increase in heat transfer due to an increasing TI at low Re (like the ones in the rotor tests) are more significant compared to higher Re. Since the rotor tests have relatively low Re, the effect of TI should be significant.

It is believed that the relatively high values of TI calculated during the tests have a direct impact on the misrepresentation of the stagnation point, supposed laminar region measurements and low Re tests. To quantify the effect of the TI on the measured Fr, correlation (3.14) is used together with the Re_d of the rotor experiments. The aim is to check if the TI of the experiments would have an impact on the calculated Fr_0, which could in turn explain the increasing values at the stagnation point and supposed laminar region seen in the experiments. Thus, the TI as well as the Re_d are calculated using equation (3.13) and (3.15) for each of the tests. They are then used in the Fr_0 correlation and the results are shown in Figure 5.21. Since the correlation provides the Fr_0 based on the L.E. diameter, the values in the figure are converted to their chord-based counterparts based on equation (3.15). The results are for the tests at $S/c = 0$ and for $\theta = 0°$ and $\theta = 6°$.

The results of Figure 5.21 indicate that the approximate application of the (Van Fossen et al., 1995) correlation does indeed show an effect of the TI on the calculated Fr_0. All the data shown in the figure corresponding to the different Ω and θ showed an increase of the Fr_0, and the

maximum increase was almost 9.8% for the test with $\Omega = 1300$ RPM and $\theta = 6°$. The higher Ω generally caused a higher predicted Fr_0, mainly due to the higher Re. As discussed in the fixed wing tests (section 5.1.9), the laminar region near the L.E. will experience increases of Fr_x that are proportional to the those on the stagnation point (Van Fossen et al., 1995), the work of (Yeh et al., 1993) also shows significant increase downstream the laminar region, but is difficult to quantify without proper turbulence scale estimation.
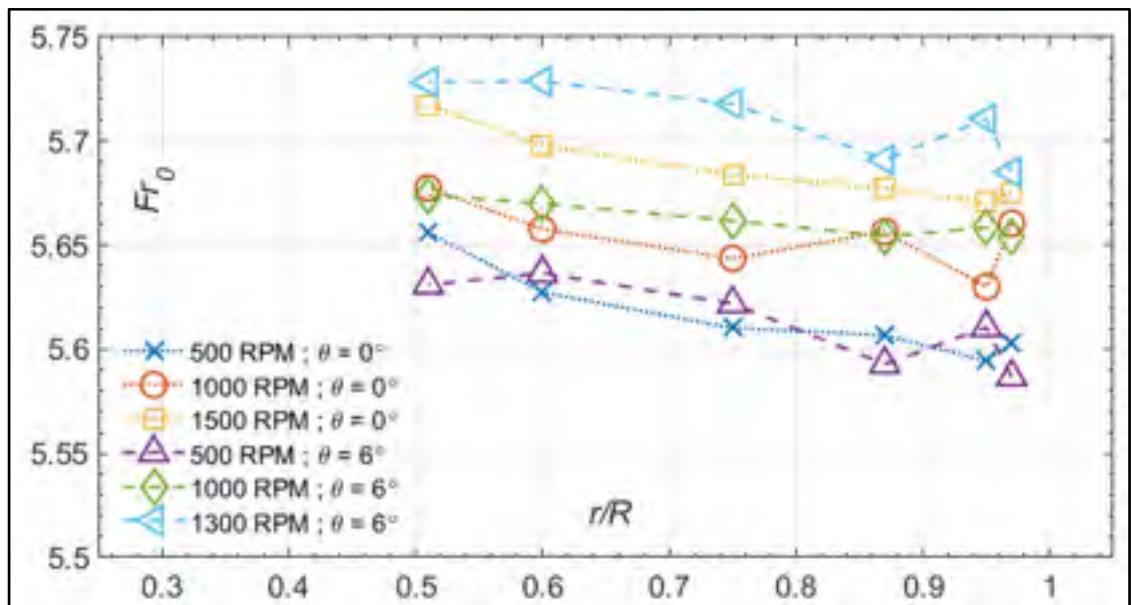

Figure 5.21 Stagnation Point Fr_0 versus r/R Obtained Through (Van Fossen et al., 1995) Correlation for 500 RPM $\leq \Omega \leq$ 1500 RPM and at $\theta = 0°$ and $\theta = 6°$

Therefore, it is felt like the tests at $\theta = 0°$ show a turbulence augmentation of heat transfer in the laminar region and forced the flow into an early transition. This is suspected based on the shape of the Fr_x curves of Figure 5.16 that resemble those of the fixed wing tests. The low Re plus the zero pitch alone are unlikely to cause a transition and subsequent turbulent flow, at least not with the furthest placed RTD being at $S/c = 0.44$. The TI involved could also explain the agreement of heat transfer measurements with the numerical tools that are based on a fully turbulent CFD database and with correlation parameters $0.342 \leq m \leq 0.371$.

The tests at $\theta = 6°$ also showed Fr_x variations that resemble more a transitional flow, especially since the peak of Fr_x values moved between $S/c = 0.3$ at $r/R = 0.75$ and $S/c = 0.15$ at $r/R = 0.6$ (which could be due to the movement of the transition point). Although similar Re were seen at the tests with $\theta = 0°$, the increased pitch is a factor for inducing transition. The correlation parameter was also in the range $0.355 \leq m \leq 0.449$, showing no agreement with what's expected from a strictly laminar flow ($m = 0$).

Finally, the rotor tests show that there will always be some level of turbulence present over the rotor blades when subjected to a freestream of air. The level of turbulence itself is minimized with an increased Ω (or decreased V_∞) and vice versa. This turbulence will cause turbulent augmentation of the heat transfer at the stagnation point, laminar and turbulence regions as indicated by (Ames, 2017). According to the same source, it will affect the transition location as well. So the use of a fully turbulent CFD database for heat transfer estimation with the BEMT-RHT and UVLM-RHT was a good approximation to begin with, given the good agreement between numerical and experimental data at $\theta = 0°$. The limitation of the two numerical tools was seen when transition was involved (more obvious at $\theta = 6°$) and the agreement with experimental data was mostly lost. It should also be noted that in the experiments, the flow is unsteady due to the rotation of the blades whereas the numerical tools benefit from a steady-state CFD database to estimate the heat transfer. The tests could not prove if an averaging of the Fr over the blade sections could have provided a better agreement with the experimental data, since the instrumental limitations of the tests prohibited such investigation. However, the similarity of the m parameter between the rotor tests and fully turbulent CFD simulations, as well as the good agreement between numerical and experimental Fr_x after the supposed transition peak, may suggest that the averaging could provide better results. More investigation however is needed.

5.3 Conclusion

This chapter presented the results of the experimental components of this thesis. The first part of the chapter investigated heat transfer measurements, at different Re and α, on a heated fixed

wing having a NACA 0012 airfoil shape. The other was about heat transfer measurements made in the radial and chord directions of a heated spinning rotor with a NACA 0012 blade shape.

For the fixed wing experiments, the data was collected based on $1 \times 10^5 \le Re \le 1.4 \times 10^6$ and $0° \le \alpha \le 15°$ using 10 RTDs distributed across the chord between $- 0.62 \le S/c \le + 0.87$. The total experimental error was estimated at 17.5% for $Re \le 6 \times 10^5$ and 22.5% for $Re \ge 6 \times 10^5$. The Fr_x measurements at the stagnation point when $\alpha = 0°$ were in range of those obtained by the experiments of (Poinsatte, 1990), especially for $Re \ge 4 \times 10^5$. When compared to the predictions of fully turbulent CFD, both experimental data fell short by an average of 8%. With the experimental error involved, the present experiments show a discrepancy with CFD as high as 36.9%. The Fr_x values at lower Re showed increasing values however, when constant values were more likely expected.

In terms of the chordwise variation of the Fr_x, the experiments showed a different behavior than that of fully turbulent CFD simulations and resembled more the curves of the BO 28 experiments of (Li et al., 2009). The latter attributed the decrease of Fr_x near the L.E. to laminar flow, consequent increase to flow transition and following decrease to fully turbulent flow. All three patterns were seen through the present test results. Moreover, a comparison with a CFD implementation of the B-C transitional model at $Re = 1.25 \times 10^6$ showed a similar Fr_x behavior. The experimental data showed Fr_x values that were in range of their numerical counterparts, however the maximum discrepancy was 35.5% compared to the fully turbulent CFD, and up to 50% compared to the CFD transitional model. The increase of α between the tests showed the Fr_x to increase on the suction side and decrease on the pressure side.

The Fr_x and Re were correlated based on $Fr_x = A \times Re^m \times Pr^{1/3}$ at each of the measured S/c. When the A values determined from correlating the fully turbulent CFD data was used to correlate the experimental data, the m parameter almost matched between the two approaches. This indicated that in the experiments, the Fr_x was varying with Re in a similar way that is expected

for turbulent flows. The *m* values were also in the same order of magnitude as previously established fully turbulent flat plate correlations.

A similar conclusion was found when the Fr_{Avg} from experiments was correlated and compared to the correlated CFD data. The average discrepancy between the experimentally and numerically determined Fr_{Avg} was 4.44% for $\alpha = 0°$, 18.02% for $\alpha = 5°$, 23.90% for $\alpha = 10°$ and 32.3% for $\alpha = 15°$ with the experimental data always overpredicting the Fr_{Avg}. The increase of α showed increasing Fr_{Avg} values, contradicting the fully turbulent CFD predictions, most likely due to the presence of laminar to turbulent transition.

The turbulence intensity *TI* was suspected to affect the measured Fr_x based on 3 observed points. The first was the increase of Fr_x at the stagnation point where the literature indicates a constant value is more expected. The second was the absence of an Fr_x behavior in the laminar flow region where the Fr_x values should not change with *Re*. Finally, the correlation parameters from experiments that agree with those of the fully turbulent CFD. By applying the calculated *TI* and *Re* from the tests to the correlation of (Van Fossen et al., 1995), it was found that a turbulence heat transfer augmentation is expected to cause an increase up to 12% at the stagnation point and near the L.E. This augmentation, when combined with the estimated experimental error, could explain the limitations found in the measured Fr_x values.

For the rotor tests, the measurements were made at 3 different radial locations per test. Rotor speeds up to 1500 RPM were used with $\theta = 0°$ and $\theta = 6°$. The total experimental error was estimated at 25.1%. In the chordwise direction, the Fr_x variation resembled what was seen in the fixed wing tests. An initial decrease of values was seen, followed by a sharp increase of Fr_x and an eventual decrease at the last point of measurement.

It was possible to correlate the measured Fr_x based on $Fr_x = A \times Re^m \times Pr^{1/3}$ at each of the measured *S/c*. The parameter *m* was determined to be between $0.331 \leq m \leq 0.445$, even for the tests at $\theta = 0°$. As discussed previously, these values correspond more to an Fr_x correlation under turbulent flow conditions. While it's no surprise that at the tests with higher *Re*, transition

will occur and subsequent turbulent will develop, the range of m values was surprising especially near the L.E. and for the tests with the lower Re.

It was found that there were significant TI values occurring on the rotor sections during tests, in the range of 9% $\leq TI \leq$ 47%. A review of the literature indicates that with similar TI values, turbulent heat transfer augmentation is bound to happen. When the correlation of (Van Fossen et al., 1995) was applied, a heat transfer augmentation of up to 11% was predicted at the stagnation point. The TI will cause an increase of heat transfer throughout the chord and span of the rotor, mainly due to the interaction of the rotation and incoming tunnel velocities. Therefore, the collapse of the Fr_x curves into in the laminar region and at the stagnation point is unlinkely and is confirmed in the results of Figure 5.16 and Figure 5.17.

In terms of comparing the measured Fr_x to the values predicted by the BEMT-RHT and UVLM-RHT, the agreement was better for the non-lifting rotor test case compared to the rotor at θ = 6°. Both numerical tools predicted similar Fr_x values, with no more than 10% discrepancy. For the rotor at θ = 0°, most points agreed with numerical predictions between 5% and 12% while the point at S/c = 0.12 consistently showed experimental values up to 43% less. At θ = 6°, most points at r/R = 0.95 agreed within 10% of numerical predictions. At r/R = 0.75, the point at S/c = 0.15 and S/c = 0.3 showed Fr_x values up to 55% than the numerical predictions and were thought to be the results of a flow transition in that region. Finally, at r/R = 0.6 the point at S/c = 0.3 was in range of the numerical predictions, while the other points showed a discrepancy up to 80% higher.

Concluding, the BEMT-RHT and UVLM-RHT are numerical tools based on a coupling between classical aerodynamic methods and a fully turbulent CFD heat transfer database. The rotor tests showed that for a rotor subjected to a freestream of air, a level of turbulence will be present throughout the blade sections. This TI will cause increases of the heat transfer throughout the airfoil sections that are higher than what's found on a no-to-low turbulence airfoil flow. As a result, the stagnation and laminar regions did not show a uniform value of the Fr_x as seen in the work of (Poinsatte, 1990) and (Li et al., 2009). Moreover, the

experimental data show that the variation of Fr_x with Re resemble more what's expected from the fully turbulent CFD simulations. The use of the fully turbulent CFD database with the BEMT-RHT and UVLM-RHT was therefore useful in calculating the Fr_x on the rotor blades. Its main limitation however was in the lack of a proper estimation of the transition effect on heat transfer.

CONCLUSION

This thesis presented the development of the BEMT-RHT and UVLM-RHT, two numerical tools that predict heat transfer rates on helicopter rotor blades. State-of-the-art research showed that CFD simulations are capable to successfully modeling the problem with a high-fidelity approach. However, since low and medium-fidelity approaches were the target of this work, a coupled technique was adopted for the numerical models' development. Previous works showed that coupled classical aerodynamic methods with viscous CFD databases produce a higher-fidelity analysis while maintaining a computationally inexpensive solution. The originality of the present research is in the introduction of an added layer of the coupling technique to predict rotor blade heat transfer using the BEMT and the UVLM. The new approach implemented the viscous coupling of the two methods from one hand and introduced a link to a new NACA 0012 CFD-determined heat transfer correlation. This way, the convective heat transfer on rotor blades was estimated while benefiting from the viscous extension of the BEMT & UVLM.

The main objective of this thesis was to implement a new methodology of coupling between CFD determined viscous plus heat transfer databases and classical rotor aerodynamic methods to calculate the external convective heat transfer onto a rotating blade while heated in a computationally inexpensive approach. The main objective was split into four specific objectives as follows:

- Build a database of airfoil viscous and heat transfer data using 2D CFD simulations and correlate the average heat transfer data using a curve fitting method
- Develop & validate a low-fidelity (steady-state) numerical tool that uses a viscous implementation of the BEMT as a rotor aerodynamic modeling tool, and apply a coupling method to the heat transfer correlations to allow blade heat transfer calculation
- Develop & validate a medium-fidelity (unsteady) numerical tool that uses a viscous implementation of the UVLM as a rotor aerodynamic modeling tool, and apply a coupling method to the heat transfer correlations to allow blade heat transfer calculation

- Compare the convective heat transfer predictions of the low and medium fidelity tools to measurements obtained through experimental work designed and conducted in the Icing Wind Tunnel (IWT) of the UQAC on the surface of a heated fixed wing and a heated 2-blade rotor

For the first specific objective, a flat plate test case was simulated using SU2 to verify its thermal capabilities. Comparisons of the predicted C_f with correlations from the literature indicate an agreement within 98%. The predicted Fr_x also showed an agreement between 92% and 98% with flat plate correlations for either TBC imposed. NACA 0012 CFD RANS simulations were ran using SU2 for a range of $2 \times 10^5 \leq Re \leq 3 \times 10^6$ and $0° \leq \alpha \leq 30°$. A fully turbulent flow was assumed and two TBCs were investigated: the constant T_S and the constant Q_S. The CFD determined Fr_x values at the stagnation point of the airfoil were 8% higher than values measured by experiments from the literature, which was deemed acceptable. A comparison between the CFD simulations with the different TBCs showed that the constant Q_S predicts Fr_{Avg} values 2% to 4% lower than a constant T_S, at the same Re and α. To come up with the new NACA 0012 correlation, the Fr_{Avg} was calculated for each simulation. This way, one value of the Fr_{Avg} was obtained for each unique combination of Re & α. From the other hand, the Fr_{Max} was defined as the average Fr values over the first zone measuring 20% of the c after the L.E. Similar to the Fr_{Avg}, a unique value for the Fr_{Max} was defined for each Re & α. The results of the calculated Fr_{Avg} and Fr_{Max} were then correlated using curve fitting method and resulted with 2 correlations for each parameter, one for each different TBCs. The correlations variables were the Re and α while the constants were the Pr and other constants determined by the curve fitting. Aside from the Fr_{Avg} and Fr_{Max} correlations, the NACA 0012 CFD simulations also produced viscous data that were incorporated in the BEMT and UVLM to increase their fidelity. The data were mainly in the form of $C_{L\alpha}$, C_L and C_D. To link either method to the correlations or the viscous data, the Re and α_{Eff} were needed at each blade radial location.

For the second specific objective, the BEMT was implemented based on the work of (Leishman, 2000) and could model multi-blade rotors in hover and axial flight. The classical BEMT was fitted with Prandtl's scheme to account for tip loss effects. To validate the implemented BEMT in terms of rotor aerodynamic performance, two experimental test cases from the literature for a rotor in hover and axial flight were simulated. For the case of a 2-blade hovering rotor, the BEMT predicted C_T and C_{Ly} values 15% to 20% higher than experiments, which is expected by similar implementations of the BEMT. For the 2-blade rotor in axial flight, the *FM* results of the BEMT agreed within $\pm$ 7% of the experiments.

The *Re* and α_{Eff} were readily obtained from the BEMT and required no scheme to calculate, so the coupling to the viscous database and heat transfer correlations was straightforward. The viscous database was interpolated and the corresponding viscous parameters at each blade radius were incorporated into the calculation procedure. The *Re* & α_{Eff} were also used with the new heat transfer correlations and the Fr_{Avg} and Fr_{Max} at each blade element was calculated. The BEMT-RHT was considered a low-fidelity method since it could predict the heat transfer only at steady-state conditions.

For the third specific objective, the UVLM was inspired by the formulation (Katz & Plotkin, 2001) and could model multi-blade rotors in hover, IGE, axial and forward flight. Modifications to the original UVLM included first modifying the code to model rotors instead of fixed wing. The Lamb-Oseen viscous core model was added to the procedure of induced velocities calculation to eliminate singularities that may arise from blade-wake interactions. To account for compressibility effects, the Prandtl–Glauert compressibility correction factor was also added. Finally, a slow start method was implemented on the first 2 or 3 simulated rotor revolutions to stabilize the wake and eliminate instabilities. To validate the implemented UVLM in terms of rotor aerodynamic performance, four experimental test cases from the literature were simulated. For the case of a 2-blade hovering rotor, the implemented UVLM predicted C_T and C_{Ly} values within 98% agreement with experiments. The *TVAL & TVRL* by the UVLM agreed within 90% for a 4-blade rotor in ground effect and thrust predictions matched those of the experiments and other numerical implementations up to $h/R = 0.52$. In

extreme ground effect, the UVLM did not provide satisfactory results. For a 2-blade rotor in axial flight, the *FM* results of the UVLM agreed within ± 7% of the experiments. The UVLM also predicted *TVAL* & *TVRL* values within 92% of the experiments. Finally, the UVLM was also validated within 75% compared to experiments results of a 2-blade rotor in forward flight although 87% agreement with a free wake method from the literature was noted.

For the UVLM, the α_{Eff} across the simulated blade radius needed an extra layer of calculations to be determined. A viscous coupling algorithm based on the α - method was implemented to obtain the α_{Eff} at each blade radial location. The coupling algorithm follows an iterative procedure between the inviscid terms calculated by the UVLM and the CFD-determined viscous database, predicting the α_{Eff} and substituting the inviscid terms with viscous data from the database at the same time. The Fr_{Avg} and Fr_{Max} at each blade radial location were then calculated using the calculated Re & α_{Eff} with the new heat transfer correlations. The UVLM-RHT was considered of medium-fidelity since it could predict the heat transfer while the blade moves with the Ψ.

A modified version of the Bell 429 tail rotor was used to implement the new rotor heat transfer numerical tools. The 4-blade rotor was modeled in four different flight conditions. The BEMT-RHT was used to model hovering and axial flight conditions, while the broader range of applicability of the UVLM-RHT allowed modeling of hovering, axial and forward flight as well as the ground effect. It was found that the Fr_{Avg} predicted by the BEMT-RHT and the UVLM-RHT was within 1% for both the hovering test case and axial flight. The Fr_{Max} showed a higher discrepancy between 4% to 8% due to a difference in the computation of α_{Eff} by each method. Although both methods provided relatively quick results, the BEMT-RHT takes a fraction of the simulation time compared to the UVLM-RHT. For the same flight conditions, the proposed Fr correlations showed that the Re has a greater impact on the heat transfer than the α_{Eff} predicted by either method. The Fr_{Avg} variation in the radial direction was almost the same for the rotor in hover, IGE, axial flight or when the blade is at $\Psi = 90°$ or $\Psi = 270°$ in forward flight. The highest discrepancy found was for the case of axial flight near the rotor hub and was less than 5%. In forward flight, the Fr_{Avg} changed with Ψ due to the movement

of the blade between advancing and retreating regions. At the angle of maximum velocity, the Fr_{Avg} increased by around 17%. At the Ψ with corresponding minimum velocity, the Fr_{Avg} decreased by as much as 25%. Remarkable differences in Fr_{Max} between the different flight conditions were noted. Compared to the hovering rotor with no ground effect, the Fr_{Max} of the IGE rotor increased up to 9% due to an increase in the α_{Eff}. Similarly, the rotor in axial flight showed a different α_{Eff}, leading to a difference of $\pm$ 8% in Fr_{Max}. Finally, as the blades of the rotor in forward flight traveled across the plane of rotation, the Fr_{Max} increased by around 19% at the point of maximum velocity and decreased by 14% when the velocity was minimum.

For the fourth and final specific objective, fixed wing experiments were done in the IWT on a NACA 0012 profile whose wall is almost 90% covered with heating elements that operated at a constant Q_S TBC. It was tested at $\alpha = 0°$, 5°, 10° and 15° and a range of Re between 1×10^5 $\leq Re \leq 1.4 \times 10^6$. 10 RTDs were distributed on the surface to provide Fr_x measurements between $- 0.625 \leq S/c \leq 0.874$. Comparisons of the stagnation point Fr_x values to experimental indicated a discrepancy of no more than 8% compared to the results of previous experiments, specifically for $Re \geq 4 \times 10^5$. For lower Re, the agreement was not satisfactory and is thought to be a result of a varying turbulence intensity and experimental error. Further away from the L.E., the variation of the Fr_x resembled more the transitional behavior seen in an experiment from the literature and another CFD transitional model implementation. The experimental data only showed an agreement with fully turbulent CFD data after a peak of Fr_x values that was found usually around $S/c = \pm 0.625$, where the fully developed flow is supposedly located. A curve fitting process on the data at each S/c to determine the correlation of Fr_x to Re^m showed that the m values for all points were between 0.3 and 0.4. These values correspond more to a turbulent flow behavior, where for a laminar flow the $m = 0$. When the Fr_{Avg} from the experiments was compared to that from CFD, the m values were within 12% of each other, although the Fr_{Avg} were between 4.44% and 32.3% higher than CFD.

Another set of experiments was done on a 2-blade rotor with a NACA 0012 profile, the blades of which were heated at a constant Q_S TBC. The rotor speeds were varied between 500 RPM and 1500 RPM, the range of Re between the different r/R and Ω was $1 \times 10^5 \leq Re \leq 4 \times 10^5$,

the rotor was tested at $\theta = 0°$ and $\theta = 6°$. The RTDs were distributed to provide measurements between $0.6 \leq r/R \leq 0.95$ and $0 \leq S/c \leq 4/7$. The variation of the Fr_x in the chord direction resembled what was seen in the fixed wing tests. A decrease of the Fr_x near the L.E., followed by a sharp increase of values and a final decrease afterwards was seen at the $\theta = 0°$ tests, and was more obvious with the tests at $\theta = 6°$. The correlation of the Fr_x with the Re at all S/c showed m values that were similar to those found through the fully turbulent CFD simulations. When the BEMT-RHT and UVLM-RHT were used, most points agreed with experiments between 5% and 12% at $\theta = 0°$, while the point at $S/c = 0.12$ consistently showed experimental values up to 43% less. At $\theta = 6°$, the measured Fr_x at $r/R = 0.95$ agreed within 10% of numerical predictions. At $r/R = 0.75$, the point at $S/c = 0.15$ and $S/c = 0.3$ showed Fr_x up to 55% discrepancy with the numerical predictions, and at $r/R = 0.6$ the point at $S/c = 0.3$ was in range of the numerical predictions, while the other points showed a discrepancy up to 80% higher. It was found that the TI caused a heat transfer augmentation on the tested rotor blades, leading to an Fr_x behavior that resembles more what's seen in turbulent flows than flows with no-to-low TI.

Future work for this research is about expanding the heat transfer modeling on helicopter rotor blades into a complete de-icing/anti-icing simulation. With the convective heat transfer estimated by the BEMT-RHT and UVLM-RHT, the later steps of the typical implementation of icing codes described in section 1.1 may be applied. Since the proposed Fr correlation are for a NACA 0012 in fully turbulent flow conditions, the heat transfer database could be expanded to account for transitional flow heat transfer. There is evidence in the literature and in the results of experiments of this thesis that laminar and transitional flows significantly affect heat transfer rates, an investigation resulting with a correlation for such flow conditions would be interesting.

APPENDIX I

TESTING PROCEDURE FOR FIXED WING & ROTOR EXPERIMENTS

For each fixed wing test, the following procedure was followed:

1. Adjust *IWT* air speed and temperature on *IWT* software, stabilize around desired (e.g. 0 °C)
2. Wait for RTD temperatures to stabilize around air temperature (± 0.5 °C was tolerated)
3. Press "*start button*" on control system and start chronometer at the same time to start the test
4. At Time = 20 sec, activate the RTD recorder
5. At Time = 60 sec, activate the heating elements
6. At Time = 600 sec, after the RTD readings have stabilized, turn off heaters
7. At Time = 900 sec, turn off RTD recorder
8. Stop test recording on *IWT* softwar5e and chronometer at the same time, record the time lag between RTD recorder and last chronometer reading

For every rotor test, the following procedure was followed:

1. Make sure on the thermocouple recorder that the temperatures on the rotor are stabilized around desired air temperature (a gradient of ± 0.5 °C may exist)
2. Adjust rotor speed, wind velocity and temperature on SRB software, wait for speed to stabilize and air temperature to stabilize around desired (e.g. 0 °C)
3. Press *Demarrer Test* (on SRB) + Chronometer at the same time to mark the start of the test
4. At Time = 10 sec, activate the thermocouple recorder
5. At Time = 20 sec, activate the blade heating element
6. At Time = 300 sec, after the thermocouple readings have stabilized, turn off heaters
7. At Time = 360 sec, turn off thermocouple recorder

Stop test recording on wind tunnel PC and chronometer at the same time, record the time lag between thermocouple recorder and last chronometer reading

APPENDIX II

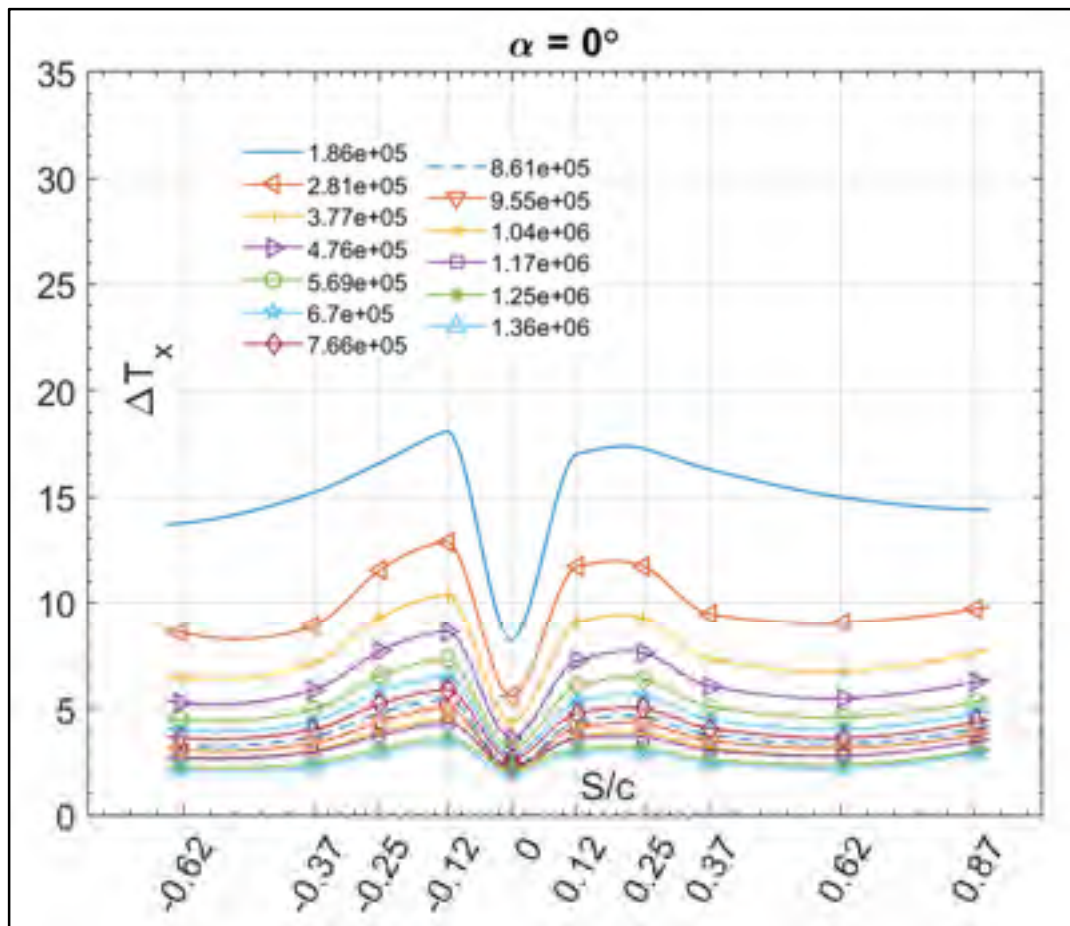## MEASURED TEMPERATURE DIFFERENCE PLOTS FOR FIXED WING EXPERIMENTS

Figure II-1 Measured ΔT_x Variation on NACA 0012 wall for $1.86 \times 10^5 \leq Re \leq 1.36 \times 10^6$ at $\alpha = 0°$
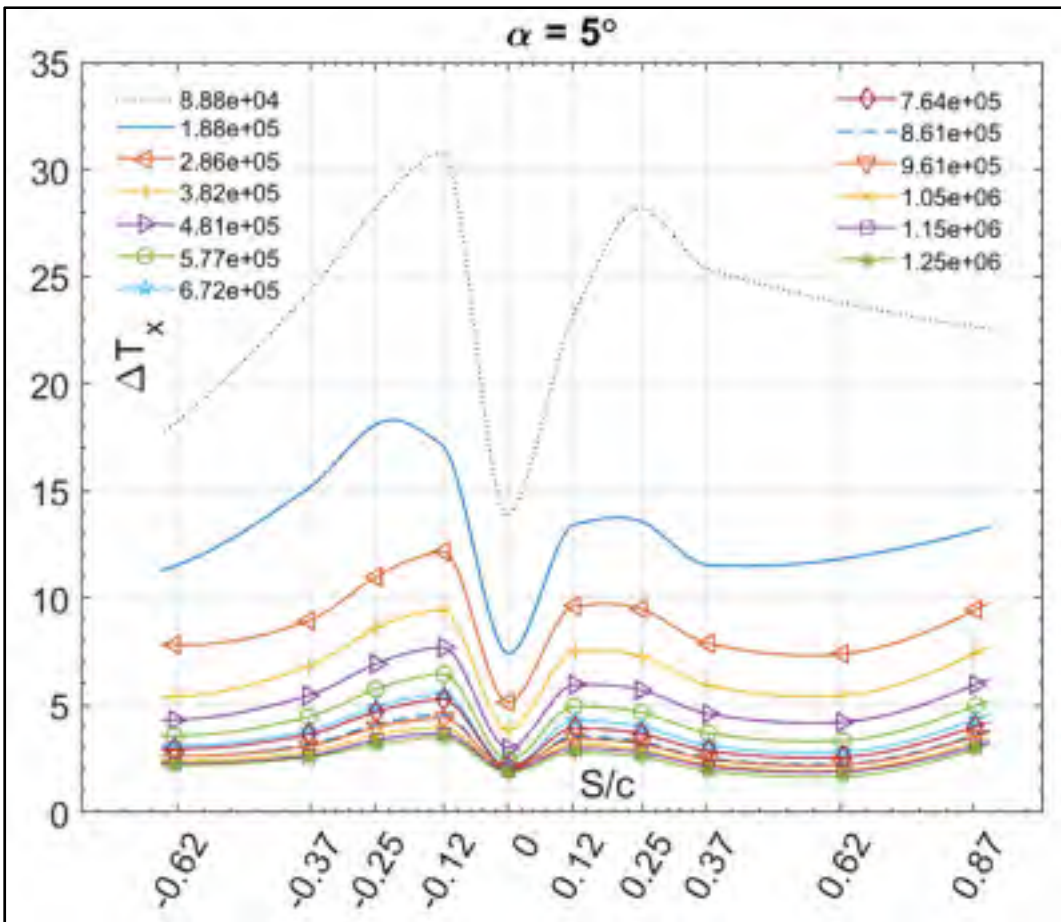
Figure II-2 Measured ΔT_x Variation on NACA 0012 wall for $8.88 \times 10^4 \leq Re \leq 1.25 \times 10^6$ at $\alpha = 5°$
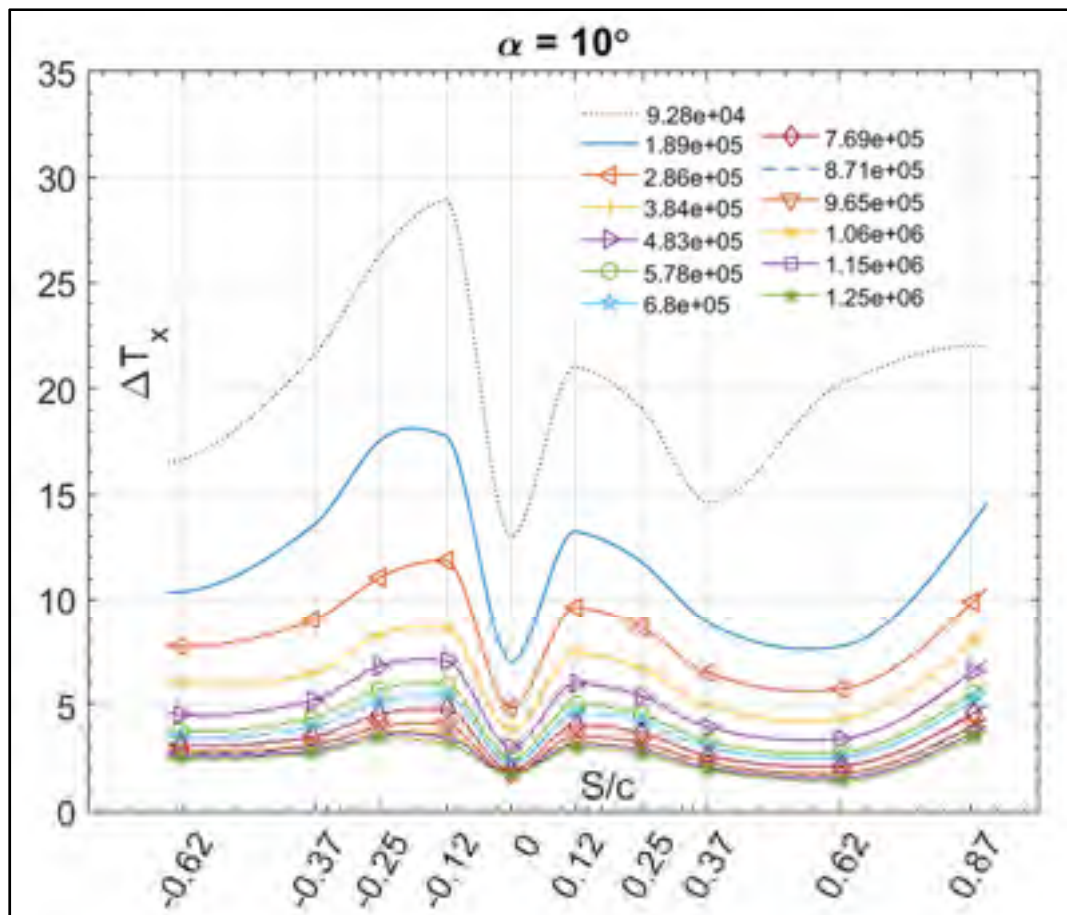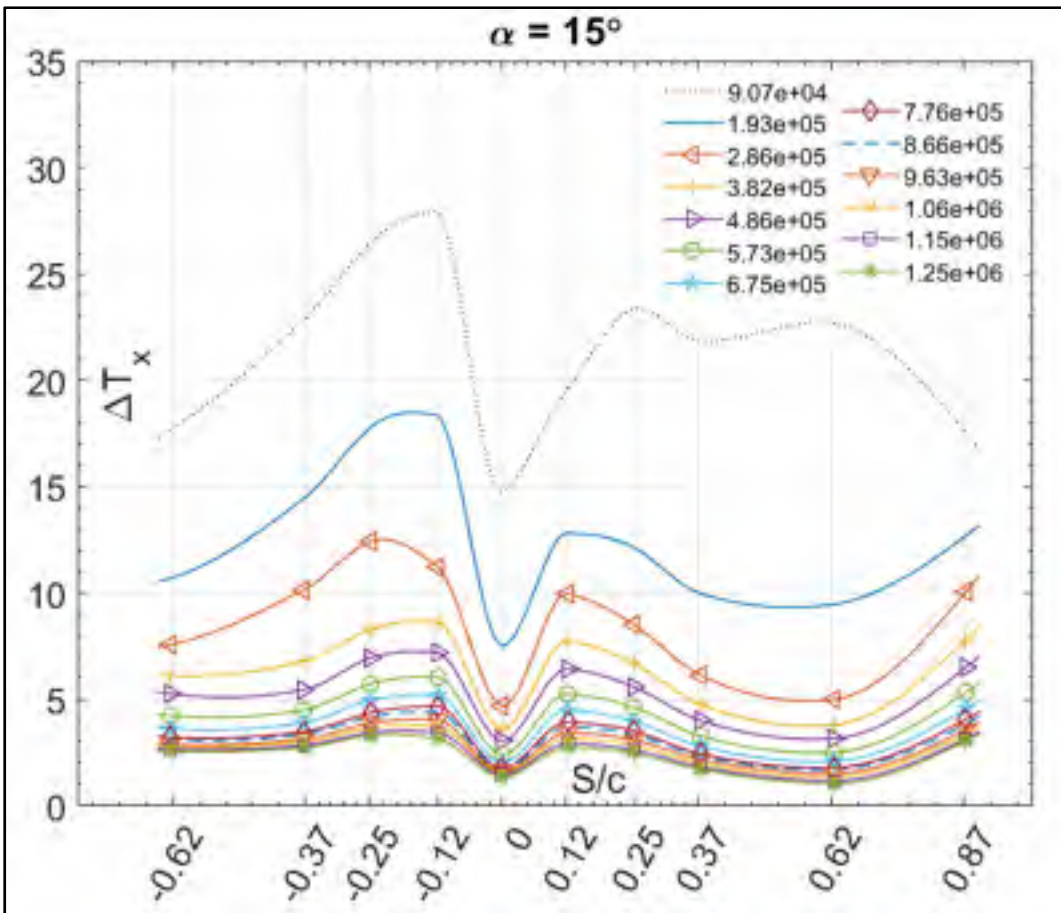
Figure II-3 Measured ΔT_x Variation on NACA 0012 wall for $9.28 \times 10^4 \leq Re \leq 1.25 \times 10^6$ at $\alpha = 10°$

Figure II-4 Measured ΔT_x Variation on NACA 0012 wall for $9.07 \times 10^4 \leq Re \leq 1.25 \times 10^6$ at $\alpha = 15°$

APPENDIX III

MEASURED TEMPERATURE DIFFERENCE PLOTS FOR ROTOR EXPERIMENTS
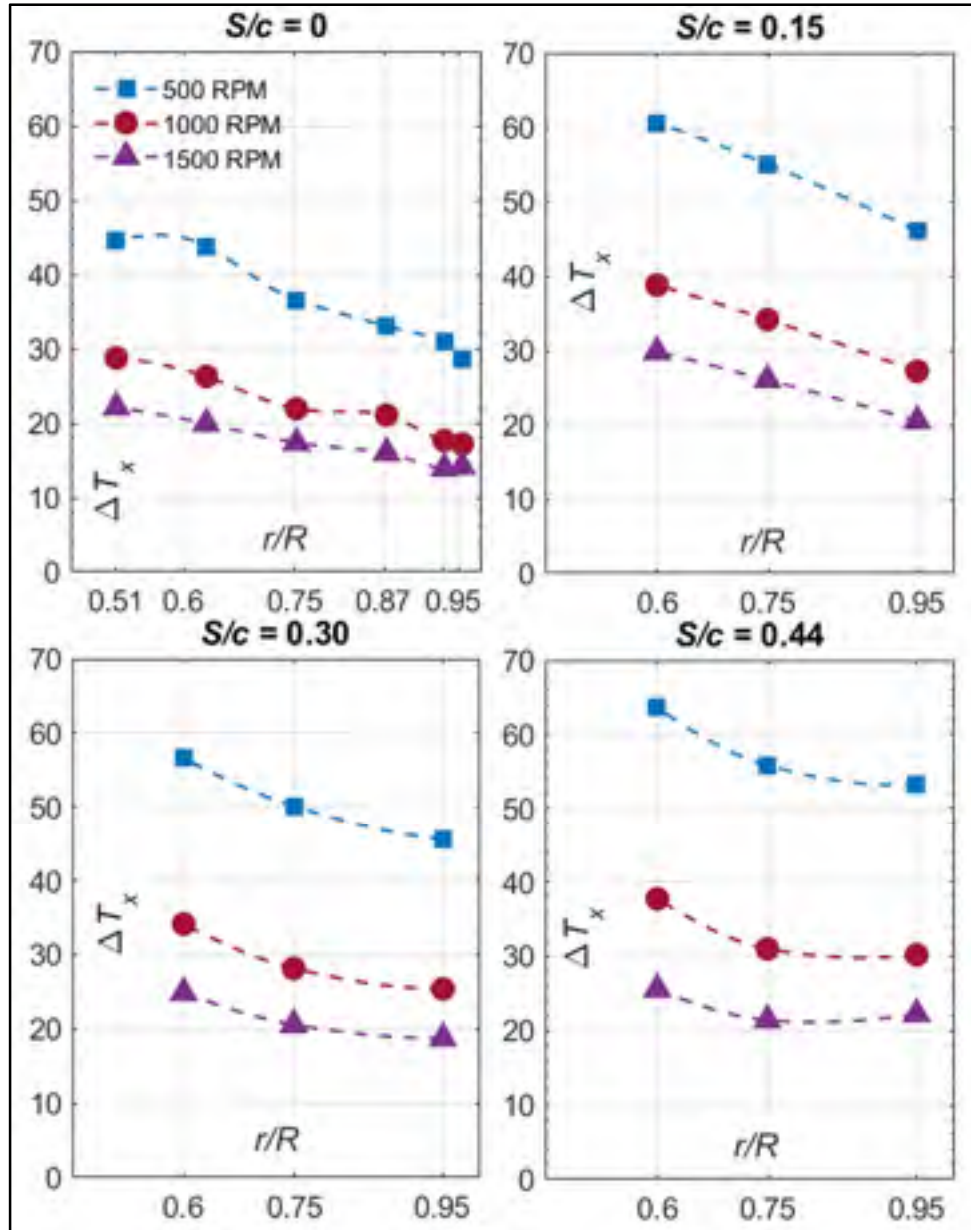
Figure III-1 Radial Variation of ΔT_x at Four Different Chord Locations (S/c = 0, 0.15, 0.3 & 0.44), for Three Rotor Speeds (Ω = 500 RPM, 1000 RPM and 1500 RPM) & θ = 0°
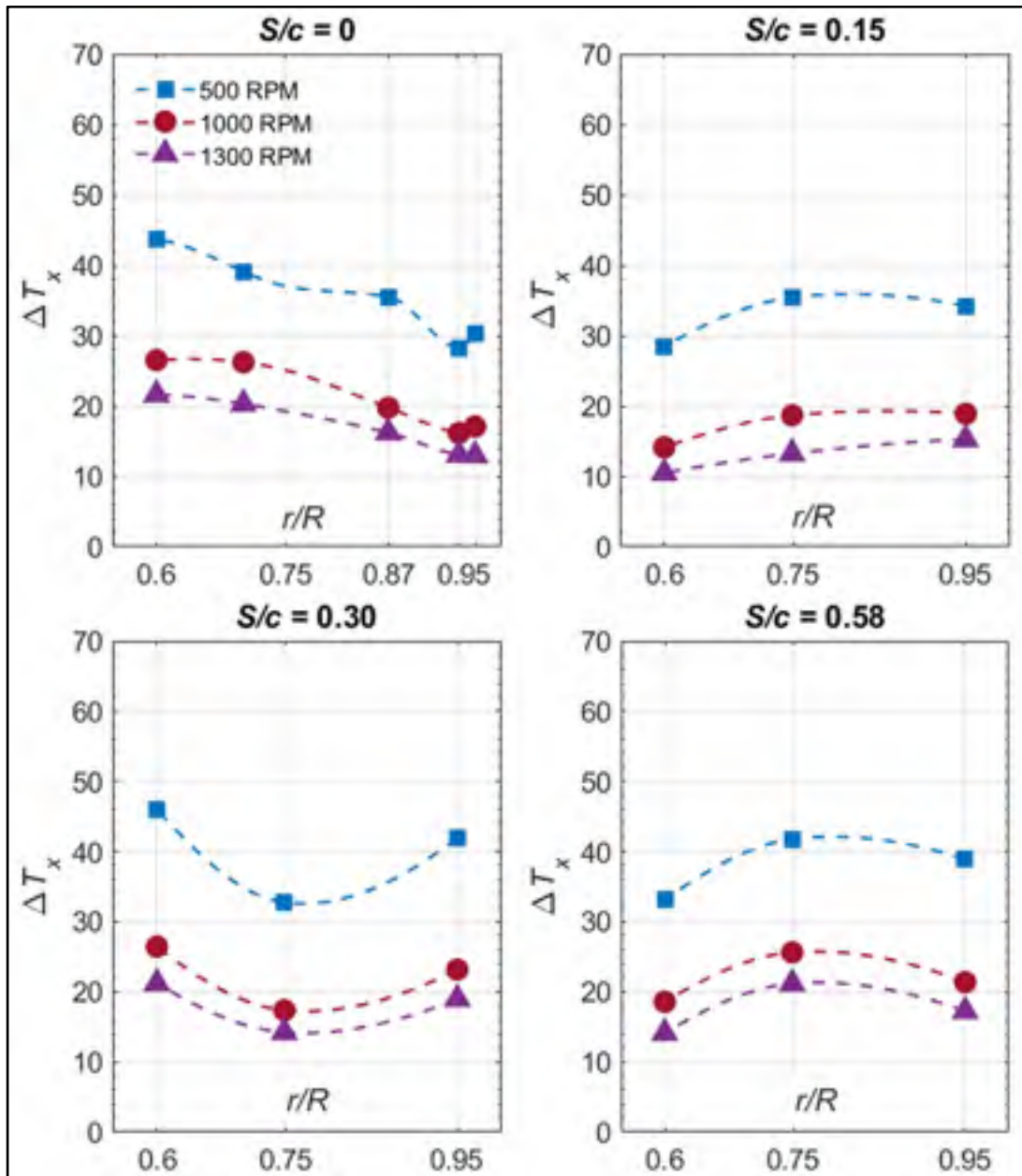
Figure III-2 Radial Variation of ΔT_x at Five Different Chord Locations ($S/c = 0$, 0.15, 0.3 & 0.58), for Three Rotor Speeds ($\Omega = 500$ RPM, 1000 RPM and 1300 RPM) & $\theta = 6°$

LIST OF REFERENCES

Abdollahzadeh, M., Esmaeilpour, M., Vizinho, R., Younesi, A., & Pàscoa, J. (2017). Assessment of RANS turbulence models for numerical study of laminar-turbulent transition in convection heat transfer. *International Journal of Heat and Mass Transfer, 115*, 1288-1308. DOI: 10.1016/j.ijheatmasstransfer.2017.08.114

Achenbach, E. (1975). Total and local heat transfer from a smooth circular cylinder in cross-flow at high Reynolds number. *International Journal of HeatMass Transfer, 18*(12), 1387-1396. DOI: 10.1016/0017-9310(75)90252-5

Aliaga, C. N., Aubé, M. S., Baruzzi, G. S., & Habashi, W. G. (2011). FENSAP-ICE-Unsteady: unified in-flight icing simulation methodology for aircraft, rotorcraft, and jet engines. *Journal of Aircraft, 48*(1), 119-126. DOI: 10.2514/1.C000327

Ames, F. E. (2017). Turbulence Effects on Convective Heat Transfer. In F. A. Kulacki (Ed.), *Handbook of Thermal Science and Engineering* (pp. 1-33). Cham: Springer International Publishing.

Aubert, R. (2003). History of Ice Protection System Design at Bell Helicopter. Paper presented at the *FAA In-flight Icing / Ground De-icing International Conference & Exhibition, June 16 - 20 2003*, Chicago, Illinois, United States. Retrieved from https://saemobilus.sae.org/content/2003-01-2093

Aubert, R. (2015). Additional Considerations for Analytical Modeling of Rotor Blade Ice. Paper presented at the *SAE 2015 International Conference on Icing of Aircraft, Engines, and Structures, 22 - 25 June 2015*, Prague, Czech Republic. Retrieved from https://saemobilus.sae.org/content/2015-01-2080

Aupoix, B., & Spalart, P. (2003). Extensions of the Spalart–Allmaras turbulence model to account for wall roughness. *International Journal of Heat and Fluid Flow, 24*(4), 454-462. DOI: 10.1016/S0142-727X(03)00043-2

Beaugendre, H., Morency, F., & Habashi, W. G. (2003). FENSAP-ICE's three-dimensional in-flight ice accretion module: ICE3D. *Journal of Aircraft, 40*(2), 239-247. DOI: 10.2514/2.3113

220

Beaugendre, H., Morency, F., & Habashi, W. G. (2006). Development of a second generation in-flight icing simulation code. *Journal of Fluids Engineering, 128*(2), 378-387. DOI: 10.1115/FEDSM2003-45816

Bhagwat, M. J., & Leishman, J. G. (2002). Generalized viscous vortex model for application to free-vortex wake and aeroacoustic calculations. Paper presented at the *58th Annual Forum Proceedings- American Helicopter Society, 11-13 June 2002*, Montreal, Canada. Retrieved from https://vtol.org/store/product/generalized-viscous-vortex-model-for-application-to-freevortex-wake-and-aeroacoustic-calculations-1996.cfm

Bourgault-Cote, S., Parenteau, M., & Laurendeau, E. (2019). Quasi-3D multi-layer ice accretion model using a Vortex Lattice Method combined with 2.5 D RANS solutions. Paper presented at the *54th 3AF International Conference on Applied Aerodynamics, 25-27 March 2019*, Paris, France Retrieved from https://www.researchgate.net/publication/332379630_Quasi-3D_multi-layer_ice_accretion_model_using_a_Vortex_Lattice_Method_combined_with_25D_RANS_solutions

Butsuntorn, N., & Jameson, A. (2008). Time spectral method for rotorcraft flow with vorticity confinement. Paper presented at the *26th AIAA Applied Aerodynamics Conference, 18-21 August 2008*, Honolulu, Hawaii, United States. Retrieved from https://arc.aiaa.org/doi/abs/10.2514/6.2008-7340

Cakmakcioglu, S. C., Bas, O., & Kaynak, U. (2018). A correlation-based algebraic transition model. *Proceedings of the Institution of Mechanical Engineers, Part C : Journal of Mechanical Engineering Science, 232*(21), 3915-3929. DOI: [10.1177/0954406217743537](10.1177/0954406217743537)

Caradonna, F. (1999). Performance measurement and wake characteristics of a model rotor in axial flight. *Journal of the American Helicopter Society, 44*(2), 101-108. DOI: 10.4050/JAHS.44.101

Caradonna, F. X., & Tung, C. (1981). Experimental and analytical studies of a model helicopter rotor in hover. Paper presented at the *6th European Rotorcraft and Powered Lift Aircraft Forum; September 16 - 19, 1980*, Bristol, England. Retrieved from https://ntrs.nasa.gov/search.jsp?R=19820004169

Cheeseman, I., & Bennett, W. (1955). *The effect of ground on a helicopter rotor in forward flight*. London, United Kingdom: Retrieved from http://naca.central.cranfield.ac.uk/reports/arc/rm/3021.pdf

Chung, K. H., Kim, J. W., Ryu, K. W., Lee, K. T., & Lee, D. J. (2006). Sound generation and radiation from rotor tip-vortex pairing phenomenon. *American Institute of Aeronautics and Astronautics (AIAA) Journal, 44*(6), 1181-1187. DOI: 10.2514/1.22548

Churchill, S., & Bernstein, M. (1977). A correlating equation for forced convection from gases and liquids to a circular cylinder in crossflow. *Journal of Heat Transfer, 99*(2), 300-306 DOI: 10.1115/1.3450685

Coffman, H. (1987). Helicopter rotor icing protection methods. *Journal of the American Helicopter Society, 32*(2), 34-39. DOI: 10.4050/JAHS.32.34

Coffman, J., H. (1983). Review of helicopter icing protection systems. Paper presented at the *Aircraft Design, Systems and Technology Meeting, 17-19 October 1983*, Fort Worth, TX, U.S.A. Retrieved from https://arc.aiaa.org/doi/pdf/10.2514/6.1983-2529

Colmenares, J. D., López, O. D., & Preidikman, S. (2015). Computational study of a transverse rotor aircraft in hover using the unsteady vortex lattice method. *Mathematical Problems in Engineering*. DOI: 10.1155/2015/478457

Cross, J. L. (1988). *Tip aerodynamics and acoustics test: a report and data survey*. Moffett Field, CA, United States: Retrieved from https://ntrs.nasa.gov/search.jsp?R=19890008208

Edmunds, M., Malki, R., Williams, A., Masters, I., & Croft, T. (2014). Aspects of tidal stream turbine modelling in the natural environment using a coupled BEM–CFD model. *International Journal of Marine Energy, 7*, 20-42. DOI: 10.1016/j.ijome.2014.07.001

Farrokhfal, H., Pishevar, A. R., & Management. (2014). A New Coupled Free Wake-CFD Method for Calculation of Helicopter Rotor Flow-Field in Hover. *Journal of Aerospace Technology, 6*(2), 129-147. DOI: http://dx.doi.org/10.5028/jatm.v6i2.366

Ferlisi, C. (2018). *Rotor Wake Modelling Using the Vortex-Lattice Method*. (M.A.Sc. Thesis École Polytechnique de Montréal, Montréal, Québec.). Retrieved from https://publications.polymtl.ca/3059/1/208_CarloFerlisi.pdf

Filippone, A., Bakker, R., Basset, P., Rodriguez, B., Green, R., Bensing, F., & Visingardi, A. (2011). Rotor wake modelling in ground effect conditions. Paper presented at the *The 35th European Rotorcraft Forum, 22 - 25 September 2009*, Hamburg, Germany. Retrieved from https://www.researchgate.net/publication/272999525_Rotor_Wake_Modelling_in_Ground_Effect_Conditions

Flemming, R. (2003). A History of Ice Protection System Development at Sikorsky Aircraft. Paper presented at the *FAA In-flight Icing / Ground De-icing International Conference & Exhibition, June 16 - 20 2003*, Chicago, Illinois, United States. Retrieved from https://saemobilus.sae.org/content/2003-01-2092

Fortin, G., & Perron, J. (2009). Spinning rotor blade tests in icing wind tunnel. Paper presented at the *1st AIAA Atmospheric and Space Environments Conference, 22-25 June 2009* San Antonio, Texas, United States. Retrieved from https://arc.aiaa.org/doi/abs/10.2514/6.2009-4260

Froessling, N. (1958). *Evaporation, heat transfer, and velocity distribution in two-dimensional and rotationally symmetrical laminar boundary-layer flow*. Retrieved from https://ntrs.nasa.gov/search.jsp?R=20030068788

Gallay, S. (2016). *Algorithmes de couplage RANS et écoulement potentiel.* (PhD Thesis, École Polytechnique de Montréal, Montréal, Québec.). Retrieved from https://publications.polymtl.ca/2061/

Gallay, S., & Laurendeau, E. (2015). Nonlinear generalized lifting-line coupling algorithms for pre/poststall flows. *AIAA Journal, 53*(7), 1784-1792. DOI: 10.2514/1.J053530

Gallay, S., & Laurendeau, E. (2016). Preliminary-design aerodynamic model for complex configurations using lifting-line coupling algorithm. *Journal of Aircraft, 53*(4), 1145-1159. DOI: 10.2514/1.C033460

Gao, H., & Agarwal, R. K. (2019). Numerical Study of a Hovering Helicopter Rotor Blade in Ground Effect. Paper presented at the *AIAA Scitech 2019 Forum, Jan 7-11, 2019*, San Diego, California, United States. Retrieved from https://arc.aiaa.org/doi/abs/10.2514/6.2019-1099

Gennaretti, M., Bernardini, G., Serafini, J., & Romani, G. (2018). Rotorcraft comprehensive code assessment for blade–vortex interaction conditions. *Aerospace Science and Technology, 80,* 232-246. DOI: 10.1016/j.ast.2018.07.013

Gent, R., Moser, R., Cansdale, J. T., & Dart, N. (2003). *The Role of Analysis in the Development of Rotor Ice Protection Systems* (0148-7191). United States: Retrieved from https://saemobilus.sae.org/content/2003-01-2090

Glauert, H. (1928). The effect of compressibility on the lift of an aerofoil. *Proceedings of the Royal Society of London. Series A, Containing Papers of a Mathematical and Physical Character, 118*(779), 113-119. DOI:

Gouttebroze, S., Saeed, F., & Paraschivoiu, I. (2000). CANICE - Capabilities and Current Status. Paper presented at the *NATO/RTO Workshop, Assessment of Icing Code Prediction Capabilities, Dec. 6-7, 2000*, Capua, Italy. Retrieved from https://www.researchgate.net/profile/Farooq_Saeed/publication/228932401_Ice_Accr etion_Simulation_Code_CANICE/links/56b5066208ae3c1b79ab1fef/Ice-Accretion-Simulation-Code-CANICE.pdf

Guffond, D., & Brunet, L. (1988). *Validation du Programme Bidimensionnel de Capitation // Oce National D'Etudes et de Recherches Aerospatiales.*

Guidelines for Aircraft Ground Icing Operations 4th Edition. (2019). Retrieved from https://tc.canada.ca/en/aviation/publications/tp-14052-guidelines-aircraft-ground-icing-operations

Habashi, W. G. (2009). Recent advances in CFD for in-flight icing simulations. *Japan Society of Fluid Mechanics, 28*(2), 99-118. DOI: https://pdfs.semanticscholar.org/c425/00a34b46464392df2aee6f7f4260086b53ec.pdf

Habashi, W. G., Aubé, M., Baruzzi, G., Morency, F., Tran, P., & Narramore, J. C. (2004). FENSAP-ICE: a fully-3d in-flight icing simulation system for aircraft, rotorcraft and UAVS. Paper presented at the *24th International Congress of The Aeronautical Sciences, 29 August - 3 September 2004*, Yokohama, Japan. Retrieved from http://www.icas.org/ICAS_ARCHIVE/ICAS2004/PAPERS/608.PDF

Han, Y., & Palacios, J. (2017). Surface roughness and heat transfer improved predictions for aircraft ice-accretion modeling. *American Institute of Aeronautics and Astronautics (AIAA) Journal*, 1318-1331. DOI: 10.2514/1.J055217

224

He, C., & Zhao, J. (2009). Modeling rotor wake dynamics with viscous vortex particle method. *American Institute of Aeronautics and Astronautics (AIAA) Journal, 47*(4), 902-915. DOI: 10.2514/1.36466

Helicopter Flying Handbook. (2012). Retrieved from https://www.faa.gov/regulations_policies/handbooks_manuals/aviation/helicopter_flying_handbook/

Hilpert, R. (1933). Heat Transfer from Cylinders. *Forsch. Geb. Ingenieurwes, 4*(5), 215. DOI:

Incropera, F. P., Lavine, A. S., Bergman, T. L., & DeWitt, D. P. (2007). *Fundamentals of Heat and Mass Transfer* (7th ed.). New York: John Wiley & Sons.

Katz, J., & Plotkin, A. (2001). *Low Speed Aerodynamics* (2nd ed. Vol. 13). New York: Cambridge University Press.

Kays, W. M., & Crawford, M. (1993). *Convective Heat and Mass Transfer* (3rd ed.). New York: McGraw-Hill.

Kim, J. W., Park, S. H., & Yu, Y. H. (2009). Euler and Navier-Stokes simulations of helicopter rotor blade in forward flight using an overlapped grid solver. Paper presented at the *19th AIAA Computational Fluid Dynamics; 22 - 25 June 2009*, San Antonio, Texas, United States. Retrieved from https://arc.aiaa.org/doi/abs/10.2514/6.2009-4268

Lavoie, P., Pena, D., Hoarau, Y., & Laurendeau, E. (2018). Comparison of thermodynamic models for ice accretion on airfoils. *International Journal of Numerical Methods for Heat & Fluid Flow, 28*(5), 1004-1030. DOI: 10.1108/HFF-08-2016-0297

Leary, W. M. (2002). *We Freeze to Please: A History of NASA's Icing Research Tunnel and the Quest for Flight Safety* (Vol. 4226). Washington D.C., United States: National Aeronautics and Space Administration NASA.

Lee, J.-B., Yee, K.-J., Oh, S.-J., & Kim, D.-H. (2009). Development of an unsteady aerodynamic analysis module for rotor comprehensive analysis code. *International Journal of Aeronautical and Space Sciences, 10*(2), 23-33. DOI: 10.5139/IJASS.2009.10.2.023

Leishman, G. (2000). *Principles of Helicopter Aerodynamics* (1st ed.). Cambridge, United Kindom: Cambridge University Press.

Leishman, J. G., Bhagwat, M. J., & Bagai, A. (2002). Free-vortex filament methods for the analysis of helicopter rotor wakes. *Journal of Aircraft, 39*(5), 759-775. DOI: 10.2514/2.3022

Li, G., Gutmark, E. J., Ruggeri, R. T., & Mabe, J. (2009). Heat Transfer and Pressure Measurements on a Thick Airfoil. *Journal of Aircraft, 46*(6), 2130-2138. DOI: 10.2514/1.44093

Lienhard, J. (2020). Heat transfer in flat-plate boundary layers: a correlation for laminar, transitional and turbulent flow. *Journal of Heat Transfer, 142*(6). DOI: 10.1115/1.4046795

Light, J. S. (1993). Tip vortex geometry of a hovering helicopter rotor in ground effect. Paper presented at the *45th AHS Annual Forum; May 22 - 24, 1989*, Boston, MA; United States. Retrieved from https://ntrs.nasa.gov/search.jsp?R=19900041141

Masters, I., Williams, A., Croft, T., Togneri, M., Edmunds, M., Zangiabadi, E., . . . Karunarathna, H. (2015). A comparison of numerical modelling techniques for tidal stream turbine analysis. *MDPI - Energies, 8*(8), 7833-7853. DOI: 10.3390/en8087833

MATLAB. (2019a). Modified Akima piecewise cubic Hermite interpolation. Natick, Massachusetts.The MathWorks Inc. Retrieved from https://www.mathworks.com/help/matlab/ref/makima.html

MATLAB. (2019b). Solve nonlinear least-squares (nonlinear data-fitting) problems. Natick, Massachusetts.The MathWorks Inc. Retrieved from https://www.mathworks.com/help/optim/ug/lsqnonlin.html

Moffat, R. J. (1988). Describing the uncertainties in experimental results. *Experimental thermal and fluid science, 1*(1), 3-17. DOI: 10.1016/0894-1777(88)90043-X

Montreuil, E., Chazottes, A., Guffond, D., Murrone, A., Caminade, F., & Catris, S. (2009). ECLIPPS: 1 Enhancement of Prediction Capability in Icing Accretion and related Performance Penalties Part I: Three-dimensional CFD Prediction of the Ice Accretion. Paper presented at the *1st AIAA Atmospheric and Space Environments Conference, 22-25 June 2009*, San Antonio, Texas, United States. Retrieved from https://arc.aiaa.org/doi/abs/10.2514/6.2009-3969

Morency, F., Tezok, F., & Paraschivoiu, I. (1999). Anti-icing system simulation using CANICE. *Journal of Aircraft, 36*(6), 999-1006. DOI: 10.2514/2.2541

Mu, Z., Lin, G., Shen, X., Bu, X., & Zhou, Y. (2018). Numerical simulation of unsteady conjugate heat transfer of electrothermal deicing process. *International Journal of Aerospace Engineering, 2018*. DOI: 10.1155/2018/5362541

Newton, J., Vanfossen, J., Poinsatte, P., & Dewitt, K. (1988). Measurement of local convective heat transfer coefficients from a smooth and roughened NACA-0012 airfoil: Flight test data. Paper presented at the *26th Aerospace Sciences Meeting, 11-14 January 1988*, Reno, Nevada, United States. Retrieved from https://ntrs.nasa.gov/search.jsp?R=19880004170

Olczak, A., Stallard, T., Feng, T., & Stansby, P. (2016). Comparison of a RANS blade element model for tidal turbine arrays with laboratory scale measurements of wake velocity and rotor thrust. *Journal of Fluids and Structures, 64*, 87-106. DOI: 10.1016/j.jfluidstructs.2016.04.001

Özgen, S., & Canıbek, M. (2009). Ice accretion simulation on multi-element airfoils using extended Messinger model. *Journal of Heat and Mass Transfer, 45*(3), 305-322. DOI: 10.1007/s00231-008-0430-4

Parenteau, M., & Laurendeau, É. (2018). Nonlinear Frequency-Domain Solver for Vortex Lattice Method. *American Institute of Aeronautics and Astronautics (AIAA) Journal, 56*(6), 2242-2251. DOI: 10.2514/1.J056704

Parenteau, M., Plante, F., Laurendeau, E., & Costes, M. (2017). Unsteady Coupling Algorithm for Lifting-Line Methods. Paper presented at the *55th Aerospace Sciences Meeting, 9 - 13 January 2017*, Grapevine, Texas, USA. DOI: 10.2514/6.2017-0951

Parenteau, M., Sermeus, K., & Laurendeau, E. (2018). VLM Coupled with 2.5 D RANS Sectional Data for High-Lift Design. Paper presented at the *55th Aerospace Sciences Meeting, 8–12 January 2018*, Kissimmee, Florida, USA. DOI: 10.2514/6.2018-1049

Pendenza, A., Habashi, W. G., & Fossati, M. (2015). A 3D mesh deformation technique for irregular in-flight ice accretion. *International Journal for Numerical Methods in Fluids, 79*(5), 215-242. DOI: 10.1002/fld.4049

Peng, L., Yuanli, K., Yupeng, S., & Xunan, H. (2018). Transient simulation and analysis of wing electrothermal ice protection system. *The Journal of Engineering, 2018*(13), 438-445. DOI: http://dx.doi.org/10.1049/joe.2018.0047

Pérez, A. M., Lopez, O., & Poroseva, S. V. (2019). Free-Vortex Wake and CFD Simulation of a Small Rotor for a Quadcopter at Hover. Paper presented at the *AIAA Scitech 2019 Forum; 7-11 January 2019*, San Diego, California, United States. Retrieved from 10.2514/6.2019-0597

Piperni, P., DeBlois, A., & Henderson, R. (2013). Development of a multilevel multidisciplinary-optimization capability for an industrial environment. *AIAA Journal, 51*(10), 2335-2352. DOI: 10.2514/1.J052180

Poinsatte, P. (1990). *Heat transfer measurements from a NACA 0012 airfoil in flight and in the NASA Lewis icing research tunnel.* (MSc Thesis, University of Toledo, Ohio, United States.). Retrieved from https://ntrs.nasa.gov/search.jsp?R=19900009887

Poinsatte, P., Newton, J., De Witt, K., & Van Fossen, J. (1991). Heat transfer measurements from a smooth NACA 0012 airfoil. *Journal of Aircraft, 28*(12), 892-898. DOI: 10.2514/3.46114

Potapczuk, M. G. (2013). Aircraft icing research at NASA Glenn research center. *Journal of Aerospace Engineering, 26*(2), 260-276. DOI: 10.1061/(ASCE)AS.1943-5525.0000322

Pourbagian, M., & Habashi, W. G. (2012). Parametric analysis of energy requirements of in-flight ice protection systems. Paper presented at the *20th Annual conference of the CFD society of Canada, May 9-11, 2012*, Canmore, Alberta, Canada. Retrieved from http://www.sinmec.ufsc.br/~dihlmann/MALISKA/proceedings_cfd_society_of_canada_conference_may_2012/papers/Pourbagian_Habashi.pdf

228

Pourbagian, M., & Habashi, W. G. (2015). Aero-thermal optimization of in-flight electro-thermal ice protection systems in transient de-icing mode. *International Journal of Heat and Fluid Flow, 54*, 167-182. DOI: 10.1016/j.ijheatfluidflow.2015.05.012

Reid, T., Baruzzi, G. S., & Habashi, W. G. (2012). FENSAP-ICE: unsteady conjugate heat transfer simulation of electrothermal de-icing. *Journal of Aircraft, 49*(4), 1101-1109. DOI: 10.2514/1.C031607

Richardson, D., Wahl, H., & Clifford, J. (1958). Solutions for Helicopter Rotor Blade Icing. *Journal of the American Helicopter Society, 3*(3), 3-9. DOI: 10.4050/JAHS.3.3.3

Rizzi, A. (2011). Modeling and simulating aircraft stability and control—The SimSAC project. *Progress in Aerospace Sciences, 47*(8), 573-588. DOI: 10.1016/j.paerosci.2011.08.004

Rodert, L. A., Clousing, L. A., & McAvoy, W. H. (1942). *Recent Flight Research on Ice Prevention*: NACA.

Rumsey, C., Smith, B., and Huang, G. (2014a). 2D Finite Flat Plate Validation Case. *Turbulence Modeling Resource.* Langley Research Center. Retrieved from https://turbmodels.larc.nasa.gov/finiteflatplatenumerics_val.html

Rumsey, C., Smith, B., and Huang, G. (2014b, 08/01/2019). 2D NACA 0012 Airfoil Validation Case *Turbulence Modeling Resource.* Langley Research Center. Retrieved from https://turbmodels.larc.nasa.gov/naca0012_val.html

Ryerson, C. C., Peck, L., & Martel, C. J. (2003). *Army aviation operations in icing conditions* (0148-7191). United States: Retrieved from https://saemobilus.sae.org/content/2003-01-2094

SAE. (1995). *Droplet Sizing Instrumentation Used in Icing Facilities - Aerospace Standard AIR4906*. United States: Retrieved from https://saemobilus.sae.org/content/air4906

SAE. (2003). *Calibration and Acceptance of Icing Wind Tunnels - Aerospace Standard ARP5905*. United States: Retrieved from https://saemobilus.sae.org/content/ARP5905/

SAE. (2013). *Rotor Blade Electrothermal Ice Protection Design Considerations - Aerospace Standard AIR1667A*. United States: DOI: 10.4271/AIR1667A

Shaw, R. J. (2014). History of Flight. National Aeronautics and Space Administration (NASA). Retrieved from https://www.grc.nasa.gov/www/k-12/UEET/StudentSite/historyofflight.html

Shen, W. Z., Mikkelsen, R., Sørensen, J. N., & Bak, C. (2005). Tip loss corrections for wind turbine computations. *Wind Energy: An International Journal for Progress and Applications in Wind Power Conversion Technology, 8*(4), 457-475. DOI: 10.1002/we.153

Spera, D. A. (1994). *Wind Turbine Technology*. United States: Taylor & Francis Group.

Sugiura, M., Tanabe, Y., Sugawara, H., Matayoshi, N., & Ishii, H. (2017). Numerical simulations and measurements of the helicopter wake in ground effect. *Journal of Aircraft*, 209-219. DOI: 10.2514/1.C033665

Sun, Z., Chen, J., Shen, W. Z., & Zhu, W. J. (2016). Improved blade element momentum theory for wind turbine aerodynamic computations. *Renewable energy, 96*, 824-831. DOI: 10.1016/j.renene.2016.05.035

Tan, J., & Wang, H. (2013a). Panel/full-span free-wake coupled method for unsteady aerodynamics of helicopter rotor blade. *Chinese Journal of Aeronautics, 26*(3), 535-543. DOI: 10.1016/j.cja.2013.04.050

Tan, J., & Wang, H. (2013b). Simulating unsteady aerodynamics of helicopter rotor with panel/viscous vortex particle method. *Journal of Aerospace Science and Technology, 30*(1), 255-268. DOI: 10.1016/j.ast.2013.08.010

Van Dam, C. (2002). The aerodynamic design of multi-element high-lift systems for transport airplanes. *Progress in Aerospace Sciences, 38*(2), 101-144. DOI: 10.1016/S0376-0421(02)00002-7

Van Fossen, G. J., Simoneau, R., & Ching, C. (1995). Influence of turbulence parameters, Reynolds number, and body shape on stagnation-region heat transfer. *Journal of Heat Transfer*. DOI: 10.1115/1.2822619

Vatistas, G. H., Kozel, V., & Mih, W. (1991). A simpler model for concentrated vortices. *Experiments in Fluids, 11*(1), 73-76. DOI: 10.1007/BF00198434

Villeneuve, E., & Perron, J. (2012). *Icing Wind Tunnel Certification Tests in Accordance with SAE ARP5905 and AIR4906.*

Villeneuve, E., Volat, C., & Ghinet, S. (2020). Numerical and Experimental Investigation of the Design of a Piezoelectric De-icing System for Small Rotorcraft Part 3/3: Numerical Model and Experimental Validation of Vibration-Based De-Icing of a Flat Plate Structure. *Journal of Aerospace, 7*(5), 54. DOI: 10.3390/aerospace7050054

Wang, X., Naterer, G., & Bibeau, E. (2007a). Convective droplet impact and heat transfer from a NACA airfoil. *Journal of Thermophysics and Heat Transfer, 21*(3), 536-542. DOI: 10.2514/1.27850

Wang, X., Naterer, G., & Bibeau, E. (2007b). Experimental correlation of forced convection heat transfer from a NACA airfoil. *Experimental thermal and fluid science, 31*(8), 1073-1082. DOI: 10.1016/j.expthermflusci.2006.11.008

Wang, X., Naterer, G., & Bibeau, E. (2008a). Convective heat transfer from a NACA airfoil at varying angles of attack. *Journal of Thermophysics and Heat Transfer, 22*(3), 457-463. DOI: 10.2514/1.34405

Wang, X., Naterer, G., & Bibeau, E. (2008b). Multiphase Nusselt Correlation for the Impinging Droplet Heat Flux from a NACA Airfoil. *Journal of Thermophysics and Heat Transfer, 22*(2), 219-226. DOI: 10.2514/1.32401

Watts, M. E., Cross, J. L., & Noonan, K. W. (1988). *Two-dimensional aerodynamic characteristics of the OLS/TAAT airfoil*. Retrieved from Moffett Field, CA, United States: Retrieved from https://ntrs.nasa.gov/search.jsp?R=19890004845

Wie, S. Y., Lee, S., & Lee, D. J. (2009). Potential panel and time-marching free-wake-coupling analysis for helicopter rotor. *Journal of Aircraft, 46*(3), 1030-1041. DOI: 10.2514/1.40001

Wright, W. (2008). *User Manual for LEWICE Ver. 3.2*. Retrieved from Cleveland, Ohio: Retrieved from https://ntrs.nasa.gov/search.jsp?R=20080048307

Yeh, F., Hippensteele, S., & Van Fossen, G. J. (1993). High Reynolds number and turbulence effects on aerodynamics and heattransfer in a turbine cascade. Paper presented at the *29th Joint Propulsion Conference and Exhibit, June 28 - 30 1993* Monterey, CA, U.S.A. Retrieved from 10.2514/6.1993-2252